The Role of Wettability Alteration in Subsurface CO_2 Storage: Modeling and Numerical Analysis

Abay M. Kassa

Thesis for the degree of Philosophiae Doctor (PhD)
University of Bergen, Norway
2021

UNIVERSITY OF BERGEN

The Role of Wettability Alteration in Subsurface CO_2 Storage: Modeling and Numerical Analysis

Abay M. Kassa

Thesis for the degree of Philosophiae Doctor (PhD)
at the University of Bergen

Date of defense: 06.12.2021

Year: 2021

Title: The Role of Wettability Alteration in Subsurface CO_2 Storage: Modeling and Numerical Analysis

Name: Abay M. Kassa

Print: Skipnes Kommunikasjon / University of Bergen

Preface

This dissertation is submitted as a partial fulfillment of the requirements for the degree of Doctor Philosophy (PhD) at the University of Bergen. The advisory committee has consisted of Sarah E. Gasda (NORCE Norwegian Research Centre As), Kundan Kumar (University of Bergen), and Florin A. Radu (University of Bergen).

The PhD project has been financially supported by CHI project (n. 255510) granted through the CLIMIT program of the Research Council of Norway.

Acknowledgments

During my study, I was fortunate to interact with many people from whom I have benefited greatly. It is a great honor to have the opportunity to mention a few of them. First and foremost, my thanks go to Sarah E. Gasda (PhD, Research Director), Kundan Kumar (PhD, Assoc. Prof.) and Florin A. Radu (PhD, Prof.) who have shared their knowledge and experience with me, and brought me in contact with interesting research communities. Their encouragement, active interest in my work, discussion on the topic and appreciation during the entire years have been very indispensable. You have not only been merely great colleagues/supervisors but also friends.

My gratitude also goes to the porous media group at the University of Bergen and Uni Research CIPR (NORCE from 2019) community for welcoming me and helping me to come out of my difficult time, (the time when I lost my wife,i.e., 2018), financially and morally. I am especially grateful to David Landa-Marbán and Abduljelil Kedir who have been supporting and listening to my complaints including many lengthy discussions. I am also grateful to all my co-authors that have contributed to the papers. The financial support from Research Council of Norway through the CHI project (n. 255510) granted is appreciated.

This acknowledgment can not be complete without mentioning Ethiopian community in Bergen. In particular, I would like to thank Mr. Johnathan, Mrs. Hana, Dr. Aklilu, Dr. Akeza, Dr. Teferi, and Mrs. Genet for your support and encouragement.

Abay Molla Kassa
Bergen, August 2021

Abstract

This dissertation is aimed to provide mathematical frameworks to assess large-scale deployment of CO_2 in a subsurface formation, where the formation wettability is assumed to be altering through exposure time to the wettability-altering agent. Particularly, this thesis addresses: upscaling the pore-scale process to the macroscale laws, developing an alternative time stepping method, and quantifying the upscaled models for the subsurface CO_2 storage technology. These three components are organized to investigate and understand the effect of the wettability change on the interaction of CO_2-water in a porous medium.

Wettability refers to the tendency of a fluid to be in contact with the solid surface over the other fluid. This property changes due to many factors (e.g., reservoir temperature, pressure, pH, fluid compositions, and exposure time to the reactive fluid) and the change in wettability is known as *wettability alteration*. Wettability alteration (WA) takes place at the pore scale, but strongly controls the fluid-fluid interaction that is observed at the macroscale. One of the goals of this thesis is to develop a mathematical framework that upscales the effect of exposure time-dependent WA process to Darcy-scale models such as capillary pressure and relative permeability functions also known as *saturation* or *flow* functions. The upscaling processes introduce a pore-scale WA mechanism that follows a sorption-based model as a function of WA agent and exposure time to a WA agent. This model is then coupled with a bundle-of-tubes (BoT) model to simulate time-dependent WA induced capillary pressure and relative permeability data. The resulting saturation functions are then used to quantify the WA induced dynamic components of the saturation functions. More importantly, this part of the study also draws a clear relationship between the pore-scale and upscaled models behaviors.

The developed saturation functions are non-local in time. Coupling these functions adds extra complexity and non-linearity to the solution process of multi-phase flow model. This thesis develops a monotone fixed-point iterative linearization scheme to approximate the solution for the resulting non-standard model. The scheme treats the capillary pressure function semi-implicitly in time and introduces an L-scheme type stabilization term in both the saturation and pressure equations. The convergence of the scheme is proved theoretically. The theoretical convergence analysis and numerical results show that the scheme is linearly convergent. However, the proposed linearization scheme shows flexibility for the choice of time-step size for reasonably large alteration (possibly jumps) in the cap-

illary pressure function (i.e., saturation discontinuity). Furthermore, the scheme is designed so that it can be combined with Newton's method in a straightforward manner. This may improve the convergence rate of the scheme.

The third part of this study concerns the full compositional flow model, where the saturation functions are dependent on solvents (e.g., dissolved CO_2 in water), phase saturation, and exposure time to the solvent. Here, we quantify the role of the exposure time-dependent WA processes on the applicability of CO_2 storage in saline aquifers. To do so, we design horizontal and vertical CO_2-water flow scenarios. For the horizontal flow scenario, we compare the CO_2-water front locations for static (i.e., initial-wet condition) and WA induced dynamic saturation functions based on the capillary number. The analysis shows that the CO_2 front scales well with the capillary number. More precisely, the effect of WA on the CO_2 front movement decreases while the capillary number increases. On the other hand, the integrity of caprock is evaluated with and without WA effects in the saturation functions for the vertical flow scenario. We design a correlation model that can be used to forecast the total CO_2, caused by WA, in the caprock for a given rate of WA dynamics, caprock permeability, entry pressure, and of course time.

Outline

This thesis is organized into two parts. The first part gives an overview of scientific theory and mathematical methods that are relevant to the thesis. The second part contains papers that are either published or submitted for publication in scientific journals.

Part I consists of five chapters. Chapter 1 introduces the concepts related to CO_2 storage technology in different aquifers in which the wettability plays a vital role to control the distribution of CO_2 in the formation. In Chapter 2, we summarize mathematical models for single-phase, multiphase, and compositional flow in porous media. Mathematical frameworks that are used to upscale processes from the pore to the macroscale are discussed in Chapter 3. Chapter 4 is devoted to space-time discretization of the mathematical models introduced in Chapter 2. Finally, a summary of papers, conclusion, and outlook are given in Chapter 5.

Part II contains the following scientific papers:

Paper A A. M. Kassa, S. E. Gasda, K. Kumar, and F. A. Radu. Impact of time-dependent wettability alteration on the dynamics of capillary pressure. *Adv Water Resour*, 142: 1-11, 2020.

Paper B A. M. Kassa, K. Kumar, S. E. Gasda, and F. A. Radu. Modeling of relative permeabilities including dynamic wettability transition zones. *J. Pet. Sci. and Eng.*, 203:1-15, 2021.

Paper C A. M. Kassa, K. Kumar, S. E. Gasda, and F. A. Radu. Implicit linearization scheme for nonstandard two-phase flow in porous media. *Int J Numer Meth Fluids*, 93:445461, 2020.

Paper D A. M. Kassa, S. E. Gasda, D. Landa-Marbán, T. H. Sandve, and K. Kumar. Field-scale impacts of long-term wettability alteration in geological CO_2 storage. *Preprint submitted to Int. J. Greenh. Gas Control.*

Part I

Background

Contents

Part II: Scientific results

Nomenclature

Abbreviations

CO_2	Carbon dioxide
AMs	Arc meniscus
BC	Brooks-Corey
BoT	Bundle-of-tubes
CA	Contact angle
CCS	Carbon capture and storage
conc.	CO_2 concentration
E	CO_2 emissions
FEM	Finite element method
FVM	Finite volume method
Gt	Gigatonne
H&G	Hassanizadeh and Gray
IMPES	Implicit pressure explicit saturation
IPCC	Intergovernmental panel on climate change
LET	Model having parameters L, E, and T

MRST	MATLAB Reservoir Simulation Toolbox
MS-P	Mayer and Stowe and Princen
MTM	Main terminal meniscus
ODE	Ordinary differential equation
OPM	Open Porous Media Toolbox
PDE(s)	Partial differential equation(s)
ppm	Part per million
REV	Representative elementary volume
$scCO_2$	Supper critical carbon dioxide
SFLD	Scaled CO_2-water front location difference
SVC	Sub volume control
TPFA	Two-point flux approximation
WA	Wettability alteration

Superscripts

λ	Pore-size distribution index in Brooks-Corey model
$a_w,\ a_n$	Fitting parameters in Skjæveland model for mixed-wet capillary pressure
e	Effective
f	Final wetting state
i	Iteration step in iterative solvers
in	Initial wetting state
int	Fluid-fluid interface
k	Component index in fluid phases
L, E, T	Fitting parameters in the LET model
$m_{vg},\ n_{vg}$	Fitting parameters in the van Genuchten model

n	The n-th time step
res	Reservoir
st	Static wettability condition
dy	Dynamic
0	Initial condition for simulation time

Subscripts

α	Phase indicator
max	Maximum
min	Minimum
b	Bulk
c	Capillary
ch	Characteristics
cor	Corner
h	Hinging
i, j, k	Index counter
m	The m-th tube
N	Neumann boundary condition
n	Nonwetting phase
p	Pore/void space
r, l	Right and left
rn	Nonwetting-phase residual saturation
rw	Wetting-phase residual saturation
s	Solid phase
T	Total
w	Wetting phase

D	Dirichlet boundary condition

List of symbols

α	The half angle
β	The parameter in the interpolation model
$\chi,\ \overline{\chi}$	Pore-scale and averaged exposure time respectively
δt	Time step size
Δ	Difference operator
$\delta,\ \gamma$	Parameters in the Weibull distribution
$\emptyset$	Empty set
η	Dynamic parameter in the modified LET model
Γ	Boundary (interface in grid block)
λ	Mobility
$\langle \cdot, \cdot \rangle$	Inner product
$\mathbb{D}, \mathrm{D}$	Diffusion coefficient: tensor and scalar
$\mathbb{K}, \mathrm{K}$	Domain permeability: tensor and scalar
$\mathbb{R}$	Real numbers space
$\mathcal{C}a$	Capillary number
$\mathcal{F}$	Source term
$\mathcal{G}$	Conductance
$\mathcal{T}$	Regular decomposition of a porous medium
μ	Fluid viscosity
∇	Gradient operator
$\nabla\cdot$	Divergence operator
Ω	Porous medium domain
ω	The dynamic coefficient in the interpolation model

$\overline{\varphi}$	Maximum surface saturated concentration
$\partial\Omega$	The boundary of Ω
ϕ	Porosity
Φ	The fugasity coefficient
$\pi_{i,j}$	Face pressure at interface i, j for TPFA
ψ	The basis function in the finite element method
ρ	Fluid density
σ	Fluid-fluid interfacial tension
τ	Dynamic coefficient in non-equilibrium saturation functions
τ_o	Tortuosity
θ	Contact angle
φ	The dynamic term in the contact angle model
$\vec{f}$	Smooth vector field function
$\vec{c}$	The length from the center of the cell to the center of cell face
$\vec{g}$	Gravity
$\vec{j}$	The diffusion flux
$\vec{n}$	Unit normal vector
$\vec{u}$	Darcy velocity
ξ	Perturbation parameter
A	Cross-sectional area
a_{v}, b_{v}	The van der Waals constants
a_{ns}	specific inter-facial areas between the fluid-solid interface
a_{wn}	Specific inter-facial areas between the fluid-fluid interface
C	CA model parameter
c	Entry pressure

C^0	A space of continuous functions
cL	Contraction constant in L-scheme and Pseudo monolithic linearization scheme
co	Constant
f	Dynamic term in the saturation functions
g	Smooth function
H^1	A subspace of functions in which their first derivatives are square integrable
J^+	Rate of adsorption
J^-	Rate of desorption
$k_1,\ k_2$	Rate constants for adsorption and desorption processes
k_r	Relative permeability
L	Tube length
L^2	The space of square integrable functions
L_{fnw}	Bounding cross-sectional fluid-fluid length
L_{sn}, L_{sw}	Bounding cross-sectional solid-fluid lengths
N	Node in the finite element discretization
n_c	The number of components in phase α
p	Pressure
pF	Represents the discrete pressure term in the pressure equation
Q	Volumetric flux
q	Influx through the boundary
R	Radius of the inscribed circle
r	Radius of curvature
s	Saturation

sF	Represents the discrete saturation term in the transport equation
T	Temperature
Tr	Half transmissibility
V	Cross-sectional volume
v	Molar mass volume
V_h	Galerkin (discrete) finite element space
w	Weight function
x, y	The position at the porous domain along the lateral direction
y_{rand}	The random variable in Weibull distribution
z	The position at the porous domain in the vertical direction
R	Universal gas constant

Chapter 1

Introduction

The carbon problem refers to the increase of carbon dioxide (CO_2) concentration in the atmosphere and its immediate consequence of shifts in mean global temperature. A systematic climate monitoring shows that the atmospheric CO_2 has been increasing since the industrial revolution [87, 88]. This CO_2 increase is shown by the Keeling curve [88] in Figure 1.1 named after Charles Keeling who initiated the ongoing measurement of the atmospheric CO_2. According to Figure 1.1, atmospheric CO_2 has been increasing in average for over half a century. At the beginning of the measurement, in 1958, the CO_2 concentration in the atmosphere was approximately 315 part per million (ppm) which grew to around 410 ppm in 2018. The CO_2 concentration in the atmosphere increased by 1.62 ppm per year in average since 1950s. Though the causality between CO_2 concentration and global warming leads to research and political debate, overwhelming scientific consensus agrees that accumulation of CO_2 in the atmosphere contributes to global warming [92] which results in climate change. Climate change is one of the greatest threats to the world's ecosystem. Extreme weather events (e.g., drought, storm, heatwave, and flooding), sea-level rise, and disrupted water system are among its numerous possible consequences.

Forestation and substitution of the power plants that emit CO_2 to the atmosphere by renewable energy are thought of as carbon mitigation mechanisms. In 2004, the stabilization wedge was introduced which allude to a measure corresponding to avoidance of 25Gt of CO_2 emission for 50 subsequent years [90, 89]. In Pacala and Socolow [90] proposed a "flat-path" (constant) CO_2 emissions scenarios of the current emission rate over the next 50 years. For example, if the current rate of CO_2 emissions is 16Gt/year, the flat-path model implies that the rate would held constant

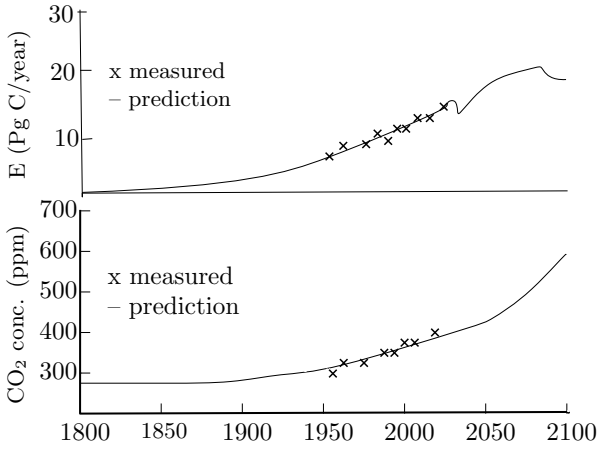

Figure 1.1: Atmospheric carbon dioxide evolution in time measured at Mauna Loa, where "CO_2 conc." and "E" stand for CO_2 concentration and emissions respectively (modified from `https://sioweb.ucsd.edu/programs/keelingcurve/`).

at 16Gt/year for the next 50 years instead of increasing the emission rate. Furthermore, the UN member parties agreed at the Paris summit in December 2015 to take actions toward the possible mitigation of CO_2 with the goal of limiting average warming to 2°C.

The decarbonization of the main sources of CO_2 emission such as coal-fired electricity and heat power plant may decrease the total CO_2 emission by 40%. IPCC report, see `https://www.ipcc.ch/sr15/`, has summarized that an average increase of 1.5 degree and 2 degree scenarios can be achieved by low-carbon technologies. However, poverty and availability of abundant and cheap coal impose anthropogenic energy resources (like coal and petroleum) as a key supply of energy in the market. Due to this, there are more than 3000 operating coal-fired plants and many under construction across the world. This shows that CO_2 emitting plants may continue alive to satisfy the energy demand. As a consequence, alternative CO_2 mitigation strategy (e.g., large-scale subsurface CO_2 storage) is proposed, while allowing coal to meet the world's energy demand.

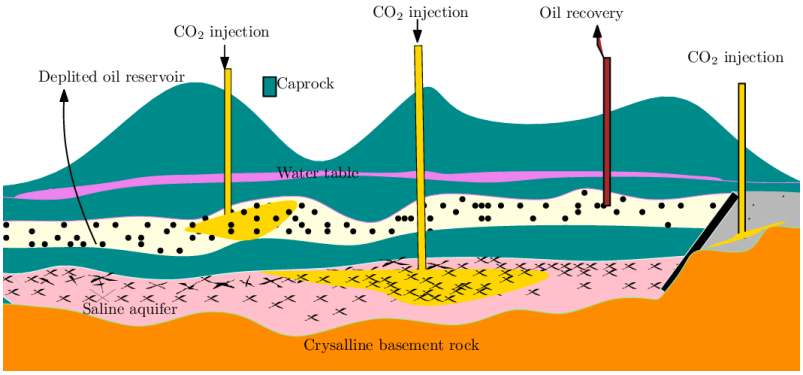

Figure 1.2: Geological formations for possible storage of CO_2, image adapted from IPCC 2005 report

1.1 Carbon capture and storage

Carbon capture and storage (CCS) of anthropogenic CO_2 has been identified as one of the solutions for the carbon problem. It has been argued in [24] that CCS is a global endeavor to tackle climate change and is essential to achieve the climate targets adopted in the Paris agreement. The CCS technology basically involves three steps: (1) capturing of CO_2 before it is released to the atmosphere, (2) transport it to the storage site, and (3) storing the captured CO_2 in underground geological formations. Large-scale CO_2 storage may not be limited by the need for new technological developments. However, it is believed that works on better capture technology would improve the CO_2 storage operation and reduce the capturing cost. This is due to the fact that above 80% of the cost associated with CCS technology goes to the capturing processes and is considered as the limiting factor in the CCS process. In addition, lack of regulatory frameworks and international (or political) agreements are also factors that are slowing the implementation of geological large-scale CO_2 storage application.

Subsurface formations are good candidates to store the captured CO_2. A tremendous storage capacity for large-scale CO_2 sequestration application is available in the subsurface formations. For instance, saline aquifers, unminable coal beds, and depleted hydrocarbon reservoirs are promising sites for subsurface CO_2 storage [57, 87, 89]. The description of these formations are depicted in Figure 1.2. The saline aquifers, saturated with brine, are the deepest formation among others. These formations have

been rarely used to store chemical wastes, and are not fully understood as compared to the depleted oil/gas fields. However, it is known that saline aquifers are the largest candidates, and they are best situated for large-scale CO_2 storage and chemical waste disposal in the world [68, 77, 36]. CO_2 storage in depleting oil fields has been practiced since the era of enhanced oil recovery [4], and is a relatively well understood approach. The interesting part of this approach is that the CCS operation cost might be partly/fully offset by the revenue of the recovered hydrocarbon. We refer to [74] for the pros and cons of storing CO_2 in these two reservoirs.

Subsurface CCS applications rely on four trapping mechanisms: (1) dissolution trapping, (2) mineral trapping through geochemistry reactions, (3) residual trapping, and (4) structural (or hydrodynamic) trapping. Dissolution of CO_2 in brine increases the density of the aqueous phase [54] which balances the buoyancy force, density driven upward flow, and resulting in a downward convective CO_2 saturated water flow. On the other hand, CO_2 can be stored permanently as a cement by chemical reactions between CO_2, active ions dissolved in the brine, and formation minerals. Structural trapping depends on low permeable caprock (e.g., mud rocks, halite, or tight carbonates) that overlays the storage formation. The low-permeable caprock may act as a barrier for buoyant upward CO_2 flow resulting in retention of CO_2 below the caprock, see Figure 1.3, as long as CO_2 is the non-wetting phase to the caprock. Residual trapping occurs due to hysteresis in the relative permeability and capillary pressure functions. These trapping mechanisms occur on different timescales [36]. For example, the dissolution and mineral trapping mechanism are identified as slow processes compared to the structural and residual trapping mechanisms. Due to this, structural and capillary/residual trapping are identified as the most significant physical mechanisms to ensure permanent subsurface CO_2 storage within the geological formation. The latter controls the extent of the relative movement of the CO_2 plume in the subsurface systems which consists of multiple fluids within a pore space, which also determines the storage capacity of the formation. The efficiency of these trapping mechanisms are associated with the wettability of the system. Therefore, understanding the impact of wettability dynamics on CO_2 storage application is of societal relevance.

1.2 Impact of wettability on CO_2 storage

CO_2 is stored in a formation secured by a low permeable caprock. Figure 1.3 is an example of such CO_2 storage formations. Since CO_2 is less dense

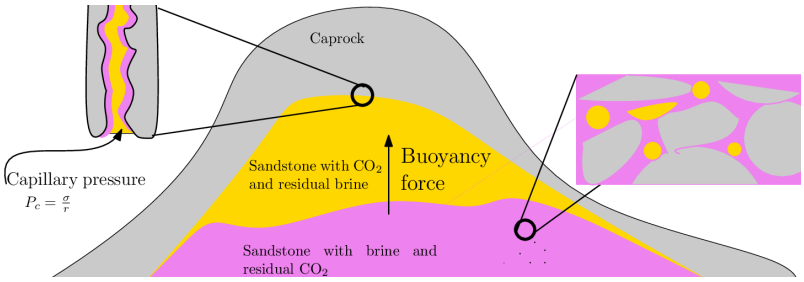

Figure 1.3: Pressures acting on a fluid column at the reservoir-seal interface for structural trapping. If CO_2 has migrated upward through the underlying water column then a fraction of the CO_2 is residually trapped in the pore space of the reservoir rock.

than the formation fluid, the buoyancy force pushes the CO_2 towards the caprock as illustrated in Figure 1.3. This buoyant fluid exerts a force from below onto the caprock to enter into the caprock pores [52]. The sustainability of the storage capacity of the caprock is determined by its wettability. Wettability refers to the tendency of one fluid over the other to spread on or adhere to a solid surface. It controls the entrance of CO_2 to the caprock pores.

In general, wettability is one of the main determining factors in CO_2-water flow in a porous medium [39, 52]. This pore-scale property regulates the distribution and migration of CO_2 in the subsurface system [8, 18, 39, 19]. In other words, a CO_2 profile in the reservoir and its eventual invasion of the brine saturated caprock is determined by the (surface) wetting ability of CO_2. For example, strong water-wet condition results in a high (positive) capillary force. In this case, CO_2 bubbles render to be immobilized [36]. In contrast, the capillary force falls below zero for intermediate and hydrophobic conditions. In this case, the original non-wetting phase (i.e., CO_2 in our case) may spontaneously invade the caprock. These all imply that CO_2-water distribution might be affected by wettability alteration (WA).

There are many chemical and physical processes that lead to a WA [52, 53, 112, 113]. Exposure to the composition of fluids is considered as one of the leading factor for WA process. For instance, the composition of CO_2 provokes the surface within the pores to undergo a WA [116, 3, 117, 112]. Usually, WA is assumed to occur instantaneously and is described as a function of the altering agent concentration. However, in some cases,

it might take prolonged time in the scale of weeks and months [23, 95, 112, 117] to observe WA. Such WA occurs when surface processes such as adsorption or chemical alteration are gradual rather than spontaneous. In this case, WA depends on exposure time to the wettability-altering agent in addition to the wettability-altering agent itself. WA is measured by the fluid-fluid contact angle (CA). Though there is no explicit time-dependent CA measurements for CO_2-water, repeated drainage-imbibition capillary pressure measurements show a clear reduction in capillary pressure curves over time [92, 112, 113, 115, 116]. The authors attributed these deviations from the expected capillary curve to a WA of the rock sample due to long-term CO_2 exposure, similar to aging [95]. This hypothesis was confirmed through observations of a wetting angle increase from 0° to 75° after 6 months of exposure time.

Core-flooding experiments [65, 112, 117, 115] reported that WA is a critical factor in geological CO_2 storage processes. The WA may put the performance of the caprock in question by altering the strength of the capillary force directly at the pore level. If CO_2 is a non-wetting phase, the capillarity acts to trap CO_2 beneath the low permeable (brine saturated) caprock [55, 65, 112]. Altering the wetting property may weaken the capillary force (see Figure 1.3) of the caprock and may lead to CO_2 invasion of the caprock. This implies that wettability change might be a threat for CO_2 applications. In contrast, WA may retard the movement of CO_2 plume. That is, CO_2 may displace the resident fluid when the wettability is altered to intermediate/CO_2-wet condition, particularly for lateral flow. This increases the storage capacity of the storage formation.

Despite the fact that the above experimental studies were performed at the steady-state condition, the measured capillary pressure curves showed non-static behavior in time. This implies that standard saturation functions (e.g., the van Genuchten [44] and Brooks-Corey [22]) may not well suited for saturation functions under long-term WA processes. Furthermore, in [92], imbibition measurements for gaseous and scCO_2-water systems did not match after scaling by interfacial tension. Similarly, Tokunaga et al. [112] reported that coalescence was not achieved, for both drainage and imbibition capillary pressures after scaling by interfacial tension. This implies that classical scaling techniques are not capable to explain the capillary pressure–saturation path deviations. These all show that standard saturation functions cannot be readily applied without additional dynamics to capture the impact of wettability change in the CO_2 storage application.

In general, WA shifts the pore draining or imbibing/filling sequences, i.e., which pore or throat should be drained or imbibed first during fluid

displacements. The shift in pore-filling order impacts averaged quantities such as residual saturation, capillary pressure, and relative permeabilities functions. This process is also observed in pore-scale drainage and imbibition displacement experiments [2, 51, 61, 64]. The shift in averaged quantities, in turn, affect containment of CO_2 at the field scale. Therefore, a unified characterization of wettability dynamics in the CO_2-water system is needed for safe and efficient CO_2 storage.

Studying and characterizing the impact of exposure time-dependent WA on the dynamics and fate of CO_2 plume in a subsurface system is important. The impact of WA on the fate of CO_2 plume can be characterized from laboratory experiments. However, these approaches are time and resource consuming. Furthermore, laboratory experiments are only applied in small scales (e.g., centimeters). Due to these, modeling and numerical simulations can be employed to predict the injected CO_2 plume behavior. As we discussed above, wettability is a pore-scale process and highly associated with capillarity and relative movement of fluids in a pore network. As a consequence, one may consider detailed pore-scale simulations to evaluate the CO_2-water interaction under time-dependent WA process. However, the pore-scale simulation is only possible in the scale of millimeters. That means, applying pore-scale simulation for large-scale CO_2 deployment is not possible. Therefore, systematic upscaling of the impact of dynamic wettability change into the relative permeability–and capillary pressure–saturation relationships is an important step towards understanding the risk and opportunities of CO_2 storage applications.

1.2.1 Wettability upscaling procedures

Upscaling is a process of transforming small-scale phenomenon, e.g., pore scale to a larger scale, e.g., core scale, through averaging techniques. In this thesis, volume averaging is employed to upscale the effect of time-dependent WA through the saturation functions [29, 13]. The following are the main steps we follow:

- First of all we choose the pore-scale model that represent a porous medium. For this particular study, we choose a bundle-of-capillary-tubes model because it is simple to implement and captures the necessary physics to upscale the WA effect in the saturation functions. Furthermore, the simulation process takes short time and thus we can generate many drainage-imbibition data for saturation functions.

- Once we choose the pore-scale model, the next step is designing a reliable wettability model. We describe wettability dynamics at the

pore scale using a mechanistic model for CA change as a function of exposure time to a wettability-altering agent. The model is developed based on the insights from laboratory experiments, giving the flexibility to incorporate other data if necessary.

- The designed wettability model is then coupled with a bundle-of-tubes model through the Washburn equation [118]. The fully coupled model is employed to simulate WA induced saturation functions and associated quantities.
- After designing the dynamic pore-scale model, we simulate numbers of drainage-imbibition displacements data to capture the trends in the saturation functions. Then, we calculate averaged quantities such as phase saturation, averaged capillary pressure, flux, and phase relative permeability data.
- We used the simulated data to analyze the impact of WA on the core-scale capillary pressure and relative permeabilities. Then we design a reliable core-scale models that capture WA induced dynamic components in the saturation functions. Here, the term “reliable" refers to the ability to predict time-dependent capillary pressure and relative permeabilities curves with a few numbers of fitting parameters.
- Once we design the dynamic saturation functions, we calibrate the fitted models with generic paths in the saturation-time domain to examine the robustness of the developed models. Finally, we study the relation between the upscaled models parameters and the parameter controlling rate of change of wettability over time at the pore scale.

These steps are applied one after the other to develop WA induced dynamic capillary pressure and phase relative permeability functions. These upscaled dynamic saturation functions can be then coupled with large-scale models for CO_2 storage applications. Numerical modeling and simulations are applied on the resulting dynamic CO_2-water flow model to evaluate the impact of exposure time-dependent WA on the subsurface CO_2 plume movement at the scale of meters and kilometers.

1.3 Importance of mathematical modeling and its challenges

CO_2 storage applications are situated in deep subsurface systems covering in cubic kilometers and thus, it is difficult (if not possible at all) to

perform laboratory experiments in a such scale. As a consequence, mathematical modeling and simulations have been used as a key technology to explore and investigate the CO_2-water (or multi-phase flow ingeneral) flow dynamics and properties in a reservoir scale [88].

Generally, the multi-phase flow problems in a porous medium can be modeled by a system of coupled non-linear, possibly degenerate, transient partial differential equations derived from Darcy's law and mass conservation equations [50, 20, 99, 73]. Usually, assumptions are made to simplify the complexity of models that functionally represent the physical problem. However, over simplified models may lead to a wrong prediction of the migration of CO_2 plume and CO_2 affected fluids in a storage reservoir. Demonstration of such fluid flow prediction should involve simulation models relying on translating physics into tractable mathematical formulations. A unified, theoretical and numerical, analysis of the advanced mathematical formulation would provide insights that can mimic realistic processes in the reservoir system and guidance that are important for the original problem. This thesis, for instance, considers an injection of CO_2 into brine saturated saline aquifers, where the wettability of the aquifers is assumed to be changing over time. Obviously, the inclusion of wettability change imposes an extra (dynamic) non-linearity and adds complexity (e.g., non-locality in time) to the saturation functions and thus, in the large-scale CO_2-water flow model.

The non-linearity and non-locality (in time) of the model imposes a challenge for the solution processes. Usually, it is impossible to draw qualitative analysis for such mathematical models, and it is quite challenging to develop robust numerical schemes. The subsurface multi-phase flow applications are performed in a complex porous geological formations and are long-term processes. These also bring extra challenge for the solution and analysis of the model. Nevertheless, this thesis explores the impact of time-dependent WA process on CO_2 plume movement in complex geometries through numerical experiments: from the pore to the macroscale.

1.4 Thesis contribution

In this work, our interest is to investigate the impact of wettability evolution on the fate of CO_2 in the subsurface flow processes. In Section 1.2, we have learned that the impact of WA on immiscible fluids systems is potentially significant. Building novel mathematical models that consider the dynamic WA mechanism is necessary to enhance the prediction of the CO_2 evolution in a subsurface system. This thesis covers the development

of mathematical models and simulation technologies in CO_2-water flow in porous media including the changes in wettability over exposure time to the WA agent. Specifically,

1. **Development of dynamic models.** We propose a strategy to upscale pore-scale time-dependent WA dynamics to a Darcy-scale through saturation functions. To do so, we introduce a time-dependent CA change model at the pore-level, where the pore-scale model is represented by a bundle-of-tubes model. The resulting dynamic pore-scale model is used to simulate capillary pressure and relative permeability curves. The simulated data has been used to develop mathematical models to predict the dynamics of capillary pressure and relative permeabilities for a porous medium that changes its wettability according to exposure time to WA agent. The developed models are independent of the numbers of drainage-imbibition displacements. Furthermore, these studies show the relation between the pore-scale and upscaled model parameters.

2. **Development of a linearization scheme for a non-local (in time) two-phase flow model.** The WA process introduces non-local terms in time on the top-of equilibrium capillary pressure-saturation (P_c-s_α) and relative permeability-saturation ($k_{r\alpha}$-s_α) relationships. Coupling these models with two-phase mass balance equations would result in a non-standard model. We propose a linearization scheme, inexact Newton's method, to solve the resulting non-standard two-phase flow model. The scheme treats the non-linearity in the capillary pressure function semi-implicitly in time while other non-linearities are up-winded from the previous iteration. We prove the linear convergence of the scheme theoretically and verify it with numerical examples. The numerical experiments show the flexibility of the proposed scheme over the iterative implicit pressure explicit saturation method on the choice of time-step size.

3. **Simulation and WA quantification.** The role of time-dependent WA process on the fate of CO_2 is analyzed through numerical simulations. The time-dependent WA effect is included into the two-phase two-component (TPTC) flow model through the saturation functions. The resulting model is then used to quantify how WA affects the migration of CO_2. For this purpose, we design two scenarios: horizontal and vertical CO_2-water flow. A non-dimensional grouping, i.e., capillary number ($\mathcal{C}a$) is used to quantify the WA effect in the horizontal CO_2-water flow scenario. This study shows

that WA dynamics in both saturation functions, P_c and $k_{r\alpha}$, affect the fluid flow for low capillary number flow regimes. Furthermore, we observe a clear relation between WA and the advancing CO2-water front that scales with capillary number. On the other hand, the vertical flow scenario is designed to quantify the effect of WA on caprock containment. Similar to the horizontal case, we test a range of different model parameters in order to characterize and quantify the independent and combined effect of P_c and $k_{r\alpha}$ alteration on the CO_2-water redistribution. We obtained a scaling relation to predict the CO_2 mass in the caprock over time as a function of caprock properties (i.e., permeability and initial wetting-state entry pressure) and rate of change of wettability.

Chapter 2

Mathematical models

In this chapter, we will introduce mathematical models that are used to describe the interactions of multiple fluids in porous media. We start with the mass conservation law for single-phase flow in porous media. Then we extend the single-phase flow model to describe two-phase multi-component flow processes. In order to develop a set of equations to describe flow processes in a porous medium, we need to introduce basic definitions and properties of the fluids and rock materials.

2.1 Fluid and rock properties

In this section, basic porous media parameters and properties are introduced and highlighted. After introducing the basic definitions, the formulation of mass balance laws for single and multiple fluids are presented to provide a foundation for the modeling aspect of the porous media flow.

2.1.1 Porous media

A site for CO_2 storage comprises a solid part, known as skeleton, and interconnected pores that allow fluids to breakthrough. Such a material is called porous medium. The void spaces can be filled with single or multiple fluids. Typical examples of a porous medium includes the soil, foam rubber, and human organs (e.g., lungs, brain, and kidneys) to name a few. An exemplary porous medium is illustrated in Figure 2.1. In practice, a real porous medium is complex. The complexity is derived due to the scale, pore-scale to macroscale, differences within a single porous domain

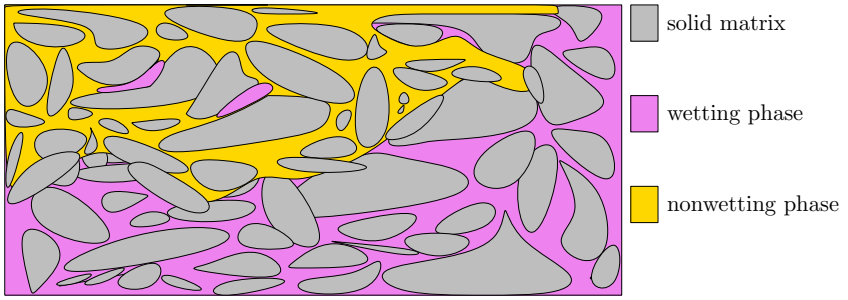

Figure 2.1: Schematic representation of a porous medium saturated by two fluids.

[88]. It is not possible to describe the flow processes point-wisely in such complex material. Rather, a *representative elementary volume* (REV), the smallest volume which contains a representative void and skeleton, is used to define mean properties of the domain locally [15]. Thus, we used averaged quantities (porosity and permeability) to describe porous media properties.

We define the porosity, $\phi(\vec{x}, t)$, as the fraction of voids available for fluids, and stated as:

$$\phi = \frac{\text{Volume of voids in the REV}}{\text{Volume of REV}}. \tag{2.1}$$

The porosity is a dimensionless averaged quantity which ranges from zero to one. Thus, $1-\phi$ represents the solid skeleton of the REV. If the porosity depends on the location, the medium is called *heterogeneous*, otherwise it is known as *homogeneous*.

Another important property of a porous medium is its ability to allow fluids to flow through the pores. This property is called intrinsic permeability. The permeability has a complex relation with the porosity of a medium and usually the Kozeny-Carman equation [28] is used to define their connection. However, the permeability might depend on the flux direction in addition to the location. Due to this, the permeability is usually represented as a tensor:

$$\mathbb{K} = \begin{pmatrix} \mathrm{K}_{xx} & \mathrm{K}_{xy} & \mathrm{K}_{xz} \\ \mathrm{K}_{\mathrm{yx}} & \mathrm{K}_{yy} & \mathrm{K}_{yz} \\ \mathrm{K}_{\mathrm{zx}} & \mathrm{K}_{zy} & \mathrm{K}_{zz} \end{pmatrix}, \tag{2.2}$$

for a 3D domain. The permeability tensor, $\mathbb{K}$, is symmetric and positive definite and has a unit of meter square (m^2) or Darcy (D), where 1D =

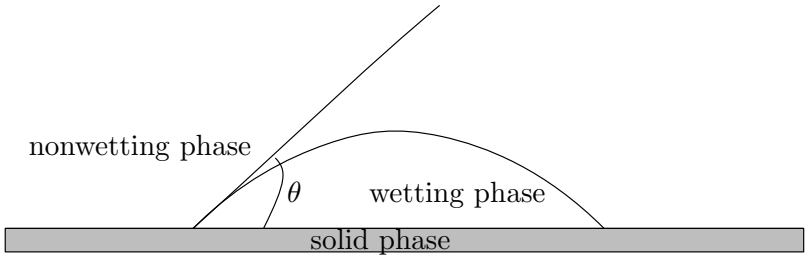

Figure 2.2: The contact angle between wetting and non-wetting phases.

$9.8 \times 10^{-12}\mathrm{m}^2$. If the permeability of a porous medium depends on the direction of the flux, the medium is called *anisotropic*, otherwise it is known as *isotropic*. On the other side, part of a porous medium may not allow fluids to flow through and this is refereed to as *impermeable*. Note that we will use the notations $\mathbb{K}$ and K interchangeably for a tensor and scalar permeability.

2.1.2 Phase, component, and wettability

A phase can be defined as a chemically homogeneous quantity that is separated by a sharp interface from the other quantity that has its own chemical homogeneity [14]. In this regards, multiple immiscible fluids coexist in a void space to form a *multi-phase* system and we call each fluid a phase of the system. If the solubility (solubility is the process of the existence of one phase as a fraction of component in the other phase) is considered, the system is known as a compositional multi-phase system. In this thesis, we only consider two phase and two components to describe CO_2 migration in porous media.

Wettability is an important property that is used to describe if a phase is wetting or non-wetting to the solid surface. The wetting property is measured by the contact angle (CA) created between the fluid-fluid interface and solid surface, see Figure 2.2. By convention, the CA (θ) is measured from the denser fluid. Nevertheless, the fluid that tends to be in contact with the solid surface is called wetting phase if $\theta < 90°$. If $\theta > 90°$, the fluid is considered as a non-wetting phase for the system. Nevertheless, CA at a three-phase contact line is determined by a balance of surface tensions [78]. Formally, the CA on the isotropic and homogeneous surface is related with the surface tensions by the Young's law:

$$\sigma_{sn} - \sigma_{sw} = \sigma \cos(\theta), \tag{2.3}$$

where σ_{sn}, σ_{sw}, and σ are the solid-non-wetting, solid-wetting and wetting-non-wetting interfacial force respectively. This surface tension interaction between the solid and the fluids may be altered. The wetting property alteration and its upscaling processes is discussed in detail in Chapter 3.

Residual and effective saturations

The saturation of a phase $\alpha \in \{w, n\}$ is defined as the volume fraction of the void occupied by phase α. Mathematically, the phase α saturation is given as:

$$s_\alpha = \frac{V_\alpha}{V_p}, \tag{2.4}$$

where V_α is the volume of the phase α in the REV and V_p represents the volume of the void space in the REV.

In fluid displacements, there are basically two scenarios: drainage and imbibition. A drainage process is a displacement in which the non-wetting phase displaces the wetting phase, resulting in a wetting phase saturation decease up to a stationary saturation profile. This stationary saturation is called wetting phase *residual/irreducible* saturation and can be denoted as s_{rw}. The imbibition displacement, a process in which the wetting phase displaces the non-wetting phase, increases the wetting phase up to a state where further increase is not possible. This process results in a non-wetting phase residual saturation and is denoted as s_{rn}. Now we define the effective phase saturation as:

$$s^e_\alpha = \frac{s_\alpha - s_{r\alpha}}{1 - s_{rw} - s_{rn}}, \tag{2.5}$$

where $s_{r\alpha}$ is the phase α residual saturation. Enhanced strategies should be applied to mobilize the residual saturation. The effective saturation coincides with the phase saturation if the residual saturations are mobilized (i.e., $s_{r\alpha} = 0$). For brevity, the phase saturation, s_α, is used for the modeling and analysis purposes in this thesis.

2.1.3 Fluid properties

The density and viscosity of a fluid are essential physical properties to describe flow process in porous media.

Density

Fluids (liquid and gas) in a porous medium are composed of molecules with a certain mass and space between them. This implies that a given

fluid has a volume and mass in terms of particles (at macroscale) in which we can associate with the density as:

$$\rho(x,t) = \frac{m}{\Omega}, \tag{2.6}$$

where $\Omega(x,t)$ is a volume and m is the mass of particles contained in the volume. Note that the density of a pure substance may depend on temperature and pressure. The density usually increases with increasing pressure and decreasing temperature [16]. The density also depends on the compositions of the phases.

Viscosity

The fluid can also be characterized by its viscosity. The viscosity, μ, can be considered as an internal frictional force that controls the fluids relative movement on the solid surface. The viscosity may also depend on the pressure, composition of phases, and temperature distribution.

2.2 Mass conservation

Conservation of mass is the basic principle that is applied to develop governing equations for a fluid flow in a porous medium. A mass in a volume Ω is said to be conserved if the mass added/lost at time t_1 is equivalent to the mass at time t_2 [87], i.e., a volume Ω that contains the same set of fluid particles at time t_2 as it did for arbitrary time t_1. This implies that the mass entered into the volume is balanced by the mass leaving the volume. This can be described mathematically by the Eulerian description as:

$$\int_{\Omega} \frac{\partial}{\partial t}(\phi\rho)dV + \int_{\partial\Omega} (\rho\vec{u}) \cdot \vec{n} dS = \int_{\Omega} \mathcal{F} dV, \tag{2.7}$$

where $\vec{u}$ represents the mass flux and $\vec{n}$ denotes the unit vector normal to the boundary surface $\partial\Omega$. We say Equation (2.7) is a mass conservation equation when the term $\mathcal{F}$ is either zero (no source or sink) or associated with an external source. If $\mathcal{F}$ represents internal changes to the system, we say Equation (2.7) is a mass balance law or transport equation.

The surface integral term in Equation (2.7) can be replaced with a volume integral by applying the Gauss's divergence theorem, which reads as:

$$\int_{\Omega} \nabla \cdot \vec{f} dV = \int_{\partial\Omega} \vec{f} \cdot \vec{n} dS, \tag{2.8}$$

for a smooth function $\vec{f}$. Using this relation and assuming the integrands in Equation (2.7) are smooth, Equation (2.7) can be described in volume integral form:

$$\int_{\Omega} \Big[\frac{\partial}{\partial t}(\phi\rho) + \nabla \cdot (\rho \vec{u}) - \mathcal{F}\Big] dV = 0. \tag{2.9}$$

The integral in Equation (2.9) holds for any arbitrary volume Ω, and thus the integral (2.9) is valid independent of the integration volume. This implies that the integrand should be zero in Ω and time. Thus we obtain the mass conservation equation in differential form:

$$\frac{\partial}{\partial t}(\phi\rho) + \nabla \cdot (\rho \vec{u}) = \mathcal{F}. \tag{2.10}$$

Equation (2.10) is used to describe compressible single-phase flow in a compressible medium. Numbers of possible simplification of this model can be found in [88]. For example, if we consider an incompressible fluid and assume the porosity is independent of time, that is:

$$\frac{\partial}{\partial t}(\phi\rho) + \vec{u} \cdot \nabla\rho = 0, \tag{2.11}$$

then the mass conservation Equation (2.10) can be reduced to:

$$\rho \nabla \cdot \vec{u} = \mathcal{F}. \tag{2.12}$$

Equation (2.12) is known as the continuity equation for incompressible fluid in an incompressible porous medium. The volumetric flux, $\vec{u}$, can be related with the pressure gradient using the Darcy's law [88].

2.3 Darcy's law

In 1856, a French engineer named Henry Darcy derived a constitutive equation that relates the volumetric flux ($\vec{u}$) to the pressure gradient linearly. Since then there have been many extensions done on the Darcy's model to describe flow in a porous medium. The Darcy's law for a single-phase flow, in its general form, can be read as:

$$\vec{u} = -\frac{\mathrm{K}}{\mu}\Big(\nabla p + \rho \vec{g} \nabla z\Big), \tag{2.13}$$

where K is the permeability of the porous medium, μ is the dynamic viscosity of the fluid, z is the vertical position in Ω and $\vec{g}$ is the gravity

vector. The term, $\nabla p + \rho \vec{g} \nabla z$, represents the force per volume acting on the fluid. Similar to the Newton's second law of motion, the Darcy's law in Equation (2.13) relates the movement of an object with the force applied on it. Note that Darcy has derived Equation (2.13) empirically from experimental observations; however, a similar model can be derived by applying volume averaging analysis on the Stokes Equation [69].

The general mass balance Equation (2.10) and the Darcy's law (2.13) can be combined to model the flow behavior and it reads as:

$$\frac{\partial}{\partial t}(\phi\rho) + \nabla \cdot \Big[\rho \frac{\mathrm{K}}{\mu}\big(\nabla p + \rho \vec{g} \nabla z\big)\Big] = \mathcal{F}. \tag{2.14}$$

Equation (2.14) represents a mass conservation law for general single-phase flow in a porous medium. Similarly, Equation (2.12) and the Darcy's law above can be coupled to represent the continuity equation in terms of reservoir pressure for incompressible system.

2.4 Boundary and initial conditions

The mass balance equation introduced above can be closed with appropriate boundary and initial conditions. The boundary conditions are used to determine the mass in/out to the system, while the initial condition describes the behavior of the system before an extraction or injection operation is performed.

In this thesis, the boundary conditions are given either by the Neumann or Dirichlet condition. The Neumann condition is used to describe the mass (in or out) flux through the boundary (say Γ_N):

$$\vec{u} \cdot \vec{n} = q \qquad \text{on } \Gamma_N, \tag{2.15}$$

where q is the amount of fluid that crosses the boundary. The $q > 0$ is set for the fluid influxes to the domain and $q < 0$ when the fluid leaves the domain. If the boundary does not allow the fluid to flow across the boundary, the condition is called no-flow condition. This condition is represented by the homogeneous Neumann condition, i.e., $q = 0$.

If a porous medium, Ω, boundary (say Γ_D) is connected to other porous media, the Dirichlet boundary condition can be set as:

$$p = p_D \qquad \text{on } \Gamma_D. \tag{2.16}$$

For the above mass balance equation, one can impose an initial condition of the reservoir in the form of:

$$p = p^0 \qquad \text{in } \Omega. \tag{2.17}$$

2.5 Extension to two-phase flow

In this section, we will consider two immiscible fluids, say water and CO_2, in a porous medium. To this end, for each phase $\alpha \in \{w, n\}$, where w and n stand for wetting (water) and non-wetting fluid (CO_2) respectively, the phase Darcy's flux $\vec{u} : \Omega \times [0, t^f] \to \mathbb{R}^d$, for $d = 2, 3$ is given by:

$$\vec{u}_\alpha = -\lambda_\alpha \big(\nabla p_\alpha - \rho_\alpha \vec{g} \nabla z\big), \tag{2.18}$$

where $\lambda_\alpha : \Omega \times [0, t^f] \to \mathbb{R}$ is the phase α mobility. The phase mobility is defined as $\lambda_\alpha = \frac{\mathrm{K} k_{r\alpha}}{\mu_\alpha}$, where $k_{r\alpha}(\cdot, s_w) \in [0, 1]$ is the phase α relative permeability.

For each phase α, the mass balance for immiscible fluids is directly adopted from the single-phase mass conservation equation:

$$\partial_t(\phi \rho_\alpha s_\alpha) + \nabla \cdot (\rho_\alpha \vec{u}_\alpha) = \mathcal{F}_\alpha, \text{ in } \Omega, \tag{2.19}$$

where $\mathcal{F}_\alpha$ is the phase α source or sink term. From (2.18) and (2.19), we obtained two equations with four unknown variables. To close the system two constraints must be satisfied. These constraints are:

$$s_w + s_n = 1, \tag{2.20}$$

and

$$p_n - p_w = P_c(s_w), \tag{2.21}$$

where P_c is the capillary pressure relating the phase saturation to the phases pressure difference. Equations (2.18)-(2.21) with appropriate initial and boundary conditions are used to describe two-phase flow dynamics in a porous medium.

2.5.1 Elliptic-parabolic formulation

The simplest model for two-phase flow in a porous medium is obtained by assuming incompressible fluids and the porosity is independent of time. In this case, Equation (2.19) can be rewritten as:

$$\phi \partial_t s_\alpha + \nabla \cdot \vec{u}_\alpha = \frac{\mathcal{F}_\alpha}{\rho_\alpha}. \tag{2.22}$$

Summing up the mass balance models in Equation (2.19) over phases would give an elliptic equation usually termed as pressure equation:

$$-\nabla \cdot \Big[\lambda_T \nabla p_n - \lambda_w \nabla P_c - (\lambda_w \rho_w + \lambda_n \rho_w) \vec{g} \nabla z\Big] = \sum_\alpha \frac{\mathcal{F}_\alpha}{\rho_\alpha}, \tag{2.23}$$

where $\lambda_T = \lambda_w + \lambda_n$ is the total mobility. In Equation (2.23), we have one equation and two unknowns namely p_n and s_w. As a consequence, the transport equation for the wetting or non-wetting phase saturation should be coupled with Equation (2.23) to close the system. Therefore, we get a system of two equations with two unknowns:

$$-\nabla \cdot \Big[\lambda_T \nabla p_n - \lambda_w \nabla P_c - (\lambda_w \rho_w + \lambda_n \rho_n)\, \vec{g} \nabla z\Big] = \mathcal{F}_T, \tag{2.24a}$$

$$\phi \partial_t s_w - \nabla \cdot \lambda_w \Big[\nabla p_n - \nabla P_c - \rho_w \vec{g} \nabla z\Big] = \mathcal{F}_w, \tag{2.24b}$$

where $\mathcal{F}_T = \frac{\mathcal{F}_w}{\rho_w} + \frac{\mathcal{F}_n}{\rho_n}$ is the total source and $\mathcal{F}_w = \frac{\mathcal{F}_w}{\rho_w}$ is the wetting phase source/sink term. This formulation is important for splitting-schemes, see Chapter 4. Note that, the two-phase flow model introduced above represents a single component in each phase. However, extension to a multi-component flow model is straightforward. The following section introduces a Darcy-scale two-phase two-component flow in a porous medium.

2.6 Two-phase two-component flow model

A fluid phase may consist of more than one component, that can be either pure chemical substances or consists of several substances which form a mixture [41]. Thus, the fractions of different components contained in a phase α determine its composition of phase α. The mass fraction, X_α^k, in phase α is defined as a ratio of mass of component k to the total mass of phase α, i.e.,

$$X_\alpha^k = \frac{m^k}{\sum_k m^k}. \tag{2.25}$$

Now assuming mass transfer between phases and allowing each phase to comprise more than one component, the mass conservation equation for two-phase flow can be extended to describe component, $k \in \{\mathrm{CO}_2, \mathrm{water}\}$, mass balance:

$$\phi \sum_\alpha \partial_t (\rho_\alpha s_\alpha X_\alpha^k) + \sum_\alpha \nabla \cdot (\rho_\alpha X_\alpha^k \vec{u}_\alpha + \vec{j}_\alpha^{\,k}) = \mathcal{F}^k \text{ in } \Omega, \tag{2.26}$$

where $\mathcal{F}^k$ is representing the external source/sink term of component k in phase α, and $\vec{j}_\alpha^{\,k}$ is a component k diffusion flux in phase α. The diffusion flux [108] in phase α, $\vec{j}_\alpha^{\,k}$, is given by the Fick's law in the form of:

$$\vec{j}_\alpha^{\,k} = -\rho_\alpha \mathbb{D}_\alpha^k \tau_{o\alpha} \nabla X_\alpha^k, \tag{2.27}$$

where $\mathbb{D}_\alpha^k$ is the dispersion coefficient. Note again that we may use $\mathbb{D}_\alpha^k$ and/or just D_α^k interchangeably respectively for the tensor and scalar diffusion coefficient. According to Millington and Quirk [81] the tortuosity, $\tau_{o\alpha}$, can be related with phase saturation and domain porosity as:

$$\tau_{o\alpha} = \frac{(\phi s_\alpha)^{2.3}}{\phi^2}. \tag{2.28}$$

The phase pressures difference, the sum of saturations in Equation (2.20), and the sum of mass fractions:

$$\sum_k X_\alpha^k = 1 \tag{2.29}$$

contributes additional three Equations. The rest of the equations can be complemented from the phase equilibrium equations and the system is supplemented with appropriate initial and boundary conditions.

2.6.1 Phase equilibria

The two-phase compositional flow model is closed by the phase equilibrium condition. The thermodynamic equilibrium criterion dictates a minimum of the Gibbs free energy at constant pressure, temperature, and composition. The mathematical description of the state of thermodynamic equilibrium can be given as:

$$f_w^k(p, T, X_w^k) = f_n^k(p, T, X_n^k),\ k = 1, 2, \ldots, m \tag{2.30}$$

for a composition of m components in phase α. Here, f_α^k is the fugasity of component k in phase α, and is defined as:

$$f_\alpha^k = \Phi_\alpha^k X_\alpha^k p_\alpha^k, \tag{2.31}$$

where Φ_α^k is the *fugacity coefficient* [102]. Fugacity coefficients are calculated from equations of state (EOS), which establish a relationship between pressure, molar volume, and temperature. The simplest EOS is the ideal gas law:

$$pv = \mathrm{R}T, \tag{2.32}$$

where R is the universal gas constant and v is the molar volume. In 1873, J.D. van der Waals proposed the EOS including the repulsive and attractive forces [16]:

$$pv = \frac{\mathrm{R}Tv}{v - b_\mathrm{v}} - \frac{a_\mathrm{v}}{v}, \tag{2.33}$$

where a_{v} and b_{v} are the van der Waals constants. The attractive force term, $\frac{a_{\mathrm{v}}}{v}$ in the van der Waals EOS, is modified by Redlich and Kwong in 1949 [101] to include the temperature effect in the EOS. Furthermore, an other extension of the van der Waals EOS is proposed by Peng and Robinson in 1976 [91]. This approach also modifies the attraction force. The detailed overview regarding the different EOS can be found in [93].

The system (2.26)-(2.31) can be completed with appropriate boundary and initial conditions, and the resulting closed system can be solved with appropriate numerical methods.

2.6.2 Boundary and initial conditions

The initial conditions of the compositional flow system can be given as

$$p_\alpha(\cdot,0) = p_\alpha^0(\cdot),\ s_\alpha(\cdot,0) = s_\alpha^0(\cdot),\ \text{and}\ X_\alpha^k(\cdot,0) = X_\alpha^{k,0} \qquad \text{in } \Omega. \quad (2.34)$$

One can assume that the boundary of the system is divided into disjoint sets such that $\partial\Omega = \Gamma_D \cup \Gamma_N$. We denote by $\vec{n}$ the outward unit vector normal to $\partial\Omega$, and set the boundary conditions as:

$$p_\alpha = p_{\alpha,D},\ s_\alpha = s_{\alpha,D},\ \text{on } \Gamma_D \times (0,t^f], \quad (2.35)$$

$$\vec{u}_\alpha = q_\alpha,\ \text{on } \Gamma_N \times (0,t^f], \quad (2.36)$$

where $q_\alpha \in \mathbb{R}^d$ is the phase inflow rate. In order to make the model uniquely determined, it is required that $\Gamma_D \neq \emptyset$.

2.7 Saturation functions

The capillary pressure, P_c, and phase relative permeability, $k_{r\alpha}$, are related with the wetting-phase saturation heuristically for equilibrium flow and uniformly wetted medium. The Brooks-Corey [22] and the van Genuchten [44] models are the most commonly applied saturation functions for such systems. Both, the Brooks-Corey and van Genuchten functions, are developed with the assumption that the porous medium in consideration is homogeneous in terms of wettability. Under this condition, Brooks and Corey [22] capillary pressure model reads as:

$$P_c^{st}(s_w) = c s_w^{-\frac{1}{\lambda}}, \quad (2.37)$$

whereas the phase relative permeability-saturation relationship is described as:

$$k_{rw}^{st} = s_w^{\frac{2+3\lambda}{\lambda}}, \text{ and } k_{rn}^{st} = (1-s_w)^2\Big(1 - s_w^{\frac{2+\lambda}{\lambda}}\Big), \tag{2.38}$$

where the superscript *st* stands for the static condition, c is the entry pressure and λ is the pore-size distribution index (also know as *shape parameter*) for the Brooks-Corey constitutive models. An alternative to the Brooks-Corey models for uniformly-wet media is the van Genuchten saturation function. The van Genuchten capillary pressure function is given by:

$$P_c^{st} = c\Big(s_w^{\frac{-1}{m_{vg}}} - 1\Big)^{\frac{1}{n_{vg}}}, \tag{2.39}$$

and the van Genuchten relative permeability is governed by:

$$k_{rw}^{st} = \sqrt{s_w}\Big(1 - \Big(1 - s_w^{\frac{1}{m_{vg}}}\Big)^{m_{vg}}\Big)^2, \text{ and}$$

$$k_{rn}^{st} = \sqrt{1-s_w}\Big(1 - \Big(1 - s_w^{\frac{1}{m_{vg}}}\Big)^{m_{vg}}\Big)^{2m_{vg}}, \tag{2.40}$$

where $m_{vg} = 1 - 1/n_{vg}$ is fitting parameter which can be calibrated from laboratory experiment data.

As we discussed in Section 1.2, the coexistence of compositional fluids may result in a wettability heterogeneity within the grid block. Skjæveland et al., [109] combined the Brooks-Corey capillary pressure models for the hydrophilic and hydrophobic conditions to describe the mixed-wet medium at equilibrium flow condition. The developed model is read as:

$$P_c^{st} = c_w s_w^{-\frac{1}{a_w}} + c_n(1-s_w)^{-\frac{1}{a_n}}, \tag{2.41}$$

where c_w and a_w stand for the hydrophilic condition fitting parameters, and c_n and a_n stand for the hydrophobic condition fitting parameters. Similar models are developed in [5, 6, 31] to describe the capillary pressure behavior in the mixed-wet reservoir. Furthermore, Lomeland [76] developed relative permeability functions for the mixed-wet conditions. The models are named as LET models and can be read as:

$$k_{rw}^{st} = \frac{s_w^{L_w}}{s_w^{L_w} + E_w(1-s_w)^{T_w}}, \text{ and}$$

$$k_{rn}^{st} = \frac{(1-s_w)^{L_n}}{(1-s_w)^{L_n} + E_n s_w^{T_n}}, \tag{2.42}$$

where L_α, T_α, and E_α are empirical data fitting parameters. Furthermore, alternative relative permeability and capillary pressure function are proposed in [75, 66].

Chapter 3

Time-dependent saturation functions

In this chapter, we design procedural frameworks to upscale the effect of pore-scale WA processes to the core scale. Particularly, this chapter is devoted to design WA induced dynamic saturation functions.

3.1 Existing dynamic saturation models

Hassanizadeh and Gray [46] have developed a time-dependent capillary pressure model (named as H&G model) for non-equilibrium flow condition. The H&G model incorporates the transition time effect in the steady-state capillary pressure model as follows:

$$P_c^{\mathrm{dy}} = P_c^{st}(s_w) - \tau \partial_t s_w, \tag{3.1}$$

where τ is the dynamic coefficient determined from experimental data. Barenblantt [11] developed dynamic relative permeability and capillary pressure functions based on existing steady-state functions. These dynamic functions are read as:

$$P_c^{\mathrm{dy}} = P_c^{st}(\varsigma), \text{ and } k_{r\alpha} = k_{r\alpha}^{st}(\varsigma), \tag{3.2}$$

where the newly introduced variable ς is defined as:

$$\varsigma = s_w + \tau \partial_t s_w. \tag{3.3}$$

This shows that the Barenblantt model includes the redistribution time effect directly into the steady state models. Both, the H&G and Barenblantt models capture the dynamics induced by the flow instabilities, but not the WA process. This implies that these dynamic models are not readily applied to describe a system under a long-term WA.

The WA induced dynamics, in the saturation functions, is distinct from the dynamics due to non-equilibrium flow conditions [11, 46]. To recap, WA alteration is a chemistry-induced pore-scale process that alters the saturation functions (permanently) apart from the flow conditions or other instabilities. In contrast to non-equilibrium condition, wettability change potentially alters the saturation functions even when the system is at rest. Therefore, a new approach is needed that handles permanent and continual alteration of saturation functions regardless of the flow condition.

3.2 Upscaling the WA effect

There are numbers of models to describe either non-equilibrium or steady state flow saturation functions [75, 5, 76, 66, 98, 46, 11, 109, 44, 44]. These models are designed based on the assumption that the wettability of the system is static in time. However, Section 1.2 has pointed out that there are many factors that can provoke the surfaces within the pores to undergo a dynamic (time-dependent) wettability change. This pore-scale wettability change impacts the saturation path for drainage and imbibition displacements which leads to saturation functions shift from the initial (static) wetting-state curves towards the final wetting-state curves. Laboratory and pore-scale simulations have shown a WA induced dynamic deviation in saturation functions. However, mathematical representation and characterization of the effect of time-dependent WA process on the saturation functions at the core-scale has gotten less attention.

This thesis, particularly papers A and B, has a special interest in upscaling and representing the impact of exposure time-dependent WA on the saturation functions. The upscaling process is conceptualized in Figure 3.1. The idea relies on describing the wettability evolution in Figure 3.1a mathematically at the pore-level. The designed wettability evolution model is then coupled with a suitable pore-scale model such as Figure 3.1b in our case. The coupled dynamic pore-scale model is used to simulate time-dependent WA induced relative permeability and capillary pressure data. The simulated data is then used to develop dynamic saturation functions at the Darcy scale (Figure 3.1c). In the following sections, we discuss the modeling approach for WA induced (dynamic) saturation functions.

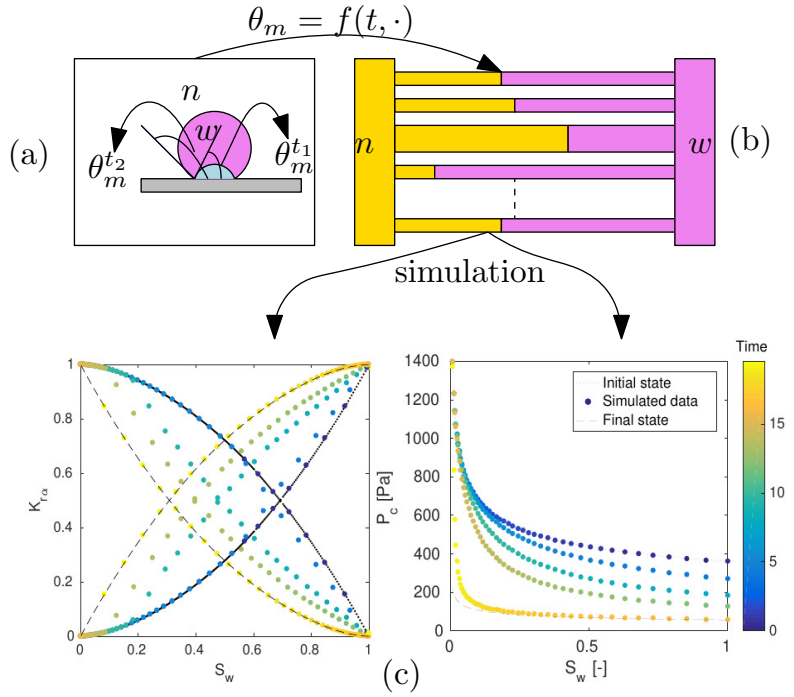

Figure 3.1: An example workflow for the upscaling process of the wettability dynamics: (a) CA measurements, (b) pore-scale model, and (c) averaged quantities at the macroscale.

3.3 Modeling approach

The wettability change may introduce a dynamic term in the saturation functions leading to a dynamic deviation from the initial wetting-state curves. This dynamic deviation is referred to as *dynamic component*. The dynamic component in the saturation functions is measured as a difference between the dynamic function and the static (initial/final wetting state) saturation curve, and is described as follows:

$$P_c(a, b, \cdot) - P_c^{st,in}(a, b, \cdot) := f^{\mathrm{dy}}(\cdot), \tag{3.4a}$$

$$k_{r\alpha}(a, b, \cdot) - k_{r\alpha}^{st,in}(a, b, \cdot) := f_{\alpha}^{\mathrm{dy}}(\cdot), \tag{3.4b}$$

where $P_c^{st,in}$ and $k_{r\alpha}^{st,in}$ represent the initial (static) wetting-state saturation functions, a and b are data fitting parameters, and f^{dy} and f_α^{dy} are the dynamic terms that are assumed to deviate from the static (initial) wetting state saturation curve. The initial and final wetting-state saturation functions can be governed by well-known models, such as van Genuchten or Brooks-Corey [22, 44], Purecell [71], and LET models [76, 75] to name a few.

Characterization of the dynamic components f^{dy} and f_α^{dy} is important to understand and predict the effect of wettability dynamics on the fluid distribution and the potential of the caprock for CO_2 storage applications. There might be many ways to characterize the dynamic components in Equations (3.4a) and (3.4b). Papers A and B have investigated two approaches to quantify the dynamic components in Equations (3.4a) and (3.4b). Paper A has explored the interpolation approach by scaling the dynamic component f^{dy} in Equation (3.4a) with the difference between the initial and final wetting-state saturation curves. This gives a non-dimensional quantity, we call it the *dynamic coefficient*, ω, and is defined as follows:

$$\omega\big(P_c^{st,f} - P_c^{st,in}\big) = f^{\mathrm{dy}}, \tag{3.5}$$

where $P_c^{st,f}$ is the final wetting-state capillary pressure data. This can be substituted into Equation (3.4b) to obtain a dynamic interpolation model

$$P_c = (1-\omega)P_c^{st,in} + \omega P_c^{st,f}. \tag{3.6}$$

for the capillary pressure dynamics. Similar functional forms to Equation (3.6) have been used to include the impact of instantaneous WA (i.e., only chemistry dependent) into the saturation functions [31, 121, 5, 1, 106]. In our case, ω is designed to capture the dynamics caused by fluid-history and time-dependent wettability changes.

On the other hand, in Paper B, we have found that the interpolation approach is not the best approach to upscale the effect of WA on relative permeabilities. As a consequence, Paper B has investigated a way to modify the existing models to include the wettability dynamics directly through the parameters and we call it a *parameter-based* dynamic model. The approach starts with correlating the dynamic term with the parameters of the standard model. Thus, the relative permeability in Equation (3.4b) can be rewritten as:

$$k_{r\alpha} = k_{r\alpha}^{st,in}(a(\cdot), b(\cdot), \cdot), \tag{3.7}$$

where $a(\cdot)$ and $b(\cdot)$ are data fitting parameters that depend on the WA processes. This means the dynamics are related to parameters of the underlying static relative permeability model. This approach is motivated by

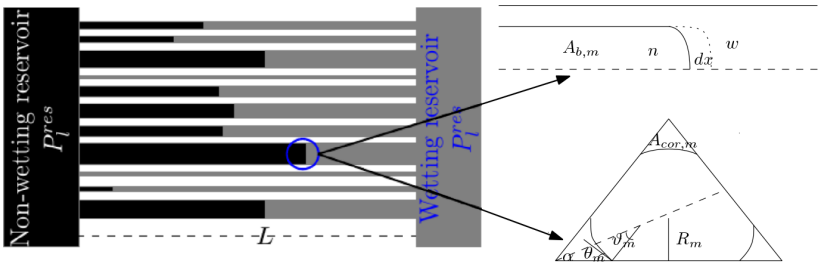

Figure 3.2: Fluid displacement in non-interactive bundle of tubes (BoT). Here, the left reservoir contains non-wetting fluid that displaces the wetting fluid to the right and vice versa.

the fact that the parameters in the standard relative permeability models are adjusted to different values when wettability changes from one state to another.

3.3.1 Overall workflow

To characterize the dynamic terms using the approaches above, we need time-dependent WA induced saturation functions data measured from laboratory experiments. However, measuring saturation functions for a porous medium that undergoes wettability change is costly in terms of time and resource. Rather, we design a general theoretical approach as follows:

- We design numerical experiments that account time-dependent WA in each individual pore, where experiments take place under static flow conditions. The WA process is introduced to the experiment through a CA change model as a function of exposure time to the WA agent in addition to the fluid-rock chemistry.

- The experiment is run over time and the WA progress for pores occupied by the WA agent. Thus, capillary pressure and relative permeabilities are altered continuously throughout the experiment. The experiment continues along several drainage-imbibition cycles until WA is completed and the end wetting state is reached.

- We generate WA-induced P_c-s_α and $k_{r\alpha}$-s_α data for each drainage-imbibition displacements. The capillary pressure is measured as the difference between the left and right reservoir pressures, see Figure

3.2. That is:

$$P_c = P_l^{res} - P_r^{res}, \tag{3.8}$$

where P_l^{res} and P_r^{res} are pressures in the left (non-wetting phase) and right (wetting phase) reservoirs respectively. The relative permeability is inferred from Darcy's law:

$$k_{r\alpha}(s_\alpha) = \frac{Q_\alpha \mu_\alpha L}{\mathrm{K} A_T \Delta P_\alpha}, \tag{3.9}$$

where Q_α is the volumetric flow rate, and A_T is the cross-sectional area of the domain.

- The next step after measuring the data is performing correlations for both the interpolation-based and parameter-based dynamic models in Equations (3.6) and (3.7), respectively. This step involves applying insight about time-dependent WA and detailed analysis to arrive at a reliable dynamic saturation functions for reservoir simulation.
- Once we develop these models, we extend our analysis to a generic path in saturation-time domain in order to ensure the robustness of the model. Furthermore, we draw a link between the upscaled models parameters and pore-scale model parameter.

3.4 Pore-scale model

Fluid-fluid interface movement caused by fluids pressures difference can be quantified from pore-scale modeling. There are various choices of pore-scale models available. Following [12, 120, 38, 29, 48, 49], we represent the pore-scale model by a straight tubes of circular (the cross-section is filled by only one fluid) and polygonal (multiple fluids may coexist in the cross-section) tubes. These tubes are connected with two (wetting and nonwetting) reservoirs. This pore-scale representation of a porous medium can be conceptually modeled as depicted in Figure 3.2. We assume that a displacement from one reservoir to the other is done by a piston-like manner controlled by the entry/threshold pressure, and it is stated as:

$$P_{c,m}(r, \theta_m) = \frac{\sigma}{r_m(\theta_m, R_m)}, \ m = 1, 2, \cdots, N, \tag{3.10}$$

where r_m is the radius of curvature in the m-th tube, θ_m is the fluid-fluid CA which used to define the rock surface wettability, N stands for number

of tubes, σ is fluid-fluid interfacial tension (IFT), and R_m is the radius of the inscribed circle.

The fluid-fluid interface movement along the tube can be approximated by the Lucas-Washburn flow model [118]:

$$\frac{dx_m^{int}}{dt} = \frac{G_m(\Delta P - P_{c,m}(r_m, \theta_m))}{8(\mu_n x_m^{int} + \mu_w(L - x_m^{int}))}, \tag{3.11}$$

where, μ_n and μ_w are non-wetting and wetting fluid viscosities respectively, the superscript int stands for fluid-fluid interface, $\mathcal{G}_m$ is the conductance and is implemented following the work of Hui et al. [51] for a given CA distribution. $\Delta P = P_l^{res} - P_r^{res}$ is the pressure drop used to drive the interface. From Equation (3.11), one can then determine the required time to reach a pre-specified interface position.

If the tubes are circular, the radius of curvature is estimated from Young-Laplace equation and reads as:

$$r_m(\theta_m, R_m) = \frac{R_m}{2\cos\theta_m}, \tag{3.12}$$

whereas r_m can be determined from the MS-P method, named after Mayer and Stowe [79] and Princen [96, 97], for polygonal pores.

3.4.1 MS-P method for polygonal pores

The MS-P method is used to calculate the entry pressure in polygonal pores. The method is based on the thermodynamic description of immiscible fluids in a porous medium that equates the virtual work with the change of free energy for interface displacement in the direction along the pore/throat [82]. This can be described as:

$$P_c ds_n = \sigma\Big(da_{wn} + \cos(\theta) da_{ns}\Big), \tag{3.13}$$

where a_{wn} and a_{ns} are specific inter-facial areas between the fluid-fluid and fluid-solid interfaces respectively. The derivation for Equation (3.13) can be found in [47].

Now consider a polygonal tube, particularly an equilateral triangular tube, with uniform cross-section area along the tube. Further, we assume that the pore surface is homogeneous in terms of the wetting property. A non-wetting phase invasion into a wetting phase saturated and strongly water-wet (i.e., $\theta_m < \frac{\pi}{2} - \alpha_m$, where α_m is the half-angle) polygonal tube may create distinct fluid configurations. Figure 3.3 shows an exemplary

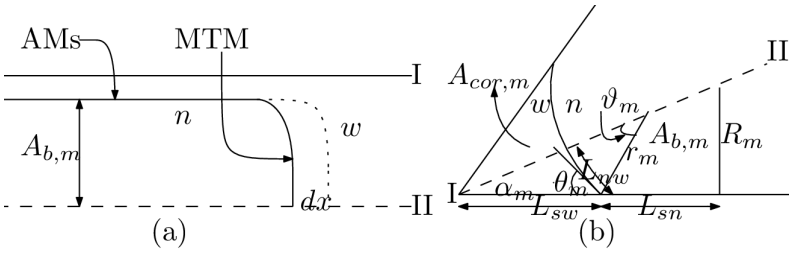

Figure 3.3: Fluid configuration after drainage into a water-wet polygonal pore.

fluid configuration in which the non-wetting phase occupies the bulk area of the tube and the wetting fluid remains in the corners. In Figure 3.3, the *main terminal meniscus* (MTM) is an invading interface, separating the bulk fluids, whereas an interface separating the bulk fluid from the corner fluid is referred as *arc meniscus* (AMs). According to Figure 3.3, the change of saturation can be described as $ds_n = \frac{A_{b,m}dx}{V_p}$ and the change of interfacial area can be stated as: $da_{sn} = \frac{L_{sn}dx}{V_p}$ and $da_{wn} = \frac{L_{nw}dx}{V_p}$, where V_p is the tube volume. After substituting these expressions into Equation (3.13), we obtain:

$$P_{c,m}A_{b,m} = \sigma\Big(L_{nw} + \cos\theta_m L_{sn}\Big). \tag{3.14}$$

Substituting Equation (3.10) into Equation (3.14) would give us the radius of curvature r_m as:

$$r_m = \frac{A_{b,m}}{L_{nw} + \cos\theta_m L_{sn}}, \tag{3.15}$$

where $A_{b,m}$ is the bulk surface area that is occupied by the displacing fluid. From geometry considerations of Figure 3.3b, the area covered by the bulk fluid can be found as:

$$A_{b,m} = \frac{R_m^2}{2\tan(\alpha_m)} - A_{cor,m}, \tag{3.16}$$

where A_{cor} is the area covered by the corner fluid and is calculated as:

$$A_{cor,m} = \frac{r_m L_{sw}\sin(\vartheta_m + \alpha_m)}{2} + \frac{r_m^2\vartheta_m}{2}, \tag{3.17}$$

and

$$L_{sw} = \frac{r_m\sin(\vartheta)}{\sin(\alpha_m)}, \quad L_{nw} = r_m\vartheta_m, \quad L_{sn} = \frac{R_m}{\tan(\alpha_m)} - L_{sw}, \tag{3.18}$$

where $\vartheta_m = \frac{\pi}{2} - \theta_m - \alpha_m$. Incorporating Equations (3.16)-(3.18) into (3.14) and solving the resulting equation analytically will give the entry pressure as:

$$P_{c,m} = \frac{\sigma}{R_m}\left\{\cos\theta_m + \sqrt{\frac{\tan(\alpha_m)}{2}\Big[\sin(2\theta_m) + \pi\Big(1 - \frac{2\alpha_m + 2\theta_m}{\pi}\Big)\Big]}\right\}. \tag{3.19}$$

If $\theta_m > \frac{\pi}{2} - \alpha$, the AMs in Figure 3.3 is displaced by the non-wetting fluid and the length, L_{nw}, which bounds the CO_2-water, becomes zero. In this regard, the bulk area $A_{b,m}$ is the same as the area of the entire cross-section and the fluid-solid length L_{sn} is becoming the total perimeter of the cross-section. These relations can be described mathematically as:

$$L_{nw} = 0,\ A = A_{b,m} = \frac{R_m^2}{2\tan\alpha},\ L_{sn} = \frac{R_m}{\tan\alpha}. \tag{3.20}$$

Inserting Equation (3.20) into (3.14) yields the Young-Laplace equation:

$$P_{c,m} = \frac{2\sigma\cos\theta}{R_m} \tag{3.21}$$

which is equivalent to the entry pressure for the cylindrical pore. The entry pressure for imbibition and secondary drainage displacements can be obtained from the MS-P method according to fluid configurations and degrees of wettability change in similar fashion.

3.4.2 Fluid displacements and configurations

As discussed above, a non-wetting phase (CO_2/scCO_2) invasion into configuration A, see Figure 3.4, may leave the water in the corners if $\theta < \frac{\pi}{2} - \alpha$. This corner water increases when the imbibition is initiated and creates configurations B or C before the MTM has displaced the non-wetting fluid. Particularly, B occurs when $\theta_m < \frac{\pi}{2} + \alpha_m$ and C when $\theta_m \geq \frac{\pi}{2} + \alpha_m$. A water invasion (imbibition) into B is always resulting to configuration D, and an invasion into C is to D or E. During secondary drainage the displacement may occur from either D or E to B, C or F. Configuration F occurs only if $\theta_m < \frac{\pi}{2} - \alpha_m$, and smaller than the previous advancing CA. The fluid configurations and CA values play a vital role to determine the entry pressure and saturation profiles during imbibition and secondary drainage (or scanning curves). The entry pressures for polygonal pores during drainage/imbibition displacement and existence/collapse of layer from configuration E can be obtained following the MS-P method, and are

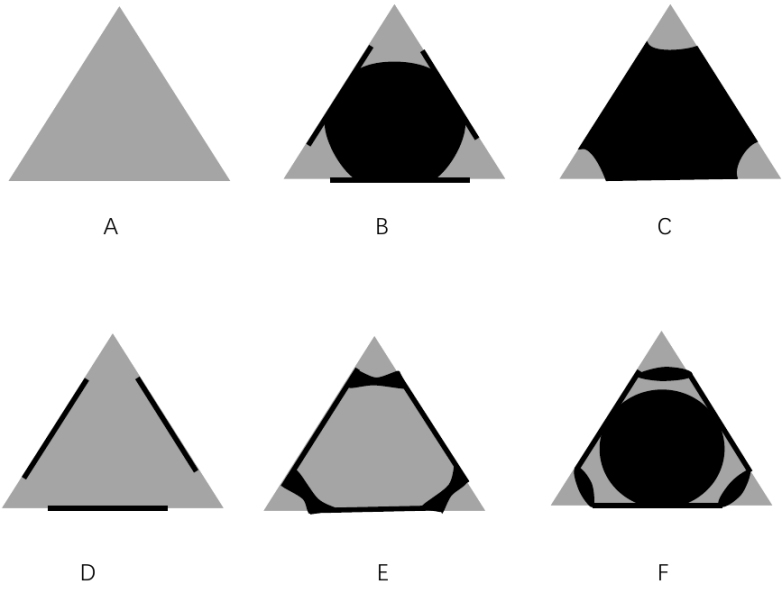

Figure 3.4: Fluid configurations for primary drainage, imbibition, and secondary drainage (water in light color and oil in dark color). The bold lines along the sides indicate altered wettability. This fluid configuration is adapted from [48].

explained in detail in [48]. This thesis, particularly Paper B implements the entry pressures formulated by Helland et al. [48] while considering a time-dependent wettability change model in each tube.

3.5 Rock surface wettability

The conceptual definition of wettability is quite simple. However, representing it mathematically is quite difficult because it is a complex interaction between surface free energies, surface mineralogy, and fluid composition [19]. In addition, pore morphologies and exposure time length scales contribute their part for the complexity of wettability.

3.5.1 Time-dependent WA model

The models introduced in Section 3.3 are designed to capture a time-dependent WA process. Papers A and B have considered a general functional form to describe a WA process at the pore-level as represented by a dynamic change in CA:

$$\theta_m(\cdot) := \theta_m^{in} + \varphi(\cdot)(\theta_m^f - \theta_m^{in}), \tag{3.22}$$

where θ_m^f and θ_m^{in} are the ultimate and initial contact angles respectively. We note that model (3.22) is general in the way that it can handle a decreasing or increasing CA and $\varphi(\cdot)$ can be any function of interest, i.e., the model can handle any φ that is physically reasonable to measure the wettability dynamics.

Here, for example, we develop a model for φ by assuming that the adsorption/desorption of a wettability-altering agent onto a solid surface is the root cause for surface wetting property change [17, 35]. This assumption is based on the observations from the laboratory CA measurements and molecular dynamics simulation [60, 53]. In these measurements adsorption type relations between CA, pressure [34, 60, 53], and CA with exposure time [59, 105] are observed. These and related measurement results are summarized in [54]. Similar CA evolution along the surfactant concentration and exposure time are reported in [30] and [83] respectively for oil droplet on a metal surface immersed in ionic surfactant solutions. An adsorption model, particularly the Langmuir adsorption-type model can be proposed to predict CA evolution along pressure, time, and surfactant concentration [84].

Given the insights above, we assume that the CA evolves according to the rate of adsorption of the WA agent on the surface of the pores [80, 37]. This can be stated as:

$$\frac{d\varphi}{dt} = J^+ - J^-, \tag{3.23}$$

where J^+ and J^- represent a rate of adsorption and desorption of a WA agent respectively. These processes are described as:

$$J^+ = k_1 \chi_m \Big(1 - \varphi \;/\; \overline{\varphi}\Big), \;\; J^- = k_2 \varphi, \tag{3.24}$$

where k_1 and k_2 are rate constants and $\overline{\varphi}$ represents maximum surface saturated concentration, whereas χ_m is the measure of exposure time to the WA agent concentration and is defined as Equation (3.30).

Now let us assume that the ODE (3.23) has a solution of the form:

$$\varphi = \sum_{i=0}^{\infty} \xi_i \varphi_i, \tag{3.25}$$

where, ξ is a small perturbation parameter. Substituting (3.25) into (3.23) results in:

$$\sum_{i=0}^{\infty} \xi_i \frac{d\varphi_i}{dt} = k_1 \chi_m \Big(1 - \sum_{i=0}^{\infty} \xi_i \varphi_i / \overline{\varphi}\Big) - k_2 \sum_{i=0}^{\infty} \xi_i \varphi_i. \tag{3.26}$$

The expression in Equation (3.26) can be rearranged in the following manner:

$$\xi_0 \Big[\frac{k_1}{k_2} \chi_m \big(1 - \varphi_0/\overline{\varphi}\big) - \varphi_0\Big] - \Big[\sum_{i=1}^{\infty} \frac{\xi_i}{k_2} \frac{d\varphi_{(i-1)}}{dt} + \big(1 + \frac{k_1}{k_2} \chi_m/\overline{\varphi}\big) \sum_{i=1}^{\infty} \xi_i \varphi_i\Big] = 0. \tag{3.27}$$

Then the first order approximation for φ can be obtained as:

$$\varphi \approx \frac{\chi_m}{C + \chi_m}, \tag{3.28}$$

where $C = \frac{k_1}{k_2 \overline{\varphi}}$ is a CA model parameter that controls the speed and extent of alteration. Equation (3.28) is substituted into Equation (3.22) to predict the wettability evolution.

We design χ_m in a way that it makes the alteration process permanent and to continue until the ultimate wetting state. There might be different types of WA mechanisms. In this thesis, we consider two mechanisms namely *uniform* and *non-uniform* WA. The uniform WA mechanism assumes that the WA agent is dissolved into the wetting phase from the non-wetting phase and defines χ_m in Equation (3.28) as an average quantity:

$$\overline{\chi} := \frac{1}{t_{ch}} \int_0^t s_n d\tau, \tag{3.29}$$

for each tube equally, where $t_{ch} < \infty$ is a pre-specified characteristic time. This leads to a uniform WA in space at a time t. On the other hand, the non-uniform WA relies on the assumption that the wettability altering agent occurs only in the non-wetting phase i.e., dissolution/diffusion is not

considered. This implies that only the surface exposed to the wettability altering agent is subject to the wettability change. For this case, we define:

$$\chi_m := \begin{cases} \frac{1}{t_{ch}} \int_0^t \frac{x_m^i}{L} d\tau & \text{for cylindrical pore,} \\ \frac{1}{t_{ch}} \int_0^t \frac{A_{b,m} x_m^i}{AL} d\tau & \text{for polygonal pore.} \end{cases} \tag{3.30}$$

According to Equation (3.30) each pore experiences different exposure time (maybe in the scale of weeks or months) and thus wettability heterogeneity across the REV/bundle may occur.

The definition of the exposure time χ_m or $\overline{\chi}$ distinguishes the proposed time-dependent WA model from the instantaneous WA mechanisms, and in general the proposed model above has the following features:

- The model describes a permanent WA process, i.e., the wetting property will not be restored to the original wetting condition when the WA agent is removed from the pore/REV. This is in contrast to the instantaneous WA in which the wetting property is restored to the initial wetting state when the WA agent is displaced by the other fluid. However, the model handles a reversal alteration if the other fluid is capable of modifying the wettability of the rock surface.

- The model is designed in such a way that the WA process can be halted at any intermediate point, between the initial and final wetting conditions, before reaching the ultimate wetting state if the WA agent is removed from the pore/REV. In this case, the variables χ_m and $\overline{\chi}$ become constant in time because the saturation or WA agent is zero in the pore or REV.

- The model is also designed to continue the alteration process starting from the halted point if the WA agent is reintroduced to the pore or REV. This is due to the fact that the variables χ_m and $\overline{\chi}$ start to evolve the exposure history since the pore space is reoccupied by the WA agent.

- The model is designed to handle an increasing (i.e., a wettability change from hydrophilic to intermediate/hydrophobic condition) or decreasing (i.e., a wettability evolution that alters the wetting property of the rock surface from hydrophobic down to hydrophilic condition) CA evolution in time. This implies that the model evolves smoothly from any initial wetting state to a final wetting state.

- The dynamic CA change may put an effort on the pore surface wetting condition to range from hydrophilic to hydrophobic-wet condition. Furthermore, the above developments may impose a dynamic and mixed-wet condition within a single pore if the pores are polygonal. The mixed-wet condition is used to describe a pore surface wettability that has connected wetting and non-wetting parts.

In papers A and B, this time-dependent CA change and a bundle-of-tubes model was coupled to simulate capillary pressure, relative permeabilities, and associated averaged quantities such as phase saturation and $\overline{\chi}$.

3.6 Simulation approaches and correlation models

As discussed in Section 3.4, the pore-scale system is represented by a bundle-of-tubes model. The pore sizes are drawn from the truncated Weibull distribution [48, 33, 40, 51] which is commonly employed for pore-network simulation. This distribution can be defined as:

$$R = \Big(R_{\max} - R_{\min}\Big)\Big\{-\delta \ln\Big[y_{rand}(1-\exp(-1/\delta)) + \exp(-1/\delta)\Big]\Big\}^{1/\gamma} + R_{\min}, \tag{3.31}$$

where $R_{\max}$ and $R_{\min}$ are the pore radii of the largest and smallest pore sizes respectively, δ and γ are dimensionless parameters, and $y_{rand} \in (0, 1)$ is a random variable. This distribution assigns the radius value in the bundle as depicted in Figure 3.2.

The pore-scale model descriptions such as entry pressure, time-dependent WA process, and bundle-of-tubes model are coupled together, through the Washburn equation (3.11), and programmed to simulate time-dependent WA induced saturation functions data. Papers A and B have implemented the pore-scale simulation in MATLAB® to generate upscaled quantities such as saturation, exposure time in average sense, capillary pressure and relative permeabilities. To do so, there are basically two displacement directions, i.e., drainage and imbibition.

During drainage, we control the pressure drop ΔP by increasing the non-wetting phase pressure in a step-wise manner. In each increase, the non-wetting phase occupies the bulk area of the tubes, and we calculate the averaged quantities such as saturations ($s_\alpha,\ \alpha \in \{w, n\}$), exposure time to the WA agent ($\overline{\chi} = \frac{1}{t_{ch}} \int_0^t s_n d\tau$), capillary pressure, and relative permeabilities. The capillary pressure and phase α relative permeability are calculated from Equations (3.8) and (3.9) respectively.

During imbibition, we decrease the non-wetting phase pressure in a step-wise manner. In each decrease, the wetting phase reoccupies the tubes and capillary pressure, saturation, exposure time (i.e., $\overline{\chi}$), and relative permeabilities are calculated in the same fashion as we did for drainage displacement. We repeat the drainage and imbibition displacements and measure the associated averaged quantities in order to capture the behavior of the WA induced dynamics in relative permeabilities and capillary pressure curves. The simulated curves, and the modeling approaches discussed in Section 3.3 are coupled to quantify the WA induced dynamics in the saturation functions. Following this approach, Papers A and B have developed time-dependent saturation models respectively.

For instance, the interpolation model given by Equation (3.6) is designed to capture time-dependent WA mechanisms in the capillary pressure, where the dynamic coefficient $\omega(\cdot)$ is designed to upscale the effect of (pore-scale) time-dependent WA mechanisms, and is governed by:

$$\omega(s_w, t) = \begin{cases} \frac{\beta_1 \overline{\chi}}{\beta_1 \overline{\chi}+1}, & \text{for uniform WA,} \\ \frac{\beta_2 s_w \chi}{\beta_2 s_w \overline{\chi}+1}, & \text{for non} - \text{uniform WA,} \end{cases} \tag{3.32}$$

where β_1 and β_2 are fitting parameters determined from laboratory experiment. The terms in Equation (3.32) are substituted into Equation (3.6) to correlate the simulated capillary pressure data. Figure 3.5 compares the proposed WA induced dynamic capillary pressure model and the simulated data.

On the other hand, in Paper B, the LET model is modified to handle the WA induced dynamics in the relative permeabilities, and has the form:

$$k_{rw} = \frac{\mathrm{F}(\overline{\chi}) s_w^L}{\mathrm{F}(\overline{\chi}) \mathrm{s}_w^L + 1 - s_w}, \text{ and } k_{rn} = \frac{1 - s_w}{1 - s_w + \mathrm{F}(\overline{\chi}) s_w}, \tag{3.33}$$

where L is fitting parameter determined from the initial wetting-state relative permeabilities data, whereas $\mathrm{F}(\overline{\chi})$ is given as:

$$\mathrm{F}(\overline{\chi}) = \begin{cases} \eta \overline{\chi} + \mathrm{E}^{in} & \text{if} \quad \overline{\chi} < \frac{E^f - E^{in}}{\eta}, \\ E^f & \text{if} \quad \frac{E^f - E^{in}}{\eta} \leq \overline{\chi}. \end{cases} \tag{3.34}$$

E^{in} and E^f are empirical data fitting parameters for the initial and final wetting-state condition and η is a parameter associated with the WA induced dynamics in the relative permeability data. The dynamic LET model in Equations (3.33) and (3.34), see Figure 3.6, matches well with the simulated relative permeability data.

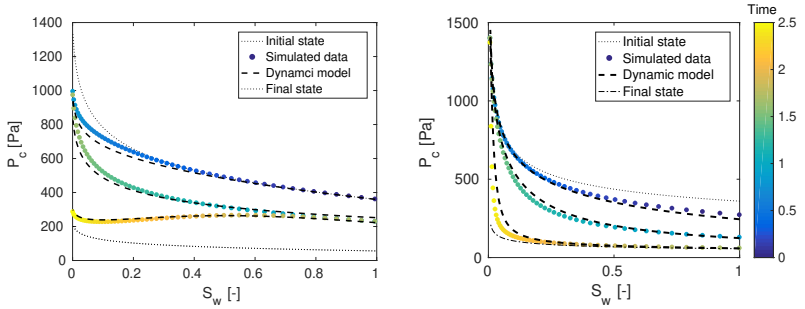

Figure 3.5: Comparison of the dynamic models in Equation (3.6) and (3.33) with the simulated capillary pressure: uniform (a) and non-uniform (b) WA cases in the capillary pressure. The color of each data point indicates the exposure time over 2.5 years.

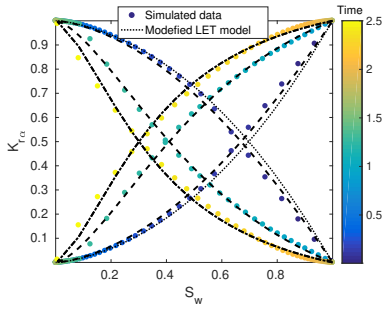

Figure 3.6: Comparison of the dynamic model in Equation (3.33) with the simulated relative permeability data. The color of each data point indicates the time elapsed in years, with the total elapsed time equal to 2.5 years.

The dynamic capillary pressure and relative permeabilities are reduced to the initial wetting-state curves for the unexposed REV, i.e., when $\overline{\chi}$ is zero. The dynamic capillary pressure meets the final wetting state when $\omega = 1$, and by Equation (3.32) the maximum value of ω is one for any value of $\overline{\chi}$. However, dynamic relative permeabilities may continue further after the end wetting-state curve is attained. Paper B has developed a controlling strategy such that $\eta\overline{\chi} + E^{in} = E^{f}$ holds for the final wetting-state

curve, see Equation (3.34). From this we can estimate the exposure time needed to reach the final wetting state such that the relative permeability is represented by the end wetting-state curve.

3.6.1 The relation between the upscaled and pore-scale models

The response of the upscaled model parameters η, β_1, and β_2 to a change in the pore-scale model parameter C is studied in Papers A and B. According to Paper A, the parameters β_1 and β_2 are represented as a power function of the pore-scale parameter C:

$$\beta_1 = 2C, \text{ and } \beta_2 = b_1 C^{-b_2}, \tag{3.35}$$

for the uniform and non-uniform WA cases respectively, where $b_1 > 0$ and $b_2 > 0$ are fitting parameters and are determined from laboratory experiment. When C becomes zero, the wettability changes instantaneously from the initial-wet to final-wet condition. Similarly the capillary pressure function jumps from the initial-wet to the final-wet condition curve.

On the other hand, the parameter η is related linearly, but inversely, to parameter C as:

$$\eta = \nu_1 C + \nu_2, \tag{3.36}$$

where $\nu_1 < 0$ and $\nu_2 > 0$ are empirical fitting parameters. From Equation (3.36), we observe that the relative permeability function (3.33) alteration is high when $C = 0$ and this is up to the value of ν_2. Thus ν_2 shall be chosen so that the relative permeability function is reached at the final wetting state quickly.

The general form of the dynamic saturation functions can be obtained by incorporating the relationships β_1-C, β_2-C and η-C into models (3.32) and (3.33) respectively. This implies that the dynamic saturation behaviors are estimated by knowing the CA change at the pore level over exposure time to the WA agent.

The next step is coupling the proposed dynamic saturation functions with the conservation models discussed in Chapter 2 to investigate the impact of the WA dynamics on the CO_2 plume movement at the Darcy scale. The saturation functions introduced above are non-linear and non-local in time. The non-linearity and non-locality of the saturation functions impose a difficulty, as we mentioned in Section 1.3, to find analytical solution for the resulting two-phase flow model. Thus, a numerical approach is employed to study the impact of pore-scale time-dependent WA processes on the fluid distribution at the core and field scale.

Chapter 4

Numerical framework

In the previous Chapters, we described a multi-phase flow process by non-linear partial differential equations (PDEs). The non-linearities are introduced through saturation functions. In Chapter 3, we introduced the effect of time-dependent WA processes into the saturation functions. This adds additional complexity on the top of the standard (static) saturation functions and imposes an extra challenge to solve the multi-phase flow model analytically. Note that analytical solutions for multi-phase flow is possible in only restrictive cases. As a consequence, numerical methods have been employed to approximate the solution of such flow problems. In this chapter, we mention some basic numerical methods which are commonly applied to approximate the solutions of a multi-phase flow problem.

4.1 Space discretization

The porous domain is subdivided into a finite set of polyhedral elements to reduce the PDE into a system of algebraic equations. The continuity Equation (2.14) is used as a prototype model to define space discretization schemes. In this section, we will highlight two space discretization methods: finite volume method (FVM) and finite element method (FEM).

4.1.1 Finite volume scheme

There are different FVMs to discretize a given PDE. Two-point flux approximation (TPFA) is the simplest to implement and commonly applied scheme in industries and open source simulators such as the MATLAB®

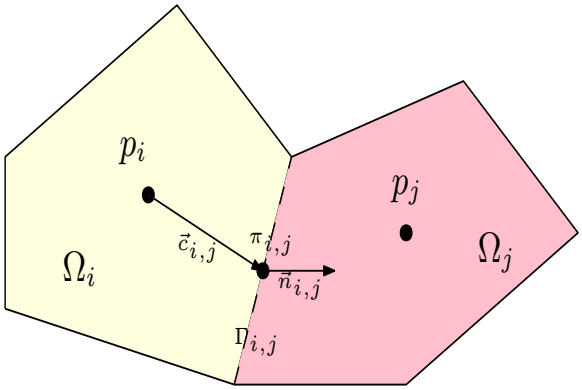

Figure 4.1: A cartesian decomposition of a domain ω into grid volumes Ω_i and Ω_j that are used to define a TPFA scheme (this figure is adapted from [72]).

Reservoir Simulation Toolbox (MRST) [72] and Open Porous Medium (OPM) toolbox [100]. Following [72], we summarize the TPFA for the Poisson equation.

4.1.1.1 Two-point flux approximation

Now let us recall the continuity equation and Darcy's law without gravity term for a single phase flow as follows:

$$\nabla \cdot \vec{u} = q \text{ and } \vec{u} = -\mathrm{K}\nabla p \qquad \text{in } \Omega. \tag{4.1}$$

Let us assume that the domain Ω is decomposed into finite grid cells. Figure 4.1 shows sample two cells that are used to define the TPFA scheme.

Given Equation (4.1), the TPFA represents the unknowns in terms of average values which are defined over a set of finite volumes. Thus, we integrate Equation (4.1) over a grid cell Ω_i and apply the Gauss's divergence theorem to develop a FVM discretization for Equation (4.1). This can be written in integral form as:

$$\int_{\partial\Omega_i} \vec{u} \cdot \vec{n} dS = \int_{\Omega_i} q dx \tag{4.2}$$

in a volume Ω_i, where the left hand side represents the flux across the

interface which can be defined as:

$$u_{i,j} = \int_{\Gamma_{i,j}} \vec{u} \cdot \vec{n} dS, \tag{4.3}$$

where $\Gamma_{i,j} = \partial\Omega_i \cap \partial\Omega_j$ is an interface that separates the two grid cells. The interface, $\Gamma_{i,j}$, is associated with a single grid cell (let us say Ω_i) with a certain normal vector $\vec{n}_{i,j}$. But, each interior half-face has a twin since the grid cells are assumed to be matching. This implies that the half-faces (i.e., $\Gamma_{i,j}$ and $\Gamma_{j,i}$) have identical areas $A_{i,j} = A_{j,i}$ with opposite normal vectors (i.e., $\vec{n}_{i,j} = -\vec{n}_{j,i}$). If we apply a midpoint rule to approximate the integral in Equation (4.3), the flux can be approximated as:

$$u_{ij} \approx -A_{i,j}(\mathrm{K}\nabla p)(x_{i,j}) \cdot \vec{n}_{i,j}, \tag{4.4}$$

where $x_{i,j}$ represents the center of $\Gamma_{i,j}$. The term ∇p in Equation (4.4) can be approximated by the difference between the pressure at the face center and the pressure at the center of the grid cell with the assumption that pressure is linear (or constant) inside each cell. This implies that the pressure at the cell center is identical to the average pressure p_i of the cell Ω_i, thus it follows:

$$u_{i,j} \approx A_{i,j}\mathrm{K}_i \frac{(p_i - \pi_{i,j})\vec{c}_{i,j}}{|\vec{c}_{i,j}|^2} \cdot \vec{n}_{i,j}, \tag{4.5}$$

where $\pi_{i,j}$ is a pressure at the interface $\Gamma_{i,j}$ and is known as face pressure, and $\vec{c}_{i,j} = \Delta x_{i,j}$. The same approximation of the flux above can be applied in the cell Ω_j to give,

$$u_{j,i} \approx -A_{j,i}\mathrm{K}_j \frac{(p_j - \pi_{j,i})\vec{c}_{j,i}}{|\vec{c}_{j,i}|^2} \cdot \vec{n}_{j,i}. \tag{4.6}$$

Now the continuity of fluxes and face pressures, i.e., $u_{i,j} = -u_{j,i} = u_{ij}$ and $\pi_{i,j} = -\pi_{j,i} = \pi_{ij}$, would give us the following

$$-Tr_{j,i}^{-1} u_{ij} \approx p_j - \pi_{j,i}, \text{ and } Tr_{i,j}^{-1} u_{ij} \approx p_i - \pi_{i,j}, \tag{4.7}$$

where $Tr_{i,j} = \frac{A_{i,j}\mathrm{K}_i \vec{c}_{i,j}}{|\vec{c}_{i,j}|^2} \cdot \vec{n}_{i,j}$ and $Tr_{j,i} = \frac{A_{j,i}\mathrm{K}_j \vec{c}_{j,i}}{|\vec{c}_{j,i}|^2} \cdot \vec{n}_{j,i}$ are one-sided transmissibilities and are refereed to as *half-transmissibilities*. Combining the fluxes in Equation (4.7) will eliminate the face pressures and one can obtain a TPFA scheme,

$$u_{ij} \approx \left[Tr_{i,j}^{-1} + Tr_{j,i}^{-1}\right]^{-1} (p_i - p_j). \tag{4.8}$$

When the grid cell Ω_i has more than one neighbor grid cells, the expression in Equation (4.8) can be substituted into Equation (4.2) to give a linear system,

$$\sum_j \left[Tr_{i,j}^{-1} + Tr_{j,i}^{-1} \right]^{-1} (p_i - p_j) = q_i, \forall \Omega_i \subset \Omega. \tag{4.9}$$

This approach is extended to approximate the solution of transient multiphase (multi-component) flow in MRST and OPM simulators. Paper C, [63], implements this discretization in MRST for Equations (2.24a)-(2.24b) to study the convergence of the linearization scheme proposed in therein. Here, we apply upwind discretization techniques for the relative permeabilities.

4.1.2 Finite element method

This section follows the work of Chen [26]. We denote the space of real valued square integrable functions by $L^2(\Omega)$, and by $H^1(\Omega)$ its subspace containing functions having also the first order weak derivatives in $L^2(\Omega)$. Let $H_0^1(\Omega)$ be the space of functions in $H^1(\Omega)$ which vanish on the boundary. Further, we denote the inner product on $L^2(\Omega)$ by $\langle \cdot, \cdot \rangle$, and $\| \cdot \|$ represents the norm of $L^2(\Omega)$.

Once again, we consider the continuity equation to show the FEM discretization of a given PDE. Thus, we start with multiplying Equation (4.1) by a test function $v \in H_0^1(\Omega)$ and applying integration by parts to get the following form:

$$-\int_\Omega \nabla \cdot (K \nabla p) v dx = \int_\Omega K \nabla v \cdot \nabla p dx = \int_\Omega q v dx. \tag{4.10}$$

Equation (4.10) is known to be bilinear variational form, and can be rewritten as

$$\langle K \nabla p, \nabla v \rangle - \langle q, v \rangle = 0 \tag{4.11}$$

for all $v \in V$. Now let $\mathcal{T}_h$ be a regular decomposition of Ω, which decomposes Ω into closed d-simplices, h stands for the mesh diameter i.e., $\Omega = \bigcup_{\mathcal{T} \in \mathcal{T}_h} \mathcal{T}$, see Figure 4.2. The Galerkin finite element space is given by:

$$V_h = \left\{ v_h \in H_0^1(\Omega) : v_h|_{\mathcal{T}} \in P_1(\mathcal{T}), \mathcal{T} \in \mathcal{T}_h \right\}, \tag{4.12}$$

where $P_1(\mathcal{T})$ denotes the space of linear polynomials on any simplex $\mathcal{T}$ and $v_h|_{\mathcal{T}}$ is the restriction of v_h at the element $\mathcal{T}$. We use the definition of

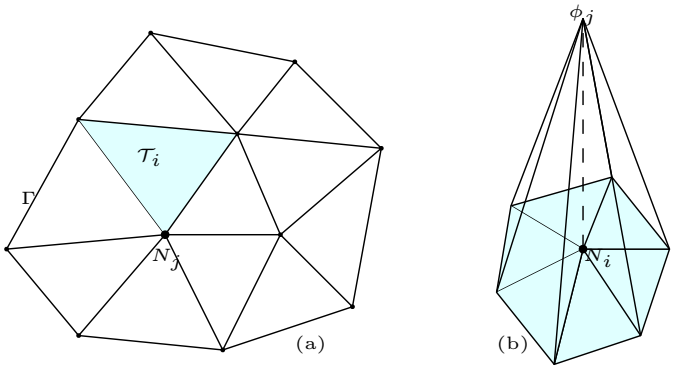

Figure 4.2: An example of finite element triangulation (a) and the representation of the basis function at node N_j (b).

spaces and notations above to write the discrete form of Equations (4.11) which finds $p_h \in V_h$ such that:

$$\langle \mathrm{K}\nabla p_h, \nabla v_h \rangle - \langle q_h, v_h \rangle = 0, \tag{4.13}$$

holds for all $v_h \in V_h$. This formulation is extended for non-local two-phase flow model in order to analyze the theoretical convergence of the linearization scheme proposed in Paper C. Now let us define the basis function $\psi_i \in V_h$ for each interior node N_i of $\mathcal{T}_h$ as:

$$\psi_j(N_i) = \begin{cases} 1 & \text{if } i = j \\ & \qquad i, j = 1, 2, 3, \ldots, M \\ 0 & \text{if } i \neq j. \end{cases} \tag{4.14}$$

The FEM relies on rewriting the unknowns in Equation (4.13) as linear combinations of basis functions. This can be represented as follows:

$$v(x) = \sum_{i=1}^{M} p_i \psi_i(x), \tag{4.15}$$

where $p_i = v(N_i)$ is a discrete unknown at node N_i. This representation is substituted into Equation (4.13) to give

$$\sum_{j=1}^{M} p_j \Big\langle \mathrm{K}_j \nabla \psi_j, \nabla \psi_i \Big\rangle = \Big\langle q_h, \psi_i \Big\rangle, \tag{4.16}$$

where the basis function ψ_i is used as a test function. Equation (4.16) can be further rewritten as

$$\sum_{j=1}^{M} A_{i,j} p_j = \Big\langle q_h, \psi_i \Big\rangle, \ 1 \leq i \leq M \tag{4.17}$$

where $A_{i,j}$ is the entities of the the coefficient matrix also known as weighted stiffness matrix and is calculated as:

$$A_{i,j} = \int_T \mathrm{K}_j \nabla \psi_i \nabla \psi_j dx. \tag{4.18}$$

In practice, the element of the stiffness matrix is computed using numerical quadrature integration method, particularly for higher order basis functions. The details of FEMs can be found in [26].

4.2 Time discretization

Above, we have highlighted common discretization techniques for the spatial differential operators. However, the multi-phase flow and component transport models are not only space dependent but also time dependent. This implies that the discretization above is not sufficient for solving a multi-phase flow problem in a porous medium. Thus the problem should also be discretized in time. Let us consider the following ODE,

$$\partial_t p_h = F(p_h, x), \tag{4.19}$$

where F is a linear/non-linear function which can be the discretized form of the PDE.

Let the total simulation time interval $[0, t^f]$ be divided into N time steps in such a way that $0 = t^0 < t^1 < \cdots < t^N = t^f$, and define the time step $\delta t = T^f/N$, as well as $t^n = n\delta t, \ n \in \{1, 2, \ldots, N\}$. Then, the first-order discretization, particularly the forward and backward Euler method, rewrites the previous ODE as:

$$\frac{p_h^{n+1} - p_h^n}{\delta t} \approx F(x, p_h^n), \text{ and } \frac{p_h^{n+1} - p_h^n}{\delta t} \approx F(x, p^{n+1}) \tag{4.20}$$

respectively, where $p_h^{n+1} = p_h(x, t + \delta t)$ and $p_h^n = p_h(x, t)$. The Crank-Nicholson method, a second order scheme, approximates the given ODE as:

$$\frac{p_h^{n+1} - p_h^n}{\delta t} \approx \frac{1}{2}\big[F(x, p_h^n) + F(x, p_h^{n+1})\big]. \tag{4.21}$$

The general (implicit and/or explicit) higher order discretizations in time are given by Runge-Kutta methods. The discretized Equations (4.20) and (4.21) may result in a non-linear system of equations that may be difficult to solve directly. As a consequence, iterative methods are usually applied to solve the algebraic equations.

4.3 Iterative linearization schemes

Iterative linearization methods are sequential procedures that start with an initial guess to generate a sequence of solution points approaching the exact solution as the iteration tends to infinity. Thus, iterative methods can only give approximate information about the given system, but to any desired degree. However, in many cases, iterative methods can reach the true solution within machine precision and be more efficient than a direct method in terms of computation time. We refer to [114] for the comparison between iterative and non-iterative methods. This section focuses on iterative methods for solving systems of non-linear equations arising from discretizing the PDEs. There are several iterative methods which are often applied to PDEs [99, 73, 20]. In the following sections, we discuss the Newton's method and the splitting /L-scheme methods.

4.3.1 Newton's method

In numerical computation, the Newton's/Newton-Raphson/ method is an algorithm that finds successively better approximations to the roots (or zeroes) of a real-valued function. Let us introduce the Newton's method for a single variable equation, $g(x) = 0$, where g is smooth and real valued for $x \in \mathbb{R}$. If x^0 is a (good enough) initial guess for a zero of $g(x)$, then the Taylor's expansion of g around x^0 can be given as:

$$g(x^0 + \Delta x) = g(x^0) + g'(x^0)\Delta x + \frac{g''(x^0)(\Delta x)^2}{2!} + \cdots , \tag{4.22}$$

where $\Delta x = x^1 - x^0$. Let us assume that the first order Taylor's expansion approximates $g(x)$, then one would get:

$$x^1 = x^0 - \frac{g(x^0)}{g'(x^0)}. \tag{4.23}$$

This implies that x^1 becomes the new estimate of the zero's of $g(x)$, and the next guesses can be updated by:

$$x^{n+1} = x^n - \frac{g(x^n)}{g'(x^n)}, \tag{4.24}$$

with the hope that the sequence converges to the real solution within finite steps. This method is second order convergent, i.e., the estimate:

$$|x^{n+1} - x| \leq co|x^n - x|^2, \tag{4.25}$$

holds for constant co that is independent of n, where x is the actual solution. However, the convergence of Newton's method is local and conditional. Nevertheless, the Newton's method is commonly applied to solve the discretized form of Equations (2.24a)-(2.24b). Let these PDEs be reduced to a system of algebraic equations of the following form:

$$pF(p_h^{n+1}, s_w^{n+1}) = 0, \tag{4.26}$$

$$\frac{s_w^{n+1} - s_w^n}{\delta t} + sF(p_h^{n+1}, s_w^{n+1}) = 0. \tag{4.27}$$

In order to apply the Newton's method, one needs to calculate the Jacobian of the system. Then, one can apply the approach of Equation (4.24) to linearize the system as

$$\mathcal{X}^{n+1} = \mathcal{X}^n + \frac{\mathfrak{F}(\mathcal{X}^n)}{\mathfrak{F}'(\mathcal{X}^n)}, \tag{4.28}$$

where $\mathcal{X}^{n+1} = \begin{bmatrix} p_h^{n+1} \\ s_w^{n+1} \end{bmatrix}$, $\mathfrak{F} = \begin{bmatrix} pF \\ sF \end{bmatrix}$, and $\mathfrak{F}'$ is the Jacobian of $\mathfrak{F}$. The Newton's method is the most applied method in reservoir simulation due to its quadratic convergence properties (i.e., fast convergence). However, in terms of the computational cost and memory requirements, it is an expensive method because it requires to compute the Jacobian matrix at each iteration. Another concern is how close the initial guess is to the true solution, that results in the restrictions on the time-step. Furthermore, if robustness is the most important factor, then Newtons method will rarely be a good choice. It is worth mentioning also that several modifications to Newtons method have been developed in order to increase its robustness, see e.g [32] for more details.

4.3.2 Splitting schemes

Splitting schemes are commonly applied in the numerical solution of two-phase flow problems. Among many, the IMPES and L-scheme are discussed

in this section.

4.3.2.1 IMplicit Pressure Explicit Saturation

The IMplicit Pressure Explicit Saturation (IMPES) method [45, 86, 85, 10, 25] is an important tool used to simulate multi-phase flow in porous media. This method decouples the pressure equation from the transport equation, and solves the pressure implicitly and updates the saturation explicitly by evaluating the non-linear terms at the previous saturation profile. The method solves the linear system of equations

$$pF(p_h^{n+1}, s_w^n) = 0 \tag{4.29}$$

for the reservoir pressure p_h^{n+1} provided that s_w^n is known from the previous time step. Once p_n^{n+1} is obtained then the method updates the saturation profile explicitly from

$$\frac{s_w^{n+1} - s_w^n}{\delta t} + sF(p_h^{n+1}, s_w^n) = 0. \tag{4.30}$$

As shown in Equations (4.29)-(4.30), the IMPES scheme (proposed by Sheldon [107]) decouples the pressure equation from the transport one. This decoupling approach may be more advantageous than the fully implicit scheme in terms of computational time. The explicit resolution of the saturation profile usually leads to erroneous calculations of the saturation field and in the worst cases, the computed saturation may be out of the bounds. In general, the decoupling process puts the IMPES scheme to be limited by numerical stability restrictions on the size of the time step. In the literature [111, 27, 104, 42], different stability criterion have been proposed and studied for the IMPES scheme. Franc et al. [43] have compared different stability conditions and highlighted their effectiveness for different porous media.

The iterative coupling techniques are also applied to improve the stability of the classical IMPES scheme. The iterative IMPES linearises the given two phase flow problem by evaluating the non-linear terms from the previous iteration step [67]. Thus, the non-linear model (4.26)-(4.27) can be reformulated as a system to find $p_h \in V_h$, satisfying

$$pF(p_h^{n+1,i+1}, s_w^{n+1,i}) = 0 \tag{4.31}$$

for a given $s_w^{n+1,i}$. The obtained solution $p_{nw}^{n+1,i+1}$ and $s_w^{n+1,i}$ are now used to update the current iteration saturation $s_w^{n+1,i+1}$ explicitly as follows,

$$\frac{s_w^{n+1,i+1} - s_w^n}{\delta t} + sF(p_h^{n+1,i+1}, s_w^{n+1,i}) = 0. \tag{4.32}$$

This sequential steps should be repeated until a pre-defined stopping criteria is satisfied. Paper C implements this scheme and compares it with a semi-implicit discretization method proposed in the paper for a non-local two-phase flow model.

Furthermore, in [67], the capillary pressure term in the pressure equation is treated implicitly in time. The authors apply a first order Taylor's expansion to approximate the capillary pressure. This linearizes the capillary pressure term at the current time step. Then they evaluate other non-linear terms (particularly the mobilities) at the previous time step. The authors have illustrated the improvements of the IMPES scheme with numbers of numerical experiments.

4.3.2.2 L-scheme

The L-scheme is a linearization method and was proposed to solve the Richards equation [94, 110, 73]. It linearizes the Richards equation by adding an artificial stabilization term and evaluating the non-linear terms at the previous iteration solutions. This linearization scheme has been also successfully applied for two-phase flow problems [99], poromechanics [103, 58], and fully coupled reactive transport [56] problems.

The L-scheme solves the pressure equation in the same fashion as the IMPES does, i.e., the scheme first solves the pressure for a given saturation profile as:

$$pF(p_h^{n+1,i+1}, s_w^{n+1,i}) = 0. \tag{4.33}$$

Then it updates the saturation by solving

$$cL(s_w^{n+1,i+1} - s_w^{n+1,i}) + \frac{s_w^{n+1,i} - s_w^n}{\delta t} + sF(p_h^{n+1,i+1}, s_w^{n+1,i}) = 0, \tag{4.34}$$

where cL is the stabilization parameter. A good choice of cL makes the scheme efficient and robust. The term $cL(s_w^{n+1,i+1} - s_w^{n+1,i})$ tend to zero as $i \to \infty$ which implies the convergence of the scheme for a given time step. The scheme converges to the solution linearly, see [73] for Lipschitz continuous and [99, 20] for Hölder continuous problems. The speed of the L-scheme can be improved by using Anderson acceleration [7, 21]. Besides, the scheme does not involve the computation of the Jacobian of the system and thus, it can be successfully applied to less regular problems.

4.3.3 Pseudo monolithic (inexact Newton's method)

In Paper C, we have proposed an iterative linearization scheme that couples the pressure, and saturation equations at the $(n+1)$-th time step by treat-

ing the capillary pressure function implicitly in the pressure and transport equations. To illustrate the scheme, let us go a step-back and start with the continuous pressure and saturation equations without the gravity term as follows:

$$-\nabla \cdot \Big(\lambda_T \nabla p_n - \lambda_w \nabla P_c\Big) = \mathcal{F}_T^n, \tag{4.35a}$$

$$\phi \partial_t s_w - \nabla \cdot \Big(\lambda_w \nabla p_n - \lambda_w \nabla P_c\Big) = \mathcal{F}_w^n. \tag{4.35b}$$

Now one can discretize Equations (4.36a) and (4.36b) in time using the Euler's backward discretization scheme to give:

$$-\nabla \cdot \Big(\lambda_T^{n+1} \nabla p_n^{n+1} - \lambda_w^{n+1} \nabla P_c^{n+1}\Big) = \mathcal{F}_T, \tag{4.36a}$$

$$\phi \frac{s_w^{n+1} - s_w^n}{\delta t} - \nabla \cdot \Big(\lambda_w^{n+1} \nabla p_n^{n+1} - \lambda_w^{n+1} \nabla P_c^{n+1}\Big) = \mathcal{F}_w. \tag{4.36b}$$

The scheme applies a chain rule on the capillary pressure term and evaluates the non-linear terms at the previous time step to linearise the capillary pressure terms in the pressure (4.36a) and saturation (4.36b) equations. This can be read as follows:

$$\nabla P_c^{n+1} \approx \frac{\partial P_c^n}{\partial s_w} \nabla s_w^{n+1} + \frac{\partial P_c^n}{\partial \overline{\chi}} \nabla \overline{\chi}^{n+1}. \tag{4.37}$$

The obtained approximate term for the capillary pressure is then substituted back to the two-phase flow model to give the following linear system:

$$-\nabla \cdot \Big[\lambda_T^n \nabla p_n^{n+1} - \lambda_w^n \Big(\frac{\partial P_c^n}{\partial s_w} \nabla s_w^{n+1} + \frac{\partial P_c^n}{\partial \overline{\chi}} \nabla \overline{\chi}^{n+1}\Big)\Big] = \mathcal{F}_T^n, \tag{4.38a}$$

$$\phi \frac{s_w^{n+1} - s_w^n}{\delta t} - \nabla \cdot \Big[\lambda_w^n \nabla p_n^{n+1} - \lambda_w^n \Big(\frac{\partial P_c^n}{\partial s_w} \nabla s_w^{n+1} + \frac{\partial P_c^n}{\partial \overline{\chi}} \nabla \overline{\chi}^{n+1}\Big)\Big] = \mathcal{F}_w^n. \tag{4.38b}$$

From the Equations (4.38a) and (4.38b), it is clear that the pressure and saturation equations are coupled at the current time step. Furthermore, an iteration step can be applied to improve the stability of the scheme. This leads to an evaluation of the non-linear terms at the current time step.

In addition to the outer iteration steps, a stabilization/correction term of L-scheme type

$$s_w^{n+1,i+1} = (1 - cL) s_w^{n+1,i} + cL \tilde{s}_w^{n+1,i+1}, \tag{4.39}$$

is introduced on the top of Equations (4.38a) and (4.38b) to give:

$$-\nabla\cdot\Big[\lambda_T^{n+1,i}\nabla p_n^{n+1,i+1} - \lambda_w^n\Big(\frac{\partial P_c^{n,i}}{\partial s_w}\nabla \tilde{s}_w^{n+1,n+1} + \frac{\partial P_c^{n,i}}{\partial \overline{\chi}}\nabla\overline{\chi}^{n+1,i+1}\Big)\Big] = \mathcal{F}_T^{n+1,i}, \tag{4.40a}$$

$$\phi\frac{\tilde{s}_w^{n+1,i+1}-s_w^n}{\delta t} - \nabla\cdot\Big[\lambda_w^{n+1,i}\nabla p_n^{n+1,i+1} - \lambda_w^{n+1,i}\Big(\frac{\partial P_c^{n,i}}{\partial s_w}\nabla \tilde{s}_w^{n+1,n+1} + \frac{\partial P_c^{n,i}}{\partial \overline{\chi}}\nabla\overline{\chi}^{n+1,i+1}\Big)\Big] = \mathcal{F}_w^{n+1,i}. \tag{4.40b}$$

Solving Equations (4.40a)-(4.40b) would give us $p_n^{n+1,i+1}$ and $\tilde{s}_w^{n+1,i+1}$ for the $i+1$ iteration steps at the current time step. Once $\tilde{s}_w^{n+1,i+1}$ is obtained, the scheme corrects the saturation profile for the current iteration from Equation (4.39). The choice of cL in each iteration is discussed in Paper C. We note that:

1. $s_w^{n+1,i+1}$ is used as a previous iteration values for the next iteration and we set $s_w^{n+1,0} = s_w^n$ for the first iteration step
2. The scheme is equivalent to iterative IMPES if we choose $cL = 0$, and thus $cL \in (0, 1]$.

The convergence of this scheme is proved theoretically and illustrated with numerical examples in Paper C.

4.4 Sensitivity analysis

A multi-phase flow model comprises of multiple model parameters. These parameters can be quantified from laboratory experiments. However, performing laboratory experiments is costly in terms of time and resources. Thus, only experimental studies may not be sufficient to quantify the parameters in the model. As a consequence, numerical simulations have been used to assess the sensitivity of model parameters on the impact of the output of the model.

4.4.1 Parameter quantification

Parametric analysis is a technique used to study how a small perturbation in the parameters (inputs) affect the output of the system. Among many

advanced parametric analysis, a one-at-a-time sensitivity analysis is the simplest method to work with [70]. This approach varies one parameter at a time, while keeping the others fixed. This approach is adopted in this thesis, particularly Paper D [62], to understand the impact of WA on the CO_2-water migration and quantify the caprock integrity.

The permeability, porosity, entry pressure, and injection rate are important parameters in multi-phase flow processes. The combinations of these parameters determine the role of the saturation functions on the fluids movement. In [119], a sensitivity analysis for CO_2-water system is reported by varying the entry pressure and shape parameters of the saturation function. A similar approach is implemented in Paper D to investigate the role of permeability, porosity, entry pressure, and injection rate on the impact of WA induced dynamic saturation functions in the interaction of the CO_2-water system. For this purpose, we design two-flow scenarios: horizontal and vertical CO_2-water flow. For the horizontal flow case, we vary four parameters (i.e., K, ϕ, q, and C) one after the other and perform numerical simulations in order to study the trend of the CO_2 migration in porous media. For the purpose of quantifying the impact of WA induced dynamics in P_c and $k_{r\alpha}$ compared to a static-wet system, we define the scaled front location difference, SFLD, as:

$$\text{SFLD} = \frac{x^{in} - x^{\text{dy}}}{x^{in}}, \tag{4.41}$$

where x^{in} and x^{dy} denote the CO_2 front location for static and dynamic capillary pressure and relative permeabilities functions, respectively. The quantity in Equation (4.41) is then measured at the end of the simulation time for each parameters combinations. The obtained SFLD is analyzed based on dimensionless grouping, that is the capillary number ($\mathcal{C}a$). The capillary number at the macroscale [9] can be defined as,

$$\mathcal{C}a = \frac{q\Delta x \mu_n}{\text{K}\phi c_w}. \tag{4.42}$$

In Paper D, we also quantify the role of model parameters on the caprock integrity for the vertical flow scenario. We developed a data based model that depends on the caprock permeability, entry pressure, and dynamic parameter. The proposed caprock integrity model can be used to estimate the amount of CO_2 in the caprock, and has the form,

$$\hat{m} = g(c_w, \text{K}, C, t), \tag{4.43}$$

where $\hat{m}$ is the scaled mass of CO_2 in the caprock at time t. The form of the function, g, is determined from a systematic data analysis of numbers of

reservoir simulations. For instance, in Paper D, we designed a linear model to predict the role of dynamic capillary pressure and relative permeabilities on the containment of caprock for CO_2 storage application. The details of the two approaches introduced above are discussed in Paper D for dynamic TPTC model.

Chapter 5

Summary and outlook

This chapter provides a short summary of the scientific results that are included in Part II and connects these results with the approaches discussed in the previous chapters. Paper A presents a framework that upscales the pore-scale underpinnings of time-dependent WA mechanism to the Darcy-scale capillary pressure function. Paper B evaluates the framework presented by Paper A for time-dependent WA induced dynamic relative permeability function. This paper comes up with an alternative approach to upscale pore-scale WA processes in the relative permeabilities. Paper C incorporates the dynamic capillary pressure function into an immiscible two-phase flow model and proposes an implicit linearization scheme. Finally, Paper D provides a sensitivity analysis and WA quantification on the role of dynamic saturation functions in the distribution and migration of CO_2 plume in the subsurface formation.

5.1 Main results

5.1.1 Paper A

Title: Impact of time-dependent wettability alteration on the dynamics of capillary pressure

Authors: A. M. Kassa, S. E. Gasda, K. Kumar, and F. A. Radu

Journal: Advances in Water Resources 142, 2 (2020)

Wettability is a pore-scale property that plays an important role on multiphase flow behavior in a porous medium. In particular, wettability affects the residual saturation and the saturation function path at the pore level. This, in turn, impacts the capillary pressure-saturation relationships at the core scale. For instance, it is known that a change in wettability is the main cause for capillary pressure function alteration. However, wettability is assumed to be constant throughout the reservoir life time and homogeneous across the reservoir in many macroscale subsurface flow applications.

There are a few measurements for CO_2-water system that characterize WA induced capillary pressure-saturation path alteration. In these measurements, the capillary pressure showed a steadily reduction over time. Interestingly, coalescence was not achieved for both drainage and imbibition capillary pressure curves after scaling by interfacial tension. This implies that classical scaling techniques are not capable to explain the capillary pressuresaturation path deviations. This capillary pressure function deviation was explained as a results of wettability change but did not explicitly measure any changes in CA. For these systems, the standard capillary pressure function that assume static wettability as well as the Leverett-J function are not sufficient to describe the physics. Thus, designing a framework to upscale the WA dynamics in the capillary pressure function is important for the understanding of the migration of fluids in the formation.

The upscaling process in Paper A starts with assuming a WA mechanism that follows the sorption-type model that is dependent on the exposure time to the WA agent in addition to the chemistry. This pore-scale WA model is designed to evolve from an arbitrary initial-wet condition to the final-wet condition through time. The designed wettability model is then coupled with the pore-scale model, a bundle-of-tube (BoT) approach, to simulate time-dependent capillary pressure and associated data. The simulated data is then used to quantify the WA induced dynamics in the capillary pressure, and thus develop a dynamic capillary pressure model for Darcy-scale flow processes. An interpolation-based capillary pressure model is designed successfully. The model captures the pore-scale wettability dynamics by adding a dynamic term as a coefficient to move the capillary pressure curve from the initial-wet to final-wet condition through time. The new dynamic model resolves the existing interpolation models, which are only chemistry dependent, used in the studies of reservoir simulation by including the WA dynamics in time and quantifying the pore-scale WA process to the interpolation model in a systematic manner.

The proposed interpolation approach results in an upscaled model that

allows for a long-term change in capillary pressure as a function of upscaled variables, saturation, and exposure time to a WA agent. The exposure time in its average sense is simply the integration of saturation history over time per each volume (grid cell). The model consists of three main components: two capillary pressure functions at the initial and final wetting state and a dynamic interpolation coefficient that moves from one state to the other. The initial and final capillary pressure functions can be determined *a priori* from static experiments using inert fluids. The initial and final wetting condition curves can be described by any suitable existing capillary pressure models. For instance, the initial- and final-wetting states are represented by classical Brooks-Corey functions in Paper A. The dynamic coefficient is thus the only variable correlated to dynamic capillary pressure simulations. In this study, we have shown that the coefficient can be easily correlated to saturation and exposure time via a single parameter.

The model shows an excellent agreement with the simulated time-dependent capillary pressure–saturation data. Particularly, the model is independent of the saturation history. This implies that the model parameter does not need to be adjusted for an arbitrary capillary pressure–saturation path. Furthermore, a clear relationship between the pore-scale WA model parameter and the dynamic capillary pressure model parameter is observed in this paper. The result also shows the implications of wettability for experimental methodology as well as macroscale simulation of wettability-altering fluids.

5.1.2 Paper B

Title: Modeling of relative permeabilities including dynamic wettability transition zones

Authors: A. M. Kassa, S. E. Gasda, K. Kumar, and F. A. Radu

Journal: Journal of Petroleum Science and Engineering, (2021)

This paper explores the effect of time-dependent wettability change in the relative permeability–saturation relations. As we point out in summary of Paper A above, wettability change regulates the fluids distribution and controls the relative movement of fluids. Thus, modeling the impact of wettability change in the relative permeability function is essential to fully understand fluids interaction in a porous medium.

This paper starts with evaluating the potential of the interpolation-based model because it was successfully applied to capture the dynamic

wettability effect in the capillary pressure function. The result shows that the interpolation-based approach would be the last option to correlate WA induced dynamics in the relative permeability functions. This might be the reason why the WA process is impacting the saturation functions in different ways. The capillary pressure function, see Paper A, is affected by the wettability change directly, and a small change in wettability exerts a large impact on the dynamics of the capillary pressure function. However, the relative permeability alteration occurs when the WA affects the pore filling/draining orders of pore sizes. This leads to a longer exposure time to observe a relative permeability deviation from the initial-wet state curve. Furthermore, unlike the capillary function, the relative permeability curves are constrained between zero and one for any change of wettability. These features of the relative permeability impact the modeling approach to upscale the pore-scale WA process to the relative permeability behavior.

In Paper B, we introduce an alternative approach to upscale the WA effects in the relative permeability functions. The approach relies on modifying the existing relative permeability models by formulating the parameters as a function of exposure time and WA agent. This approach is motivated by the fact that the parameters in the standard relative permeability models are adjusted to different values when the wettability changes from one state to the other.

Paper B considers a similar wettability change model (i.e., a sorption model that is exposure time and WA agent dependent) as in Paper A. However, a triangular bundle-of-tubes is considered to represent the pore-scale model. These tubes allow mixed-wet condition within a pore which leads to corner and layer invasion. As we did in Paper A, we couple the bundle of tubes model with the WA model and simulate time-dependent relative permeability curves. The simulated data is used to characterize and quantify the wettability dynamics in the relative permeabilitysaturation curves. Following this approach, the LET model [76] is modified successfully to predict the time-dependent relative permeability curves.

The modified LET model agrees well with the simulated relative permeability data. Similar to the interpolation-based model in Paper A, the modified LET model is independent of the relative permeability–saturation path. This implies that the model parameter does not need to be adjusted for an arbitrary saturation history. Furthermore, a clear relationship between the pore-scale WA model parameter and the dynamic capillary pressure model parameter is observed in this paper. The result also shows the implications of wettability for experimental methodology as well as macroscale simulation of wettability-altering fluids.

5.1.3 Paper C

Title: Implicit linearization scheme for nonstandard two-phase flow in porous media

Authors: A. M. Kassa, K. Kumar, S. E. Gasda, and F. A. Radu

Journal: International Journal for Numerical Methods in Fluids, (2020)

In this paper, we introduced the dynamic capillary pressure model that is proposed in Paper A into the two-phase porous media flow model. This time-dependent capillary pressure function introduces a non-local (in time) term in the mass balance law, see Equations (2.24a) and (2.24b) in Chapter 2. The resulting model is highly non-linear and considers the history of the exposure of the REV to the WA agent. Due to the non-linearity and dynamic heterogeneity of the designed model, it is impossible to derive analytic solutions. As a consequence, a numerical approach is the only option to predict such flow dynamics. However, developing robust algorithms for finding numerical solutions is also a challenge in itself even for standard models.

Paper C presents a monotone fixed-point iterative, inexact Newton, linearization scheme for the resulting non-standard two-phase flow model. First of all, the scheme treats the capillary pressure function (the non-local term) semi-implicitly in time. The chain rule is applied to represent the capillary pressure term in the pressure and transport equations, where semi-backward Euler discretization is applied in time. This allows the saturation profile to be evaluated at the current time step. Then we introduce an L-scheme type stabilization term in the pressure and saturation equations. Finally, an iteration step is introduced over the linearized mass balance law to improve further the stability of the scheme. The scheme take the advantage over the Newton's method by not calculating the Jacobian of the system, and over the IMPES by treating the capillary pressure implicitly.

The convergence of the proposed linearization scheme is proved theoretically by setting some physically reasonable assumptions on the model behaviors. For instance, the saturation functions are assumed to be bounded and Lipschitz continuous. The theoretical convergence analysis of the scheme is further supported by illustrative numerical examples, where the potential of the scheme is evaluated for reservoir heterogeneity in addition to the dynamic change of the capillary pressure function over exposure time to the WA agent. The numerical results show that the scheme converges, linearly, within a few number of iterations even for large alterations

(jumps) in the capillary pressure function. As a complement, the scheme is compared with the IMPES method. The newly proposed scheme shows an improvement over the IMPES in terms of convergence stability and number of iterations. The iterative IMPES shows restriction on the choice of the time step, whereas the proposed scheme converges for large time step size.

The advantage of the scheme is its flexibility to choose large time step size even for large capillary pressure function alteration (or saturation discontinuity). The numerical results show that the scheme slowly converges to the solution for large time step size and large alteration in capillarity. However, its quality to handle large time step size makes the scheme compatible with Newton's method in a straightforward manner. This implies that an alternating between the scheme with Newton's method may improve the convergence rate.

5.1.4 Paper D

Title: Field-scale impacts of long-term wettability alteration in geological CO_2 storage

Authors: A. M. Kassa, S. E. Gasda, D. Landa-Marbán, T. H. Sandve, and K. Kumar

Journal: https://arxiv.org/abs/2108.06601, (2021)

A drastic reduction of CO_2 emissions is a challenge because 85% of the power generation is supplied by coal-fired power plants. Due to this, the concentration of CO_2 in the atmosphere may continue to rise unless strong measures are implemented to reduce the net CO_2 emissions. Thus, alternative strategies such as forestation and storing CO_2 in a subsurface formation should be considered to mitigate the carbon problem. Subsurface CO_2 storage is an emerging solution strategy to reduce the amount of CO_2 emissions into the atmosphere. Saline aquifers, coal beds, and depleted oil/gas reservoirs are promising candidates for CO_2 storage applications. Among these, the Saline aquifers are the deepest and largest formations and are of interest in Paper D.

Paper D examines the storage capacity of saline aquifers theoretically by coupling exposure time-dependent capillary pressure and relative permeability functions, that are developed in Papers A and B respectively, with a two-phase compositional flow model. In this paper, we studied the impact of variability of model parameters on the migration of CO_2 in a

dynamically altering aquifer. The variability of these parameters control the capillary, viscous, and buoyancy forces, which are the main factors that influence CO_2 migration during and post injection. This paper simulates the CO_2-water migration for different parameters combinations and quantifies the behavior of horizontal and vertical migration of CO_2 plume.

The horizontal CO_2 plume movement is analyzed based on a dimensionless number, that is, the capillary number. The capillary number at macro scale relates the viscous force with capillary force. This number is used to asses the role of WA induced dynamic saturation functions in the CO_2 plume movement. The assessment shows that the WA induced dynamic saturation functions play a significant role in the capillary dominating flow regime by increasing the storage efficiency of the aquifer, whereas very viscous flow will not be greatly impacted by wettability dynamics in the saturation functions. This implies that the horizontal CO_2 plume movement is similar regardless of the values of $\beta(C)$ and/or $\eta(C)$ for viscous force dominating flow regime. In other words, the impact of WA induced dynamic saturation functions on the CO_2 plume migration decreases as the capillary number of the flow increases.

This paper also quantifies the vertical migration of CO_2. For this purpose, we designed a two-layered section in which 50% of the storage is saturated with CO_2 provided that the CO_2 never escape the caprock for initial-wet constitutive curves. Then we introduce a WA agent to the system through the saturation functions. As the wetting property of the caprock is altered towards final-wet condition, the CO_2 bubbles up to the caprock due to the buoyancy force. Multiple numerical simulations are performed to quantify the trend of the buoyant CO_2 invasion of the caprock. We measure the total CO_2 in caprock over time for different fluid-rock parameters and proposed a simple model to evaluate the caprock integrity for CO_2 storage applications. More interestingly, the proposed model is used for such a system to predict the total CO_2 in the caprock for the given time, WA rate (i.e., C value), caprock entry pressure and permeability without doing intensive numerical simulations.

5.2 Conclusion

This thesis deals with the modeling and numerical analysis of the impact of time-dependent wettability dynamics for a two-phase (particularly CO_2-water interaction) flow process in porous media: from pore scale to macroscale processes. Wettability, a pore-scale property, strongly determines the distribution and relative movement of immiscible fluids at the

pore level. This, in turn, controls the capillarity and relative permeability of immiscible fluids in porous media at macroscale. In this thesis, we designed frameworks to upscale the impact of WA process to the saturation functions at the Darcy's scale. Paper A has shown that an interpolation-based model can successfully capture the pore-scale underpinnings of time-dependent WA in the capillary pressure. However, the interpolation-based models showed a limitation to upscale WA induced dynamics in the relative permeability functions. As a consequence, another approach (parametric approach in Paper B) is proposed to upscale the WA process in the relative permeability functions. The designed approach modifies the existing static models by including the WA process through model parameters. Among many, the LET model is found to be flexible to include the wettability dynamics in the relative permeabilities functions. The interpolation and the modified LET models respectively showed an agreement with the BoT simulated WA induced dynamic saturation functions data. More importantly, the models are independent of the saturation-time paths generated by the drainage-imbibition displacements. Furthermore, we quantified the relationships between the pore-scale WA model and macroscale model parameters. The implication of this result is that by knowing the mechanism that controls CA change at the pore scale, which can be obtained by a relatively simple batch experiment, one can quantify *a priori* the macroscale dynamics without having to perform pore-scale simulations.

The resulting time-dependent saturation functions introduce non-local (in time) terms in a Darcy-scale two-phase flow problem. The non-locality is introduced due to the dynamic saturation functions. These functions are exposure time (fluid history) dependent in addition to the current wetting phase saturation profile. This adds extra complexities on the regularity of these functions, and thus the resulting two-phase flow model is challenging to solve. This thesis, however, proposed an alternative (robust) monolithic linearization scheme that treats the dynamic capillary pressure term implicitly in time for the resulting non-standard two-phase flow model. The convergence of the proposed scheme is proved theoretically and illustrated with numerical examples in Paper C. The numerical results showed that the scheme is flexible on the choice of time-step size for reasonably fast WA induced capillary pressure function alteration. This implies that combining the scheme with a Newton's method is a straightforward application. This would further improve the convergence speed and accuracy of the approximation to simulate such complex models.

Another important contribution of this thesis is quantifying the impact of time-dependent WA in the CO_2-water displacement scenario at the field

scale. The impact of WA on the CO_2 plume movement is quantified based on: (1) the non-dimensional grouping (particularly the capillary number) for horizontal displacement scenario and (2) modeling of the caprock integrity for vertical WA induced CO_2-water redistribution. From the numerical experiment, we observed that the dynamic saturation functions strongly impact the movement of CO_2 plume in the capillary-dominated flow regime and enhanced the storage efficiency of the aquifer. Non-trivial CO_2 redistribution is also observed for most dynamic case in low capillary number regime. However, the numerical experiment results showed that the effect of WA dynamics in the saturation functions decreases along the capillary number. Implying that the WA is less significant in viscous flow regime. The second objective of Paper D was quantifying the caprock integrity under different WA rates and fluid-rock properties. In this experiment, we observed that the capillarity act to trap the CO_2 beneath the caprock for initial-wet relative permeability and capillary pressure functions. And, the CO_2 plume can migrate far deep into the caprock for final-wet capillary pressure and initial-wet relative permeability functions compared to the final-wet capillary pressure and relative permeability functions. The proposed scaling model showed that the long-term (gradual) WA possess little risk to CO_2 containment beneath low permeable caprock.

5.3 Future studies

This thesis can be considered as a starting stepping-stone to understand the impact of time-dependent WA processes on the behaviors of multi-phase flow (e.g., CO_2 storage, oil recovery, and unsaturated flow applications to name a few) in porous media. Particularly, we believe that this thesis inspires more interesting works related to safe and secure CO_2 storage applications both in laboratory experiment and theory (pore to field scale).

For example, we note that the pore-scale model (i.e., non-interacting capillary tubes) is simplistic in that it does not represent interactions between pores, and does not possess realistic pore-geometry (i.e., converging-diverging throat diameters). Additionally, there is no natural hysteresis or residual saturation in the BoT model. Thus, coupling advanced pore-scale model with time-dependent WA process will be the interest of the future works to investigate and represent the time-dependent WA dynamics in the residual saturation and associated saturation functions. Furthermore, the inclusion of WA effect in the relation between capillary pressure, interfacial area, and saturation is also interesting aspect to understand the safety of CO_2 storage application.

Secondly, robust and fast solvers for the resulting non-standard two-phase flow model shall be examined in more detail manner. We recall that the proposed scheme, in this thesis, is only compared with the IMPES scheme. Therefore, a further study on the comparison of the linearization schemes for such a model is important to accurately and efficiently predict the impact of WA on the CO_2 storage application. Regarding the field-scale WA quantification, more general sensitivity analysis is needed to fully characterize the impact of WA on storage capacity and caprock integrity. Further study is needed to determine whether the fundamental nature of dynamic behavior that we observed in Paper D will hold when higher-dimensional flow and WA induced residual saturation are coupled. Theoretical studies that treat a two-dimensional flow condition, reservoir heterogeneity, and long-term WA is important to fully understand the impact of WA in CO_2 storage application.

Finally, we note that the pore-scale WA model was not calibrated with experimental data. And thus, a laboratory experiment is in need to calibrate further the pore-scale WA model.

Bibliography

[1] B. Adibhatla, X. Sun, and K. K. Mohanty. "Numerical studies of oil production from initially oil-wet fracture blocks by surfactant brine imbibition". In: *SPE international improved oil recovery conference in Asia*. SPE J., 2005. DOI: 10.2118/97687-MS.

[2] A. Ahmed and T. W. Patzek. "The impact of wettability alteration on two-phase flow characteristics of sandstones–A quasi-static description". In: *Water Resour. Res.* 39 (2003), pp. 1–10. DOI: 0.1029/2002WR001366,2003.

[3] S. M. Al-Mutairi, S. A. Abu-Khamsin, and M. E. Hossain. "An experimental investigation of wettability alteration during CO_2 immiscible flooding". In: *J. Pet. Sci. Eng.* 120 (2014), pp. 73–77. DOI: 10.1016/j.petrol.2014.05.008.

[4] V. Alvarado and E. Manrique. "Enhanced oil recovery: An update review". In: *Energies* 3 (2010), pp. 1529–1575. DOI: 10.3390/en3091529.

[5] P. Ø. Andersen, S. Evje, H. Kleppe, and S. M. Skjæveland. "A model for wettability alteration in fractured reservoirs". In: *SPE J.* 20 (2015), pp. 1261–1275. DOI: 10.2118/174555-PA.

[6] P. Ø. Andersen, S. M. Skjæveland, and D. C. Standnes. "A novel bounded capillary pressure correlation with application to both mixed and strongly wetted porous media". In: *Abu Dhabi international petroleum exhibition and conference*. Abu Dhabi, UAE: Society of Petroleum Engineers, 2017, pp. 1–12. DOI: https://doi.org/10.2118/188291-MS.

[7] D. Anderson. "Iterative procedures for non-linear integral equations". In: *J. ACM* 12 (1965), pp. 547–560. DOI: 10.1145/321296.321305.

[8] W. Anderson. "Wettability literature survey-part 5: The effects of wettability on relative permeability". In: *J. Pet. Technol.* 39 (1987), pp. 1453–1468. DOI: 10.2118/16323-PA.

[9] R. T. Armstrong, A. Georgiadis, H. Ott, D. Klemin, and S. Berg. "Critical capillary number: Desaturation studied with fast X-ray computed microtomography". In: *Geophys. Res. Lett.* 41 (2014), pp. 55–60. DOI: 10.1002/2013GL058075.

[10] K. Aziz and A. Settari. "Petroleum reservoir simulation". In: Applied Science Publishers Ltd., 1979.

[11] G. Barenblatt, T. Patzek, and D. Silin. "The mathematical model of nonequilibrium effects in water-oil displacement". In: *SPE J.* 8 (2003), pp. 409–416. doi: 10.2118/87329-PA.

[12] J. T. Bartley and D. W. Ruth. "Relative permeability analysis of tube bundle models". In: *Transp Porous Media* 36 (1999), pp. 161–187. doi: 10.1023/A:1006575231732.

[13] J. T. Bartley and D. W. Ruth. "Relative permeability analysis of tube bundle models, including capillary pressure". In: *Transp Porous Media* 45 (2001), pp. 447–480. doi: 10.1023/A:1012297432745.

[14] J. Bear and Y. Bachmat. *Introduction to modeling of transport phenomena in porous media*. Springer Science & Business Media, 1990. doi: 10.1023/A:1006575231732.

[15] J. Bear and A. Verruijt. *Modeling groundwater flow and pollution: Theory and application of transport in porous medium*. D. Reidel, 1987. doi: 10.1007/978-94-009-3379-8.

[16] A. Bielinski. "Numerical simulation of CO_2 sequestration in geological formations". PhD thesis. 2006.

[17] M. J. Blut. *Multi-phase flow in permeable media: A pore-scale perspective*. Cambridge university press, 2017.

[18] J. E. Bobek, C. C. Mattax, and M. O. Denekas. "Reservoir rock wettability–Its significance and evaluation". In: *Trans.* 213 (1958), pp. 155–160. doi: https://doi.org/10.2118/895-G.

[19] D. Bonn, J. Eggers, J. Indekeu, J. Meunier, and E. Rolley. "Wetting and spreading". In: *Rev. Mod. Phys.* 81 (2009), pp. 739–805. doi: 10.1103/RevModPhys.81.739.

[20] J. Both, K. Kumar, J. Nordbotten, I. Pop, and F. Radu. "Iterative linearisation schemes for doubly degenerate parabolic equations". In: *Numerical Mathematics and Advanced Applications ENUMATH 2017*. Springer International Publishing, Cham. ISBN 978-3-319-96415-7, 2019, pp. 49–63. doi: 10.1007/978-3-319-96415-7.

[21] J. Both, K. Kumar, J. Nordbotten, and F. Radu. "Anderson accelerated fixed-stress splitting schemes for consolidation of unsaturated porous media". In: *Comput. Math. Appl.* 77 (2019), pp. 1479–1502. doi: 10.1016/j.camwa.2018.07.033.

[22] Brooks and Corey. *Hydraulic properties of porous media*. Tech. rep. Colorado State University, 1964.

[23] J. S. Buckley, Y. Liu, and S. Monsterleet. "Mechanisms of wetting alteration by crude oils". In: *SPE J.* 3 (1988). url: https://doi.org/10.2118/37230-PA.

[24] M Bui et al. "Carbon capture and storage (CCS): The way forward". In: *Energy Environ. Sci.* 11 (2018), pp. 1062–1176. doi: 10.1039/C7EE02342A.

[25] H. Cao. "Development of techniques for general purpose simulators". In: Stanford University Press, 2002.

[26] Z. Chen. *Finite element methods and their applications: Part of the scientific computation book series (SCIENTCOMP)*. Springer, 2005.

[27] K. Coats. "IMPES stability: Selection of stable timesteps". In: *SPE J.* 8 (2003), pp. 181–187. doi: 10.2118/84924-PA.

[28] A. Costa. "Permeability-porosity relationship: A reexamination of the Kozeny-Carman equation based on a fractal pore-space geometry assumption". In: *Geophys. Res. Lett.* 33 (2006), pp. 1–5. doi: 1029/2005GL025134.

[29] H. K. Dahle, M. A. Celia, and S. M. Hasanizadeh. "Bundle-of-tubes model for calculating dynamic effects in the capillary pressure-saturation relationship". In: *Transp Porous Media* 58 (2005), pp. 5–22. doi: https://doi.org/10.1007/s11242-004-5466-4.

[30] A. Davis, S. A. Morton III, R. Counce, D. DePaoli, and M.-C. Hu. "Ionic strength effects on hexadecane contact angles on a gold-coated glass surface in ionic surfactant solutions". In: *Colloids Surf. A* 221 (2003), pp. 69–80. doi: 10.1016/S0927-7757(03)00132-8.

[31] M. Delshad, N. F. Najafabadi, G. A. Anderson, G. A. Pope, and K. Sepehrnoori. "Modeling wettability alteration by surfactants in naturally fractured reservoirs". In: *SPE Res Eval & Eng* 12 (2009). doi: https://doi.org/10.2118/100081-PA.

[32] P. Deuflhard. *Newton methods for nonlinear problems: Affine Invariance and Adaptive Algorithms*. Springer, Heidelberg. ISBN 978-3-642-23898-7, 2011. doi: 10.1007/978-3-642-23899-4.

[33] C. E. Diaz, I. Chatzis, and F. A. L. Dullien. "Simulation of capillary pressure curves using bond correlated site percolation on a simple cubic network". In: *Transp Porous Media* 2 (1987), pp. 215–240. doi: https://doi.org/10.1007/BF00165783.

[34] J. L. Dickson, G. Gupta, T. S. Horozov, B. P. Binks, and K. P. Johnston. "Wetting phenomena at the CO_2/water/glass interface". In: *Langmuir* 22 (2006), pp. 2161–2170. doi: 10.1021/la0527238.

[35] Y. Du, K. Xu, L. Mejia, P. Zhu, and M. T. Balhoff. "Microfluidic investigation of low-salinity effects during oil recovery: A no-clay and time-dependent mechanism". In: *SPE J.* (2019), pp. 2841–2858. doi: 10.2118/197056-PA.

[36] A. A. Emad, S. Vialle, A. Barifcani, M. Sarmadivaleh, and I. S. "Impact of reservoir wettability and heterogeneity on CO_2-plume migration and trapping capacity". In: *Int. J. Greenh. Gas Control.* 58 (2017), pp. 142–158. doi: 10.1016/j.ijggc.2017.01.012.

[37] T. S. van Erp, T. Trinh, S. Kjelstrup, and K. S. Glavatskiy. "On the relation between the Langmuir and thermodynamic flux equations". In: *Front. Phys.* (2014), pp. 1–14. doi: 10.3389/fphy.2013.00036.

[38] C. W. Extrand. "Forces, pressures and energies associated with liquid rising in non-uniform capillary tubes". In: *J. Colloid Interface Sci.* 450 (2015), pp. 135–140. doi: https://doi.org/10.1016/j.jcis.2015.03.007.

[39] O. Falode and E. Manuel. "Wettability effects on capillary pressure, relative permeability, and irredcucible saturation using porous plate". In: *J. Pet. Eng.* 2014 (2014), pp. 1–12. doi: 10.1155/2014/465418.

[40] D. Fenwick and M. Blunt. "Three-dimensional modeling of three phase imbibition and drainage". In: *Adv Water Resour* 25 (2 1998), pp. 121–143. doi: https://doi.org/10.1016/S0309-1708(96)00037-1.

[41] B. Flemisch. "Tackling coupled problems in porous media: development of numerical models and an open source simulator". PhD thesis. Vom Stuttgart Research Centre for Simulation Technology, 2013.

[42] P. A. Forsyth. "Adaptive implicit criteria for two-phase flow with gravity and capillary pressure". In: *SIAM J. Sci. Stat. Comput.* 10 (1989), pp. 227–252. doi: 10.1137/0910017.

[43] J. Franc, P. Horgue, R. Guibert, and G. Debenest. "Benchmark of different CFL conditions for IMPES". In: *C. R. Mecanique* 344 (2016), pp. 715–724. doi: 10.1016/j.crme.2016.08.003.

[44] M. T. van Genuchten. "A closed-form equation for predicting the hydraulic conductivity of unsaturated soils". In: *Soil Sci Soc Am J* 44 (1980), pp. 892–898. doi: https://doi.org/10.2136/sssaj1980.03615995004400050002x.

[45] L. J. Gerritsen M. G. adn Durlofsky. "Modeling fluid flow in oil reservoirs". In: *Annu. Rev. Fluid Mech.* 37 (2005), pp. 211–238. doi: 10.1146/annurev.fluid.37.061903.175748.

[46] S. Hassanizadeh, M. Celia, and H. Dahle. "Dynamic effects in the capillary pressure–saturation relationship and its impacts on unsaturated flow". In: *Vadose Zone J* 1 (2002), pp. 38–57. doi: https://doi.org/10.2113/1.1.38.

[47] J. O. Helland. "Modelling of three-phase capillary pressure for mixed-wet reservoirs". PhD thesis. University of Stavanger, 2005.

[48] J. O. Helland and S. M. Skjæveland. "Physically based capillary pressure correlation for mixed-wet reservoirs from a bundle-of-tubes model". In: *Proceedings of the SPE/DOE improved oil recovery symposium*. SPE, 2006, pp. 171–180. url: https://doi.org/10.2118/89428-PA.

[49] J. O. Helland and S. M. Skjæveland. "Relationship between capillary pressure, saturation, and interfacial area from a model of mixed-wet triangular tubes". In: *Water Resour. Res.* 43 (2007), pp. 1–15. doi: 10.1029/2006WR005698.

[50] Helmig. *Mutiphase flow and transport processes in the subsurface*. Springer, 1997.

[51] M. Hui and M. J. Blunt. "Effects of wettability on three-phase flow in porous media". In: *J. Phys. Chem. B* 104 (2000), pp. 3833–3845. doi: 10.1021/jp9933222.

[52] S. Iglauer, A. Hassan, M. Sarmadivaleh, K. Liu, and C. Pham. "Contamination of silica surfaces: Impact on water-CO_2-quartz and glass contact angle measurements". In: *Int. J. Greenh. Gas Control.* 22 (2014), pp. 325–328. doi: https://doi.org/10.1016/j.ijggc.2014.01.006.

[53] S. Iglauer, M. Mathew, and F. Bresme. "Molecular dynamics computations of brine-CO_2 interfacial tensions and brine-CO2-quartz contact angles and their effects on structural and residual trapping mechanisms in carbon geo-sequestration". In: *J. Colloid Interface Sci.* 386 (2012), pp. 405–414. doi: 10.1016/j.jcis.2012.06.052.

[54] S. Iglauer, C. H. Pentland, and A. Busch. "CO_2 wettability of seal and reservoir rocks and the implications for carbon geo-sequestration". In: *Water Resour. Res.* 51 (2014), pp. 729–774. doi: 10.1002/2014WR015553.

[55] S. Iglauer, T. Rahman, M. Sarmadivaleh, A. Al-Hinai, M. A. Fernø, and M. Lebedev. "Influence of wettability on residual gas trapping and enhanced oil recovery in three-Phase flow: A pore-scale analysis by use of microcomputed tomography". In: *SPE J.* 21 (2016), pp. 1916–1929. DOI: https://doi.org/10.2118/179727-PA.

[56] D. Illiano, I. S. Pop, and F. A. Radu. "Iterative schemes for surfactant transport in porous media". In: *Comput. Geosci.* 25 (2020), pp. 805–822.

[57] IPCC. *IPCC special report on carbon dioxide capture and storage.* Tech. rep. 2005.

[58] "Iterative solvers for biot model under small and large deformations". In: *Comput. Geosci.* 25 (2020), pp. 687–699.

[59] M. Jafari and J. Jung. "The change in contact angle at unsaturated CO_2-water conditions: Implication on geological carbon dioxide sequestration". In: *Geochem. Geophys. Geosyst.* 17 (2016), pp. 3969–3982. DOI: 10.1002/2016GC006510.

[60] J. W. Jung and J. Wan. "Supercritical CO_2 and ionic strength effects on wettability of silica surfaces: Equilibrium contact angle measurements". In: *Energy Fuels* 26 (2012), pp. 6053–6059. DOI: 10.1021/ef300913t.

[61] A. M. Kassa, S. E. Gasda, K. Kumar, and A. F. Radu. "Impact of time-dependent wettability alteration on dynamic capillary pressure". In: *Adv Water Resour* 142 (2020), pp. 1–9. DOI: https://doi.org/10.1016/j.advwatres.2020.103631.

[62] A. M. Kassa, S. E. Gasda, D. Landa-Marbán, T. H. Sandve, and K. Kumar. "Field-scale impacts of long-term wettability alteration in geological CO_2 storage". In: *Preprint submitted to* (). DOI: arxiv.org/abs/2108.06601.

[63] A. M. Kassa, K. Kumar, S. E. Gasda, and F. A. Radu. "Implicit linearization scheme for nonstandard twophase flow in porous media". In: *Int J Numer Methods Fluids* 93 (2020), pp. 445461.

[64] A. M. Kassa, E. G. Sarah, K. Kumar, and A. F. Radu. "Modeling of relative permeabilities including dynamic wettability transition zones". In: *J. Pet. Sci. Eng.* 203 (2021), pp. 1–15. DOI: https://doi.org/10.1016/j.petrol.2021.108556.

[65] Y. Kim, J. Wan, T. J. Kneafsey, and T. K. Tokunaga. "Dewetting of silica surfaces upon reactions with supercritical CO_2 and brine: Pore-scale studies in micromodels". In: *Environ. Sci. Technol.* 46 (2012), pp. 4228–4235. DOI: 10.1021/es204096w.

[66] A. Kjosavik, J. K. Ringen, and S. M. Skjaeveland. "Relative permeability correlation for mixed-wet reservoirs". In: *SPE J* 7 (2002), pp. 49–58. DOI: 10.2118/77328-PA.

[67] J. Kou and S. Sun. "On iterative IMPES formulation for two-phase flow with capillarity in heterogeneous porous media". In: *Int. J. Numer. Anal. Mod. B* 1 (2010), pp. 30–40.

[68] K. Lackner. "A guide to CO_2 sequestration". In: *Science* 300 (2003), pp. 1677–1678. DOI: 10.1126/science.1079033.

[69] D. Landa-Marbán. "Mathematical modeling of microbial enhanced oil recovery with focus on bio-plug technology: from the pore to the core scale". PhD thesis. University of Bergen, 2019.

[70] J. Li, J. Liu, M. G. Trefry, J. Park, K. Liu, B. Haq, C. D. Johnston, and H. Volk. "Interactions of microbial-enhanced oil recovery processes". In: *Transp Porous Med* 87 (2011), pp. 77–104. doi: 10.1007/s11242-010-9669-6.

[71] K. Li and R. N. Horne. "Comparison of methods to calculate relative permeability from capillary pressure in consolidated water-wet porous media". In: *Water Resour. Res.* 42 (2006), pp. 1–9. doi: https://doi.org/10.1029/2005WR004482.

[72] K. A. Lie. *An Introduction to Reservoir Simulation Using MATLAB/GNU Octave: User Guide for the Matlab Reservoir Simulation Toolbox (MRST)*. Cambridge CB2 8BS: Cambridge University Press, 2019. doi: 10.1017/9781108591416.

[73] F. List and F. A. Radu. "A study on iterative methods for solving Richards equation". In: *Comput. Geosci.* 20 (2016), pp. 341–353. doi: 10.1007/s10596-016-9566-3.

[74] M. Loizzo, B. Lecampion, T. Bérard, A. Harichandran, and L. Jammes. "Reusing O&G-depleted reservoirs for CO_2 storage: Pros and cons". In: *SPE J.* (2010), pp. 166–172. doi: https://doi.org/10.2118/124317-PA.

[75] F. Lomeland and E. Ebeltoft. "A new versatile capillary pressure correlation". In: Abu Dhabi, UAE: SPE, 2008, pp. 1–18.

[76] F. Lomeland, E. Ebeltoft, and T. W. Hammervold. "A new versatile relative permeability correlation". In: *International Symposium of the Society of Core Analysts*. Society of Core Analysts, 2005.

[77] C. W. MacMinn, M. L. Szulczewski, and R. Juanes. "CO2migration in saline aquifers. Part 2. Capillary and solubility trapping". In: *J. Fluid Mech.* 688 (2011), pp. 321–351. doi: 0.1017/jfm.2011.379.

[78] L. Makkonen. "Young's equation revisited". In: *J. Phys.: Condens. Matter* 28 (2016). doi: 10.1088/0953-8984/28/13/135001.

[79] R. Mayer and R. A. Stowe. "Mercury porosimetry–breakthrough pressure for penetration between packed spheres". In: *J. Coll. Sci.* 20 (1965), pp. 89–911. doi: https://doi.org/10.1016/0095-8522(65)90061-9.

[80] S. McKee and D. Swailes. "On the derivation of the Langmuir isotherm for adsorption kinetics". In: *J. Phys. A Math. Gen.* 24 (1991), pp. 207–2010.

[81] A. Millington and J. Quirk. "Permeability of porous solids". In: *Trans. Faraday Soc.* 57 (1961), pp. 1200–1207. doi: 10.1039/TF9615701200.

[82] N. R. Morrow. "Physics and thermodynamics of capillary action in porous media". In: *Ind. Eng. Chem.* 62 (1970), pp. 32–56. doi: 10.1021/ie50726a006.

[83] S. A. Morton III, D. J. Keffer, R. M. Counce, and D. W. DePaoli. "Behavior of oil droplets on an electrified solid metal surface immersed in ionic surfactant solutions". In: *Langmuir* 21 (2005), pp. 1758–1765. doi: 10.1021/la0480235.

[84] S. A. Morton III, D. J. Keffer, R. M. Counce, D. W. DePaoli, and H. M. Z. C. "Thermodynamic method for prediction of surfactant-modified oil droplet contact angle". In: *J. Colloid Interface Sci.* 270 (2004), pp. 229–241. doi: https://doi.org/10.1016/j.jcis.2003.08.006.

[85] P. Mostaghimi, J. R. Percival, and D. Pavlidis. "Anisotropic mesh adaptivity and control volume finite element methods for numerical simulation of multiphase flow in porous media". In: *Math. Geosci.* 47 (2005), pp. 417–440. doi: 10.1007/s11004-014-9579-1.

[86] A Negara, A. Salama, and S. Sun. "Multi-phase flow simulation with gravity effect in anisotropic porous media using multipoint flux approximation". In: *Comput. Fluids* 114 (2015), pp. 66–74. DOI: 10.1016/j.compfluid.2015.02.012.

[87] J. M. Nordbotten. "Sequestration of carbon in saline aquifers–mathematical and numerical analysis". PhD thesis. University of Bergen, 2005.

[88] J. M. Nordbotten and M. A. Celia. *Geological storage of CO_2: Modeling approaches for large-scale simulation*. Wiley, 2012. DOI: 10.1002/9781118137086.

[89] J. M. Nordbotten, M. A. Celia, H. K. Dahle, and S. M Hassanizadeh. "On the definition of macroscale pressure for multi-phase flow in porous media". In: *Water Resour. Res.* 44 (2008), pp. 1–8. DOI: 10.1029/2006WR005715.

[90] S. Pacala and R. Socolow. "Stabilization wedges: Solving the climate problem for the next 50 years with current technologies". In: *Science* 305 (2004), pp. 968–972. DOI: 10.1126/science.1100103.

[91] D. Y. Peng and D. B. Robinson. "A new two-constant equation of state". In: *Ind. Eng. Chem. Fundam.* 15 (1976), pp. 5964. DOI: https://doi.org/10.1021/i160057a011.

[92] W. J. Plug and J. Bruining. "Capillary pressure for the sand-CO_2-water system under various pressure conditions. Application to CO_2 sequestration". In: *Adv Water Resour* 30 (2007), pp. 2339–2353. DOI: https://doi.org/10.1016/j.advwatres.2007.05.010.

[93] B. Poling, J. Prausnitz, and J. OConnel. *The properties of gases and liquids*. McGraw-Hill, Inc., 2001.

[94] I. Pop, F. Radu, and P. Knabner. "Mixed finite elements for the Richards equations: Linearization procedure". In: *J. Comput. Appl. Math.* 168 (1999), pp. 365373. DOI: https://doi.org/10.1016/j.cam.2003.04.008.

[95] S. E. Powers, W. H. Anckner, and T. F. Seacord. "Wettability of NAPL-contaminated sands". In: *J. Environ. Eng.* 122 (1996), pp. 889–896. DOI: https://doi.org/10.1061/(ASCE)0733-9372(1996)122:10(889).

[96] H. Princen. "Capillary phenomena in assemblies of parallel cylinders. I. Capillary rise between two cylinders". In: *J. Coll. Int. Sci.* 30 (1969), pp. 69–75. DOI: https://doi.org/10.1016/0021-9797(69)90379-8.

[97] H. Princen. "Capillary phenomena in assemblies of parallel cylinders. II. Capillary rise in systems with more than two cylinders". In: *J. Coll. Int. Sci.* 30 (1969), pp. 59–371. DOI: https://doi.org/10.1016/0021-9797(69)90403-2.

[98] W. R. Purcell. In: *J. Pet. Technol.* (1949)), pp. 36–48. DOI: 10.2118/949039-G.

[99] F. A. Radu, J. M. Nordbotten, I. S. Pop, and K. Kumar. "A robust linearization scheme for finite volume based discretizations for simulation of two-phase flow in porous media". In: *J. Comput. Appl. Math.* 289 (2015), pp. 134–141. DOI: 10.1016/j.cam.2015.02.051.

[100] A. F. Rasmussen et al. "The open porous media flow reservoir simulator". In: *Comput. Math. with Appl.* 81 (2019), pp. 159–185. DOI: https://doi.org/10.1016/j.camwa.2020.05.014.

[101] O. Redlich and J. N. S. Kwong. "On the thermodynamics of solutions. V. An equation of state. Fugacities of gaseous solutions". In: *Chem. Rev.* 44 (1949), pp. 233–244. DOI: 10.1021/cr60137a013.

[102] R. Reid, J. Prausnitz, and B. Poling. *The properties of gases and liquids*. McGraw-Hill Inc., 1987.

[103] "Robust iterative schemes for non-linear poromechanics". In: *Comput. Geosci.* 22 (2018), pp. 10211038. doi: 10.1007/s10596-018-9736-6.

[104] P. Sammon. "An analysis of upstream differencing". In: *SPE Reserv. Eng.* 3 (1988), pp. 1053–1056. doi: 10.2118/14045-PA.

[105] S. Saraji, L. Goual, M. Piri, and H. Plancher. "Wettability of scCO$_2$/Water/Quartz Systems: Simultaneous measurement of contact angle and interfacial tension at reservoir conditions". In: *Langmuir* 29 (2013), pp. 1–39. doi: 10.1021/la3050863.

[106] M. H. Sedaghat and S. Azizmohammadi. "Dynamic wettability alteration in naturally fractured rocks". In: *Comput Geosci* - (2019), pp. 1–11. doi: 10.1007/s10596-019-09843-6.

[107] J. Sheldon and W. Cardwell. "One-dimensional incompressible noncapillary two-phase fluid flow in a porous medium". In: *Trans.* 216 (1959), pp. 290296. doi: 10.2118/978-G.

[108] I. Sin, V. Lagneau, and J. Corvisier. "Integrating a compressible multicomponent two-phase flow into an existing reactive transport simulator". In: *Adv Water Resour* 100 (2017), pp. 62–77. doi: 10.1016/j.advwatres.2016.11.014.

[109] S. M. Skjæveland, L. M. Siqveland, A. Kjosavik, W. L. H. Thomas, and G. A. Virnovsky. "Capillary pressure correlation for mixed-wet reservoirs". In: *SPE Reservoir Evaluation & Engineering*. Vol. 3. SPE, 2000, pp. 60–67. url: https://doi.org/10.2118/60900-PA.

[110] M. Soldička. "A robust and efficient linearization scheme for doubly non-linear and degenerate parabolic problems arising in flow in porous media". In: *SIAM J. Sci. Comput.* 23 (2002), pp. 1593–1614.

[111] M. R. Todd, P. M. Ódell, and G. e. a. Hirasaki. "Methods for increased accuracy in numerical reservoir simulators". In: vol. 12. 1972, pp. 515530. doi: 10.2118/3516-PA.

[112] T. K. Tokunaga and W. Jiamin. "Capillary pressure and mineral wettability influences on reservoir CO_2 capacity". In: *Rev. Mineral. Geochem.* 77 (2013), pp. 481–503. doi: https://doi.org/10.2138/rmg.2013.77.14.

[113] T. K. Tokunaga, J. Wan, J. Jung, T. W. Kim, Y. Kim, and W. Dong. "Capillary pressure and saturation relations for supercritical CO_2 and brine in sand: High-pressure $P_c(S_w)$ controller/meter measurements and capillary scaling predictions". In: *Water Resour. Res.* 49 (2013), pp. 4566–4579. doi: 10.1021/acs.est.5b00826.

[114] L. N. Trefethen and D. Bau. *Numerical linear algebra*. Society for Industrial and Applied Mathematics (SIAM), 1997. doi: 10.1137/1.9780898719574.

[115] S. Wang, I. M. Edwards, and A. F. Clarens. "Wettability phenomena at the CO_2-brine-mineral interface: Implications for geologic carbon sequestration". In: *Environ Sci Technol* 47 (2013), pp. 234–241. doi: https://doi.org/10.1021/es301297z.

[116] S. Wang and T. K. Tokunaga. "Capillary pressure-saturation relations for supercritical CO_2 and brine in Limestone/Dolomite sands: Implications for geologic carbon sequestration in carbonate reservoirs." In: *Environ. Sci. Technol.* 49 (2015), pp. 72087217. doi: 10.1021/acs.est.5b00826.

[117] S. Wang, T. K. Tokunaga, J. Wan, W. Dong, and Y. Kim. "Capillary pressure–saturation relations in quartz and carbonate sands: Limitations for correlating capillary and wettability influences on air, oil, and supercritical CO_2 trapping". In: *Water Resour. Res.* (2016), pp. 6671–6690. DOI: 10.1002/2016WR018816.

[118] E. Washburn. "The dynamics of capillary flow". In: *Phys. Rev* 7 (1921), pp. 273–283.

[119] H. Wu, R. S. Jayne, and R. M. Pollyea. "A parametric analysis of capillary pressure effects during geologic carbon sequestration in a sandstone reservoir". In: *Greenhouse Gas Sci Technol.* 8 (2018), pp. 1039–1052. DOI: 10.1002/ghg.1815.

[120] W. S. Xu, P. Y. Luo, L. Sun, and N. Lin. "A prediction model of the capillary pressure J–function". In: *Plos One* 11 (2016), pp. 1–9. DOI: https://doi.org/10.1371/journal.pone.0162123.

[121] L. Yu, H. Kleppe, T. Kaarstad, and S. M. Skjæveland. "Modelling of wettability alteration processes in carbonate oil reservoirs". In: *Netw. Heterog. Media* 3 (2008), pp. 149–183. DOI: https://doi.org/10.2118/174555-PA.

Part II

Scientific results

A

Paper 5.1.1

Impact of time-dependent wettability alteration on the dynamics of capillary pressure

A. M. Kassa, S. E. Gasda, K. Kumar, and F. A. Radu

In Advances in Water Resources, volume 142, pp 1–11, 2020
DOI: 10.1016/j.advwatres.2020.103631

Advances in Water Resources 142 (2020) 103631

Contents lists available at ScienceDirect

Advances in Water Resources

journal homepage: www.elsevier.com/locate/advwatres

Impact of time-dependent wettability alteration on the dynamics of capillary pressure

Abay Molla Kassa [a,b,*], Sarah Eileen Gasda [a], Kundan Kumar [b], Florin Adrian Radu [b]

[a] NORCE Norwegian Research Center, Bergen, Norway
[b] Department of Mathematics, University of Bergen, Norway

ARTICLE INFO

Keywords:
Wettability alteration
Dynamic capillary pressure
Dynamic wettability
Bundle-of-tubes simulation
Upscaling

ABSTRACT

Wettability is a pore-scale property that has an important impact on capillarity, residual trapping, and hysteresis in porous media systems. In many applications, the wettability of the rock surface is assumed to be constant in time and uniform in space. However, many fluids are capable of altering the wettability of rock surfaces permanently and dynamically in time. Experiments have shown wettability alteration (WA) can significantly decrease capillarity in CO_2 storage applications. For these systems, the standard capillary-pressure model that assumes static wettability is insufficient to describe the physics. In this paper, we develop a new dynamic capillary-pressure model that takes into account changes in wettability at the pore-level by adding a dynamic term to the standard capillary pressure function. We assume a pore-scale WA mechanism that follows a sorption-based model that is dependent on exposure time to a WA agent. This model is coupled with a bundle-of-tubes (BoT) model to simulate time-dependent WA induced capillary pressure data. The resulting capillary pressure curves are then used to quantify the dynamic component of the capillary pressure function. This study shows the importance of time-dependent wettability for determining capillary pressure over timescales of months to years. The impact of wettability has implications for experimental methodology as well as macroscale simulation of wettability-altering fluids.

1. Introduction

Wettability plays an important role in many industrial applications, in particular subsurface porous media applications such as enhanced oil recovery (EOR) and CO_2 storage (Blunt, 2001; Bonn et al., 2009; Iglauer et al., 2014, 2016; Yu et al., 2008). The wetting property of a given multiphase system in porous media is defined by the distribution of contact angles. The contact angle (CA) is controlled by surface chemistry and associated forces acting at the molecular scale along the fluid-fluid-solid interface (Bonn et al., 2009). In porous media applications, microscale wettability determines the strength of pore-scale capillary forces and the movement of fluid interfaces between individual pores. At the core-scale, wettability impacts upscaled quantities and constitutive functions such as residual saturation, relative permeability, and capillary pressure, which in turn affect field-scale multiphase flow behavior.

The standard assumption is that wettability is a static property of the multiphase system. However, the composition of many fluids is capable of provoking the surfaces within pores to undergo wettability alteration (WA) via a change in CA. CA change can alter capillary forces at the pore scale, and thus affect residual saturations of the system (Ahmed and Patzek, 2003; Blunt, 1997). This effect has been exploited extensively in the petroleum industry, where optimal wetting conditions in the reservoir are obtained through a variety of means that includes chemical treatment, foams, surfactants, and low-salinity water flooding (see for example Morrow et al., 1986; Buckley et al., 1988; Jadhunandan and Morrow, 1995; Haagh et al., 2017; Singh and Mohanty, 2016).

Wettability is also recognized as a critical factor in geological CO_2 sequestration which exerts an important role on caprock performance (Kim et al., 2012; Tokunaga and Wan, 2013). The sealing potential of the caprock is highly dependent on CO_2 being a strongly non-wetting fluid, and WA may lead to conditions that allow for buoyant CO_2 to leak (Chiquet et al., 2007a; Chalbaud et al., 2009). Besides, WA can affect residual saturation and subsequently impact the trapping efficiency of injected CO_2 (Iglauer et al., 2014). Therefore, reliable quantification of wettability is needed for safe and effective CO_2 storage.

Despite the fact that WA is known to impact core-scale capillarity and relative permeability behavior, few detailed measurements are available to characterize the alteration of the constitutive function themselves. Plug and Bruining (2007) have reported brine-CO_2 (gas, liquid) drainage-imbibition experiment and showed capillary instability for a

* Corresponding author at: NORCE Norwegian Research Center, Bergen, Norway.
E-mail address: abka@norceresearch.no (A.M. Kassa).

https://doi.org/10.1016/j.advwatres.2020.103631
Received 10 July 2019; Received in revised form 6 May 2020; Accepted 15 May 2020
Available online 20 May 2020

supercritical CO_2-brine system, meaning that the capillary pressure measurements change steadily over time. The imbibition curve also exhibited a significant deviation from the expected curve that was not explained by classical scaling arguments. The authors proposed WA as an explanation but did not explicitly measure any changes in CA. Additionally, recent experiments measured capillary pressure curves for a silicate sample using a fluid pairing of supercritical CO_2 and brine (Wang and Tokunaga, 2015). Repeated drainage-imbibition cycles were performed for 6 months, and a clear reduction in capillary pressure was recorded for each subsequent drainage cycle. The authors also attributed these deviations from the expected capillary curve to a change in wettability of the rock sample over time due to CO_2 exposure, similar to aging. This hypothesis was confirmed through observations of a wetting angle increase from 0° to 75° after 6-months of exposure. It is also reported similar $P_c - S$ instability and deviation in dolomite/carbonate (Wang et al., 2016), and quartz (Tokunaga et al., 2013; Wang et al., 2016) sands for $scCO_2$ -brine system. More literature on WA and $P_c - S$ measurements can be found in (Tokunaga and Wan, 2013).

The above experiments reveal that capillary pressure curves are not static for rocks that undergo WA, despite the fact they were performed following the standard multi-step procedure, i.e. where "equilibrium" is obtained after each incremental step in pressure. Therefore, the standard capillary pressure models cannot be readily applied without additional dynamics to capture the long-term impact of WA. Capillary pressure dynamics due to WA are distinct from non-equilibrium flow dynamics (e.g. Hassanizadeh et al., 2002; Dahle et al., 2005; Barenblatt et al., 2003) or from CA hysteresis generated by receding and advancing angles (e.g. Krumpfer and McCarthy, 2010; Eral et al., 2013). WA alteration is a chemistry-induced pore-scale phenomenon that alters the capillary pressure function separately from the flow conditions or other instabilities. That is, contact angle has the potential to change even when the system is at rest. On the other hand, NE models are formulated to address dynamics in only for systems that are flowing, and therefore a new approach is needed to account for permanent and continual alteration of capillary pressure functions for both flowing and non-flowing systems. We note that capillary driven flow may initiate if the CA change is large.

The standard approach to WA is to assume a change in surface chemistry that occurs instantaneously, which results in an immediate shift in saturation functions (Delshad et al., 2009; Lashgari et al., 2016; Yu et al., 2008; Andersen et al., 2015; Adibhatia et al., 2005). This implementation entails a heuristic approach that interpolates between the two end wetting states as a linear function of chemical agent concentration. Lashgari et al. (2016) have derived an instantaneous WA model from Gibbs energy and adsorption isotherms. The proposed WA model is coupled with $P_c - S$ relation through residual saturation. These models neglect the impact of WA over longer timescales (months to years). They also do not capture pore-scale heterogeneity in wetting properties. In the available literature, only one study (Al-Mutairi et al., 2012) has included the effect of exposure time on WA and constitutive relations for core scale simulation. But this numerical study does not sufficiently incorporate or upscale pore-scale processes to core-scale constitutive laws.

To our knowledge, a rigorous mathematical upscaling of long-term dynamics in $P_c - S$ functions introduced by exposure to a WA agent has not been previously performed. The focus of this paper is to propose a new dynamic capillary pressure model by upscaling the WA dynamics from the pore- to the core-scale. Section 2 describes our approach. We start with direct simulations of $P_c - S$ curves from a pore-scale model represented by a cylindrical bundle-of-tubes. WA is introduced at the pore scale using a mechanistic model for CA change as a function of exposure time to a reactive agent. This model is developed based on the insights from laboratory experiments, giving the flexibility to incorporate other data as appropriate. We emphasize the CA model is only meant as a basis on which to demonstrate the upscaling approach. In Section 3, we present the resulting curves generated by the pore-scale model using two different pore-scale models for CA change. These curves are then used to correlate the dynamic term in the upscaled $P_c - S$ function. Finally, we analyze the link between pore-scale parameters and upscaled correlations.

2. Approach

The extended $P_c - S$ relationship introduces a dynamic component that captures the changing wettability as measured by the deviation of the dynamic capillary pressure from the equilibrium (static) capillary pressure. This relationship can be described as follows:

$$P_c(\cdot) - P_c^{\mathrm{st,in}} := f^{\mathrm{dyn}}(\cdot), \tag{1}$$

where $P_c^{\mathrm{st,in}}$ represents the capillary pressure for the system given a static initial wetting state, and f^{dyn} represents the deviation from the static state. The initial static curve can be described by the Brooks-Corey model,

$$P_c^{\mathrm{st,in}} = c_w \left(\frac{S_w - S_{wc}}{1 - S_{wc}} \right)^{-a_w}, \tag{2}$$

where c_w is the entry pressure, $1/a_w$ is the pore-size distribution index, whereas S_{wc} is the residual water saturation.

The objective of this study is to characterize and quantify the dynamic term f^{dyn}, the key term of interest in the $P_c - S$ model, for a system that undergoes WA. We propose an interpolation model to handle the WA dynamics in $P_c - S$ relation. To obtain an interpolation model, the dynamic component in Eq. (1) can be scaled by the difference between two static curves, each representing the initial and final wetting-state capillary pressure curves, to give a non-dimensional quantity ω we call the *dynamic coefficient*, which is defined as follows

$$\omega\left(P_c^{\mathrm{st,f}} - P_c^{\mathrm{st,in}}\right) = f^{\mathrm{dyn}}, \tag{3}$$

where $P_c^{\mathrm{st,f}}$ is the final wetting state capillary pressure. In the previous studies (e.g. see Delshad et al., 2009; Lashgari et al., 2016; Yu et al., 2008; Andersen et al., 2015; Adibhatia et al., 2005), the coefficient ω is assumed only chemistry dependent. Here, ω in Eq. (3) is assumed to be a function of not only the chemistry but also the exposure time to the WA agent.

The expression in Eq. (3) can be substituted into Eq. (1) to obtain a dynamic interpolation model

$$P_c = (1 - \omega) P_c^{\mathrm{st,in}} + \omega P_c^{\mathrm{st,f}}. \tag{4}$$

We note that in the model presented above, we have defined the "total" capillary pressure P_c as simply the measured difference in phase pressures at any point in time. In a reservoir simulation, this would be capillary pressure in a given grid cell, whereas in a laboratory experiment designed to measure $P_c - S$ data, it corresponds to the pressure drop across the sample at equilibrium. For quasi-static displacement in a bundle of capillary tubes, P_c is the difference between boundary condition pressures, i.e., $P_c = P_l^{res} - P_r^{res}$, (see Fig. 1).

The exact nature of ω and its functional dependencies can only be determined from a full characterization of $P_c - S$ curves under different conditions. These curves can be derived from laboratory experiments, but this approach is costly and time-consuming. Alternatively, one may take a more theoretical approach by simulating $P_c - S$ curves using a pore-scale model that includes the impact of WA.

For a system that undergoes WA, a significant change in CA could lead to the wetting phase becoming non-wetting and vice versa. For clarity, we will continue to use *w* subscript for the phase that was originally wetting and *nw* for the phase that is originally non-wetting regardless of the actual state of wettability in the system.

2.1. Pore-scale model

There are various choices of pore-scale models available. The easiest to implement and analyze is the bundle-of-tubes (BoT) model which is a collection of capillary tubes with a distribution of radii. Herein, we

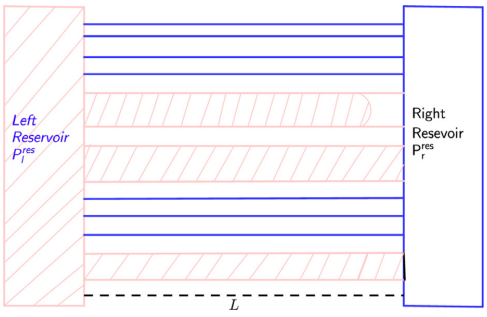

Fig. 1. Fluid displacement in a non-interactive bundle-of-tubes (BoT). Here, the left reservoir contains non-wetting fluid that displaces the wetting fluid to the right and vice versa.

describe the model and the approach for the implementation of time-dependent WA.

The BoT model is a popular approach due to the simplicity of implementation and the ability to study the balance of energy and forces directly at the scale of interfaces (Bartley and Ruth, 1999; Dahle et al., 2005; Helland and Skjæveland, 2006). The average behavior of a BoT model can then be used to construct better constitutive functions at the macroscale (Dahle et al., 2005; Helland and Skjæveland, 2006; 2007). There are known limitations to this pore-scale approach, i.e. lack of residual saturation and tortuosity. We emphasize that this study is a first step at studying the impact of long-term WA from pore- to core-scale, and as such these secondary aspects are beyond the scope of this work.

In this paper, we consider cylindrical BoT having length, L, and is shown in Fig. 1. These tubes are designed to connect wetting (right) and non-wetting (left) reservoirs with pressures labeled as $P_r^{\text{res.}}$ and $P_l^{\text{res.}}$ respectively. Let the reservoir pressures difference be defined as

$$\Delta P = P_l^{res} - P_r^{res}. \tag{5}$$

Initially, the tubes in the bundle are filled with a wetting phase. To displace the wetting phase fluid in the m^{th} tube, the pressure drop has to exceed the local entry pressure, $P_{c,m}$, defined as (Dahle et al., 2005)

$$\Delta P > P_{c,m}(R_m, \theta_m), \tag{6}$$

where $P_{c,m}(R_m, \theta_m)$ is given by the Young's equation

$$P_{c,m}(R_m, \theta_m) = \frac{2\sigma\cos(\theta_m)}{R_m}, \ m = 1, 2, \cdots, N, \tag{7}$$

where R_m and θ_m are the tube radius and CA, respectively, for the m^{th} tube, N stands for number of tubes, σ is fluid-fluid interfacial tension.

As long as condition (6) is satisfied, the fluid movement across the length of tube m can be approximated by the Lucas-Washburn flow model (Washburn, 1921),

$$q_m = \frac{R_m^2(\Delta P - P_{c,m}(R_m, \theta_m))}{8(\mu_{\text{nw}} x_m^{int} + \mu_{\text{w}}(L - x_m^{int}))}, \tag{8}$$

where, μ_{nw} and μ_{w} are non-wetting and wetting fluid viscosities, respectively, the superscript *int* stands for fluid-fluid interface, and $q_m = dx_m^{int}/dt$ is the interface velocity. The interface is assumed to be trapped when it reached at the outlet of the tube, thus $q_m = 0$. A positive rate of change in x_m^{int} is associated with an increase in non-wetting saturation for tube m. From Eq. (8), one can then determine the required time to reach a specified interface position.

2.2. Pore-scale time-dependent WA model

In this paper, we consider a WA mechanism at the pore-scale that evolves smoothly from an initial to final wetting state through exposure time. The initial and final wetting states can be arbitrarily chosen, i.e. from wetting to non-wetting or vice versa.

The WA agent is defined as either the non-wetting fluid itself or some reactive component therein. We consider an alteration process within any given pore, or tube, that continues until the ultimate wetting state is reached locally in the pore. The alteration is permanent, but can also be halted at some intermediate wettability state if the WA agent is displaced from the pore. If the agent is reintroduced to the pore at some later point, alteration continues until the final state is reached.

To this end, we introduce a general functional form of pore-scale WA mechanism by CA change,

$$\theta_m(\cdot) := \theta_{m,\text{in}} + \varphi(\cdot)\Delta\Theta, \tag{9}$$

where $\Delta\Theta = \theta_{m,\text{f}} - \theta_{m,\text{in}}$, $\theta_{m,\text{f}}$ and $\theta_{m,\text{in}}$ are the ultimate and initial contact angles respectively. In Eq. (9), θ_m decreases and increases based on the choice of the initial and final wetting conditions. The term $\varphi(\cdot) \in [0, 1]$ (when $\varphi(\cdot) = 1$ the CA attains its ultimate value and CA is fixed at the initial state when $\varphi(\cdot) = 0$) in Eq. (9) is responsible for governing the WA dynamics.

WA involves complex physical and chemical processes whose description is beyond the scope of this work. However, we provide a brief summary of the role of adsorption/desorption processes in CA change (Blut, 2017; Du et al., 2019). Such a hypothesis has been supported by experiment measurements. For instance, CO_2-water core-flooding experiments show adsorption-type relations between CA and pressure (Dickson et al., 2006; Jung and Wan, 2012; Iglauer et al., 2012), and also with exposure time (Jafari and Jung, 2016; Saraji et al., 2013). Similar CA evolutions as a function of surfactant concentration and exposure time are reported in Davis et al. (2003) and (Morton et al., 2005) for an oil droplet on a metal surface immersed in ionic surfactant solutions. In Morton et al. (2004), a Langmuir adsorption model is proposed to predict the experiment observations in (Davis et al., 2003). Given the insights above, we consider a CA model that evolves according to the rate of adsorption of the WA agent on the surface of the pores. Following McKee (1991), van Erp et al. (2014), the dynamic parameter φ in Eq. (9) can be stated as,

$$\frac{d\varphi}{dt} = J^+ - J^-, \tag{10}$$

where J^+ and J^- represent rates of adsorption and desorption of a WA agent respectively at the solid surface. In McKee (1991), J^+ is taken to be proportional to the WA agent and the surface unoccupied by the adsorbed WA agent, i.e.,

$$J^+ = k_1\chi_m\left(1 - \varphi/\overline{\varphi}\right), \tag{11}$$

where k_1 is a rate constant, $\overline{\varphi}$ represents the maximum surface saturated concentration, and χ_m is a measure of the local exposure time of tube m. The desorption rate can be related with the current surface concentration and is defined as,

$$J^- = k_2\varphi \tag{12}$$

where k_2 is a rate constant for desorption rate. Combining Eqs. (10)–(12) would give us,

$$\frac{d\varphi}{dt} = k_1\chi_m\left(1 - \varphi/\overline{\varphi}\right) - k_2\varphi. \tag{13}$$

Assuming $\overline{\varphi} = 1$ and following McKee (1991), one can apply a perturbation analysis to Eq. (13) to obtain a first-order approximation for φ in terms of χ_m,

$$\varphi \approx \frac{\chi_m}{C + \chi_m}, \tag{14}$$

where $C = \frac{k_2}{k_1}$ is a parameter that controls the speed and extent of alteration. χ_m is defined as the time-integration of exposure to a WA agent, here taken to be the local non-wetting saturation of tube m,

$$\chi_m := \frac{1}{T}\int_0^t \frac{x_m^{int}}{L} d\tau, \tag{15}$$

where T is a pre-specified characteristic time. In this paper, the characteristic time is set as the time for one complete drainage displacement under static initial wetting conditions, which can be pre-computed according to Eq. (8).

As an aside, detailed laboratory work would be needed to further enrich the pore-scale CA model by fitting C to experimental data. This exercise is beyond the scope of this paper, and we consider the underlying CA change in Eq. (14) a reasonable basis for which to perform the upscaling aspect of our study.

Herein, we consider two models for exposure time at the local scale. For first we take the case where CA modification based on Eq. (14) is strictly dependent on local exposure time χ_m and leads to CA variation from tube to tube, hereafter referred to as the *non-uniform WA* mechanism. We note that wettability gradients within individual tubes are not considered in this model, and thus there is no variation in CA along the tube. This is due to the flow model in Eq. (8), where the CA only affects the entry pressure of the tube.

The second is referred to as *uniform WA*, which is based on the assumption that the WA agent dissolves into the wetting phase from the non-wetting fluid and affects all tubes simultaneously. In this case, all tubes have the same properties that are governed by the bulk exposure time across the entire bundle (i.e. REV). We can define $\overline{\chi}$

$$\overline{\chi} := \frac{1}{T}\int_0^t S_{nw} d\tau. \tag{16}$$

as the bulk or average, exposure time as a function of average saturation. The uniform model is implemented into Eq. (14) by taking $\chi_m = \overline{\chi}$.

In summary, we introduce two types of WA mechanisms, uniform and non-uniform, that serve as end members of possible WA mechanisms at the pore-scale. On the one end, non-uniform WA restricts alteration to only drained pores and excludes any interaction of the WA agent between pores. This leads to significant heterogeneity in CA from one pore to another. At the other end, the uniform case assumes the WA agent can alter all pores simultaneously. In reality, WA will lie somewhere in between, but we have chosen simpler end members to aid in further analysis of simulated data in the next section.

2.3. Simulation approach

The uniform and non-uniform approaches are coupled into the BoT model following Algorithm 1 for a single drainage-imbibition cycle. The objective is to perform simulated experiments that mimic laboratory-derived capillary pressure curves, i.e. the pressure is adjusted incrementally up or down after each step depending on if the bundle is under drainage or imbibition, respectively. Contact angles are updated continuously throughout the flow processes in a step-wise manner once the displacement is completed for each pressure increment. That is, contact angles that have been altered according to the uniform or non-uniform mechanism, are updated before the next pressure increment. This is a reasonable approximation given that it is only entry pressures in individual tubes that are affected by CA change.

We control the pressure drop ΔP in the way that the WA process is completed within a few numbers of drainage-imbibition cycles. In the first drainage-imbibition cycles, the ΔP increment is such that tubes drain/imbibe one at a time with a pressure drop close to the next tube entry pressure. In the last drainage-imbibition cycle, every ΔP increment is reduced by two and three orders of magnitude for the non-uniform and uniform case, respectively. Consequently, the flow slows down by the same magnitude irrespective of whether the tube drains or imbibes. At the completion of the numerical experiment, we obtain a set of $P_c - S$ "data points" that can be plotted in the usual way.

Once the capillary pressure curves are generated for both the uniform and non-uniform approaches, the resulting curves are used to quantify the dynamic coefficient in the interpolation function in Eq. (4). The goal is to develop a correlation model that involves only a single parameter, and this parameter should have a clear relation with changes in the pore-scale WA model parameter C.

Algorithm 1 A single drainage-imbibition cycle. Fluid and rock properties are given according to Table 2

```
Drainage displacement
set the maximum capillary pressure P_c^max
while ΔP < P_c^max do
    increase the non-wetting pressure, P_l^res
    calculate the pressure drop ΔP = P_l^res − P_r^res
    if ΔP > 2σ cos(θ_m)/R_m then
        drain the respective tubes
        calculate the elapse of time to drain tubes from Equation (8)
        calculate and store averaged quantities S_nw and χ̄
        if non-uniform WA then
            calculate χ_m for invaded pores from Equation (15)
            calculate θ_m from Equation (9) and (15)
        else if uniform WA then
            update each θ_m in bundle identically from Equation (9)
            and (16)
        end if
    end if
end while
Imbibition displacement
define the minimum entry pressure P_c^min
while ΔP > P_c^min do
    decrease the non-wetting pressure, P_l^res
    calculate the pressure drop ΔP = P_l^res − P_r^res
    if ΔP > σ cos(θ_m)/R_m then
        imbibe the respective tubes
        calculate the elapsed of time to imbibe tubes from
        Equation (8)
        calculate and store averaged quantities S_nw and χ̄
        if non-uniform WA then
            calculate χ_m from Equation (15)
            update θ_m from Equation (9) and (15)
        else if uniform WA then
            update each θ_m identically from Equation (9) and (16)
        end if
    end if
end while
```

3. Results

In this section, we present the simulated capillary pressure and associated results for each WA case. We formulate a correlation model, which is then fit to the simulated data. Finally, we investigate the sensitivity of the correlated model to the pore-scale WA parameter.

3.1. Bundle of tubes model set-up

The pore scale is described by a BoT model (see Section 2.1). Each tube in the BoT is assigned a different radius R, with the radii drawn from a truncated two-parameter Weibull distribution (Helland and Skjæveland, 2006)

$$f(R) = \frac{\left[\frac{R-R_{\min}}{R_{\text{av}}}\right]^{\eta-1}\frac{\eta}{R_{\text{av}}}\exp\left(-\left[\frac{R-R_{\min}}{R_{\text{av}}}\right]^{\eta}\right)}{1-\exp\left(-\left[\frac{R_{\max}-R_{\min}}{R_{\text{av}}}\right]^{\eta}\right)} \tag{17}$$

where $R_{\max}$, $R_{\min}$, and R_{av} are the pore radii of the largest, smallest, and average pore sizes, respectively, and η is a dimensionless parameter. The average is obtained by the mean of $R_{\max}$ and $R_{\min}$. The rock parameters and fluid properties are listed in Table 1.

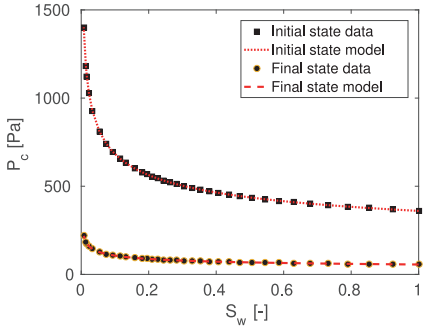

Fig. 2. Simulated $P_c - S$ data for the initial and final wetting states compared to a Brooks-Corey model with calibrated parameters given in Table 2.

3.2. Static capillary pressure for end wetting states

A starting point for the dynamic capillary-pressure models presented in Section 2 (Eqs. (1) and (4)) is characterizing the capillary pressure curves for the end wetting states. Given the same tube geometry and fluid pairing described above, the capillary pressure–saturation data are simulated under static conditions for both the initial and final wetting states.

Only a single drainage experiment is needed in the static case to fully characterize the capillary pressure curve. This is due to the lack of residual trapping in a BoT model. We emphasize that hysteresis is not possible for a BoT if the contact angles in the tubes (and other parameters) are held constant.

The simulated static curves are then correlated with the Brooks-Corey model (2). The resulting correlations can be found in Fig. 2, while fitted parameters for the Brooks-Corey model can be found in Table 2. Note that the Brooks-Corey model is undefined at zero irreducible wetting phase saturation. Thus, we left a few pores undrained to allow for comparison between the Brooks-Corey model and the simulated $P_c - S$ data.

Fig. 2 compares the Brooks-Corey formula (2) and the capillary pressure curves associated with static contact angles (initial and final wetting states).

The Brooks-Corey correlation gives an excellent match to the simulated $P_c - S$ data under static conditions. We observe that the pore-size distribution index a_w for the initial and final wetting states are the same, which is expected since the same distribution of tube radii is used in both cases. On the other hand, the coefficient c_w decreases by a factor of 0.85 from the initial to the final wetting state corresponding to a decrease in a core-scale capillary entry pressure. The Leverett-J scaling theory (Xu et al., 2016) predicts that entry pressure scales by $\cos\theta$, which agrees nicely with the reduction in $\cos\theta$ by a factor of 0.83 for a CA change from 0 to 80 degrees.

We reiterate that for the static case where no WA occurs, the Brooks-Corey model describes *both* drainage and imbibition for the BoT.

Table 1
Parameters used to simulate quasi-static fluid displacement in BoT.

parameters	values	unit	parameters	values	unit
σ_{ow}	0.0072	N/m	no. radii	500	[-]
$R_{\min}$	6	μm	$R_{\max}$	40	μm
θ_f	80	degree	θ_{in}	0.0	degree
μ_{w}	0.0015	Pa.s	μ_{nw}	0.0015	Pa.s
R_{av}	23	μm	L	0.001	m
η	1.5	[-]			

Table 2
Estimated correlation parameter values for initial and final wetting state capillary pressure curves.

Initial wetting state			Final wetting state		
param.	value	unit	param.	value	unit
c_w	360	[Pa]	c_w	56	[Pa]
a_w	0.2778	[-]	a_w	0.2778	[-]
R^2	1	-	R^2	1	-

3.3. Simulated capillary pressure data

We present the simulated capillary pressure data (see Fig. 3), comparing the results of the uniform and non-uniform approaches described previously. The uniform data are generated with the pore-scale WA parameter $C = 0.005$, while for the non-uniform data $C = 5 \times 10^{-4}$. A total of two and four drainage-imbibition cycles carried out for the uniform and non-uniform cases, respectively.

For both cases, we observe a steady decrease in capillary pressure over time. In the end, a complete wettability change has evolved from the initial to final prescribed states, whose static curves are plotted in Fig. 3 for reference. Having reached the final wetting state, any additional drainage-imbibition cycle would follow along the static curve for the final wetting state. We remark that wettability-induced dynamics also introduces an apparent hysteresis in the $P_c - S$ data. This effect is unique to the cylindrical BoT model, which we recall cannot exhibit hysteresis under static wettability conditions. However, a real porous medium may exhibit capillary pressure hysteresis with static wettability.

There are notable differences between the two sets of curves. For the uniform case (Fig. 3a), there are distinct curves for each drainage and imbibition displacement. The capillary pressure begins to decrease immediately and in a continuous manner over time. This is because the CA (Fig. 4a) is changing for all tubes simultaneously based on the average exposure time over the entire bundle. The uniformity results in the CA in smaller tubes being altered significantly at an early time (at the same rate as the larger tubes), and thus the capillary pressure is decreased even at low average wetting saturation in the first drainage curve. The fast dynamics in CA change lead to a non-monotone capillary curve at an early time.

In comparison, the non-uniform case (Fig. 3b) has a delay in exhibiting the effects of WA. The initial drainage curve is identical to the initial wetting static curve and all subsequent drainage curves follow along the previous imbibition curve. This is a result of the restriction on CA change to only tubes that are drained. In other words, at the tube-level, there is no change in entry pressure from the initial state (or the state after a single drainage-imbibition cycle) until that tube is drained. In contrast to the uniform case, the capillary pressure at low S_w is drawn towards the initial state. This can be described by examining the CA per tube radius in time, shown in Fig. 4b. Larger tubes that drain first and imbibe last, resulting in longer local exposure time, and thus more extensive CA change, compared to the smaller tubes that drain last and imbibe first. Therefore, the initial wetting state persists in the smaller tubes.

We recall that both the uniform and non-uniform cases are selected as end members of possible WA mechanisms in real porous media. In real systems, WA in different sized pores may occur in a more complex manner.

We have observed above that capillary pressure curves in Fig. 3a and b are not a unique function of saturation, that is, they exhibit hysteresis for this simple BoT geometry. We note that the $P_c - S$ data points are color-coded according to time evolved at each data point. This motivates a transformation of the data into the time domain by plotting against $\overline{\chi}$, as shown in Fig. 5 for both cases. In doing so, we obtain a unique function with respect to exposure time for both the uniform and non-uniform cases. We note that the curves in Fig. 5 show that the capillary

pressure increases and decreases with each drainage-imbibition cycle. In addition, the transformation reveals the separate drainage curves for the non-uniform case that were hidden in Fig. 3b.

3.4. Dynamic capillary pressure model development

Following the approach discussed in Section 2, we applied Eq. (3) to calculate the dynamic coefficient ω for both the uniform and non-uniform cases. The resulting coefficient is plotted in Fig. 6 as a function of both S_w (top panels) and $\overline{\chi}$ (bottom panels) for both WA cases. We recall that ω is a coefficient that interpolates between the capillary pressure at the initial and final wetting states at any given saturation, where $\omega = 0$ gives the initial capillary pressure and $\omega = 1$ gives the final $P_c - S$ curve.

For the uniform case, ω is a non-unique function of wetting-phase saturation, see Fig. 6a, but with values that are continuously increasing as the dynamic capillary pressure moves towards the final wetting state. For the non-uniform case, the dynamic coefficient in Fig. 6b also exhibits non-uniqueness with respect to saturation. Reflecting the $P_c - S$ data, the capillary pressure persists at the initial state at low saturation. This means that the value of ω decreases with decreasing S_w along the drainage path and increases only along imbibition paths. The complex relation of ω in saturation space makes it challenging to propose a functional form for $\omega - S_w$ relation in both cases.

Figs. 6c and 6d show that ω exhibits different behavior as a function of average exposure time. For the uniform case, Fig. 6c, ω is smoothly increasing and uniquely related to $\overline{\chi}$, mimicking the functional form of the pore-scale model in Eq. (9). On the other hand, the coefficient ω in the non-uniform case, Fig. 6d, is not monotonically increasing in $\overline{\chi}$ but continues to rise and fall with time despite the transformation to the temporal domain.

The curves in Fig. 6 give us important insight into the form of ω best suited to each WA case. We take each case in turn:

3.4.1. Uniform case

The smoothly varying functionality of ω and $\overline{\chi}$ in Fig. 6c motivates an adsorption-type model:

$$\omega = \frac{\overline{\chi}}{\beta_1 + \overline{\chi}}, \tag{18}$$

where β_1 is a fitting parameter obtained from the best fit to the simulated data in Fig. 6c. For this particular case, the calibrated parameter is estimated to be $\beta_1 = 0.01$.

The form of the dynamic $P_c - S$ model for the uniform case is obtained by substituting Eq. (18) into Eq. (4) to give:

$$P_c = \frac{\overline{\chi}}{\beta_1 + \overline{\chi}}\left(P_c^{\mathrm{st,f}} - P_c^{\mathrm{st,in}}\right) + P_c^{\mathrm{st,in}}. \tag{19}$$

3.4.2. Non-uniform case

The non-trivial behavior of ω in Fig. 6d makes it challenging to propose a functional relation between the dynamic coefficient ω and $\overline{\chi}$ directly as we did for the uniform WA case. Instead, we observe that ω in Fig. 6b has a well-behaved curvature for each drainage-imbibition cycle along the saturation history. Further, the curvature of each cycle is increasing with increasing exposure time. Given these insights, we proposed a model for the dynamic coefficient that has the following form,

$$\omega(S_w, \overline{\chi}) = \frac{S_w}{\alpha(\overline{\chi}) + S_w}, \tag{20}$$

where α controls the curvature of the $\omega - S_w$ curve for each drainage-imbibition cycle. Since ω is increasing function of exposure time, α should decrease along the averaged variable $\overline{\chi}$.

The function form of ω in Eq. (20) is then matched with the $\omega - S_w$ data to analyze the dynamics of α along $\overline{\chi}$. The obtained $\alpha - \overline{\chi}$ relation is decreasing as hypothesized and in particular has the follwing form,

$$\alpha(\overline{\chi}) = \beta_2/\overline{\chi}, \tag{21}$$

where β_2 is non-dimensional fitting parameter. For this particular simulation the parameter β_2 is estimated to be 0.004 for the four of drainage-imbibition cycles.

The form of the dynamic $P_c - S$ model for the non-uniform case is then obtained by substituting Eqs. (20) and (21) into Eq. (4):

$$P_c = \frac{\overline{\chi} S_w}{\beta_2 + \overline{\chi} S_w}\left(P_c^{\mathrm{st,f}} - P_c^{\mathrm{st,in}}\right) + P_c^{\mathrm{st,in}}. \tag{22}$$

The calibrated dynamic capillary pressure models in Eqs. (19) and (22) are compared with the simulated capillary pressure data in Fig. 3, with the results presented in Fig. 7 for each WA case. We observe that the proposed dynamic models agree well with simulated dynamic capillary pressure curves. The correlation coefficient for this comparison is $R^2 = 0.9921$ and $R^2 = 0.98$, for the uniform and non-uniform case, respectively. Thus, we have obtained a single-parameter model in both the uniform and non-uniform WA cases that describe the evolution of dynamic capillarity over multiple drainage-imbibition cycles rather than using a model consisting of multiple parameters that change with each cycle (or hysteresis models).

3.5. Model sensitivity to pore-scale model parameter

We hypothesize that parameters β_1 in Eq. (19) and β_2 in Eq. (22) are dependent on the parameter C in Eq. (9) that controls the dynamics of wettability alteration at the pore-scale. We investigate this sensitivity by repeating the capillary pressure simulations for different values of the pore-scale parameter C and determine the correlated value of β_1 and β_2 in each case.

For the uniform WA case, Fig. 8a shows that the interpolation model parameter is linearly proportional to the pore-scale model parameter, with a proportionality constant of 2. Thus, the relationship $\beta_1 = 2C$ can be used to predict the upscaled parameter directly from knowledge of the pore-scale process. In contrast, the non-uniform case in Fig. 8b shows a power law model, where $\beta_2 = b_1 C^{b_2}$ is correlated with estimated parameters of $b_1 = 3.3 \times 10^6$ and $b_2 = 1.8$.

The general form of dynamic capillary pressure model can now be obtained for the uniform WA by incorporating the relationship for β_1 in Eq. (19) :

$$P_c = \frac{\overline{\chi}}{2C + \overline{\chi}}\left(P_c^{\mathrm{st,f}} - P_c^{\mathrm{st,in}}\right) + P_c^{\mathrm{st,in}}. \tag{23}$$

Similarly, we obtain a general non-uniform model by substituting β_2 in Eq. (22)

$$P_c = \frac{\overline{\chi} S_w}{b_1 C^{b_2} + \overline{\chi} S_w}\left(P_c^{\mathrm{st,f}} - P_c^{\mathrm{st,in}}\right) + P_c^{\mathrm{st,in}}. \tag{24}$$

In their final form, the dynamic capillary pressure models in Eqs. (23) and (23) are dependent on two variables, saturation and time, and a single wettability parameter, C. The latter must be determined by fitting Eq. (9) with parameter C to laboratory experiments for a given sample exposed to a WA agent.

3.6. Applicability to arbitrary saturation history

We note that the saturation history used to generate the $P_c - S$ curves for the two WA cases in Figs. 3a and 3c can be thought of in each case as a single arbitrary path within an infinite number of possible paths. If a different path had been chosen, such as a flow reversal at intermediate saturation or a prolonged exposure time at a given saturation, it would result in entirely different capillary pressure dynamics.

In order to test the dynamic models developed in Eqs. (19) and (22) for any arbitrary saturation history, we generate many different $P_c - S$ curves by taking numerous different paths in the saturation-time domain. The resulting simulated data forms a surface with respect to saturation and exposure time as shown in Fig. 9a and b

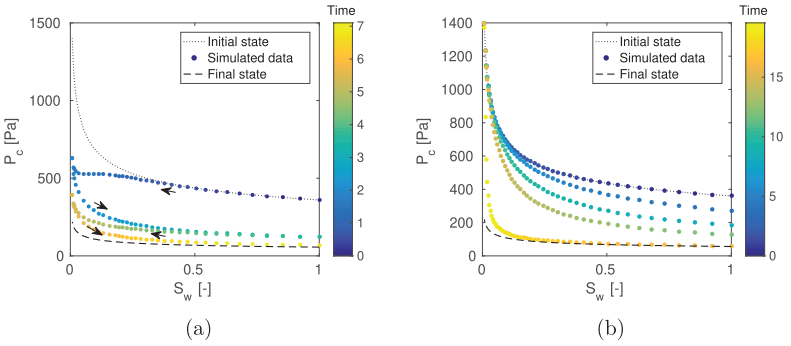

Fig. 3. Simulation results for WA-induced dynamics of capillary pressure as a function of wetting saturation given uniform (a) and non-uniform (b) WA at the pore-scale. The color of each data point indicates the time elapsed in months, with elapsed time equal to 7 months for the uniform case and 20 months for the non-uniform case. The data points are obtained following Algorithm 1. The static $P_c - S$ curves for the end wetting states, θ_{in} and θ_f, are plotted as a reference with dotted and dashed line, respectively.

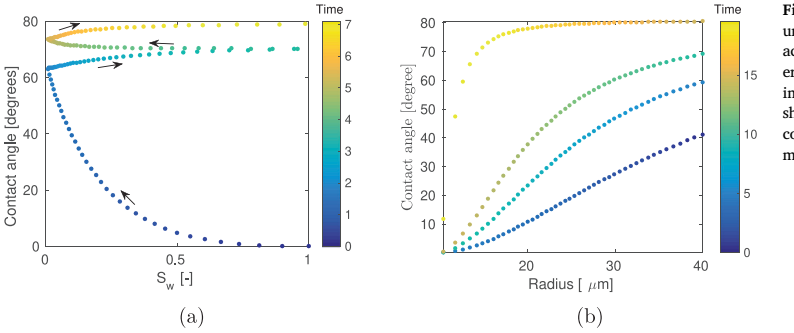

Fig. 4. CA, θ, for the uniform case (a) and non-uniform case (b). Uniform CA, which is identical across the bundle, is shown as a function of average saturation. The CA data show the drainage-imbibition fluid history paths. Non-uniform CA is shown as a function of tube radius and time. The color scale in both figures indicates time elapsed in months.

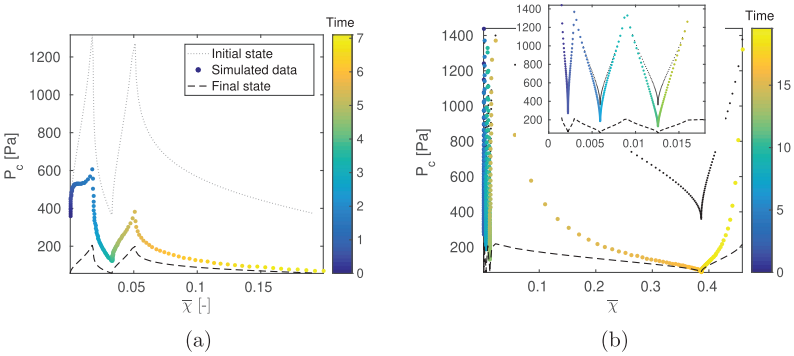

Fig. 5. Capillary pressure data plotted as a function of $\overline{\chi}$ for the uniform (a) and non-uniform (b) WA case. The color of each data point indicates the time elapsed in months. The inset plot in (b) is the resolution of the capillary pressure for the first three cycles.

We then apply the calibrated dynamic models to the same saturation-time paths used to generate the $P_c - S - \overline{\chi}$ surface. The difference between the calibrated model and the simulated data is shown in Fig. 9c and d for the uniform and non-uniform cases, respectively. A good comparison of the dynamic models to simulated data demonstrates that model calibration to a single saturation-time path is robust enough to be applied to any possible path.

3.7. Discussion

We investigated the potential of the interpolation-based model to predict the WA induced dynamics in capillary pressure–saturation relations. In the interest of completeness, we also explored other types of models to capture capillary pressure dynamics, including the mixed-wet model of Skjæveland et al. (2000). For brevity, we do not report the results of that separate study herein. We found that although other models could be calibrated with reasonable accuracy, they all involved more than one calibration parameter (up to four) that need to be adjusted in each drainage-imbibition cycle. Therefore, the single-parameter single-valued interpolation model presented in this study is the preferred model due to its reliability for replicating the simulated BoT data.

The proposed interpolation model is an upscaled model that allows for a change in capillary pressure as a function of upscaled variables, saturation, and exposure time, to a WA agent. We recall that exposure time is simply the integration of saturation history over time. The model consists of three main components – two capillary pressure functions at the initial and final wetting state and a dynamic interpolation coefficient that moves from one state to the other. The initial and final capillary

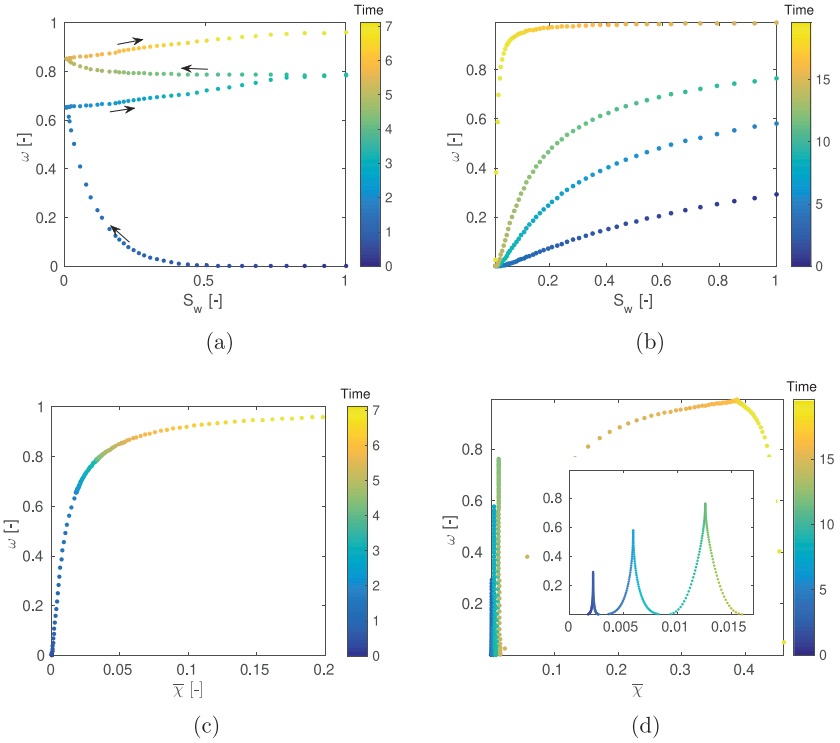

Fig. 6. Plot of the dynamic coefficient ω against wetting phase saturation (top) and $\overline{\chi}$ (bottom) for the uniform WA case (left panels) and non-uniform WA case (right panels). The data points are color-coded with exposure time in months. The inset plot in (d) is the resolution of the dynamic coefficient for the first three cycles.

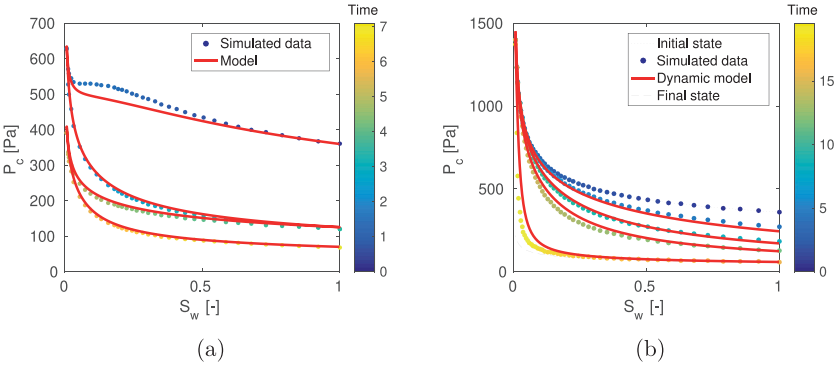

Fig. 7. Comparison of the dynamic models in Eqs. (19) and (22) with the simulated $P_c - S$ data in Fig. 3 for uniform (a) and non-uniform (b) WA cases. The data points are color-coded with exposure time in months.

pressure functions can be determined *a priori* from static experiments using inert fluids. In this study, the initial and final states are represented by classical Brooks-Corey functions. The dynamic coefficient is thus the only variable correlated to dynamic capillary pressure simulations. In this study, we have shown that the coefficient can be easily correlated to saturation and exposure time via a single parameter.

We have observed that the form of the dynamic term is dependent on the underlying mechanisms for WA. We employed two models, uniform and non-uniform, that represent two end members of real systems. One end member is identical CA throughout the REV, while the other results in severely heterogeneous CA from small to large pores. The differences in the two WA mechanisms changes the complexity of the resulting capillary dynamics. In the uniform case, the dynamic coefficient can be correlated to exposure time through a sorption-type model, which seems to be a natural result given the CA change at the pore scale is also based on a sorption model. This is an interesting observation that requires more analysis in future work. In the non-uniform case, the dynamic coefficient has no similar sorption form with increased exposure time, but

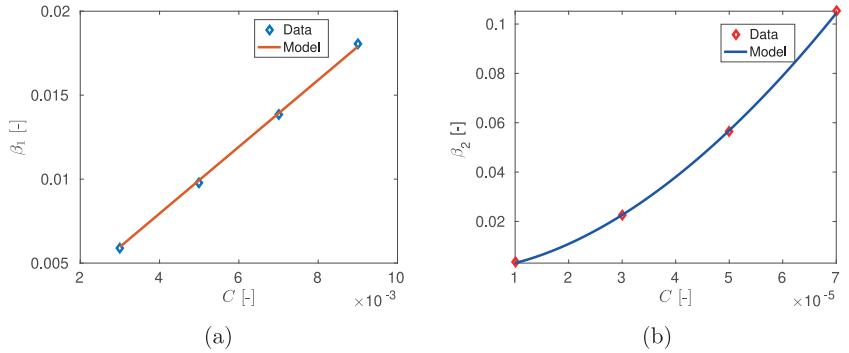

Fig. 8. The relation between pore-scale wettability parameter C and the correlation parameters β_1 and β_2 in Eqs. (19) and (22) for the uniform (a) and non-uniform (b) WA cases, respectively.

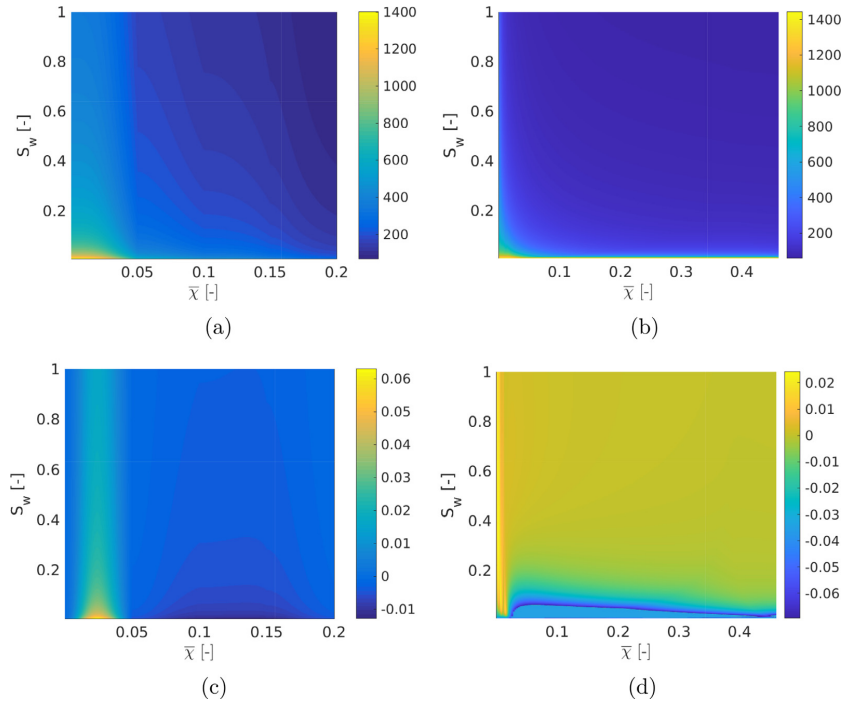

Fig. 9. *Top*: Simulated capillary pressure obtained by taking multiple paths in the $S_w \times \overline{\chi}$ domain, for the uniform (left) and non-uniform (right) cases. *Bottom*: The difference between the dynamic model (23) with the respective data, scaled by $P_c^{\max}$.

now with the product of saturation and exposure time as the dynamic variable. The additional complexity is needed to draw the capillary pressure curve back to the initial wetting at low saturation (a region of the $P_c - S$ curve dominated by smaller pores where the CA takes longer to change).

An important result of this study is quantifying the link between the pore- and core-scale. We showed that by varying the parameter that alters the speed and extent of CA change in each individual pore, we could predict the resulting impact on dynamic capillary pressure. In fact, in both the uniform and non-uniform cases, there is a very simple scaling from the pore-scale and macroscale parameters. In the uniform case, the two parameters are directly proportional, while in the non-uniform case, the macroscale parameter scales with the pore-scale parameter via a power law. The implication of this result is that by knowing the mechanism that controls CA at the pore-scale, which can be obtained by a relatively simple batch experiment, we can quantify *a priori* the macroscale dynamics without having to perform pore-scale simulations. This is an important generalization and valuable for making use of experimental data to inform macroscale constitutive functions.

We have quantified the ability of the interpolation model to capture underlying WA at the pore-scale for a simple BoT. This result is a natural development from previous studies that incorporate the interpo-

lation model directly into reservoir simulation of wettability alteration. In those studies, the model was matched directly to core-scale data in a heuristic manner. The contribution of this study is to quantify the pore-scale underpinnings to the interpolation model through a direct and systematic manner, thus providing additional evidence to the validity of this type of model for use in macroscale simulation.

Despite the satisfactory and relatively straightforward correlation of the interpolation model to simulated $P_c - S$ data, the exact quantification of the dynamics is ultimately restricted by the simplicity of the BoT model. We chose this simple approach in order to isolate the WA process from other complexities associated with real pore networks, and thus begin to assess the mechanisms linking the pore- and core-scales. Though beyond the scope of the current work, further study is needed to determine whether the fundamental nature of dynamic behavior we observe will hold when additional complexity is added. Further advancements can be made by adding complexity to the porous media (i.e. converging-diverging throat diameters or tortuosity) or to the pore-scale WA model. Theoretical work using pore-network models should also be combined with laboratory investigations to further calibrate the underlying WA mechanisms.

4. Conclusions

In this paper, we designed a framework to upscale the impact of time-dependent WA mechanisms at the pore scale on the dynamics in capillary pressure-saturation functions at the Darcy-scale. We found that an interpolation-based dynamic model can predict the change in capillary pressure due to underlying WA. The form of the dynamic interpolation coefficient is dependent on exposure time to a chemical agent, with a different mathematical form depending on the pore-scale WA mechanism. The correlated dynamic capillary pressure model shows an excellent match with simulated Pc-S data and reliably predicts capillary dynamics independent of the saturation-time path. More importantly, the model relies on a single interpolation parameter that has a clear and simple relationship with the pore-scale WA parameter.

CRediT authorship contribution statement

Abay Molla Kassa: Conceptualization, Data curation, Writing - original draft, Writing - review & editing. **Sarah Eileen Gasda:** Conceptualization, Data curation, Writing - original draft, Writing - review & editing. **Kundan Kumar:** Writing - review & editing. **Florin Adrian Radu:** Writing - review & editing.

Acknowledgement

Funding for this study was through the CHI project (n. 255510) granted through the CLIMIT program of the Research Council of Norway.

References

Adibhatia, B., Sun, X., Mohanty, K., 2005. Numerical studies of oil production from initially oil-wet fracture blocks by surfactant brine imbibition. In: SPE International Improved Oil Recovery Conference in Asia. SPE J. https://doi.org/10.2118/97687-MS.

Ahmed, A., Patzek, T.W., 2003. Impact of wettability alteration on two-phase flow characteristics of sandstones: a quasi-static description. Water Resour. Res. 39, 1–12. https://doi.org/10.1029/2002WR001366.

Al-Mutairi, S.M., Abu-Khamsin, S.A., Hossain, M.E., 2012. A novel approach to handle continuous wettability alteration during immiscible CO_2 flooding process. In: Abu Dhabi International Petroleum Conference and Exhibition. SPE https://doi.org/10.2118/160638-MS.

Andersen, P.Ø., Evje, S., Kleppe, H., Skjæveland, S.M., 2015. A model for wettability alteration in fractured reservoirs. SPE J. 20, 1261–1275. https://doi.org/10.2118/174555-PA.

Barenblatt, G., Patzek, T., Silin, D., 2003. The mathematical model of nonequilibrium effects in water-oil displacement. SPE J. 409–416. https://doi.org/10.2118/87329-PA.

Bartley, J.T., Ruth, D.W., 1999. Relative permeability analysis of tube bundle models. Transport Porous Media 36, 161–187. https://doi.org/10.1023/A:1006575231732.

Blunt, M.J., 1997. Pore level modeling of the effects of wettability. SPE J. 2, 494–510. https://doi.org/10.2118/38435-PA.

Blunt, M.J., 2001. Flow in porous media– pore-network models and multiphase flow. Curr. Opin. Colloid Interface Sci. 6, 197–207. https://doi.org/10.1016/S1359-0294(01)00084-X.

Blut, M.J., 2017. Multiphase Flow in Permeable Media: A Pore-Scale Perspective. Cambridge university press.

Bonn, D., Eggers, J., Indekeu, J., Meunier, J., Rolley, E., 2009. Wetting and spreading. Rev. Mod. Phys. 81, 739–805. https://doi.org/10.1103/RevModPhys.81.739.

Buckley, J.S., Liu, Y., Monsterleet, S., 1988. Mechanisms of wetting alteration by crude oils. SPE J. 3, 54–61. https://doi.org/10.2118/37230-PA.

Chalbaud, C., Robin, M., Lombard, J., Martin, F., Egermann, P., Bertin, H., 2009. Interfacial tension measurements and wettability evaluation for geological CO_2 storage. Adv. Water Resour. 32, 98–109. https://doi.org/10.1016/j.advwatres.2008.10.012.

Chiquet, P., Broseta, D., Thibeau, S., 2007a. Wettability alteration of caprock minerals by carbon dioxide. Geofluids 112–122. https://doi.org/10.1111/j.1468-8123.2007.00168.x.

Dahle, H.K., Celia, M.A., Hasanizadeh, S.M., 2005. Bundle-of-tubes model for calculating dynamic effects in the capillary-pressure saturation relationship. Transport Porous Media 58, 5–22. https://doi.org/10.1007/s11242-004-5466-4.

Davis, A., Morton III, S.A., Counce, R., DePaoli, D., Hu, M.-C., 2003. Ionic strength effects on hexadecane contact angles on a gold-coated glass surface in ionic surfactant solutions. Colloids Surf. A 221, 69–80. https://doi.org/10.1016/S0927-7757(03)00132-8.

Delshad, M., Najafabadi, N.F., Anderson, G.A., Pope, G.A., Sepehrnoori, K., 2009. Modeling wettability alteration by surfactants in naturally fractured reservoirs. SPE J. 12, 361–370. https://doi.org/10.2118/100081-PA.

Dickson, J.L., Gupta, G., Horozov, T.S., Binks, B.P., Johnston, K.P., 2006. Wetting phenomena at the CO_2/water/glass interface. Langmuir 22, 2161–2170. https://doi.org/10.1021/la0527238.

Du, Y., Xu, K., Mejia, L., Zhu, P., Balhoff, M.T., 2019. Microfluidic investigation of low-salinity effects during oil recovery: a no-clay and time-dependent mechanism. SPE J. 2841–2858. https://doi.org/10.2118/197056-PA.

Eral, H.B., 't Mannetje, D.J.C.M., Oh, J.M., 2013. Contact angle hysteresis: a review of fundamentals and applications. Colloid Polym. Sci. 291, 247–260. https://doi.org/10.1007/s00396-012-2796-6.

van Erp, T.S., Trinh, T., Kjelstrup, S., Glavatskiy, K.S., 2014. On the relation between the langmuir and thermodynamic flux equations. Front Phys. 1–14. https://doi.org/10.3389/fphy.2013.00036.

Haagh, M.E.J., Siretanu, I., Duits, M.H.G., Mugele, F., 2017. Salinity-dependent contact angle alteration in oil/brine/silicate systems: the critical role of divalent cations. Langmuir 33, 3349–3357. https://doi.org/10.1021/acs.langmuir.6b04470.

Hassanizadeh, S., Celia, M., Dahle, H., 2002. Dynamic effects in the capillary pressure–saturation relationship and its impacts on unsaturated flow. Vadose Zone J. 1, 38–57. https://doi.org/10.2113/1.1.38.

Helland, J.O., Skjæveland, S.M., 2006. Physically based capillary pressure correlation for mixed-wet reservoirs from a bundle-of-tubes model. In: Proceedings of the SPE/DOE Improved Oil Recovery Symposium. SPE, pp. 171–180. https://doi.org/10.2118/89428-PA.

Helland, J.O., Skjæveland, S.M., 2007. Relationship between capillary pressure, saturation, and interfacial area from a model of mixed-wet triangular tubes. Water Resour. Res. 43, 1–15. https://doi.org/10.1029/2006WR005698.

Iglauer, S., Mathew, M., Bresme, F., 2012. Molecular dynamics computations of brine-CO_2 interfacial tensions and brine-CO_2-quartz contact angles and their effects on structural and residual trapping mechanisms in carbon geosequestration. J. Colloid Interface Sci. 386, 405–414. https://doi.org/10.1016/j.jcis.2012.06.052.

Iglauer, S., Pentland, C.H., Busch, A., 2014. CO_2wettability of seal and reservoir rocks and the implications for carbon geo-sequestration. Water Resour. Res. 51, 729–774. https://doi.org/10.1002/2014WR015553.

Iglauer, S., Rahman, T., Sarmadivaleh, M., Al-Hinai, A., Fernø, M.A., Lebedev, M., 2016. Influence of wettability on residual gas trapping and enhanced oil recovery in three-phase flow: a pore-scale analysis by use of microcomputed tomography. SPE J. 21, 1916–1929. https://doi.org/10.2118/179727-PA.

Jadhunandan, P.P., Morrow, N.R., 1995. Effect of wettability on waterflood recovery for crude-oil/brine/rock systems. SPE Reservoir Eng. 10, 40–46. https://doi.org/10.2118/22597-PA.

Jafari, M., Jung, J., 2016. The change in contact angle at unsaturated CO_2-water conditions: implication on geological carbon dioxide sequestration. Geochem. Geophys. Geosyst. 17, 3969–3982. https://doi.org/10.1002/2016GC006510.

Jung, J.W., Wan, J., 2012. Supercritical CO_2 and ionic strength effects on wettability of silica surfaces: equilibrium contact angle measurements. Energy Fuels 26, 6053–6059. https://doi.org/10.1021/ef300913t.

Kim, Y., Wan, J., Kneafsey, T.J., Tokunaga, T.K., 2012. Dewetting of silica surfaces upon reactions with supercritical CO_2 and brine: pore-scale studies in micromodels. Environ. Sci. Technol. 46, 4228–4235. https://doi.org/10.1021/es204096w.

Krumpfer, J.W., McCarthy, T.J., 2010. Contact angle hysteresis: a different view and a trivial recipe for low hysteresis hydrophobic surfaces. Faraday Discuss. 146, 103–111. https://doi.org/10.1039/b925045j.

Lashgari, H.R., Xu, Y., Sepehrnoori, K., 2016. Modelling dynamic wettability alteration effect based on contact angle. SPE, pp. 1–17. https://doi.org/10.2118/179665-MS.

McKee, D., Swailes, S., 1991. On the derivation of the langmuir isotherm for adsorption kinetics. J. Phys. A Math. Gen. 24, 207–2010.

Morrow, N.R., Lim, H.T., Ward, J.S., 1986. Effect of crude-oil-induced wettability changes on oil recovery. SPE, pp. 89–103. https://doi.org/10.2118/13215-PA.

Morton III, S.A., Keffer, D.J., Counce, R.M., DePaoli, D.W., 2005. Behavior of oil droplets on an electrified solid metal surface immersed in ionic surfactant solutions. Langmuir 21, 1758–1765. https://doi.org/10.1021/la0480235.

Morton III, S.A., Keffer, D.J., Counce, R.M., DePaoli, D.W., C., H.M.Z., 2004. Thermodynamic method for prediction of surfactant-modified oil droplet contact angle. J. Colloid Interface Sci. 270, 229–241.

Plug, W.J., Bruining, J., 2007. Capillary pressure for the sand-CO_2-water system under various pressure conditions. application to CO_2 sequestration. Adv. Water Resour. 30, 2339–2353. https://doi.org/10.1016/j.advwatres.2007.05.010.

Saraji, S., Goual, L., Piri, M., Plancher, H., 2013. Wettability of scCO2/water/quartz systems: simultaneous measurement of contact angle and interfacial tension at reservoir conditions. Langmuir 1–39. https://doi.org/10.1021/la3050863.

Singh, R., Mohanty, K., 2016. Foams with wettability-altering capabilities for oil-wet carbonates: a synergistic approach. SPE J. 21, 1126–1139. https://doi.org/10.2118/175027-PA.

Skjæveland, S.M., Siqveland, L.M., Kjosavik, A., Thomas, W.L.H., Virnovsky, G.A., 2000. Capillary pressure correlation for mixed-wet reservoirs. SPE, pp. 60–67. https://doi.org/10.2118/60900-PA.

Tokunaga, T.K., Wan, J., 2013. Capillary pressure and mineral wettability influences on reservoir CO_2 capacity. Rev. Mineral. Geochem. 77, 481–503. https://doi.org/10.2138/rmg.2013.77.14.

Tokunaga, T.K., Wan, J., Jung, J., Kim, T.W., Kim, Y., Dong, W., 2013. Capillary pressure and saturation relations for supercritical CO_2 and brine in sand: high-pressure $p_c(s_w)$ controller/meter measurements and capillary scaling predictions. Water Resour. Res. 49, 4566–4579. https://doi.org/10.1002/wrcr.20316.

Wang, S., Tokunaga, T.K., 2015. Capillary pressure-saturation relations for supercritical CO_2 and brine in limestone/dolomite sands: implications for geologic carbon sequestration in carbonate reservoirs.. Environ. Sci. Technol. 49, 72087217. https://doi.org/10.1021/acs.est.5b00826.

Wang, S., Tokunaga, T.K., Wan, J., Dong, W., Kim, Y., 2016. Capillary pressure-saturation relations in quartz and carbonate sands: limitations for correlating capillary and wettability influences on air, oil, and supercritical CO_2 trapping. Water Resour. Res. 6671–6690. https://doi.org/10.1002/2016WR018816.

Washburn, E., 1921. The dynamics of capillary flow. Phys. Rev. 7, 273–283.

Xu, W.S., Luo, P.Y., Sun, L., Lin, N., 2016. A prediction model of the capillary pressure j–function. PLoS ONE 11, 1–9. https://doi.org/10.1371/journal.pone.0162123.

Yu, L., Kleppe, H., Kaarstad, T., Skjæ veland, S.M., 2008. Modelling of wettability alteration processes in carbonate oil reservoirs. Netw. Heterog. Media 3, 149–183. https://doi.org/10.3934/nhm.2008.3.149.

Paper 5.1.2

B

Modeling of relative permeabilities including dynamic wettability transition zones

A. M. Kassa, S. E. Gasda, K. Kumar, and F. A. Radu

In Journal of Petroleum Science and Engineering, volume 203, pp 1–15, 2021
DOI: 10.1016/j.petrol.2021.108556

Journal of Petroleum Science and Engineering 203 (2021) 108556

Contents lists available at ScienceDirect

Journal of Petroleum Science and Engineering

journal homepage: http://www.elsevier.com/locate/petrol

Modeling of relative permeabilities including dynamic wettability transition zones

Abay Molla Kassa [a,b,*], Sarah E. Gasda [a], Kundan Kumar [b], Florin A. Radu [b]

[a] NORCE Norwegian Research Center, Bergen, Norway
[b] Department of Mathematics, University of Bergen, Norway

ARTICLE INFO

Keywords:
Wettability alteration
Dynamic relative permeability
Dynamic wettability
Triangular bundle-of-tubes simulation
Upscaling

ABSTRACT

Wettability is a pore-scale property that impacts the relative movement and distribution of fluids in a porous medium. There are reservoir fluids that provoke the surface within pores to undergo a wettability change. This wettability change, in turn, alters the dynamics of relative permeabilities at the Darcy scale. Thus, modeling the impact of wettability change in the relative permeabilities is essential to understand fluids interaction in porous media. In this study, we include time-dependent wettability change into the relative permeability–saturation relation by modifying the existing relative permeability function. To do so, we assume the wettability change is represented by the sorption-based model that is exposure time and chemistry dependent. This pore-scale model is then coupled with a triangular bundle-of-tubes model to simulate exposure time-dependent relative permeabilities data. The simulated data is used to characterize and quantify the wettability dynamics in the relative permeability–saturation curves. This study further shows the importance of accurate prediction of the relative permeability in a dynamically altering porous medium.

1. Introduction

Wettability alteration (WA) plays an important role in many industrial applications such as microfluidics nanoprinting, enhanced oil recovery (EOR), and CO_2storage (Bonn et al., 2009; Iglauer et al., 2014, 2016; Yu et al., 2008; Blunt, 2001). Wettability refers to the tendency of one fluid over the others to spread on or adhere to a solid surface (Falode and Manuel, 2014; Bonn et al., 2009) and is defined by the fluid-fluid contact angle (CA). This pore-scale property regulates the distribution of fluids in the pore spaces and controls the relative flow of immiscible fluids in a porous medium (Anderson, 1987; Bobek et al., 1958; Falode and Manuel, 2014; Bonn et al., 2009). This, in turn, impacts constitutive relations in the multi-phase flow systems such as residual saturation, relative permeability, and capillary pressure at the Darcy scale (Ahmed and Patzek, 2003; Pentland et al., 2011; Iglauer et al., 2011, 2014; Falode and Manuel, 2014). Investigating and upscaling the impact of WA on the constitutive relations is of great importance.

Wettability is assumed to be static in time and uniform in space. However, wettability can be a dynamic process that depends on surface chemistry, composition of fluids, exposure time, and reservoir conditions (pressure and temperature) to name a few (Du et al., 2019; Salathiel, 1973; Treiber et al., 1972; Anderson, 1987; Haagh et al., 2017; Jadhunandan and Morrow, 1995; Buckley et al., 1988; Morrow, 1970). Experiments on crude oil/brine/rock systems have shown that adsorption of active components from the crude oil is able to change the wettability of the sample porous medium from water-wet to intermediate-wet system, a process known as ageing (Salathiel, 1973; Anderson, 1986; Buckley et al., 1988). It is also hypothesized that the oil reservoir may be more oil-wet than what is observed from the experiment. This is because the adsorption time of the experiment period was much less than the age of the oil in the reservoir. Furthermore, CO_2 s one of the reservoir fluids which contain active components that can provoke the surface within the pores to undergo a WA (Wang et al., 2013; Bikkina, 2011; Yang et al., 2008; Dickson et al., 2006; Iglauer et al., 2012, 2014; Jung and Wan, 2012; Espinoza and Santamarina, 2010; Farokhpoor et al., 2013; Saraji et al., 2013).

Generally, the WA process can have three phases that delineate the transition from initial to final wetting-state conditions, e.g. initial-wet, final-wet, and dynamic-wet. The end (initial and final) wetting conditions are static in time but can be uniform and/or mixed in space. A mixed-wet condition could be created by rock mineral and exposure history differences. This is due to the fact that a pore surface exposed to

* Corresponding author. NORCE Norwegian Research Center, Bergen, Norway.
E-mail address: abka@norceresearch.no (A.M. Kassa).

https://doi.org/10.1016/j.petrol.2021.108556
Received 5 August 2020; Received in revised form 18 December 2020; Accepted 15 February 2021
Available online 23 February 2021

the WA agent may be altered to a new wetting condition, while the unexposed surface keeps the initial wetting state (Kovscek et al., 1993; Blunt, 1997). This creates a mixed-wet condition even within a single pore and was observed and explained first by Salathiel et al. (Salathiel, 1973) in the 1970s. Often, WA is assumed to occur instantaneously and is considered as a function of the WA agent concentration. In some cases, however, the alteration process might take prolonged time in the scale of weeks and months (Tokunaga and Jiamin, 2013; Wang and Tokunaga, 2015; Buckley et al., 1988; Powers et al., 1996). Non-instantaneous WA, or aging, occurs when surface processes such as adsorption or chemical alteration are gradual rather than spontaneous. In this regard, the dynamic-wet phase can be a function of exposure time in addition to the WA agent concentration.

The WA process may result in a saturation function alteration for subsequent drainage-imbibition displacements and thus cause hysteresis in constitutive relations (Vives et al., 1999; Ahmed and Patzek, 2003; Delshad et al., 2003; Spiteri et al., 2008; Landry et al., 2014). For instance, core-flooding measurements for (supercritical or gas) CO_2-water system have shown that WA-induced alteration in the residual saturation and capillary pressure curves occurs despite the fact that they were measured following a standard procedure, i.e., where "pressure equilibration" is obtained after each increment in pressure (Plug and Bruining, 2007; Wang et al., 2013, 2016; Tokunaga and Jiamin, 2013; Tokunaga et al., 2013; Kim et al., 2012). In these measurements, a steadily change in capillary pressure function over time was observed. More importantly, the capillary pressure deviation from the initial-wet state curve could not be explained by classical scaling arguments. The instability and gradual change of residual saturation and capillarity through exposure time, in turn, impact the behavior of relative permeabilities.

The above experiments reveal that more complex constitutive functions are required to correlate the relative permeability and capillary pressure data that are impacted by WA. One alternative is to use mixed-wet model, e.g. Kjosavik et al. (2002) and Lomeland et al. (2005), that capture the static heterogeneity of wettability in the relative permeabilities. The main feature of these models is their flexibility to describe hysteresis and scanning curves caused by a wettability gradient in space. Other alternatives are models designed to handle the instantaneous WA process in the relative permeabilities. The first class of these models involves a heuristic approach that interpolates between the initial and final wetting states in which the WA effect is captured as a coefficient function (Delshad et al., 2009; Yu et al., 2008; Anderson et al., 2015; Adibhatia et al., 2005; Sedaghat and Azizmohammadi, 2019). Interpolation models are conceptually simple, while the initial and final wetting states are characterized by standard functions, e.g. Brooks-Corey (Brooks and Corey, 1964) or van Genuchten (van Genuchten, 1980)). The other approach incorporates the effect of the instantaneous WA into the relative permeabilities through the residual saturation directly (Lashgari et al., 2016). To date, only Al-Mutairi et al. (2012) have considered the effect of time-dependent WA in both the relative permeabilities and capillary pressure functions explicitly. The authors include a time-dependent mechanism for CA change within the residual saturation, which in turn affects the relative permeability and capillary pressure functions through the effective saturation. However, their model does not sufficiently incorporate or upscale the WA processes to core-scale laws.

Appropriate upscaling of the pore-scale time-dependent WA process connected to the capillary pressure function was the subject of our recent work (Kassa et al., 2020). There, WA dynamics were upscaled by introducing a mechanistic time-dependent CA model at the pore-level that was coupled with a cylindrical bundle-of-tubes model and used to simulate capillary pressure curves for drainage and imbibition displacements. The simulated data was used to formulate and quantify an interpolation-based capillary pressure model at the Darcy scale. The new dynamic model resolves the existing interpolation models used in the studies of reservoir simulation (Adibhatia et al., 2005; Delshad et al., 2009; Yu et al., 2008; Anderson et al., 2015; Sedaghat and Azizmohammadi, 2019) by including the dynamics in time and quantifying the pore-scale WA process to the interpolation model in a systematic manner.

One may consider employing a similar approach to (Kassa et al., 2020) and an interpolation-type model to capture the pore-scale underpinnings of WA in the relative permeability behaviors. However, time-dependent WA may impact the capillary pressure and relative permeabilities in different ways. As observed in Kassa et al. (2020), WA has a direct impact on the entry pressure in each pore and reflects it at the Darcy scale. Furthermore, a small change in CA exerts a large impact on the dynamics of the capillary pressure function. However, the relative permeability alteration occurs when the WA affects the pore filling/-draining orders of pore sizes. This may lead to a longer exposure time to observe a relative permeability deviation from the initial-wet state curve. Furthermore, unlike the capillary pressure function, the relative permeability curves are constrained between zero and one for any change of wettability. These features of the relative permeability may impact the modeling approach to upscale the pore-scale WA processes to core scale.

To our knowledge, a physically reliable model to characterize a prolonged exposure time-dependent WA induced dynamics in the relative permeability behaviors has not been proposed yet. This paper modifies and extends the approach discussed in Kassa et al. (2020) to develop a reliable model for dynamic relative permeability that accounts for pore-level time-dependent WA processes. In Section 2, we present the upscaling workflow based on simulation of dynamic relative permeability data using a pore-scale model for displacement coupled with CA change. Section 3 describes the correlation of two possible dynamic relative permeability models with associated analysis.

2. Modeling, simulation, and upscaling approach

A time-dependent WA may introduce a dynamics in the relative permeability–saturation ($k_{r\alpha}$−S_α) relationship. The dynamics can be measured by its deviation from the static initial wetting-state as:

$$k_{r\alpha}(\cdot) - k^{in}_{r\alpha}(S_\alpha) := f^{\mathrm{dyn}}_\alpha(\cdot), \tag{1}$$

where f^{dyn}_α represents the dynamic component. Alternatively, parameters of the standard models can be correlated with the dynamics,

$$k_{r\alpha}(\cdot) = k^{i}_{r\alpha}(S_\alpha, p_1(\cdot), p_2(\cdot), \ldots), \tag{2}$$

where $p_{i=1,2,\ldots,n}(\cdot)$ represent n fitting parameters that change along exposure time. In the above equations, the subscript $\alpha \in \{w, n\}$ represents the wetting and non-wetting phases, respectively. In this study, we explore both dynamic approaches in Eqs. (1) and (2) to quantify and characterize dynamics in relative permeability for a system that undergoes WA.

From the first approach, Eq. (1), we propose an *interpolation-based* model following our previous work (Kassa et al., 2020), where the dynamic component is designed to interpolate between two end wetting-state curves. To obtain an interpolation model, f^{dyn}_α can be scaled by the difference between the initial and final wetting-state relative permeability curves. The resulting non-dimensional quantity is:

$$\omega_\alpha\left(k^{f}_{r\alpha} - k^{in}_{r\alpha}\right) = f^{\mathrm{dyn}}_\alpha, \tag{3}$$

where ω is referred to as the *dynamic coefficient*, and superscript *in* and *f* represents relative permeabilities at the initial and final wettingstates, respectively. This can be substituted into Eq. (1) to obtain an interpolation model for dynamic relative permeability:

$$k_{r\alpha} = (1 - \omega_\alpha)k^{in}_{r\alpha} + \omega_\alpha k^{f}_{r\alpha}, \tag{4}$$

where ω_α is then correlated to wettability dynamics at the macroscale.

Similar models to Eq. (4) were employed to include the impact of instantaneous WA on relative permeability (Delshad et al., 2009; Yu et al., 2008; Anderson et al., 2015; Adibhatia et al., 2005; Sedaghat and Azizmohammadi, 2019).

The second approach (Eq. (2)) is a *parameter-based* approach that relies on a systematic inclusion of the dynamic term f_α^{dyn} into the relative permeability function through the model parameters. This can be done by formulating the parameters $p_i(\cdot)$ as a function of exposure time and WA agent in similar fashion as ω_α. This approach is motivated by the fact that the parameters in the standard relative permeability models are adjusted to different values when wettability changes from one state to the other.

Both the initial and final wetting-state curves can be characterized fully by the well-known relative permeability models such as van Genuchten (van Genuchten, 1980) or Brooks-Corey (Brooks and Corey, 1964), Purcell (Li and Horne, 2006), the LET model (Lomeland et al., 2005) or a model proposed by Kjosavik et al. (2002). For the sake of brevity, we focus on the Brooks-Corey (BC) and LET models in this study. The BC relative permeabilities can be derived by integrating the capillary pressure over the capillary tubes (Xu et al., 2016; Kjosavik et al., 2002). After the integration of the BC capillary pressure, one can obtain relative permeabilities:

$$k_{rw}^{in} = S_w^{a_w}, \text{and} \quad k_{rn}^{in} = \left(1 - S_w^{a_n}\right)(1 - S_w)^{m_n}, \tag{5}$$

for the water-wet system and,

$$k_{rw}^{f} = \left(1 - S_w^{a_w}\right)(1 - S_n)^{m_w}, \text{and} \quad k_{rn}^{f} = S_n^{a_n}, \tag{6}$$

for a hydrophobic system (see (Kjosavik et al., 2002)), here a_α and m_α are phase-specific parameters that can be utilized as dynamic fitting parameters $p_{i=1,2}$ in Eq. (2). Particularly, m_α is known as the tortuosity exponent.

In 2005, Lomeland et al. (2005) have proposed relative permeability models to predict the relative permeability curves for any type of wettability conditions:

$$k_{rw}^{in} = \frac{S_w^{L_w}}{S_w^{L_w} + E_w(1 - S_w)^{T_w}}, \text{and} \quad k_{rn}^{in} = \frac{(1 - S_w)^{L_n}}{(1 - S_w)^{L_n} + E_n S_w^{T_n}}, \tag{7}$$

where L_α, E_α, and T_α are empirical parameters for each phase. A detailed description and explanation of the parameters can be found in Lomeland et al. (2005). In this study, the LET parameters can be utilized as dynamic fitting parameters, $p_{i=1,2,\ldots,6}$ in Eq. (2).

2.1. Overall upscaling workflow

The two approaches described above are the basis for correlating WA-induced dynamics in relative permeability data. The first step in this workflow is generating relative permeability data by flow experiments under static flow conditions, i.e. a fixed pressure gradient and saturation. Once steady-state is reached, the relative permeability can be inferred from Darcy's Law for multi-phase flow:

$$k_{r\alpha}(S_\alpha) = \frac{Q_\alpha \mu_\alpha L}{\mathrm{K} A_T \Delta P_\alpha}, \tag{8}$$

where S_α is the average saturation of phase α, Q_α is the volumetric flow rate, K is the absolute permeability, and A_T is the cross-sectional area of the domain.

Laboratory experiments can be performed to generate $k_{r\alpha}$-$S_\alpha$data, however this approach is expensive and time-consuming. Existing laboratory data are currently unavailable for systems that undergo long-term WA. Thus, we follow a theoretical approach in which we simulate time-dependent $k_{r\alpha}$-$S_\alpha$data from a pore-scale model. The pore-scale experiments are performed in a similar fashion to laboratory experiments. A given pressure drop will induce flow through pores where the entry pressure is exceeded, which is a function of pore geometry and wetting state. Once static flow is reached, relative permeability is calculated according to Eq. (8) as a function of the average saturation, which can be computed by volume averaging over the pore-scale domain.

An important step in switching from laboratory to numerical experiments is explicitly accounting for WA in each individual pore. We model WA through a change in CA from an initial to final wetting state as a function of exposure time to the WA agent, in our case the non-wetting fluid phase. Exposure time in our study is associated with the time to reach steady state for each data point in $k_{r\alpha}$-$S_\alpha$space. This time component is driven by the displacement mechanisms occurring at the pore scale. For each new data point, time accumulates, WA progresses, and relative permeability is altered continuously throughout the experiment. The experiment continues along several drainage-imbibition cycles until WA is complete and the end wetting state is reached. The result is a complete set of $k_{r\alpha}$-$S_\alpha$data and associated WA dynamics.

The next step is to perform correlations for both the interpolation-based and parameter-based dynamic models in Eqs. (1) and (2) respectively. This procedure involves traditional curve-fitting, but we also apply insight about wettability dynamics and detailed analysis to arrive at a suitable and easy-to-implement dynamic model for reservoir simulation. We test each model for its suitability in capturing relative permeability dynamics. The goal is to develop a correlated model that involves only a few parameters.

After arriving at a suitable dynamic model correlation to the simulated data, we extend our analysis to ensure the robustness of the fitted model to a generic path in saturation-time domain. And finally, we examine the relation between the fitting parameter(s) of the upscaled relative permeability model and the parameter controlling CA change at the pore scale. This final step is important for linking the form of the macroscale model to pore-scale processes.

2.2. Pore-scale model description

We employ a triangular bundle-of-tubes to represent the pore-scale in quantifying the upscaled relative permeability given in Eq. (8). This representation of the pore scale was chosen to utilize the simplicity of a bundle-of-tubes model but with additional complexity to capture different fluid distributions and mixed wetting conditions within a single pore. Triangular tubes can support corner fluids and drainage through layers (Kovscek et al., 1993; Hui and Blunt, 2000; Helland and Skjæveland, 2006b).

A bundle-of-tubes model is a collection of capillary tubes with a distribution of radii as depicted in Fig. 1. The tubes in Fig. 1 are connected with the wetting (right with pressure P_r^{res}) and non-wetting (left with pressure P_l^{res}) phase reservoirs. Once the fluid movement is initiated in the tubes, the fluid configurations in each tube can have the form as in Fig. 1. Here, $A_{b,m}$ and $A_{c,m}$ are bulk and corner areas, respectively, that cover the cross-section of a tube and sum to be the area of the triangle (Fig. 1c). The quantity dx represents the change of interface location along the tube, whereas α_m is the half angle and θ_m is the fluid-fluid CA. Here, θ_m is the bulk surface CA in a given tube that represents the CA for an advancing or receding front during drainage or imbibition, where the angle may be hysteretic. θ_m also becomes the hinging angle $\theta_{h,m}$ if the interface hinges in the corner of the tube after displacement is completed. Detailed calculations of the areas and angles are discussed in the Apprndix A.

Let the boundary pressures difference be defined as:

$$\Delta P = P_l^{res} - P_r^{res}, \tag{9}$$

and the tubes in the bundle are filled with the wetting phase initially. Each tube has an entry pressure $P_{c,m}$ associated with it. If $\Delta P > P_{cap,m}$ is satisfied, the non-wetting fluid starts to displace the wetting phase, and

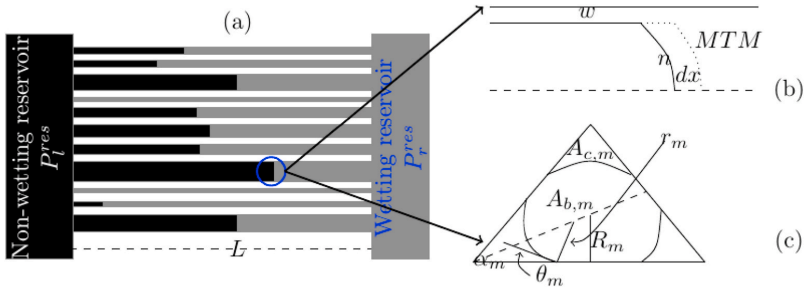

Fig. 1. The fluid displacement scenario in a bundle of tubes that is connected with wetting and non-wetting phase reservoirs. The right column shows fluid distribution during primary drainage: (b) shows the side-view and (c) shows the front view of the cross-section. The MTM refers to the main terminal meniscus. For complete (drainage-imbibition cycles) fluid configurations, see Fig. 2.

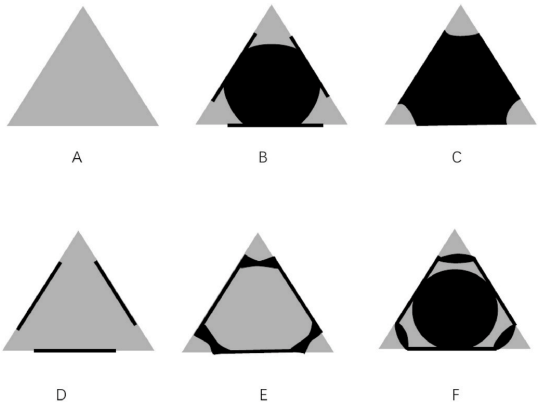

Fig. 2. Fluid configurations for initial condition (A), primary drainage (B or C), imbibition (D or E), and secondary drainage (F). Wetting phase is given in a light color and non-wetting phase in a dark color. We adopted the configurations from Helland and Skjæveland (2006b). The bold lines along the sides indicate altered wettability.

the volumetric flow rate in tube m can be approximated by the Lucas-Washburn flow model (Washburn, 1921):

$$q_m = \frac{\mathscr{G}_m(R_m,\theta_m)\left[\Delta P - P_{cap,m}\right]}{8\left[\mu_n x_m^{int} + \mu_w\left(L - x_m^{int}\right)\right]}, \tag{10}$$

where, μ_a is the phase viscosity, x_m^{int} is the location of the fluid-fluid interface along the length L of tube m, where $q_m = dx_m^{int}/dt$ is the interface velocity.

The quantity $\mathscr{G}_m$ in Eq. (10) represents the conductance of the fluids within tube m. We follow the work of Hui and Blunt (2000) to pre-compute the conductance. Conductance of tube m is a function of tube geometry, given by the inscribed radius R_m, the contact angle at the front, given by θ_m, and the configuration of fluids in the tube, which is itself dependent on wettability and filling history as described below.

The wettability change or gradient in triangular pores may create distinct fluid configurations after subsequent drainage and imbibition displacements (see Fig. 2). We summarize in brief the range of possible fluid configurations, and the reader is referred to Helland et al. (Helland and Skjæveland, 2006a) for the details of the fluid configurations. Configuration A shows a pore that is filled with the wetting phase and the wettability is representing the initial (water-wet) wetting state. A drainage into configuration A would result in either configuration B or C depending on the wettability. Subsequent imbibition into configuration B would always give configuration D, whereas imbibition into configuration C may result in either configuration D or E. Configuration F may occur after a drainage process that starts from configuration E if the receding CA is sufficiently smaller than the previous advancing CA. Otherwise, a drainage into configuration E would give configuration B or C.

The capillary pressure in Eq. (10) is given by

$$P_{cap,m} = \frac{\sigma}{r_m}, \tag{11}$$

where r_m is radius of arc meniscus (AMs) that separates the bulk from the corner fluid, and σ is fluid-fluid interfacial tension. The radius of curvature r_m is determined from the minimization of Helmholtz free energy of the system (Helland and Skjæveland, 2007). For isothermal, constant total volume, constant chemical potentials, and incompressible system, the minimization of the change in Helmholtz free energy can be simplified to (Helland and Skjæveland, 2007; Morrow, 1970; Bradford and Leij, 1997):

$$P_{cap,m} dV_n = \sigma(dA_{nw} + \cos(\theta_m) dA_{ns}), \tag{12}$$

where dV_n is the change of non-wetting fluid volume, dA_{nw} and dA_{ns} represent the change in interfacial area of fluid-fluid and fluid-solid interfaces, respectively (Helland and Skjæveland, 2007). A_{nw} and A_{ns} are longitudinal interfacial areas, distinct from the cross-sectional areas $A_{b,m}$ and $A_{c,m}$ depicted in Fig. 1.

Following (Helland and Skjæveland, 2006b; van Dijke and Sorbie, 2006; Ma et al., 1996), we calculate the entry pressure curvature, r_m, by combining Eqs. (11) and (12) for the starting configuration prior to drainage or imbibition, i.e. one of the configurations depicted in Fig. 2. Then, after a displacement occurs, the new fluid distribution is computed. This calculation involves determining the fluid volumes in the bulk ($A_{b,m}L$) and corners ($A_{c,m}L$) as a function r_m and θ_m. For mixed wetting conditions in tube m, θ_m affects the fluid configuration and thus determines the hinging CA, $\theta_{h,m}$. The hinging CA, $\theta_{h,m}$, is created after the MTM displaces the resident fluid and it evolves according to the change in θ_m. Furthermore, the areas ($A_{b,m}$ and $A_{c,m}$) are also pressure drop dependent in addition to wettability (θ_m). For example, the wetting phase in the corner area bulges out (configuration C) and starts moving (Configuration B) as (the pressure drop decreases) during the imbibition process occurring in other tubes. These calculations are based on different conditions such as the existence of the corner fluids, the fluid displacement history, the value of θ_m compared to the half angle (α_m), and similar geometrical or flow arguments. We refer the reader to the Appendix A for more details on these calculations.

2.3. Pore-scale wettability alteration

Above, we observed that the entry pressure in Eq. (12), fluid distributions in Appendix A, and conductance (Hui and Blunt, 2000) are wettability evolution dependent. In this section, we propose a model for CA change in tube m as a function of exposure time and fluid-history, based on the following assumptions:

- The CA of the pore surface is altered through exposure time to the WA agent and the alteration is permanent and cannot be restored to the original wetting condition when the WA agent is removed from the pore.
- WA is quasi-static in time if the WA agent is removed from the pore before the final wetting-state is reached. If the agent is reintroduced at some later point, alteration continues until the final state.

According to the assumptions above, only the bulk area of the tube covered by the non-wetting fluid during drainage (i.e. $A_{b,m}$) is altered dynamically in time, whereas the undrained corner surface area, defined by $A_{c,m} > 0$, remains at the initial condition. This may create a mixed-wet condition within a single tube. As we recall, wettability only impacts fluid configuration and displacement through the bulk CA θ_m. Thus, we can introduce a functional form to describe the CA change for θ_m as follows:

$$\theta_m(\cdot) := \theta_m^{in} + \varphi_m(\cdot)\left(\theta_m^{f} - \theta_m^{in}\right), \tag{13}$$

where θ_m^f, θ_m^{in} are the final and initial contact angles respectively. The WA model (13) is designed to evolve from an arbitrary initial wetting state to the final wetting condition so that φ_m is used to interpolate between end wetting conditions and has a value between zero and one.

Theoretical investigation and detailed laboratory measurement on time-dependent WA are very limited. Furthermore, WA is a complex process, where surface free energies, surface mineralogy, fluid composition and exposure time interact. However, adsorption of the WA agent onto the surface area is a natural process in CA change (Blunt, 2017). Such adsorption type wettability evolution is observed for CA measurements (Dickson et al., 2006; Jung and Wan, 2012; Iglauer et al., 2012; Jafari and Jung, 2016; Davis et al., 2003; Morton et al., 2005). These all give an insight to model φ in Eq. (13) according to the adsorption of the WA agent and can be given as follows:

$$\varphi_m := \frac{\chi_m}{C + \chi_m}, \tag{14}$$

where C is a non-dimensional parameter (it can be seen as the ratio of the adsorption and desorption rate constants) that controls the speed and extent of alteration from initial-wet to final-wet system. The derivation of Eq. (14) can be found in our previous work (Kassa et al., 2020). The variable χ_m is a measure of exposure time and is defined as:

$$\chi_m : = \frac{1}{\mathscr{T}} \int_0^t \frac{A_{b,m} x_m^{int}(\tau)}{V_{p,m}} d\tau, \tag{15}$$

where $V_{p,m}$ is the pore volume of tube m, and $\mathscr{T}$ is a macroscale characteristic time that used to scale the exposure history. Without losses of generality, the characteristic time $\mathscr{T}$ is identical for all tubes and is precomputed from Eq. (10) as the time for one complete drainage-imbibition cycle for the entire bundle of tubes under static initial wetting conditions.

The interface position x_m^{int} varies from 0 to L as determined by Eq. (10). We note the time interval used in Eq. (15) is the same for every tube, i.e. from the start of the relative permeability experiment until the current time. This implies that the integrand in Eq. (15) will be 0 or 1 for tube m during most of the experiment, since the local time for the interface to traverse the tube length is minimal compared to the total length of the experiment. This is because the pressure increments are set to drain/imbibe one tube at a time.

The dependency of exposure time on local interface displacement results in a different χ_m for different tubes. This variation in χ gives rise to a *non-uniform* wetting condition across the bundle that persists until all pores have reached the final wetting-state. Heterogeneity in CA from tube to tube is distinct from mixed-wet conditions at the tube-level that evolves from application of Eq. (13). In this study, we do not consider the further complication of a wettability gradient across the length of the tubes because the time to drain is assumed to be fast compared to the exposure time for WA to occur.

2.4. Simulation approach

The pore-scale wettability dynamics described in Eqs. (13)–(15) are coupled to the pore-scale model formulation in Section 2.2 through alteration of θ_m. A series of drainage and imbibition cycles are then performed to generate the data needed to calculate relative permeability for each phase α according to Eq. (8). The included algorithm describes the steps taken in each cycle.

Algorithm: A single drainage-imbibition cycle for simulation of relative permeability data.
Drainage displacement: Set the maximum entry pressure, $P_{cap}^{\max}$
  Calculate $P_{cap,m}$ from Eqs. (11)-(12) for each tube m
  if $\Delta P > P_{cap,m}$ **then**
    Drain the respective tubes until static flow conditions are reached
    Estimate from Eq. (10) and χ_m from Eq. (15)
    if $\theta_m^{in} < \frac{\pi}{2} - \alpha_m$ **then**
      Configuration A →B or C
      Calculate $A_{b,m}$ from Eq. (A.2) and $A_{c,m}$ from Eq. (A.5)
      Update θ_m from Eq. (13)
    end if
    Calculate S_α, $\overline{\chi} = \frac{1}{\mathscr{T}} \int_0^t (1 - S_w) d\tau$, and $k_{r\alpha}$ from Eq. (8)
  end if
  Increase ΔP
end While
Imbibition displacement:Set the minimum entry pressure, $P_{cap}^{\min}$
  Calculate $P_{cap,m}$ from Eq. (12) fro each tube m
  if $\Delta P < P_{cap,m}$ **then**
    Imbibe the respective tubes until static flow conditions are reached
    Estimate from Eq. (10) and update χ_m from Eq. (15)
  if $\theta_m < \frac{\pi}{2} + \alpha_m$ **then**
  Configuration B →D
  Estimate the area $A_{b,m} = \frac{3R_m^2}{2\tan\alpha_m}$
  else Configuration C →D or **E**
  if Configuration C →D **then**
  Estimate the area $A_{b,m} = \frac{3R_m^2}{2\tan\alpha_m}$
  else if Configuration C →E **then**
  Estimate $A_{b,m}, A_{c,m}$, and layer $= A_{c,m}(\pi - \theta_{a,m}) - A_{c,m}(\theta_{h,m}^1)$
  end if
  end if
  Calculate S_α, $\overline{\chi} = \frac{1}{\mathscr{T}} \int_0^t (1 - S_w) d\tau$, and $K_{r\alpha}$ from Eq. (8)
  Update θ_m from Eq. (13)
  end if
  Decrease ΔP
end while

The algorithm is repeated by controlling the pressure drop ΔP to generate data over a reasonable time window for carrying out the dynamic model correlation discussed below. We reduce the ΔP increment in the last cycle by three orders of magnitude compared to the first cycles in order to prolong exposure time and achieve the final WA in fewer cycles. This arbitrary control is performed for the purposes of presentation, but is not strictly necessary. After each step, a relative permeability data point is calculated according to Equation (8) and then used

to correlate the dynamic relative permeability models when a complete set of data are obtained.

3. Simulation results

The two-phase flow simulation tool at the pore-scale is implemented in MATLAB. Each tube in the bundle is assigned a different radius R, with the radii drawn from a truncated two-parameter Weibull distribution (Hui and Blunt, 2000):

$$R = (R_{\max} - R_{\min})\{-\delta \ln[y(1-\exp(-1/\delta)) + \exp(-1/\delta)]\}^{1/\gamma} + R_{\min}, \quad (16)$$

where $R_{\max}$ and $R_{\min}$ are the pore radii of the largest and smallest pore sizes respectively, and δ and γ are dimensionless parameters, and $y \in (0,1)$ is a random variable. The rock parameters and fluid properties are listed in Table 1.

These parameters are coupled to the bundle-of-tubes model to simulate fluid conductance and relative permeability curves. In the following section, we present and discuss the simulated relative permeability and related results.

3.1. Initial and final wetting-state relative permeability

In section 2, we point out that end wetting state relative permeabilities are the foundation to characterize the dynamic relative permeability curves. Thus, it is natural to examine the end-state $k_{r\alpha}$-$S_\alpha$relations before quantifying the dynamic relative permeabilities using the same pore-size distribution and fluid properties in Table 1. Thus, static $k_{r\alpha}$-$S_\alpha$data is simulated by fixing the wettability at pre-specified initial θ_m^{in} and final θ_m^f values in each tube, see Table 1.

The simulated data and correlated models are shown in Fig. 3, where we compare the correlation for both the BC (in Eqs. (5) and (6)) and LET (in Eq. (7)) models.

The fitted parameters for the correlation models are found in Table 2.

Both the BC and LET correlations give an excellent match to the static relative permeability data.

As a complement, we tested the sensitivity of the static correlations (not shown here) for different pore-size distributions. For a simple bundle of capillary tubes, we find that the parameters L_n and T_w in the LET model are unity for any pore-size distribution. Furthermore, we observe in Table 2 that E_α are the only two parameters that change with a change in wettability, whereas all BC model parameters are sensitive to wettability change. There are other important features of the static LET correlations that are noteworthy. For instance, we can represent parameters L_w and T_n with a single parameter, which we denote λ. In addition, the parameter E_n is the inverse of E_w.

Taken together, the parameter space of the LET model can be reduced significantly to a two-parameter *reduced LET* model for each phase:

$$k_{rw} = E_n S_w^{\lambda}\left(E_n S_w^{\lambda} + 1 - S_w\right)^{-1}, \quad k_{rn} = (1-S_w)\left(1 - S_w + E_n S_w^{\lambda}\right)^{-1}. \quad (17)$$

The model in Eq. (17) can be further reduced to a one-parameter model if we set λ to be constant ($\lambda = 1.3$) and allow E_n to be correlated according to the wetting condition.

We emphasize that the reduction in parameter space for the LET model is limited to simple pore geometries, and in general the full LET model is necessary to describe relative permeability in real porous media systems.

Table 1
Parameters used to simulate quasi-static fluid displacement in a bundle-of-tubes.

Parameter	value	unit	Parameter	value	unit
σ	0.0072	N/m	no. radii	500	[-]
$R_{\min}$	1	μm	$R_{\max}$	100	μm
θ_m^f	180	degree	θ_m^{in}	0.0	degree
μ_w	0.0015	Pa·s	μ_{nw}	0.0015	Pa·s
L	0.001	m	γ	0.5	[-]
δ	1.5	[-]			

3.2. Simulated relative permeability data

We simulate relative permeability for five drainage-imbibition cycles (see Fig. 4), while the tubes in the bundle are altered through time following the CA model (13). These data are generated with a pore-scale parameter $C = 10 \times 10^{-5}$, and the evolution in CA is shown in (see Fig. 5). Note that the CA change may be halted (temporarily) in the pores if the displacement is to configuration D after imbibition. In this case, the drainage curve may follow the previous imbibition path. However, the imbibition curve may show a deviation from the previous drainage curve if wettability is altered sufficiently.

According to the CA distribution in Fig. 5 and $k_{r\alpha}$-$S_\alpha$curves in Fig. 4, a change in wettability from strongly to weakly water-wet does not affect relative permeability in any significant way. In other words, the first drainage relative permeability curve overlaps with the initial wetting-state relative permeability curve even though the CA has been altered from 0° to 60°. This result is in accordance with previous work for a pore-network model with a wettability range of $\theta_m = 0°$ to 45° (Ahmed and Patzek, 2003). This negligible WA impact on $k_{r\alpha}$-$S_\alpha$is in contrast to the capillary pressure–saturation relation, where a small change of CA impacts the P_c-$S_\alpha$ath significantly (Kassa et al., 2020). However, imbibition/drainage displacement may not necessarily occur in monotonically increasing/decreasing order of pore-sizes when the wettability of the pores (some) are altered to intermediate/weakly hydrophobic. This results in a relative permeability–saturation path deviation as observed in Fig. 4.

For subsequent drainage-imbibition cycles, we observe that the wetting and non-wetting phase relative permeabilities steadily increase and decrease, respectively (see Fig. 4). This result corresponds to wettability evolving from hydrophilic to hydrophobic conditions (Fig. 5). This occurs because the original wetting phase prefers the larger pores as wettability shifts, while the originally non-wetting fluid prefers the smaller pores. As a consequence, relatively permeability is reduced for the non-wetting, while the wetting phase relative permeability is improved as the final wetting state is approached. Additional drainage-imbibition cycles would follow along the static curve for the final wetting state once the final CA (θ^f) is reached.

Analogous to the capillary pressure–saturation relation (Kassa et al., 2020), Fig. 4 shows long-term WA introduces dynamic hysteresis in the $k_{r\alpha}$-$S_\alpha$relations for a bundle-of-tubes model. The $k_{r\alpha}$-$S_\alpha$hysteresis imposes a non-unique relation between the relative permeabilities and saturation. This is one of the challenging features of WA during the quantification of the dynamics in relative permeabilities. To eliminate the hysteresis observed in the $k_{r\alpha}$-$S_\alpha$relation, we projected the simulated relative permeability data onto the temporal domain $\overline{\chi}$ in Fig. 6. The temporal domain, $\overline{\chi}$ is the measure of the exposure history in averaged sense which defined as:

$$\overline{\chi} = \frac{1}{\mathscr{T}}\int_0^t (1 - S_w)d\tau. \quad (18)$$

Unlike $k_{r\alpha}$-S_α, $k_{r\alpha}$-$\overline{\chi}$ is uniquely related but non-monotonically i.e., it raises to one and decreases to zero in time along each drainage-imbibition cycle.

The WA process also affects the corner fluid distribution in each drainage-imbibition cycle. Fig. 7 shows the evolution of volume-averaged corner saturation for the wetting and non-wetting phases. The wetting-phase corner saturation decreases through time while the layer saturation grows. This is because wettability is altered from water-wet to hydrophobic and thus, the originally non-wetting fluid prefers to be in the corners. However, when pores become more hydrophobic, the corner water increases and bulges-out during imbibition. This process may result in a layer collapse in the fifth imbibition, where the layer

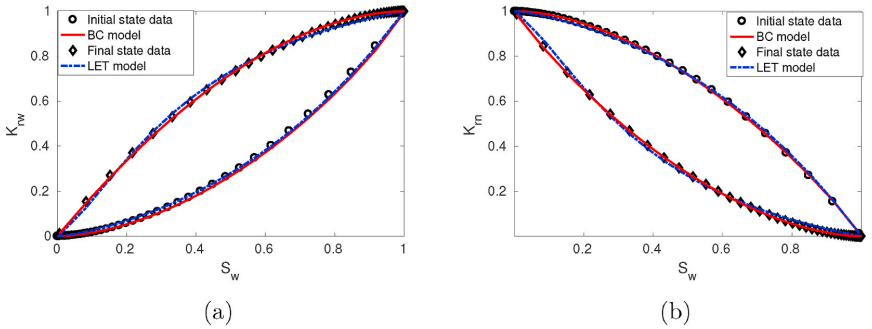

Fig. 3. The BC and LET correlation models compared to the initial and final wetting-state relative permeability curves: (a) wetting phase and (b) non-wetting phase relative permeabilities.

Table 2
Estimated correlation parameter values for initial and final wetting-state relative permeability curves.

Model	Parameters	Initial CA (θ^{in})	Final CA (θ^{f})
BC	a_w	0.9	1.839
	m_w	0.7329	0
	a_n	1.65	0.908
	m_n	0.075	0.7329
LET	L_w	1.3	1.3
	E_w	2.08	0.3
	T_w	1	1
	L_n	1	1
	E_n	0.48	3.37
	T_n	1.3	1.3

saturation increases as larger pores are imbibed and decreases when smaller pores are imbibed with increasing exposure time. Here, we have checked the establishment of corner fluids during the calculation of $k_{r\alpha}$-$S_\alpha$relations in each drainage-imbibition displacements.

3.3. Dynamic relative permeability model correlation

3.3.1. Interpolation-based dynamic model

In previous work, we successfully applied the interpolation, i.e. Eq. (4), to capture time-dependent WA mechanisms in the capillary pressure curves (Kassa et al., 2020). Thus, it is important to test the potential of the interpolation-based model to predict time-dependent dynamics in the $k_{r\alpha}$-$S_\alpha$relation. The dynamic coefficient ω_α is calculated according to Eq. (2) and plotted in Fig. 8.

In Fig. 8b, we observe that the dynamic coefficient ω_α is related to the exposure time $\overline{\chi}$ non-monotonically. Thus, it is challenging to propose a functional relationship between ω_α and $\overline{\chi}$ directly. On the other hand, the dynamic coefficient ω_α in Fig. 8a is increasing with respect to the exposure time to the WA agent. However, the ω_α-S curves in Fig. 8a have piece-wise functional forms i.e., zero and Langmuir-type function of phase saturation, that are altered with exposure time. This imposes another challenge to find a smooth model to predict the curves along with the saturation. But, one can design a piece-wise function to correlate the $\omega_\alpha - S_\alpha$ data. From Fig. 8a, we observe that the starting point of the Langmuir functional form is exposure time-dependent along the saturation path. Thus, the $\omega_\alpha - S_\alpha$ can be represented as:

$$\omega_\alpha(S_w, \overline{\chi}) := \begin{cases} \dfrac{S_w - S_w^*(\overline{\chi})}{S_w - S_w^*(\overline{\chi}) + \beta(\overline{\chi})}, & \text{for } S_w > S_w^*(\overline{\chi}), \\ 0, & \text{otherwise} \end{cases} \tag{19}$$

where S_w^* and β are time-dependent. The variable S_w^* is used to transform the starting point of the Langmuir part ω_α along the saturation to zero, and β is used to determine the curvature of the curve. From Fig. 8a, we observe that the parameters S_w^* and β are decreasing functions of exposure time, $\overline{\chi}$.

We matched the designed model in Eq. (19) with the dynamic

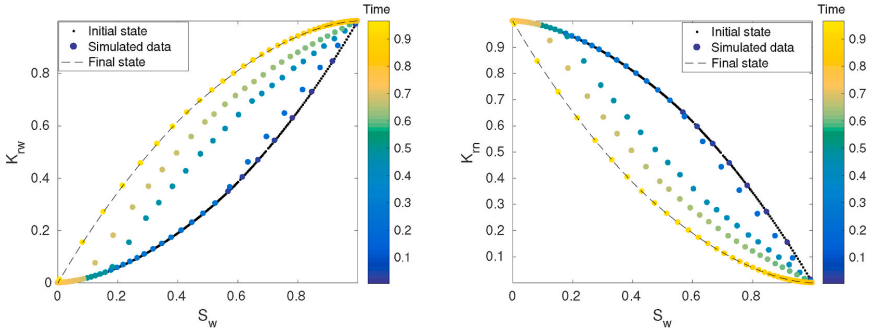

Fig. 4. Simulated dynamic relative permeability curves ((a) wetting phase and (b) non-wetting phase) with respect to wetting phase saturation. The static $k_{r\alpha}$-$S_\alpha$curves for the initial and final wetting states are shown as a reference. The color code shows the $k_{r\alpha}$-$S_\alpha$dynamics within a year of exposure time.

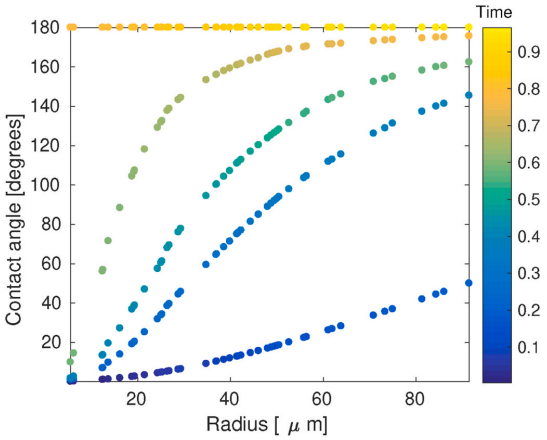

Fig. 5. Dynamic CA evolution as a function of exposure time to the WA agent per each tube. This CA distribution was recorded at the end of each drainage-imbibition cycle and the color code shows the CA dynamics during a year of exposure time.

coefficient data, $\omega_\alpha - S_w$, to describe the relations $S_w^* - \overline{\chi}$ and $\beta - \overline{\chi}$. The obtained relations have the form:

$$S_w^* = \zeta_{1i}\overline{\chi}^{b_1} + \psi_1, \text{and } \beta = \zeta_{2i}\overline{\chi}^{b_2} + \psi_2, \tag{20}$$

where ζ_i, b_i and ψ_i for $i = 1, 2$ are dimensionless fitting parameters. These parameters are estimated and given in Table 3 for this particular simulation.

The models in Eqs. (19) and (20) are then substituted back into the interpolation model (4) to give the dynamic relative permeability model and is read as:

$$k_{r\alpha} = \begin{cases} \dfrac{S_w - S_w^*(\overline{\chi})}{S_w - S_w^*(\overline{\chi}) + \beta(\overline{\chi})}\left(k_{r\alpha}^f - k_{r\alpha}^{in}\right) + k_{r\alpha}^{in}, & \text{for } S_w > S_w^*(\overline{\chi}) \\ k_{r\alpha}^{in}, & \text{otherwise.} \end{cases} \tag{21}$$

The dynamic model (21) is compared with the simulated relative permeability in Fig. 9.

According to Fig. 9, the piece-wise interpolation model predicts beyond the initial wetting state at joint-point of the initial wetting-state model and the designed interpolation model. This shows that the designed model (21) is badly correlated with the simulated $k_{r\alpha}$-$S_\alpha$data. Furthermore, the non-smoothness behavior of $\omega_\alpha - S_w$ results in a piece-wise phase relative permeability model with many dynamic parameters to be calibrated.

3.3.2. *Parameter-based dynamic model*

The second approach discussed in Section 2 relies on establishing a relation between the model parameters and $\overline{\chi}$ to upscale the effect of pore-scale wettability evolution in relative permeabilities. This is supported by the result reported in Table 2 for end wetting-state curves in which the model parameters are dependent on the wetting condition of the porous domain in addition to the pore-size distribution. As a consequence, we can formulate dynamic correlation models from

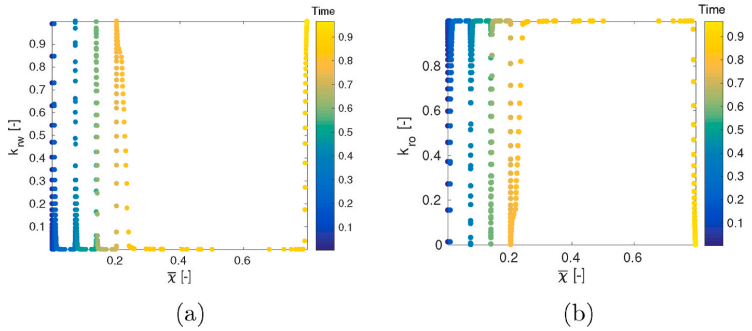

Fig. 6. Simulated relative permeability data as a function of $\overline{\chi}$ for (a) wetting phase, and (b) non-wetting phase. The color of each data point indicates the time elapsed in years.

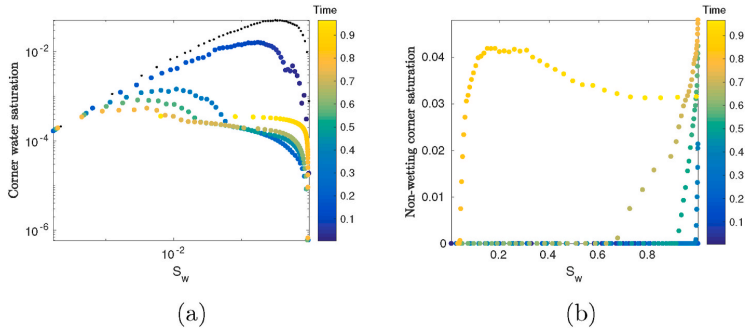

Fig. 7. Corner fluid saturations: (a) wetting phases saturation and (b) non-wetting phase saturation The color of each data point indicates the time elapsed in years.

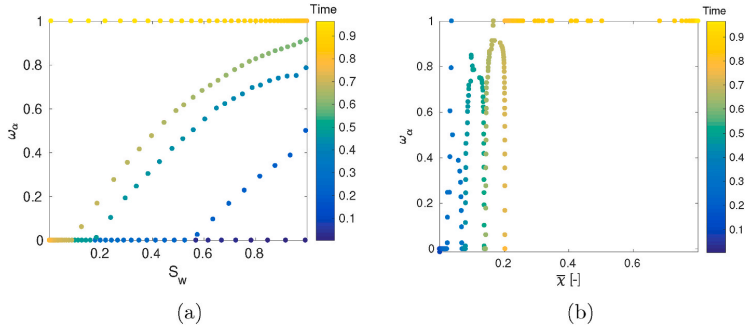

Fig. 8. The scaled dynamic deviation from the initial wetting-state relative permeability curves as a function of wetting phase saturation (a) and exposure time $\bar{\chi}$ (b).

Table 3
The estimated parameter values for the interpolation model.

Parameter	Value	Parameter	Value
ζ_1	0.0006123	ζ_2	0.001547
b_1	−2.522	b_2	−2.086
ψ_1	0.1297	ψ_2	0.2007

standard $k_{r\alpha}$-$S_\alpha$relations, i.e., BC models in Eqs. (5) and (6) or reduced LET models in Eq. (17). So far, we noticed that only $E_n = 1/E_w$ is sensitive to wettability change in the reduced LET model, whereas both parameters are sensitive in the BC model (see Table 2). A model with fewer parameters is preferred in order to ease implementation in Darcy-scale flow models. Thus, we choose the reduced LET model when correlating to dynamic data using a parameter-based approach.

Based on these observations, we rearrange the reduced LET model:

$$k_{rw} = \frac{p(\bar{\chi}, E_n^{in}) S_w^{\lambda}}{p(\bar{\chi}, E_n^{in}) S_w^{\lambda} + 1 - S_w}, \text{and} \quad k_{rn} = \frac{1 - S_w}{1 - S_w + p(\bar{\chi}, E_n^{in}) S_w^{\lambda}}, \tag{22}$$

where λ and E_n^{in} are determined from the initial wetting-state correlation. The reduced LET model (22) is then correlated to the $k_{r\alpha}$-$S_\alpha$data in Fig. 4 with the curve-fitting tool in MATLAB and matched with the $k_{r\alpha}$-$S_\alpha$data to study the functional dependencies between the p and $\bar{\chi}$. The obtained relation is linear and has the form:

$$p(\bar{\chi}, E_n^{in}) = \eta\bar{\chi} + E_n^{in}, \tag{23}$$

where E_n^{in} is as given in Table 2 and η is a *dynamic correlation parameter* for wetting and non-wetting phase relative permeabilities. For this particular simulation the dynamic parameter is estimated to be $\eta = 3.57$ for all drainage-imbibition cycles reported above. Now the dynamic term p in Eq. (23) can be substituted into the reduced LET model (22) to give the dynamic LET model:

$$k_{rw} = \frac{(\eta\bar{\chi} + E_n^{in}) S_w^{\lambda}}{1 - S_w + (\eta\bar{\chi} + E_n^{in}) S_w^{\lambda}}, \text{and} \quad k_{rn} = \frac{1 - S_w}{1 - S_w + (\eta\bar{\chi} + E_n^{in}) S_w^{\lambda}}. \tag{24}$$

The correlated dynamic LET model in Eq. (24) and the simulated $k_{r\alpha}$-$S_\alpha$data are compared in Fig. 10.

From Fig. 10, we observe that the proposed dynamic model (24) correlates well with the simulated relative permeability curves. The proposed dynamic relative permeability model is single-valued regardless of the number of drainage-imbibition cycles. However, this single-valued model is not well predictive around the junction points, particularly for low wetting-phase saturation. Despite this discrepancy, the obtained correlation result shown in Fig. 10 is acceptable and a significant improvement on the interpolation model result shown in Fig. 9. Furthermore, the dynamic LET model prediction can be improved by allowing λ to vary along the exposure time. However, this may double the number of parameters in the model that need to be calibrated.

If we compare the two dynamic models (i.e., the piece-wise interpolation model in Eq. (21) and the dynamic LET model in Eq. (24)), not only is the dynamic LET model a better fit to the data, it is easier to implement in a Darcy flow model than the piece-wise interpolation model. The reduced LET is likely more efficient to calculate because it is smooth in saturation-time space. We also note that the number of parameters in Eq. (24) is reduced by half from the original LET model. These all make the parameter-based dynamic model more reliable than using a model consisting of multiple parameters that change in each cycle (or hysteresis models). Further analysis below will concern only on the dynamic LET model.

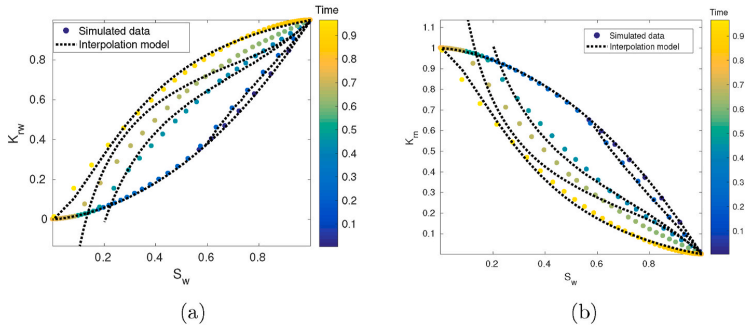

Fig. 9. Comparison of the interpolation model (21) with the simulated (wetting (a) and non-wetting (b)) relative permeabilities.

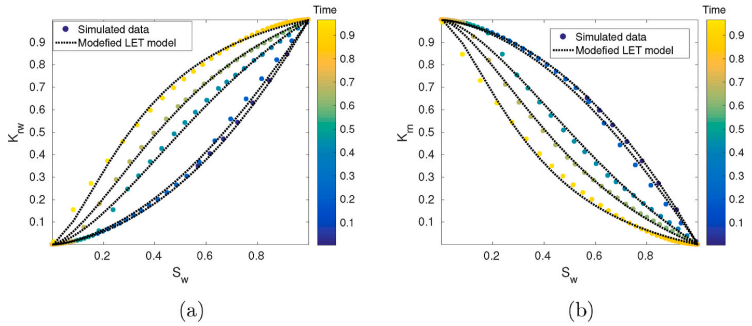

Fig. 10. Comparison of the dynamic LET model and the simulated phase relative permeability: (a) wetting phase and (b) non-wetting phase.

3.3.3. Sensitivity of correlated dynamic LET model to pore-scale WA

In this section, we will investigate the response of the upscaled model parameter η to the change in the CA model parameter C in Eq. (13). The parameter C controls the extent of WA at the pore-level, whereas η determines the WA induced dynamics in the relative permeabilities. We have simulated different drainage-imbibition $k_{r\alpha}$-$S_\alpha$curves by varying C to draw a relation between η and C. To do so, we determine the parameter η from each $k_{r\alpha}$-$S_\alpha$data that was simulated by considering different values of C. Then, we correlate the estimated parameter values of η with the chosen values of C, which can be read as:

$$\eta = \nu_1 C + \nu_2, \tag{25}$$

where ν_1 and ν_2 are fitting parameters. The correlation result is plotted in Fig. 11, where the parameters are estimated to be $\nu_1 = -1.8\times 10^4$ and $\nu_2 = 6$. Therefore, we can predict the upscaled dynamics of the relative permeabilities directly from the pore-scale WA process.

The relation in Eq. (25) can be substituted into the dynamic relative permeability model (24) to complete the upscaling process. The resulting dynamic relative permeability models are saturation, exposure time, and pore-scale WA parameter dependent. The pore-scale parameter has to be estimated from the calibration of CA model (13) with experimental data. Validating the underlying CA change model is beyond the scope of this paper. Rather, we consider the CA model as a reasonable basis to perform and analyze the upscaling process.

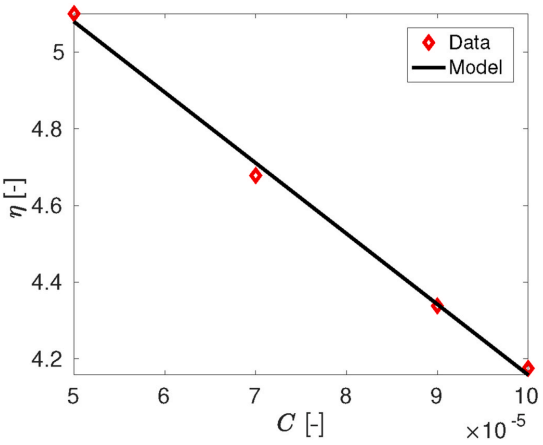

Fig. 11. The relation between pore-scale wettability parameter C and the correlation parameter η in Eq. (24).

3.4. Applicability of the dynamic LET model to arbitrary saturation history

The path in saturation-time space used to generate the relative permeability data in Fig. 12 can be considered as one of many arbitrary paths in the domain $S_w \times \overline{\chi}$. The exact path is dependent on the history of the exposure time to the WA agent and the reversal-point of saturation. This implies that the relative permeability-saturation dynamics may behave differently if one chooses a different saturation path that entails a prolonged exposure time for a fixed saturation profile and/or flow reversal at intermediate saturation.

Here, we simulate a large number of possible $k_{r\alpha}$-$S_\alpha$curves that involve different reversal-points and exposure history within the $S_w \times \overline{\chi}$. Note that we use the pore-scale model parameter $C = 10 \times 10^{-5}$. The simulated data is plotted in Fig.s. 12a and b for phase relative permeabilities. These arbitrary curves are used to test the robustness of the dynamic LET model in Eq. (24) by applying the model to generate the $k_{r\alpha}$-S_α-$\overline{\chi}$ surface and compare with the simulated data. The absolute difference between the simulated data and the surface generated by the calibrated model is depicted in Fig. 12c. According to the results in Fig. 12, we show that the dynamic LET model can be reliably applied to any saturation-time path having been calibrated against a single saturation history.

3.5. Discussion

In contrast to the dynamic capillary pressure model presented in Kassa et al. (2020), the interpolation-based approach is poorly correlated with the simulated relative permeability curves. However, further investigation (by considering advanced pore-network models) may be needed to re-evaluate the potential of capturing the WA process in the relative permeabilities based on the interpolation approach. We also examined the BC model in the parameter-based approach, though we do not report it here fully. For the sake of brevity, we have highlighted only the response of the BC model to the wettability change in Section 3.3 for end wetting conditions. In general, other models that involve more than two parameters (sensitive to CA change) could be calibrated with reasonable accuracy. But, these parameters need to be adjusted in each drainage-imbibition displacements. This complicates the modeling process and the resulting model may involve many parameters that may impose an extra challenge to analyze the WA impact on the flow dynamics at the Darcy scale.

In this study, we found that the original LET model with six total parameters (three for each phase) could be reduced to a dynamic LET model where only one parameter is needed to vary with wettability. The remaining parameters are only a function of pore-size distribution and the initial wetting state. The dynamic parameter $E_n = 1/E_w$ was then successfully correlated to the simulated dynamic relative permeability

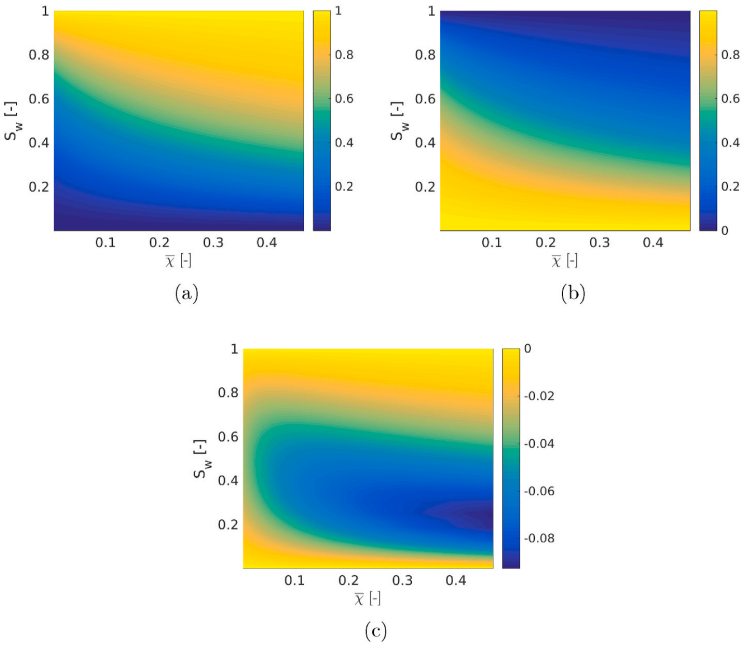

Fig. 12. Top: Simulated relative permeabilities obtained by taking multiple paths in the $S_w \times \overline{\chi}$ space, for the wetting (left) and non-wetting (right) phases. Bottom: The difference between the dynamic model with the simulated data.

data. Furthermore, we found a clear relation between E_n and the exposure time $\overline{\chi}$ by introducing a dynamic parameter η. This approach results in a single-valued dynamic relative permeability model that represents any arbitrary exposure time history.

The dynamic LET model developed here may need to be extended for real porous media with connected pores and more complex geometry. For instance, mixed-wet media may exhibit *S*-shaped relative permeability curves, particularly for the non-wetting phase (Lomeland et al., 2005). In this case, it may be necessary to introduce additional dynamic parameters into the LET model proposed herein, i.e. L_w and T_n. Further investigation using more complex pore-scale models, e.g pore-network models, will be needed to generate the dynamic relative permeability data. We expect that the parameter-based approach using the LET model will still result in the best dynamic model even with more complex porous media. Further development of the dynamic LET model is the subject of future work.

The proposed model is at the Darcy scale, that allows for a change in relative permeability as a function of averaged variables such as saturation (S_w) and exposure time to a WA agent ($\overline{\chi}$). This implies that the relative permeability in a grid block that is exposed to the WA agent may change over time even for constant saturation profile. However, if the grid block is not exposed to the WA agent, $\overline{\chi}$ is zero for this particular grid block. In this case, the dynamic model predicts the initial wetting-state curve. However, the developed model may continue further after the end wetting-state curve has attained which is in contrast to the interpolation-type model, where prolonged exposure does not contribute to the dynamics once the final wetting curve is met, see (Kassa et al., 2020). Thus it is important to propose a strategy to ensure that the relative permeability dynamics do not to cross the end-state curve. From Eq. (23), we know that the final wetting state is attained when $\eta\overline{\chi} + E_n^{in} = E_n^f$ is satisfied. From this, we can estimate the exposure time needed to reach the final wetting state, $\overline{\chi}_{\max} = \frac{E_n^f - E_n^{in}}{\eta}$, such that the relative permeability is represented by the end wetting-state curve. After knowing this we can set the dynamic variable as

$$\overline{\chi} = \begin{cases} \dfrac{1}{\mathscr{T}} \displaystyle\int_o^t (1 - S_w) d\tau, & \text{if } \ \overline{\chi} < \overline{\chi}_{\max} \\ \overline{\chi}_{\max}, & \text{if } \ \overline{\chi} \geq \overline{\chi}_{\max} \end{cases} \tag{26}$$

This controls the unnecessary dynamics once the final wetting-state curve is predicted. Nevertheless, the dynamic term in the model pushes the relative permeability towards the higher and lower end of the curve for the wetting and non-wetting phases respectively.

Previous studies (Delshad et al., 2009; Yu et al., 2008; Anderson et al., 2015; Adibhatia et al., 2005) represent the impact of instantaneous WA on relative permeabilities by an interpolation model which can be matched to core-scale data in a heuristic manner. This study reveals that the interpolation model is not the best approach to upscale the pore-scale WA process. Rather, we have shown the potential of a dynamic LET model to capture the underlying WA process at the pore-scale. The proposed dynamic LET model is smooth and simple to use for practical applications. Most importantly, the model is designed to eliminate the hysteresis in relative permeability induced by CA change caused by exposure to a WA agent during drainage and/or imbibition displacements. Similar to the developments in Kassa et al. (2020), we have quantified the link between the pore-scale model parameter *C* and the core-scale parameter η. According to the simulation results, we have shown that a very simple scaling can relate a pore-scale process with the core-scale. This result implies that knowing the mechanism that determines the CA change at the pore-level can be used to predict the macroscale dynamics without performing pore-scale simulations. This is an important and valuable generalization for making use of experimental data to inform core-scale relative permeability-saturation relations.

4. Conclusion

In this paper, we developed a dynamic relative permeability model that includes the pore-scale underpinnings of WA in the relative permeability–saturation relationships at the Darcy scale. We found that the developed model (i.e., the modified LET model in Eq (22)) is simple to use and can predict WA induced changes in the relative permeabilities. The modified LET model shows a good agreement with the simulated relative permeability data. Furthermore, this model is independent of the saturation-time paths generated by any drainage-imbibition cycles. More importantly, the WA dynamics in the relative permeabilities is controlled by a single-valued parameter that has a clear relationship with the time-dependent CA change model parameter.

Credit author statement

Abay Molla Kassa: Conceptualization, Data curation, Writing - original draft, Writing - review & editing. Sarah E. Gasda: Conceptualization, Writing - review & editing. Kundan Kumar: Writing - review & editing. Florin A. Radu: Review & editing

Declaration of competing interest

The authors declare that they have no known competing financial interests or personal relationships that could have appeared to influence the work reported in this paper.

Acknowledgement

Funding for this study was through the CHI project (n. 255510) granted through the CLIMIT program of the Research Council of Norway.

Appendix B. Supplementary data

Supplementary data to this article can be found online at https://doi.org/10.1016/j.petrol.2021.108556.

Nomenclature

Abbreviations

CO_2	Carbon dioxide
AMs	Arc meniscus
BC	Brooks-Corey
CA	Contact angle
Eq	Equation
Fig	Figure
LET	A model having parameters L, E, and T
MTM	Main terminal meniscus
WA	Wettability alteration

Superscripte

λ	Parameter in the reduced LET model
a, m	Fitting parameters in the Brooks-Corey model
b	The parameter in the interpolation model
dyn	Dynamic
f	Final wetting state
in	Initial wetting state
int	Fluid-fluid interface
k	Represents number of interface in the tube corner
L, T	Fitting parameters in the LET model
res	Reservoir

Subscripts

α	Phase indicator
max	Maximum
min	Minimum
b	Stands for bulk
c	Stands for corner
cap	Stands for capillary
h	Stands for hinging
i	The counter for the number of parameters
m	The m-th tube
n	Stands for nonwetting phase
p	Pore space
r, l	Stand for right and left respectively
s	Solid phase
T	Stands for total
w	Wetting phase

Liste of symbol

α	The half angle
β,ψ,ζ	b Fitting parameters in the interpolation model
$\chi,\overline{\chi}$	Pore-scale and averaged exposure time respectively
δ,γ	Parameters in the Weibull distribution
λ,E,η	Parameters in the modified LET model
$\mathscr{G}$	Conductance
K	Domain permeability
$\mathscr{T}$	Characteristic time
μ	Fluid viscosity
ω	The dynamic coefficient in the interpolation model
σ	Fluid-fluid interfacial tension
θ	Contact angle
φ	The dynamic term in the contact angle model
A	Cross-sectional area
C	CA model parameter
E	Fitting parameter in the LET model
f	Dynamic term in the relative permeability
k_r	Relative permeability
L	Tube length
P	Pressure
p	General parameter in the parametric approach
Q	Volumetric flux
q	Interface velocity
R	Radius of the inscribed circle
r	Radius of curvature
S	Saturation
V	Cross-sectional volume
x	The position along the tube length
y	Random variable

Appendix A. Calculations of areas covered by fluids

In Subsection 2.2, we showed the fluid configurations depending on the displacement scenario and wettability of the pore space. In this Appendix, we show how to calculate the areas that covered by the wetting and non-wetting phase fluids which demonstrated in Fig. 2. To do so, we numbered the fluid-fluid interfaces in order from the apex if there exist more than one interface in the corner, and we apply the indicator notation

$$I^k=\begin{cases}1, & \text{if interface k separates bulk nonwetting and corner water}\\ -1, & \text{if interface k separates bulk water and corner nonwetting.}\end{cases} \tag{A.1}$$

The bulk cross-sectional area $A^k_{b,m}$ in each tube in the bundle is defined as,

$$A^k_{b,m}=\begin{cases}\dfrac{3R_m^2}{\tan\alpha_m}-3r_m b^k_m\sin\left(\beta^k_m+\alpha_m\right)+3r_m^2\beta^k_m, & \text{if } I^k=1,\\ \dfrac{3R_m^2}{\tan\alpha_m}-3r_m b^k_m\sin\left(\beta^k_m-\alpha_m\right)-3r_m^2\beta^k_m, & \text{if } I^k=-1,\end{cases} \tag{A.2}$$

where

$$b^k_m=\frac{r\sin\left(\beta^k_m\right)}{\sin(\alpha_m)},\ \text{and}\ \beta^k_m=\begin{cases}\dfrac{\pi}{2}-\alpha_m-\theta^k_m \text{ if } I^k=1\\ \dfrac{\pi}{2}+\alpha_m-\theta^k_m \text{ if } I^k=-1.\end{cases} \tag{A.3}$$

Though we used a general notation for *CA* θ^k_m above, θ^k_m may be replaced by, $\theta_{r,m}$ and $\theta_{a,m}$ when the interface recedes and advances respectively, and $\theta^k_{h,m}$ if the interface, separating the bulk and corner fluids, is hinging. The hinging contact angle (if exists) changes with the entry pressure $P_{c,m}$ according to:

$$\theta^k_{h,m}=\begin{cases}\arccos\left(\dfrac{P_{c,m}b^k_m\sin(\alpha_m)}{\sigma}\right)-\alpha_m \text{ if } I^k=1\\ \arccos\left(\dfrac{P_{c,m}b^k_m\sin(\alpha_m)}{\sigma}\right)+\alpha_m \text{ if } I^k=-1.\end{cases} \tag{A.4}$$

The fluid area that occupies the corner regions can be estimated by

$$A_{c,m}\left(\theta_m\right)=3r_m^2\left(\theta_m+\alpha_m-\frac{\pi}{2}+\cos\left(\theta_m\right)\left(\frac{\cos(\theta_m)}{\tan(\alpha_m)}-\sin\left(\theta_m\right)\right)\right), \tag{A.5}$$

where θ_m is an argument to determine the appropriate area. The corner surface covered by water in configuration C is obtained by $A_{c,m}(\theta^1_{h,m})$, whereas the non-wetting fluid layer in configuration E is calculated from $A_{c,m}(\pi - \theta_{a,m}) - A_{c,m}(\theta^1_{h,m})$. The same approach can be applied if there exist many layers in the corner of the pore.

As clearly seen above the areas, $A_{b,m}$ *and* $A_{c,m}$are dependent on wettability, i.e., fluid-fluid CA. For example, fluid configuration C and D occurs only if the condition $\theta_m \leq \frac{\pi}{2} - \alpha_m$ is satisfied during the drainage displacement (Helland and Skjæveland, 2006a). Otherwise, the non-wetting phase will completely displace the wetting from the tube, including the corners, and occupy the entire cross sectional area of the tube. In this case, the entry pressure calculation is reduced to the well known Young-Laplace equation. On the other hand, the non-wetting fluid layer occurs in the corner when the condition $\theta_m > \frac{\pi}{2} + \alpha_m$ is satisfied. This implies that a dynamic change of CA can also determine the fluid distribution in a single pore.

References

Adibhatia, B., Sun, X., Mohanty, K., 2005. Numerical studies of oil production from initially oil-wet fracture blocks by surfactant brine imbibition. In: SPE International Improved Oil Recovery Conference in Asia. SPE J. https://doi.org/10.2118/97687-MS

Ahmed, A., Patzek, T.W., 2003. The impact of wettability alteration on two-phase flow characteristics of sandstones–a quasi-static description. Water Resour. Res. 39 (1–10), 0.1029/2002WR001366,-2003.

Anderson, P.Ø., Evje, S., Kleppe, H., Skjæveland, S.M., 2015. A model for wettability alteration in fractured reservoirs. SPE J. 20, 1261–1275. https://doi.org/10.2118/174555-PA.

Anderson, W., 1987. Wettability literature survey-part 5: the effects of wettability on relative permeability. J. Petrol. Technol. 39 (11), 1453–1468. https://doi.org/10.2118/16323-PA.

Al-Mutairi, S.M., Abu-Khamsin, S.A., Hossain, M.E., 2012. A novel approach to handle continuous wettability alteration during immiscible CO_2 looding process. In: Abu Dhabi International Petroleum Conference and Exhibition. SPE.

Anderson, W.G., 1986. Wettability literature survey–part 1: rock/oil/brine interactions and the effects of core handling on wettability. J. Petrol. Technol. 38 (10), 1125–1144. https://doi.org/10.2118/13932-PA.

Bikkina, P.K., 2011. Contact angle measurements of CO^2-water-quartz/calcite systems in the perspective of carbon sequestration. Int. J. Greenh. Gas Contr. 5 (5), 1259–1271. https://doi.org/10.1016/j.ijggc.2011.07.001.

Blunt, M.J., 1997. Pore level modeling of the effects of wettability. SPE J. 2, 494–510. https://doi.org/10.2118/54454-PA.

Blunt, M.J., 2001. Flow in porous media–pore-network models and multiphase flow. Curr. Opin. Colloid Interface Sci. 6 https://doi.org/10.1016/S1359-0294(01)00084-X, 197–207.

Blunt, M.J., 2017. Multiphase Flow in Permeable Media: A Pore-Scale Perspective. Cambridge university press.

Bobek, J.E., Mattax, C.C., Denekas, M.O., 1958. Reservoir rock wettability–its significance and evaluation. SPE 213, 155–160. https://doi.org/10.2118/895-G, 01.

Bonn, D., Eggers, J., Indekeu, J., Meunier, J., Rolley, E., 2009. Wetting and spreading. Rev. Mod. Phys. 81, 739–805. https://doi.org/10.1103/RevModPhys.81.739.

Bradford, S.A., Leij, F.J., 1997. Estimating interfacial areas for multi-fluid soil systems. J. Contam. Hydrol. 27, 83–105. https://doi.org/10.1016/S0169-7722(96)00048-4.

Brooks, R.H., Corey, A.T., 1964. Hydraulic properties of porous media and their relation to drainage design. Trans. ASAE 7 (1), 26–28.

Buckley, J.S., Liu, Y., Monsterleet, S., 1988. Mechanisms of wetting alteration by crude oils. SPE J. 3, 54–61. https://doi.org/10.2118/37230-PA, 01.

Davis, A.N., Morton III, S.A., Counce, R.M., DePaoli, D.W., Hu, M.Z.-C., 2003. Ionic strength effects on hexadecane contact angles on a gold-coated glass surface in ionic surfactant solutions. Colloids Surf., A 221, 69–80. https://doi.org/10.1016/S0927-7757(03)00132-8.

Delshad, M., Lenhard, R.J., Oostrom, M., Pope, G.A., 2003. A mixed-wet hysteretic relative permeability and capillary pressure model for reservoir simulations. SPE Reservoir Eval. Eng. 6, 328–334. https://doi.org/10.2118/86916-PA.

Delshad, M., Najafabadi, N.F., Anderson, G.A., Pope, G.A., Sepehrnoori, K., 2009. Modeling wettability alteration by surfactants in naturally fractured reservoirs. SPE Reservoir Eval. Eng. 12 https://doi.org/10.2118/100081-PA.

Dickson, J.L., Gupta, G., Horozov, T.S., Binks, B.P., Johnston, K.P., 2006. Wetting phenomena at the CO_2/water/glass interface. Langmuir 22, 2161–2170. https://doi.org/10.1021/la0527238.

Du, Y., Xu, K., Mejia, L., Zhu, P., Balhoff, M., 2019. Microfluidic investigation of low-salinity effects during oil recovery: a no-clay and time-dependent mechanism. SPE J. 24, 2841–2858. https://doi.org/10.2118/197056-PA, 06.

Espinoza, D.N., Santamarina, J.C., 2010. Water-CO_2-mineral systems: interfacial tension, contact angle, and diffusion – implications to CO_2 geological storage. Water Resour. Res. 46, 1–10. https://doi.org/10.1029/2009WR008634.

Falode, O., Manuel, E., 2014. Wettability effects on capillary pressure, relative permeability, and irredcucible saturation using porous plate. J. Pet. Eng. 1–12. https://doi.org/10.1155/2014/465418, 2014.

Farokhpoor, R.B., Bjørkvik, J.A., Lindeberg, E., Torsæter, O., 2013. Wettability behaviour of CO^2at storage conditions. Int. J. Greenh. Gas Contr. 12, 18–25. https://doi.org/10.1016/j.ijggc.2012.11.003.

Haagh, M.E.J., Siretanu, I., Duits, M.H.G., Mugele, F., 2017. Salinity-dependent contact angle alteration in oil/brine/silicate systems: the critical role of divalent cations. Langmuir 33, 3349–3357. https://doi.org/10.1021/acs.langmuir.6b04470.

Helland, J.O., Skjæveland, S.M., 2006a. Three-phase mixed-wet capillary pressure curves from a bundle of triangular tubes model. J. Petrol. Sci. Eng. 52, 100–130. https://doi.org/10.1016/j.petrol.2006.03.018.

Helland, J.O., Skjæveland, S.M., 2006b. Physically based capillary pressure correlation for mixed-wet reservoirs from a bundle-of-tubes model. SPE J. 11, 171–180. https://doi.org/10.2118/89428-PA, 02.

Helland, J.O., Skjæveland, S.M., 2007. Relationship between capillary pressure, saturation, and interfacial area from a model of mixed-wet triangular tubes. Water Resour. Res. 43, 1–15. https://doi.org/10.1029/2006WR005698.

Hui, M., Blunt, M.J., 2000. Effects of wettability on three-phase flow in porous media. J. Phys. Chem. B 104, 3833–3845. https://doi.org/10.1021/jp9933222.

Iglauer, S., Paluszny, A., Pentland, C.H., Blunt, M.J., 2011. Residual CO_2imaged with xray microtomography. Geophys. Res. Lett. 38, 1–6. https://doi.org/10.1029/2011GL049680.

Iglauer, S., Mathew, M., Bresme, F., 2012. Molecular dynamics computations of brine-CO_2interfacial tensions and brine-CO_2-quartz contact angles and their effects on structural and residual trapping mechanisms in carbon geosequestration. J. Colloid Interface Sci. 386, 405–414. https://doi.org/10.1016/j.jcis.2012.06.052.

Iglauer, S., Pentland, C.H., Busch, A., 2014. CO_2wettability of seal and reservoir rocks and the implications for carbon geo-sequestration. Water Resour. Res. 51, 729–774. https://doi.org/10.1002/2014WR015553.

Iglauer, S., Rahman, T., Sarmadivaleh, M., Al-Hinai, A., Fern, M.A., Lebedev, M., 2016. Influence of wettability on residual gas trapping and enhanced oil recovery in three-phase flow: a pore-scale analysis by use of microcomputed tomography. SPE J. 21, 1916–1929. https://doi.org/10.2118/179727-PA, 06.

Jadhunandan, P.P., Morrow, N.R., 1995. Effect of wettability on waterflood recovery for crude-oil/brine/rock systems. SPE Reservoir Eng. 10, 40–46. https://doi.org/10.2118/22597-PA.

Jafari, M., Jung, J., 2016. The change in contact angle at unsaturated CO_2-water conditions: implication on geological carbon dioxide sequestration. Geochem. Geophys. Geosyst. 17, 3969–3982. https://doi.org/10.1002/2016GC006510.

Jung, J.W., Wan, J., 2012. Supercritical $CO_2$and ionic strength effects on wettability of silica surfaces: equilibrium contact angle measurements. Energy Fuels 26, 6053–6059. https://doi.org/10.1021/ef300913t.

Kassa, A.M., Gasda, S.E., Kumar, K., Radu, F.A., 2020. Impact of time-dependent wettability alteration on the dynamics of capillary pressure. Adv. Water Resour. 142 https://doi.org/10.1016/j.advwatres.2020.103631.

Kim, Y., Wan, J., Kneafsey, T.J., Tokunaga, T.K., 2012. Dewetting of silica surfaces upon reactions with supercritical $CO_2$and brine: pore-scale studies in micromodels. Environ. Sci. Technol. 46, 4228–4235. https://doi.org/10.1021/es204096w.

Kjosavik, A., Ringen, J.K., Skjaeveland, S.M., 2002. Relative permeability correlation for mixed-wet reservoirs. SPE J. 7, 49–58. https://doi.org/10.2118/77328-PA, 01.

Kovscek, A.R., Wong, H., Radke, C.J., 1993. A pore-level scenario for the development of mixed wettability in oil reservoirs. AIChE J. 39 https://doi.org/10.1002/aic.690390616, 1072–1085.

Landry, C.J., Karpyn, Z.T., Ayala, O., 2014. Relative permeability of homogenous-wet and mixed-wet porous media as determined by pore-scale lattice Boltzmann modeling. Water Resour. Res. 50, 3672–3689. https://doi.org/10.1002/2013WR015148.

Lashgari, H.R., Xu, Y., Sepehrnoori, K., 2016. Modelling dynamic wettability alteration effect based on contact angle. In: SPE Improved Oil Recovery Conference. SPE, pp. 1–17. https://doi.org/10.2118/179665-MS.

Li, K., Horne, R.N., 2006. Comparison of methods to calculate relative permeability from capillary pressure in consolidated water-wet porous media. Water Resour. Res. 42 (1–9).

Lomeland, F., Ebeltoft, E., Hammervold, T.W., 2005. A new versatile relative permeability correlation. In: International Symposium of the Society of Core Analysts. Society of Core Analysts.

Ma, S., Mason, G., Morrow, N.R., 1996. Effect of contact angle on drainage and imbibition in regular polygonal tubes. Colloid. Surface. 117, 273–291. https://doi.org/10.1016/0927-7757(96)03702-8.

Morrow, N.R., 1970. Physics and thermodynamics of capillary action in porous media. Ind. Eng. Chem. 62, 32–56. https://doi.org/10.1021/ie50726a006.

Morton III, S.A., Keffer, D.J., Counce, R.M., DePaoli, D.W., 2005. Behavior of oil droplets on an electrified solid metal surface immersed in ionic surfactant solutions. Langmuir 21, 1758–1765. https://doi.org/10.1021/la0480235.

Pentland, C.H., El-Maghraby, R., Iglauer, S., Blunt, M.J., 2011. Measurements of the capillary trapping of super-critical carbon dioxide in berea sandstone. Geophys. Res. Lett. 38 https://doi.org/10.1029/2011GL046683.

Plug, W.J., Bruining, J., 2007. Capillary pressure for the sand-CO_2-water system under various pressure conditions. application to CO_2sequestration. Adv. Water Resour. 30 (11), 2339–2353. https://doi.org/10.1016/j.advwatres.2007.05.010.

Powers, S.E., Anckner, W.H., Seacord, T.F., 1996. Wettability of napl-contaminated sands. J. Environ. Eng. 122, 889–896.

Salathiel, R.A., 1973. Oil recovery by surface film drainage in mixed-wettability rocks. J. Petrol. Technol. 25, 1216–1224. https://doi.org/10.2118/4104-PA.
Saraji, S., Goual, L., Piri, M., Plancher, H., 2013. Wettability of scCO$_2$/water/quartz systems: simultaneous measurement of contact angle and interfacial tension at reservoir conditions. Langmuir 1–39. https://doi.org/10.1021/la3050863.
Sedaghat, M.H., Azizmohammadi, S., 2019. Dynamic wettability alteration in naturally fractured rocks. Comput. Geosci. 1–11. https://doi.org/10.1007/s10596-019-09843-6.
Spiteri, E.J., Juanes, R., Blunt, M.J., Orr, F.M., 2008. A new model of trapping and relative permeability hysteresis for all wettability characteristics. SPE J. 13, 277–288. https://doi.org/10.2118/96448-PA, 03.
Tokunaga, T.K., Jiamin, W., 2013. Capillary pressure and mineral wettability influences on reservoir CO$_2$capacity. Rev. Mineral. Geochem. 77 (1), 481–503. https://doi.org/10.2138/rmg.2013.77.14.
Tokunaga, T.K., Wan, J., Jung, J., Kim, T.W., Kim, Y., Dong, W., 2013. Capillary pressure and saturation relations for supercritical CO$_2$and brine in sand: high-pressure p_c (s_w) controller/meter measurements and capillary scaling predictions. Water Resour. Res. 49, 4566–4579. https://doi.org/10.1021/acs.est.5b00826.
Treiber, L.E., Archer, D.L., Owens, W.W., 1972. A laboratory evaluation of the wettability of fifty oil-producing reservoirs. SPE J. 12, 531–540. https://doi.org/10.2118/3526-PA.
van Dijke, M.I.J., Sorbie, K.S., 2006. Existence of fluid layers in the corners of a capillary with non-uniform wettability. J. Colloid Interface Sci. 293, 455–463. https://doi.org/10.1016/j.jcis.2005.06.059, 02.
van Genuchten, M.T., 1980. A closed-form equation for predicting the hydraulic conductivity of unsaturated soils. Soil Sci. Soc. Am. J. 44, 892–898.
Vives, M., Chang, Y., Mohanty, K., 1999. Effect of wettability on adverse-mobility immiscible floods. SPE J. 4, 260–267, 03.
Wang, S., Tokunaga, T.K., 2015. Capillary pressuresaturation relations for supercritical CO$_2$and brine in limestone/dolomite sands: implications for geologic carbon sequestration in carbonate reservoirs. Environ. Sci. Technol. 49, 72087217. https://doi.org/10.1021/acs.est.5b00826.
Wang, S., Edwards, I.M., Clarens, A.F., 2013. Wettability phenomena at the CO$_2$-brine-mineral interface: implications for geologic carbon sequestration. Environ. Sci. Technol. 47, 234–241. https://doi.org/10.1021/es301297z, 01.
Wang, S., Tokunaga, T.K., Wan, J., Dong, W., Kim, Y., 2016. Capillary pressure-saturation relations in quartz and carbonate sands: limitations for correlating capillary and wettability influences on air, oil, and supercritical CO$_2$trapping. Water Resour. Res. 52, 6671–6690. https://doi.org/10.1002/2016WR018816.
Washburn, E., 1921. The dynamics of capillary flow. Phys. Rev. 7, 273–283.
Xu, W.S., Luo, P.Y., Sun, L., Lin, N., 2016. A prediction model of the capillary pressure j–function. PloS One 11, 1–9. https://doi.org/10.1371/journal.pone.0162123, 09.
Yang, D.D., Gu, Y.G., Tontiwachwuthikul, P., 2008. Wettability determination of the reservoir brine-reservoir rock system with dissolution of CO$_2$at high pressures and elevated temperatures. Energy Fuels 22, 504–509. https://doi.org/10.1021/ef700383x, 01.
Yu, L., Kleppe, H., Kaarstad, T., veland, S. M. Skjæ, 2008. Modelling of wettability alteration processes in carbonate oil reservoirs. Netw. Heterogeneous Media 3, 149–183. https://doi.org/10.2118/174555-PA.

Paper 5.1.3

Implicit linearization scheme for nonstandard two-phase flow in porous media

A. M. Kassa, K. Kumar, S. E. Gasda, and F. A. Radu

C

In International Journal for Numerical Methods in Fluids, volume 93,pp 445-46, 2020 DOI: 10.1002/fld.4891

Received: 30 September 2019 | Revised: 22 May 2020 | Accepted: 6 July 2020

DOI: 10.1002/fld.4891

RESEARCH ARTICLE

WILEY

Implicit linearization scheme for nonstandard two-phase flow in porous media

Abay Molla Kassa[1,2] | **Kundan Kumar**[2] | **Sarah E. Gasda**[1] | **Florin A. Radu**[2]

[1]Computational Geoscience and Modeling, NORCE Norwegian Research Centre AS, Bergen, Norway

[2]Applied Mathematics, University of Bergen, Bergen, Norway

Correspondence
Abay M. Kassa, Computational Geoscience and Modeling, NORCE Norwegian Research Center AS Nygårdsgaten 112, Bergen, Norway.
Email: abka@norceresearch.no

Funding information
Norges Forskningsråd, Grant/Award Number: ES557814-100833

Summary

In this article, we consider a nonlocal (in time) two-phase flow model. The nonlocality is introduced through the wettability alteration induced dynamic capillary pressure function. We present a monotone fixed-point iterative linearization scheme for the resulting nonstandard model. The scheme treats the dynamic capillary pressure functions semiimplicitly and introduces an L-scheme type stabilization term in the pressure as well as the transport equations. We prove the convergence of the proposed scheme theoretically under physically acceptable assumptions, and verify the theoretical analysis with numerical simulations. The scheme is implemented and tested for a variety of reservoir heterogeneities in addition to the dynamic change of the capillary pressure function. The proposed scheme satisfies the predefined stopping criterion within a few number of iterations. We also compared the performance of the proposed scheme against the iterative implicit pressure explicit saturation scheme.

KEYWORDS

dynamic capillary pressure, iterative coupling, linearization, porous media, two-phase flow

1 | INTRODUCTION

Unsaturated groundwater flow, enhanced oil recovery, and subsurface carbon dioxide (CO_2) storage[1-5] are typical applications of multiphase porous media flow with high societal relevance. Numerical simulations including mathematical modeling and numerical methods have been applied to understand such flow processes. The governing mathematical models are highly nonlinear and possibly degenerate systems of partial differential equations. Usually, the nonlinearities are introduced through constitutive models such as relative permeabilities—and capillary pressure—saturation relations. We describe these relations by either van Genuchten[6] or Brooks and Corey[3,7] parametrizations. These parameterizations are only suited for rock surfaces that experience a static and uniform wetting property.

In this article, we focus on the two-phase flow that considers dynamic pore-scale wettability alteration (WA) processes. WA mechanisms have been exploited in the petroleum industry, where optimal wetting conditions in the reservoir are obtained through a variety of means that include chemical treatment, foams, surfactants, and low-salinity water flooding.[8-13] The WA processes are assumed to be instantaneous in the above studies. Here, rather, we considered exposure time-dependent WA mechanisms. In our previous work,[14] we upscaled time-dependent WA processes to Darcy-scale phenomenon, and we have developed an interpolation-based dynamic capillary pressure model. The proposed model is (macroscale) fluid history and time-dependent (see Section 2.2 and Reference 14 for the details) in addition to the current

wetting phase saturation. This implies that a nonlocal capillary diffusion term in time is introduced in a two-phase flow model. These all impose an additional complexity onto the standard two-phase porous media flow model.

Due to the nonlinearity and dynamic heterogeneity of the designed model, it is impossible to derive analytic solutions. As a consequence, a numerical approach is the only option to predict such flow dynamics. However, developing efficient algorithms for finding numerical solutions is also a challenge in itself even for standard models.[15] Besides the nonlinearity and heterogeneity of the designed model, long-term temporal dynamics adds an extra difficulty for proposing a reliable numerical model. Implicit discretization in time has been employed to handle long-term subsurface evolution as it allows large time step sizes. Newton-type methods are usually applied to solve the resulting nonlinear system of equations. These approaches are second-order convergent. However, this order of convergence comes at a price of a costly computation of the Jacobian of a system at each time step.[16-19] In addition, these methods are only locally convergent.[19,20] However, the Newton method can be improved by line search strategies as, for example, Armijo's rule.

The other alternative approach is the splitting and then coupling (splitting-coupling) scheme. It splits the entire system into subsystems. The decomposed subproblems are then solved sequentially and are coupled by data exchanges at each time step. The implicit pressure explicit saturation (IMPES) scheme is a widely used splitting-coupling approach to model two-phase flow and component transport processes.[5,17-22] IMPES solves the pressure equation implicitly and updates the saturation explicitly. This approach eliminates the nonlinear terms in the pressure and saturation equations by evaluating them at saturation and fluid properties up-winded from the previous time step. As a consequence, the scheme is conditionally stable, and hence it requires a sufficiently small time step size to approximate the solution.

Several techniques can be implemented to improve the IMPES approach. A very straightforward approach imposes a large time step for the pressure and then subdivides the time step size for the transport equation.[17,22] This approach relies on the assumption that the reservoir pressure changes slowly in time compared with saturation evolution. The other approach solves the transport equation implicitly using a Newton method while the pressure is treated in the same way as the classical IMPES.[23,24] In Kou and Sun,[20] the capillary pressure function in the pressure equation is approximated by a linear function. This helps to couple the pressure and saturation equations at the current time step. However, the scheme involves the calculation of matrix inverse and multiple numbers of matrix multiplications, which greatly increases the computational cost of the scheme. Furthermore, the transport equation is still solved explicitly in time, and the scheme is reduced to the classical IMPES when the capillary pressure is neglected.

Iterative coupling techniques are also applied to improve the classical IMPES scheme. For instance, in Reference 21 an iteration between the pressure and saturation equation is introduced. This iterative scheme is based on their previous work.[20] Radu et al,[19] have proposed a fixed-point iterative scheme for two-phase flow model (in global pressure formulation).

Recently, Kvashchuk and Radu,[18] have proposed an iterative linearization scheme for two-phase flow (in average pressure formulation) following IMPES. The scheme approximates the capillary pressure function by applying a chain rule and evaluating the nonlinear terms at the previous iteration. This approximates the transport equation semiimplicitly. However, the pressure equation was evaluated at the previous iteration saturation profile. This implies that the scheme lacks a coupling term at the current time step. As a consequence, the scheme might be challenged by dynamic capillary pressure forces that change the saturation distributions in a very short time.

In this article, we propose and analyse an iterative linearization scheme for the designed nonstandard model above based on an iterative IMPES approach, typically we followed the work of Kvashchuk and Radu.[18] We discretize the dynamic capillary pressure functions semiimplicitly in time, where the gradient of the dynamic capillary pressure function (in the pressure and saturation equations) is reformulated by applying the chain rule (see Equation (14) in Section 3.2). We then introduce an iteration step and evaluate the nonlinear terms at the previous iteration. We further introduce an L-scheme type[19,25] stabilization term in the pressure and transport equations. We prove the convergence and robustness of the proposed scheme under natural assumptions. The convergence proof shows that the linearization technique and the introduced stabilization terms allowed the scheme to take a large time step size. By contrast to the classical Newton method, the proposed scheme can be seen as an inexact Newton method which has the advantage of not computing the Jacobian of the system. However, this article is not intended to compare the proposed scheme with the existing linearization schemes including the Newton method. Our colleagues[25-27] have done comparison studies on the performance of linearization techniques, and concluded that the fixed-point methods are slower but robust than the Newton method.

This article is organized as follows. Section 2 describes the mathematical model of nonstandard immiscible incompressible two-phase flow in porous media. In Section 3, we introduce a linearization scheme for the resulting model, and prove the convergence of the proposed scheme. We further discuss the choice of a relaxation factor in this section. Numerical simulations in 2D and 3D models are presented in Section 4. This section shows the performance of the proposed scheme and compares it with iterative IMPES. The article ends with a conclusive remark in Section 5.

2 | NONLOCAL TWO-PHASE FLOW MODEL

Let Ω be a bounded permeable domain in $\mathbb{R}^d$, $d = 1, 2$, or 3, having a Lipschitz continuous boundary $\partial\Omega$ and let $t \in [0, T]$ be the life time of the processes. The two-phase flow in such domain is governed by Darcy's law and mass balance equations for each phase.[5] For each phase $\alpha \in \{w, o\}$, where w, o stand for wetting and nonwetting fluids, respectively, the Darcy flux $\mathbf{u}_\alpha : \Omega \times [0, \mathrm{T}] \to \mathbb{R}^d$ is given by

$$\mathbf{u}_\alpha = -\lambda_\alpha \left(\nabla P_\alpha - \rho_\alpha \mathbf{g} \nabla z\right), \tag{1}$$

where $\lambda_\alpha : \Omega \times [0, \mathrm{T}] \to \mathbb{R}$ is phase α mobility, $\rho_\alpha : \Omega \times [0, \mathrm{T}] \to \mathbb{R}$ is phase density that controls the buoyancy force, and $\mathbf{g}$ is the gravitational vector. The phase mobility is defined as $\lambda_\alpha = \frac{\mathbb{K} k_{r\alpha}}{\mu_\alpha}$, where $\mathbb{K} : \Omega \to \mathbb{R}^{d \times d}$ is the absolute permeability of the rock, $k_{r\alpha}$ is phase α relative permeability, and μ_α is phase α viscosity.

For each phase $\alpha \in \{w, o\}$, the balance of mass for the incompressible immiscible fluids yield the transport equations,

$$\phi \rho_\alpha \partial_t S_\alpha + \rho_\alpha \nabla \cdot \mathbf{u}_\alpha = f_\alpha, \text{ in } \Omega, \tag{2}$$

where ϕ is the porosity of the medium Ω, and f_α is source or sink term in each phase. From model (1) and (2), we obtained two equations with four unknown variables. To close the system the following constraints must also be satisfied:

$$0 \le S_w, S_o \le 1, \; S_w + S_o = 1, \text{ and } P_o - P_w = P_c(S_w), \tag{3}$$

where P_c is the capillary pressure that relates the phase saturation to the phase pressures difference. Equations (1) to (3) with appropriate initial and boundary conditions are used to describe two-phase flow dynamics in a porous medium.

2.1 | Model reformulation

Since we are dealing with incompressible fluids and matrix, we can sum up the mass balance models in Equation (2) to get the pressure equation,

$$-\nabla \cdot (\lambda_{\text{tot}} \nabla P_o - \lambda_w \nabla P_c - (\lambda_w \rho_w + \lambda_n \rho_w) g \nabla z) = \mathbf{f}_p + f_s \quad \text{in } \Omega, \tag{4}$$

where $\lambda_{\text{tot}} = \lambda_w + \lambda_o$ is the total mobility. In Equation (4), we have one equation and two unknowns, namely, P_o and S_w. As a consequence, the transport equation for the wetting or nonwetting phase saturation should be coupled with Equation (4) in order to close the system. Therefore, we get a system of two equations with two unknowns,

$$-\nabla \cdot (\lambda_{\text{tot}} \nabla P_o - \lambda_w \nabla P_c - (\lambda_w \rho_w + \lambda_n \rho_n) g \nabla z) = f_t \quad \text{in } \Omega, \tag{5a}$$

$$\phi \partial_t S_w - \nabla \cdot \lambda_w (\nabla P_o - \nabla P_c - \rho_w g \nabla z) = f_s \text{ in } \Omega, \tag{5b}$$

where, $f_t = f_w + f_n$ is the total source. In order to solve the two Equations (5a) and (5b), one needs to impose appropriate initial and boundary conditions, such as Neumann and Dirichlet conditions. Thus, we assume that the boundary of the system is divided into disjoint sets such that $\partial\Omega = \Gamma_D \cup \Gamma_N$. We denote by ν the outward unit vector normal to $\partial\Omega$, and set

$$P_o(\cdot, 0) = P_o^0(\cdot), \quad S_w(\cdot, 0) = S_w^0(\cdot), \quad \text{in } \Omega, \tag{6a}$$

$$P_o = P_{o,D}, \quad S_w = S_{w,D}, \quad \text{on } \Gamma_D \times (0, T], \tag{6b}$$

$$\mathbf{u}_\alpha = J_\alpha, \quad \text{on } \Gamma_N \times (0, T], \tag{6c}$$

where $J_\alpha \in \mathbb{R}^d$ is phase inflow rate. In order to make the model uniquely determined, it is required that $\Gamma_d \neq \emptyset$.

2.2 | Relative permeability and dynamic capillary pressure functions

Commonly, the Brooks and Corey[7] and van Genuchten[6] models are used to represent the capillary pressure and relative permeabilities for equilibrium system. For nonequilibrium systems, explicit time-dependency of P_c-S_w curves have been developed (eg, see References 28,29) to capture changes in capillary pressure induced by dynamic flow conditions. These models are developed under a static wettability condition.

In this article, we consider an extended capillary pressure model that captures the dynamic change of rock wettability at pore-scale. Kassa et al[14] have introduced the dynamic term as an interpolation between the end wetting state curves. This can be described mathematically as follows,

$$P_c = (1 - \omega(\cdot))P_c^{ww} + \omega(\cdot)P_c^{ow}, \tag{7}$$

where, P_c^{ww} and P_c^{ow} are end wetting (respectively, the water-wet and oil-wet) capillary pressure functions. Here, the water-wet and oil-wet capillary pressure functions are represented, respectively, with large and small (possibly negative) entry pressures. The dynamic coefficient $\omega(\cdot)$ is designed to upscale the dynamics of (pore-scale) time-dependent WA mechanism. In Reference 14 a fluid-fluid contact angle (CA) change model (that changes the wettability from an arbitrary initial wetting state to the final wetting state) was introduced at the pore-level. In Kassa et al,[14] two approaches were considered, namely, *uniform* and *nonuniform WA*. The first assumes all pores in the REV has been altered identically through exposure time to the WA agent, whereas the nonuniform WA case considers a CA change in a pore only if that particular pore is exposed to the WA agent. These CA change models were coupled with a bundle-of-tubes model to simulate WA induced capillary pressure curves. The obtained curves and the interpolation model were combined to propose the dynamic coefficient ω. According to the results in Reference 14, ω can be represented as:

$$\omega(S_w, t) = \begin{cases} \frac{\beta_1 \chi}{\beta_1 \chi + 1}, & \text{for uniform WA,} \\ \frac{\beta_2 S_w \chi}{\beta_2 S_w \chi + 1}, & \text{for nonuniform WA,} \end{cases} \tag{8}$$

where β_1 and β_2 are fitting parameters that have a clear relation with the pore-scale CA change model parameter (see the details in Reference 14).

The variable χ is defined as

$$\chi := \frac{1}{T}\int_0^t (1 - S_w)d\tau, \tag{9}$$

where T is a predetermined scaling factor, and we recommend to choose T such that $\chi \in [0, 1]$, that is, T should be above or equivalent to the life time of the exposure period. The variable χ is used to measure the averaged exposure time of the REV to the WA agent, and it is an increasing function of exposure time. Thus, the models (7) and (8) describe time-dependent WA induced dynamic capillary pressure model. The change of the capillary pressure in time continues even for constant water saturation. However, χ keeps constant for pores that are fully occupied with water, that is, $S_w = 1$. In this case, the capillary pressure is only dependent on the current water saturation path. This may lead to a discontinuity of the capillary pressure function at the interface of grid blocks. Thus, the continuity of capillary pressure results in a saturation discontinuity.

For end wetting (water-wet and oil-wet) conditions, we considered two consistent sets of capillary pressure functions. Qualitatively, these curves represent either water-wet (*ww*) or oil-wet (*ow*) conditions. We adopted the van Genuchten constitutive model for these conditions and can be read as,

$$P_c^{ww} = P_e^w(S_w^{-\frac{1}{m_w}} - 1)^{\frac{1}{n_w}}, \text{ and } P_c^{ow} = P_e^o(S_w^{-\frac{1}{m_o}} - 1)^{\frac{1}{n_o}}, \tag{10}$$

where P_e^α is phase α wetting condition entry pressure, m_α is pore volume distribution of the porous domain for the α's wetting condition and can be related to n_α as $m_\alpha = 1/n_\alpha$. In this study, only the standard van Genuchten relative permeability functions are considered to describe the relative movement of fluids,

$$k_{r\alpha}^{ww} = \begin{cases} \sqrt{1-S_w}\left(1-S_w^{\frac{1}{m_w}}\right)^{2m_w}, & \alpha = o, \\ \sqrt{S_w}\left(1-\left(1-S_w^{\frac{1}{m_w}}\right)^{m_w}\right)^2, & \alpha = w. \end{cases} \tag{11}$$

Coupling the relations $k_{r\alpha}^{ww}$-S_w and P_c-S_w-χ into the flow model (5a) and (5b) will give nonstandard dynamic two-phase flow model in a porous medium. The goal of this study is to propose a stable and flexible scheme that handles such dynamics efficiently for simulations that consider long-term time evolution.

3 | DISCRETIZATION, LINEARIZATION, AND ITERATIVE COUPLING TECHNIQUE

Let the total simulation time interval $[0,T]$ be divided into N time steps in such a way that $0 = t^0 < t^1 < \ldots < t^N = T$, and define the time step $\delta t = T/N$, as well as $t^n = n\delta t,\ n \in \{1, 2, \ldots, N\}$.

The backward Euler method is applied to discretize the resulting nonlocal two-phase flow model in time and the semidiscretized model can be read as

$$-\nabla \cdot \left(\lambda_{\text{tot}}(S_w^{n+1})\nabla P_o^{n+1} - \lambda_w(S_w^{n+1})\nabla P_c(\chi^{n+1}, S_w^{n+1})\right) = f_t^n, \tag{12a}$$

$$\phi\frac{S_w^{n+1} - S_w^n}{\delta t} - \nabla \cdot \left(\lambda_w(S_w^{n+1})(\nabla P_o^{n+1} - \nabla P_c(\chi^{n+1}, s_w^{n+1}))\right) = f_s^n. \tag{12b}$$

The superscripts $(n+1)$ and n represent the current and previous time steps, respectively. Above, we omitted the gravity term and the analysis will continue in this form for the sake of clarity and brevity of the presentation.

The above system is fully coupled and challenging to solve directly because of its nonlinearity. Due to the nonlinearity, iterative linearization and sequential coupling methods such as iterative IMPES are needed to solve such systems.

3.1 | Iterative IMPES

The iterative IMPES linearizes the given two-phase flow problem by evaluating the nonlinear terms from the previous iteration step.[21] Thus, the nonlinear model (12a) and (12b) can be reduced to

$$-\nabla \cdot \left(\lambda_{\text{tot}}(S_w^{n+1,i})\nabla P_o^{n+1,i+1} - \lambda_w(S_w^{n+1})\nabla P_c(\chi^{n+1,i}, S_w^{n+1,i})\right) = f_t^n, \tag{13a}$$

$$\phi\frac{S_w^{n+1,i+1} - S_w^n}{\delta t} - \nabla \cdot \left(\lambda_w(S_w^{n+1,i})(\nabla P_o^{n+1,i+1} - \nabla P_c(\chi^{n+1,i}, S_w^{n+1,i}))\right) = f_s^n. \tag{13b}$$

The iterative IMPES solver starts with $S_w^{n+1,i} = S_w^n$ and thus, the system above is linear and decoupled. Usually the pressure equation (13a) is solved for $P_o^{n+1,i+1}$ first. The computed pressure and the previous iteration saturation profile are used to update the current iteration saturation profile explicitly from Equation (13b). The iteration will continue until the convergence criterion has been satisfied.

3.2 | Semiimplicit time discretization

The iterative IMPES formulation above splits the pressure and saturation equations in each iteration step. Hence, the approach has missed the inherent coupled nature of the original problem (12a) and (12b). This may cause instability on the convergence of the method in particular for long-term reservoir processes.

In this article, we propose a scheme that couples the pressure, and saturation equations at the $(n+1)$th time step in addition to the current iteration step. The scheme treats the dynamic capillary pressure function (in the pressure and saturation equations) semiimplicitly in time. We then introduce a monotone fixed-point iteration.[18,19,21,25,30] The development of the scheme is discussed below.

The scheme starts with approximating the capillary pressure function at the current time step (in the pressure (12a) and saturation (12b) equations) by applying chain rule and semibackward Euler discretization in time. The resulting approximation is read as

$$\nabla P_c^{n+1} \approx \frac{\partial P_c^n}{\partial S_w}\nabla S_w^{n+1} + \frac{\partial P_c^n}{\partial \chi}\nabla \chi^{n+1}. \tag{14}$$

The obtained approximate capillary pressure is substituted back to the two-phase flow model to give the following linear system (we call this linearization technique *pseudo-monolithic* scheme),

$$-\nabla\cdot\left(\lambda_{\text{tot}}^n \nabla P_o^{n+1} - \lambda_w^n\left(\frac{\partial P_c^n}{\partial S_w}\nabla S_w^{n+1} + \frac{\partial P_c^n}{\partial \chi}\nabla \chi^{n+1}\right)\right) = f_t^n, \tag{15a}$$

$$\phi\frac{S_w^{n+1}-S_w^n}{\delta t} - \nabla\cdot\left(\lambda_w^n\left(\nabla P_o^{n+1} - \left(\frac{\partial P_c^n}{\partial S_w}\nabla S_w^{n+1} + \frac{\partial P_c^n}{\partial \chi}\nabla \chi^{n+1}\right)\right)\right) = f_s^n. \tag{15b}$$

The above approach (15a) and (15b) couples the pressure and saturation equations at the current time step weakly. But, importantly, the saturation and pressure state variables communicate each other at the same degree of decision making level. Recall that the variable χ is also a function of saturation, and thus, the number of equations and unknowns are compatible.

Then stability and accuracy of the pseudo-monolithic scheme (15a) and (15b) is improved further by introducing outer iteration steps (ie, $(i+1)$ and i), and evaluating the nonlinear terms at the current time step (n+1 instead of n) but at the previous iteration i. We controlled the convergence of the proposed fixed-point iteration by adding an L-scheme type[19,21,25] stabilization term. We named this linearization technique as *iterative pseudo-monolithic* scheme, and read as

$$-\nabla\cdot\left(\lambda_{\text{tot}}^{n+1,i}\nabla P_o^{n+1,i+1} - \lambda_w^{n+1,i}\left(\frac{\partial P_c^{n+1,i}}{\partial S_w}\nabla \tilde{S}_w^{n+1,i+1} + \frac{\partial P_c^{n+1,i}}{\partial \chi}\nabla \tilde{\chi}^{n+1,i+1}\right)\right) = f_t^n, \tag{16a}$$

$$\phi\frac{\tilde{S}_w^{n+1,i+1}-S_w^n}{\delta t} - \nabla\cdot\left(\lambda_w^{n+1,i}\left(\nabla P_o^{n+1,i} - \left(\frac{\partial P_c^{n+1,i}}{\partial S_w}\nabla \tilde{S}_w^{n+1,i+1} + \frac{\partial P_c^{n+1,i}}{\partial \chi}\nabla \tilde{\chi}^{n+1,i+1}\right)\right)\right) = f_s^n, \tag{16b}$$

$$S_w^{n+1,i+1} = (1-L^{i+1})S_w^{n+1,i} + L^{i+1}\tilde{S}_w^{n+1,i+1}, \tag{16c}$$

$$\chi^{n+1,i+1} = (1-L^{i+1})\chi^{n+1,i} + L^{i+1}\tilde{\chi}^{n+1,i+1}, \tag{16d}$$

where $L^{i+1}\in(0,1]$ is a stabilization constant that has an important role on the convergence of the proposed scheme. The choice of L^{i+1} in each iteration will be discussed later in this article. Equations (16c) and (16d) can be substituted into Equations (16a) and (16b) directly during the solution processes. Here, we note that $S_w^{n+1,i+1}$ and $\chi^{n+1,i+1}$ are used as a previous iteration values for the next iteration and we set $S_w^{n+1,0} = S_w^{n+1}$ for the first iteration step.

Remark 1. The pseudo-monolithic and the iterative pseudo-monolithic schemes reduced to IMPES and iterative L-scheme, respectively, if the capillary pressure is neglected.

Below, we demonstrate the convergence of the iterative pseudo-monolithic scheme, and in Section 4, we compare its performance against the pseudo-monolithic scheme (15a) and (15b) and the iterative IMPES.

3.2.1 | Convergence analysis of the iterative pseudo-monolithic scheme

We denote by $L_2(\Omega)$ the space of real valued square integrable functions, and by $H^1(\Omega)$ its subspace containing functions having also the first-order derivatives in $L_2(\Omega)$. Let $H_0^1(\Omega)$ be the space of functions in $H^1(\Omega)$ which vanish on the boundary. Furthermore, we denote by $\langle\cdot,\cdot\rangle$ the inner product on $L_2(\Omega)$, and by $\|\cdot\|$ the norm of $L_2(\Omega)$. L_f stays for the Lipschitz constant of a Lipschitz continuous function $f(\cdot)$.

Let T_h is a regular decomposition of Ω, which decomposes Ω into closed d-simplices; h stands for the mesh diameter. Here, we assume $\Omega = \cup_{\mathcal{T}\in\mathcal{T}_h}\mathcal{T}$. The Galerkin finite element space is given by

$$\mathbf{V}_h := \{v_h \in H_0^1(\Omega) | \mathbf{v}_h|_{\mathcal{T}} \in P_1(\mathcal{T}), \mathcal{T} \in \mathcal{T}_h\}, \tag{17}$$

where $P_1(\mathcal{T})$ denotes the space of linear polynomials on any simplex T.

We use the definition of spaces and notations above to write the variational form of Equations (12a) to (12b) which finds $P_o^{n+1}, S_w^{n+1} \in \mathbf{V}_h$ for a given S_w^n such that the following holds,

$$\left\langle \lambda_{\text{tot}}^{n+1} \nabla P_o^{n+1} - \lambda_w^{n+1} \left(\frac{\partial P_c^{n+1}}{\partial S_w} \nabla S_w^{n+1} + \frac{\partial P_c^{n+1}}{\partial \chi} \nabla \chi^{n+1} \right), \nabla v_h \right\rangle = \langle f_t^n, v_h \rangle \tag{18a}$$

$$\langle \phi S_w^{n+1} - \phi S_w^{n+1}, v_h \rangle + \delta t \left\langle \lambda_w^{n+1} \nabla P_o^{n+1} - \lambda_w^{n+1} \left(\frac{\partial P_c^{n+1}}{\partial S_w} \nabla S_w^{n+1} + \frac{\partial P_c^{n+1}}{\partial \chi} \nabla \chi^{n+1} \right), \nabla v_h \right\rangle = \langle f_s^n, \mathbf{v}_h \rangle, \tag{18b}$$

for all $v_h \in \mathbf{V}_h$. Similarly, we can also write the variational form of the iterative pseudo-monolithic method (16a) and (16b) that find $P_o^{n+1,i+1}, S_w^{n+1,i+1} \in \mathbf{V}_h$ for given S_w^n, $S_w^{n+1,i}$ such that

$$\left\langle \lambda_{\text{tot}}^{n+1,i} \nabla P_o^{n+1,i+1} - \lambda_w^{n+1,i} \left(\frac{\partial P_c^{n+1,i}}{\partial S_w} \nabla \tilde{S}_w^{n+1,i+1} + \frac{\partial P_c^{n+1,i}}{\partial \chi} \nabla \tilde{\chi}^{n+1,i+1} \right), \nabla v_h \right\rangle = \langle f_t^n, v_h \rangle \tag{19a}$$

$$\langle \phi \tilde{S}_w^{n+1,i+1} - \phi S_w^n, v_h \rangle + \delta t \left\langle \lambda_w^{n+1,i} \left(\nabla P_o^{n+1,i+1} - \left(\frac{\partial P_c^{n+1,i}}{\partial S_w} \nabla \tilde{S}_w^{n+1,i+1} + \frac{\partial P_c^{n+1,i}}{\partial \chi} \nabla \tilde{\chi}^{n+1,i+1} \right) \right), \nabla v_h \right\rangle = \langle f_s^n, v_h \rangle, \tag{19b}$$

holds for all $v_h \in \mathbf{V}_h$. The aim is to show that the linearized model (19a) and (19b) converges to the nonlinear problem (18a) and (18b) within few outer iteration steps in each time step.

The convergence analysis of the scheme is proved theoretically by assuming that the continuous model has a solution. Furthermore, the following assumptions on the coefficient functions and the discrete solutions are defining the framework in which we can prove the convergence of the proposed scheme.

A1: The mobilities satisfy the Lipschitz continuity condition in the wetting phase saturation, that is, there exist constants L_{λ_α} such that

$$\|\lambda_\alpha(S_w) - \lambda_\alpha(\overline{S}_w)\| \le L_{\lambda_\alpha} \|S_w - \overline{S}_w\|, \quad \forall S_w, \overline{S}_w \in [0,1]. \tag{20}$$

This implies that any linear combination of λ_α is also Lipschitz continuous.

A2: The dynamic capillary pressure function P_c, and its partial derivatives $\frac{\partial P_c}{\partial S_w}$ and $\frac{\partial P_c}{\partial \chi}$ are Lipschitz continuous with respect to S_w and χ. This implies, for any $\chi, \overline{\chi}, S_w, \overline{S}_w \in [0,1]$, we can find constants $L_{P_c}^{\chi}, L_{P_c'}^{\chi}, L_{P_c}^{s}$ and $L_{P_c'}^{s}$ such that

$$\begin{aligned} &\|P_c(\chi, S_w) - P_c(\chi, \overline{S}_w)\| \le L_{P_c}^s \|S_w - \overline{S}_w\|, \text{and} \\ &\left\| \frac{\partial P_c(\chi, S_w)}{\partial S_w} - \frac{\partial P_c(\chi, \overline{S}_w)}{\partial S_w} \right\| \le L_{\Phi_c'}^s \|S_w - \overline{S}_w\|, \end{aligned} \tag{21}$$

$$\begin{aligned} &\|P_c(\chi, S_w) - P_c(\overline{\chi}, S_w)\| \le L_{\Phi_c}^{\chi} \|\chi - \overline{\chi}_w\|, \text{ and} \\ &\left\| \frac{\partial P_c(\chi, S_w)}{\partial \chi} - \frac{\partial P_c(\overline{\chi}, S_w)}{\partial \chi} \right\| \le L_{P_c'}^{\chi} \|\chi - \overline{\chi}\|. \end{aligned} \tag{22}$$

Furthermore, we assume that the dynamic capillary pressure $P_c(\chi, S_w)$ is decreasing function, that is, $\frac{\partial P_c(\chi, S_w)}{\partial S_w} < 0$, and $\frac{\partial P_c(\chi, S_w)}{\partial \chi} < 0$

A3: We assumed that the initial wetting phase saturation satisfies $\|\nabla S_w^n\|_\infty \le M_s$ with $\|\cdot\|$ denoting the $L^\infty(\Omega)$-norm. This implies also $\|\nabla S_w^{n+1}\|_\infty \le M_s$ and $\|\nabla P_n^{n+1}\|_\infty \le M_p$.

A4: The total derivative of P_c with respect to S_w is bounded above by zero.

A5: Assume that for any time step $(n+1)$ with $n \ge 0$, there exist a solution for saturation S_w^{n+1} and pressure P_o^{n+1} such that the Equations (18a) to (18b) are satisfied.

From now on, we denote by

$$\mathbf{e}_p^{i+1} = P_o^{n+1,i+1} - P_o^{n+1},\ \mathbf{e}_s^{i+1} = S_w^{n+1} - S_w^{n+1,i+1},\ \tilde{\mathbf{e}}_s^{i+1} = S_w^{n+1} - \tilde{S}_w^{n+1,i+1}, \tag{23}$$

the error at iteration $i+1$. A scheme is convergent if $\|\mathbf{e}_p^{i+1}\| \to 0$, $\|\mathbf{e}_s^{i+1}\| \to 0$ when $i \to \infty$.

Theorem 1. *Assume that the conditions (A1) to (A5) are satisfied. If we choose S_w^n as the initial approximation, $S_w^{n+1,0}$, of the exact solution S_w^{n+1}, there exists a time step size δt^n with mild restriction such that the iteration $S_w^{n+1,i+1}$ and $P_o^{n+1,i+1}$ generated by the scheme (19a) and (19b) converges to S_w^{n+1} and P_o^{n+1}, respectively, in L_2 norm.*

Proof. As in References 18,19,25, we start the analysis by subtracting the linearized pressure equation (19a) from the nonlinear Equation (18a) to obtain:

$$\begin{aligned}\langle \lambda_{\text{tot}}^{n+1}\nabla P_o^{n+1} - \lambda_{\text{tot}}^{n+1,i}\nabla P_o^{n+1,i+1}, \nabla v_h\rangle - \left\langle \lambda_w^{n+1}\frac{\partial P_c^{n+1}}{\partial S_w}\nabla S_w^{n+1} - \lambda_w^{n+1,i}\frac{\partial P_c^{n+1,i}}{\partial S_w}\nabla \tilde{S}_w^{n+1,i+1}, \nabla v_h\right\rangle \\ - \left\langle \lambda_w^{n+1}\frac{\partial P_c^{n+1}}{\partial \chi}\nabla \chi^{n+1} - \lambda_w^{n+1,i}\frac{\partial P_c^{n+1,i}}{\partial \chi}\nabla \tilde{\chi}^{n+1,i+1}, \nabla v_h\right\rangle = 0,\end{aligned} \tag{24}$$

for any $v_h \in V_h$. Applying the Cauchy-Schwartz inequality

$$|\langle u, v\rangle|^2 \le \|u\|^2\|v\|^2, \tag{25}$$

followed by the assumptions (A1) to (A4), and testing with $v_h = \mathbf{e}_p^{i+1}$, we get the following estimate,

$$M_{\lambda_{\text{tot}}}^0\langle \nabla \mathbf{e}_p^{i+1}, \nabla \mathbf{e}_p^{i+1}\rangle \le \gamma_p\|\mathbf{e}_s^i\|\|\nabla \mathbf{e}_p^{i+1}\| + \left\langle \lambda_w^{n+1,i}\left(\frac{\partial P_c^{n+1,i}}{\partial S_w} - \frac{t}{T}\frac{\partial P_c^{n+1,i}}{\partial \chi}\right)\nabla \tilde{\mathbf{e}}_s^{i+1}, \nabla \mathbf{e}_p^{i+1}\right\rangle, \tag{26}$$

where $\gamma_p = L_{\lambda_{\text{tot}}}M_p + L_{\lambda_w}(M_{P_c}^s + M_{P_c}^\chi) + (L_{P_c'}^s + L_{P_c'}^\chi)M_{\lambda_w}$. Applying (A4) once more, we obtain an estimate as follows,

$$\|\nabla \mathbf{e}_p^{i+1}\| \le \frac{\gamma_p}{M_{\lambda_{\text{tot}}}^0}\|\mathbf{e}_s^i\| \tag{27}$$

Similarly, we subtract Equation (19a) from Equation (18b) to get,

$$\begin{aligned}&\frac{\phi}{\delta t}\langle \tilde{\mathbf{e}}_s^{i+1}, v_h\rangle - \left\langle \lambda_w^{n+1}\frac{\partial P_c^{n+1}}{\partial S_w}\nabla S_w^{n+1} - \lambda_w^{n+1,i}\frac{\partial P_c^{n+1,i}}{\partial S_w}\nabla S_w^{n+1} + \lambda_w^{n+1,i}\frac{\partial P_c^{n+1,i}}{\partial S_w}\nabla S_w^{n+1} - \lambda_w^{n+1,i}\frac{\partial P_c^{n+1,i}}{\partial S_w}\nabla \tilde{S}_w^{n+1,i+1}, \nabla v_h\right\rangle \\ &- \left\langle \lambda_w^{n+1}\frac{\partial P_c^{n+1}}{\partial \chi}\nabla \chi^{n+1} - \lambda_w^{n+1,i}\frac{\partial P_c^{n+1,i}}{\partial \chi}\nabla \chi^{n+1} + \lambda_w^{n+1,i}\frac{\partial P_c^{n+1,i}}{\partial \chi}\nabla \chi^{n+1} - \lambda_w^{n+1,i}\frac{\partial P_c^{n+1,i}}{\partial \chi}\nabla \tilde{\chi}^{n+1,i+1}, \nabla v_h\right\rangle \\ &- \left\langle \lambda_w^{n+1,i}\left(\nabla P_o^{n+1,i+1} - \nabla P_o^{n+1}\right), \nabla v_h\right\rangle + \left\langle \left(\lambda_w^{n+1,i} - \lambda_w^{n+1}\right)\nabla P_o^{n+1}, \nabla v_h\right\rangle = 0.\end{aligned} \tag{28}$$

Now by taking the advantage of assumptions (A1) to (A3) and applying the Cauchy-Schwartz inequality with the definition of χ, Equation (28) can be estimated as,

$$\frac{\phi}{\delta t}\|\tilde{\mathbf{e}}_s^{i+1}\| - \left\langle \lambda_w^{n+1,i}\left(\frac{\partial P_c^{n+1,i}}{\partial s_w} - \frac{t}{T}\frac{\partial P_c^{n+1,i}}{\partial \chi}\right)\nabla \tilde{\mathbf{e}}_s^{i+1}, \nabla \tilde{\mathbf{e}}_s^{i+1}\right\rangle \le M_{\lambda_w}\|\nabla \mathbf{e}_p^{i+1}\|\|\nabla \tilde{\mathbf{e}}_s^{i+1}\| + (\gamma_p + L_{\lambda_w}M_p)\|\mathbf{e}_s^i\|\|\nabla \tilde{\mathbf{e}}_s^{i+1}\|, \tag{29}$$

where we choose $v_h = \tilde{\mathbf{e}}_s^{i+1}$ as a test function. At this point, we apply assumptions (A1) and (A4). From assumption (A4), we have that $\frac{\partial P_c^{n+1,i}}{\partial S_w} - \frac{t}{T}\frac{\partial P_c^{n+1,i}}{\partial \chi} < 0$. This implies that there exists a real number $M_{P_c'} > 0$ such that,

$$\max_{S_w,t}\left\{\frac{\partial P_c^{n+1,i}}{\partial S_w} - \frac{t}{T}\frac{\partial P_c^{n+1,i}}{\partial \chi}\right\} = -M_{P_c'}.$$

Considering all these and after some algebraic manipulation, the inequality (29) can be rewritten as

$$\frac{\phi}{\delta t}\|\tilde{\mathbf{e}}_s^{i+1}\|^2 + M_{P_c'}\|\nabla\tilde{\mathbf{e}}_s^{i+1}\|^2 \le M_{\lambda_w}\|\nabla\tilde{\mathbf{e}}_p^{i+1}\|\|\nabla\tilde{\mathbf{e}}_s^{i+1}\| + \gamma_s\|\mathbf{e}_s^i\|\|\nabla\tilde{\mathbf{e}}_s^{i+1}\|. \tag{30}$$

where $\gamma_s = \gamma_p + L_{\lambda_w}M_p$. Substitute the pressure estimate (27) into (30) to give an estimate for the saturation error:

$$\frac{\phi}{\delta t}\|\tilde{\mathbf{e}}_s^{i+1}\|^2 + M_{P_c'}\|\nabla\tilde{\mathbf{e}}_s^{i+1}\|^2 \le \left(\frac{\gamma_p M_{\lambda_w}}{M^0_{\lambda_{\text{tot}}}} + \gamma_s\right)\|\mathbf{e}_s^i\|\|\nabla\tilde{\mathbf{e}}_s^{i+1}\|. \tag{31}$$

Let us define

$$C = \frac{\gamma_p M_{\lambda_w}}{M^0_{\lambda_{\text{tot}}}} + \gamma_s > 0, \tag{32}$$

and apply Young's inequality

$$ab \le \frac{a^2}{2\epsilon} + \frac{\epsilon b^2}{2},$$

for $\epsilon > 0$ to the inequality (31), and choosing the parameter ϵ to be $\epsilon = \frac{C}{M_{P_c'}}$, the estimate (31) is reduced to

$$\|\tilde{\mathbf{e}}_s^{i+1}\|^2 \le \frac{\delta t C^2}{M_{P_c'}\phi}\|\mathbf{e}_s^i\|^2. \tag{33}$$

At this stage, we can substitute the stabilization term from Equation (16c) into Equation (33) to get the following estimate,

$$\left\|\frac{1}{L^{i+1}}\mathbf{e}_s^{i+1} + \left(1 - \frac{1}{L^{i+1}}\right)\mathbf{e}_s^i\right\|^2 \le \frac{\delta t C^2}{M_{P_c'}\phi}\|\mathbf{e}_s^i\|^2. \tag{34}$$

For any choice of $L^{i+1} \in (0,1]$, $1 - \frac{1}{L^{i+1}} \le 0$, and thus, by applying the reverse triangle inequality, we can obtain,

$$\|\mathbf{e}_s^{i+1}\|^2 \le \left(L^{i+1} - 1 + \frac{\delta t C^2}{M_{P_c'}\phi}\right)\|\mathbf{e}_s^i\|^2. \tag{35}$$

Thus, the scheme converges linearly for the designed nonlocal two-phase flow model when

$$\delta t \le \frac{(2 - L^{i+1})M_{P_c'}\phi}{C^2}, \tag{36}$$

is satisfied. ∎

Remark 2. If we choose a small L, convergence of the scheme is guaranteed for large time step. However, the rate of convergence may be slow and thus, we may encounter large number of iterations.

3.2.2 | Choice of the relaxation factor

Above we observed that the choice of the relaxation factor plays an important role on the convergence of the scheme. Here, we introduce a choice strategy for the relaxation factor based on the history of the errors at previous and current iterations.

Following Reference 21, we define the length of the residual of the transport equation at the current iteration by

$$\|R_s^{n+1,i+1}\| = \|\tilde{S}_w^{n+1,i+1} - S_w^{n+1,i}\|. \tag{37}$$

The aim is finding a relaxation factor that makes (37) sufficiently small. However, this problem is highly nonlinear optimization problem and thus, challenging to come up with optimal global solution. As a consequence, we compute and bound the relaxation factor adaptively in each iteration.

To support the convergence of the iterative pseudo-monolithic scheme, the relaxation factor L should be chosen such that the residual defined by (37) is decreasing with each successive iteration, that is,

$$\|R_s^{n+1,i+1}\| \leq \|R_s^{n+1,i}\| \tag{38}$$

From (16c) and (38), there exists a constant L such that,

$$\|S_w^{n+1,i+1} - S_w^{n+1,i}\| \leq L\|S_w^{n+1,i} - S_w^{n+1,i-1}\|. \tag{39}$$

We denote the relaxation factor at the ith iteration step by L^i, and thus the relaxation equation for wetting phase saturation can be rewritten as,

$$S_w^{n+1,i+1} = (1 - L^{i+1})S_w^{n+1,i} + L^{i+1}\tilde{S}_w^{n+1,i+1}, \tag{40}$$

where $L^{i+1} \in (0,1]$. Substituting Equation (40) into Equation (39) and rearranging will give,

$$L^{i+1} \leq L\frac{\|S_w^{n+1,i} - S_w^{n+1,i-1}\|}{\|\tilde{S}_w^{n+1,i+1} - S_w^{n+1,i}\|}. \tag{41}$$

Recall that $L^{i+1} \in (0,1]$ and from Equation (38), and thus the choice of L^{i+1} should satisfy instead,

$$L^{\min} \leq L^{i+1} \leq \min\left\{L^{\max}, L\frac{\|S_w^{n+1,i} - S_w^{n+1,i-1}\|}{\|\tilde{S}_w^{n+1,i+1} - S_w^{n+1,i}\|}\right\}, \tag{42}$$

where $L^{\min}$,$L^{\max} \in (0,1]$ and L are specified a priori.

4 | NUMERICAL RESULTS

In this section, we examine the convergence and accuracy of the iterative pseudo-monolithic scheme presented in this work. Section 4.1 presents a comparison between the pseudo-monolithic (15a) and (15b) scheme and the iterative pseudo-monolithic (16a) to (16d) scheme. We also carry out comparisons between iterative IMPES, and iterative pseudo-monolithic scheme in Section 4.2. All the schemes are implemented in the open source software package MRST.[31] Here, we applied two point flux approximation to discretize the models designed below. However, we recall that we applied a Galerkin finite elements to show the convergence of the scheme theoretically. This is to show that the scheme is independent of space discretization methods.

4.1 | Analytic example

In this subsection, a porous medium flow model is designed by choosing exact solutions

$$S_w^{\text{an}} = 0.65 - tx(1-x)y(1-y),\ P_o^{\text{an}} = tx(1-x)y(1-y) + 0.2 \quad \text{in } (0, T_f) \times \Omega,$$

followed by constructing source terms and boundary conditions. For this particular example, we set $t \in [0,1]$ and $\Omega = (0,1) \times (0,1)$. Furthermore, we consider unit magnitude for rock as well as fluid properties in order to ease the construction of the source terms. We applied van Genuchten relative permeability relations (11) and dynamic capillary pressure

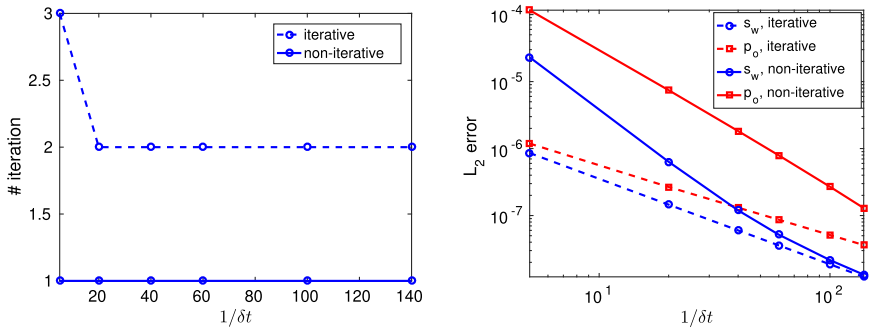

FIGURE 1 Number of iterations, A and L_2 error, B with respect to time step sizes [Colour figure can be viewed at wileyonlinelibrary.com]

model (7) with

$$\omega = \frac{\beta_1 \chi}{\beta_1 \chi + 1},$$

where the parameters are set to be $n_w = n_o = 2,\ P_e^w = 1,\ P_e^o = 0$, and $\beta_1 = 400$.

To evaluate the convergence of the scheme to the exact solution, we have considered a 80×80 regular grid cells with varying time step sizes given below

$$\delta t \in \{1/5,\ 1/20,\ 1/40,\ 1/60,\ 1/100,\ 1/140\}.$$

The outer iteration loop for the iterative pseudo-monolithic scheme is allowed to continue until $\|S_w^{n+1,i+1} - S_w^{n+1,i}\| \leq 1 \times 10^{-6}$ is satisfied. In this test, the relaxation factor choice strategy mentioned in subsection 3.2.2 is applied. Initially, L^1 is computed from (37), where we take $\|S_w^{n+1,0} - S_w^{n+1,-1}\| = 1$ in each time step.

We experimented a convergence test considering the inputs above, and Figure 1A presents the number of iterations of the iterative pseudo-monolithic scheme for different time step sizes. Furthermore, we also plotted the number of iterations of the pseudo-monolithic scheme just as a reference.

Obviously, the proposed pseudo-monolithic scheme exits the iteration steps at the first iteration for all time steps. On the other hand, the proposed iterative pseudo-monolithic scheme converges to the solution within two iterations for all time steps except for the larger time step $\delta t = 0.2$ which needs one extra iteration.

Figure 1B shows the associated L_2 error $\|S_w^{n+1} - S_w^{\text{an}}\|_{L_2(\Omega)}$ for the saturation and pressure profiles. S_w^{an} represents the analytical solution of the saturation. The pseudo-monolithic method approximates the exact solution efficiently. The iterative pseudo-monolithic scheme has improved the accuracy of the pseudo-monolithic scheme as proposed in Section 3. This explains that the efficiency and accuracy of the iterative scheme can be gained with only the cost of a few extra iterations. Note that the number of iterations can be reduced by considering larger stopping criteria for outer iterations without affecting the accuracy.

We have also performed a numerical experiment to analyze the convergence of the proposed iterative method by fixing the time step size δt for a different number of grid cells with

$$h = \{1/10,\ 1/20,\ 1/40,\ 1/60,\ 1/80,\ 1/100\}, \tag{43}$$

where h is the side length of a uniform grid cell. The obtained results are listed in Table 1. The iterative pseudo-monolithic method converges with a maximum iterations of three. This maximum number of iteration was needed for the largest time step size $\delta t = 0.2$. From Table 1, we observe that the number of iterations keeps the same while the grid size varies. This implies that the proposed iterative pseudo-monolithic scheme is not dependent on the mesh size.

1/h	10	20	40	60	80	100
Number of iterations ($\delta t = 0.2$)	3	3	3	3	3	3
Number of iterations ($\delta t = 0.05$)	2	2	2	2	2	2

TABLE 1 The required number of iteration to converge to the solution per time step for different mesh size resolutions

Parameters	Units	Example 1	Example 2
ϕ	[–]	0.2	0.2
μ_w	[cP]	1	1
μ_o	[cP]	0.45	0.45
n_w	[–]	2	2
n_o	[–]	2	2
P_e^w	[bar]	5	5
P_e^o	[bar]	0	0
L	[–]	0.5	0.5
$L^{\max}$	[–]	1	1
β_1	[–]	100	–
β_2	[–]	–	100

TABLE 2 Material properties and model parameters

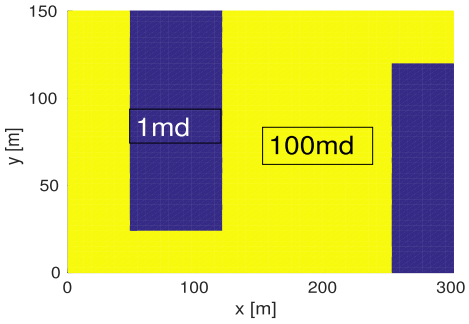

FIGURE 2 Rock permeability model for Example 1. Here "md" stands for milli darcy [Colour figure can be viewed at wileyonlinelibrary.com]

4.2 | Physical test

Above, we considered an academic example and studied the accuracy of the iterative pseudo-monolithic method over the pseudo-monolithic scheme. In the following, we will compare the iterative pseudo-monolithic scheme and IMPES by considering complex porous media geometries with fluid and rock properties given in Table 2. Note that fluid properties and model parameters given in Table 2 are applied for both iterative IMPES and iterative pseudo-monolithic schemes. The outer iteration loop is allowed to continue until $\|S_w^{n+1,i+1} - S_w^{n+1,i}\| \leq 2.5 \times 10^{-5}$ is satisfied. The relaxation factor choice strategy starts with computing L^1 from (37), where we take $\|S_w^{n+1,0} - S_w^{n+1,-1}\| = 1$ in each time step. The relative permeabilities and capillary pressure models in Examples 1 and 2 below are considering a zero residual saturations for the wetting and nonwetting fluids.

4.2.1 | Example 1

The computational domain with 300m × 150m dimensions, consisting of different subdomains for the distribution of permeability, is considered. This porous medium model is shown in Figure 2.

TABLE 3 Linearization schemes convergence comparison for the tested flow model in Example 1

δt (days)	27.5	6.85	3.43	1.71	0.85
Iterative IMPES					
Total iteration	–	–	–	–	12 237
Average iteration	–	–	–	–	3.82
Iterative pseudo-monolithic					
Total iteration	672	1820	2832	4112	5244
Average iteration	6.72	4.55	3.45	2.57	1.6

Note: The "–" sign stands for the scheme is not convergent, "Total iteration" stands for the overall number of iterations to complete the simulation, and "Average iteration" represents the average iteration number per time step.
Abbreviation: IMPES, implicit pressure explicit saturation.

We applied the water-wet van Genuchten relative permeabilities (11) and a capillary pressure function as given below,

$$P_c = \frac{\beta_1 \chi}{1 + \beta_1 \chi}(P_c^{ow} - P_c^{ww}) + P_c^{ww}, \tag{44}$$

where P_c^{ww} and P_c^{ow} are as described in Equation (10). The capillary pressure (44) is changing from P_c^{ww} to P_c^{ow} dynamically for 7.5 years. Here 7.5 years represent the life of injection for this particular simulation. Further data on the model parameters are given in Table 2 above. We complete the model by injecting the nonwetting fluid to the left-bottom corner of the domain with an injection rate of $0.35m^3$ per day and we impose a zero Dirichlet condition at the middle of the right side of the domain. The rest of the boundaries are considered impermeable.

We discretized the above model with 2500 regular grid cells and performed numerical experiments to evaluate the convergence behavior of the iterative IMPES and pseudo-monolithic scheme for different time step sizes. Table 3 shows the convergence results of the two methods. As shown in Table 3, the iterative IMPES only converges if the time step size $\delta t \leq 0.85$ day, and the iterative pseudo-monolithic scheme converges for all time step sizes. This shows that the iterative IMPES is subject to strong restrictions with respect to the time step size choice in this example. Usually, IMPES encountered a difficulty regarding the choice of time step size even for standard multiphase flow models.[20-22,32] The dynamic nature of the capillary pressure function further worsens the flexibility of iterative IMPES on the choice of the time step size in this example. By contrast, the iterative pseudo-monolithic scheme shows its strength allowing for the relaxed choice of time step sizes. The scheme is capable of taking a large time step size. Furthermore, the total and average number of iterations are increasing and decreasing, respectively, when the scheme considers smaller time step sizes. The decreasing number of average iterations per time step size is a positive sign toward the stability of the iterative pseudo-monolithic scheme.

We further studied the convergence stability of the iterative pseudo-monolithic scheme by controlling the speed of capillary pressure alteration. To do so, we vary the dynamic coefficient parameter β_1 from Equation (44). For this numerical experiment, we used the same mesh size as before and chose a larger time step size $\delta t = 30.5$ days. Table 4 shows the convergence behavior of the iterative pseudo-monolithic scheme for different dynamic coefficient parameter, β_1, values. From Table 4, we observe that the scheme requires more iterations as β_1 increases. That means the scheme needs a few extra iterations to converge as the alteration speed of the capillarity becomes faster. Furthermore, the scheme may fail to converge for this model if we choose sufficiently large $\beta_1 > 2 \times 10^4$ (not shown here). For such case, the proposed scheme is enforced to choose a relatively small time step size. Nevertheless, the results above show that the scheme converges successfully for nonlocal (in time) two-phase flow model that considers physically reasonable dynamic capillary pressure alteration (even with capillary pressure jumps). These all support the theoretical convergence analysis of the proposed scheme as discussed in Section 3. In general, the reliability of the scheme to handle the dynamic alteration of the capillary pressure and nonlocality of the problem has been successfully demonstrated.

After a successful convergence stability experiment, we also studied the impact of the dynamic coefficient parameter, β_1, on the flow path of the fluids. We used $\delta t = 30.5$ days, and we keep the grid size, fluid and reservoir parameters as above for this purpose. However, we considered two different values for the dynamic coefficient parameter β_1. Figure 3 shows the fluid distributions after 7.5 years of evolution.

β_1	100	200	10^4	2×10^4
Total iteration	622	644	768	963
Average iteration	6.9	7.2	8.5	10.7

TABLE 4 The impact of dynamic coefficient parameter on the stability of the iterative pseudo-monolithic scheme

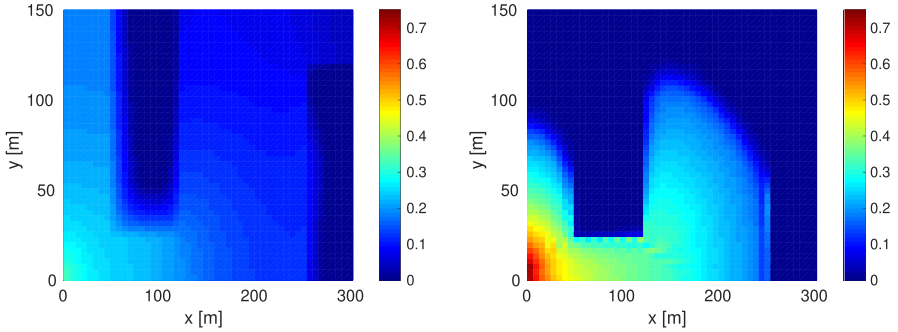

FIGURE 3 Saturation profiles: A, Demonstrates the flow path when $\beta_1 = 1$, that is, slow dynamic capillary pressure alteration and B, shows the fluid path for relatively fast dynamic alteration, that is, $\beta_1 = 2\times10^4$ [Colour figure can be viewed at wileyonlinelibrary.com]

As shown in Figure 3, the effect of the dynamic coefficient on fluid displacement is distinct. The movement of the nonwetting fluid is restricted for fast dynamic alteration processes. In other words, the displacing fluid remains the resident fluid for slow dynamic capillary pressure alteration, whereas it swipes the resident fluid when we consider a fast capillary pressure alteration. This happens because the wetting property of the volumes (occupied by the displacing fluid) is altered to the intermediate-wet system before it leaves the volume, and thus, the nonwetting fluid preferred to be in contact with the solids when we consider fast capillary pressure alteration.

4.2.2 | Example 2

We considered 50m × 50m × 10m dimensional heterogeneous medium, with permeability distribution,

$$\mathrm{K} = \begin{cases} 1 \text{ md, if } (x,y,z) \in (5\text{ m}, 50\text{ m}) \times (0\text{ m}, 30\text{ m}) \times (2\text{ m}, 8\text{ m}) \\ 100 \text{ md, else.} \end{cases} \tag{45}$$

We employed the same relative permeabilities functions as above and dynamic capillary pressure given as

$$P_c = \frac{\beta_2 S_w \chi}{1+\beta_2 S_w \chi}(P_c^{ow} - P_c^{ww}) + P_c^{ww}, \tag{46}$$

where P_c^{ww} and P_c^{ow} are as described in Equation (10). The capillary pressure is allowed to change from P_c^{ww} to P_c^{ow} dynamically according to model (46) in each subdomain for 2.5 years. Additional data on model parameters are listed in Table 2. We inject the nonwetting fluid to the west particularly at $(y,z) \in (10\text{m},15\text{m}) \times (2\text{m},8\text{m})$ with an injection rate of $0.15m^3$/day for 2.5 years, and impose a zero Dirichlet boundary condition to the east side of the domain, particularly at $(y,z) \in (10\text{m},15\text{m}) \times (2\text{m},8\text{m})$. The rest of the boundaries are considered to be impermeable.

We discretized the designed model above with 3125 grid cells and we did simulations to examine the convergence behavior of the iterative IMPES and pseudo-monolithic linearization techniques. The obtained results are published in Table 5. In Table 5, we noticed that the iterative IMPES fails to converge for time step sizes bigger than 0.26 day. This shows that the choice of a time step size is strongly restricted for iterative IMPES linearization which confirms the results reported in References 20,21,32. Unlike the iterative IMPES, iterative pseudo-monolithic scheme relaxes the choice of the

TABLE 5 Linearization schemes comparison for the tested flow model above in Example 2

δt (days)	90.25	60	30.4	9.125	2.2812	0.57	0.26
Iterative IMPES							
Total iteration	–	–	–	–	–	–	6980
Average iteration	–	–	–	–	–	–	2.2
Iterative pseudo-monolithic							
Total iteration	50	72	121	271	824	2106	3354
Average iteration	5	4.8	4.03	2.71	2.06	1.3	1.05

Note: Here "–" represents that the scheme is not convergent.
Abbreviation: IMPES, implicit pressure explicit saturation.

TABLE 6 The impact of dynamic coefficient parameter on the stability of the iterative pseudo-monolithic scheme

β_2	100	1000	2×10^3	1×10^4	2×10^4
Total iteration	50	50	50	50	50
Average iteration	5	5	5	5	5

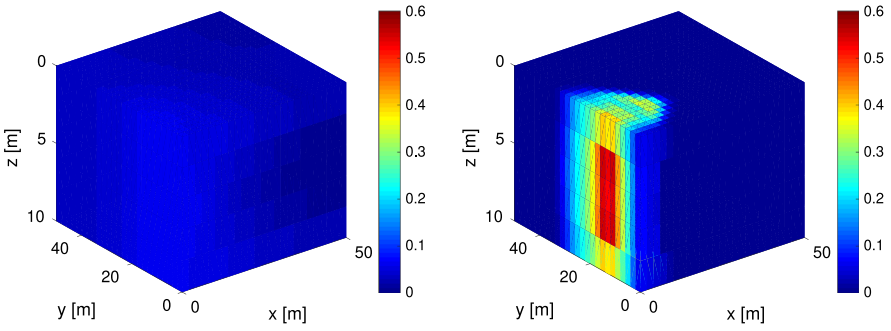

FIGURE 4 Saturation distribution obtained from iterative pseudo-monolithic scheme. Here, we applied the same grid resolution as above with time step size $\delta t = 90.25$ days. A, No dynamic capillary pressure alteration ($\beta_2 = 0$) and B, relatively fast alteration ($\beta_2 = 1\times10^5$ in Equation (46)) [Colour figure can be viewed at wileyonlinelibrary.com]

time step size. The scheme return with an approximate solution for a relatively large time step size compared with the iterative IMPES scheme. The total and average number of iterations, respectively, are increasing and decreasing when we consider smaller time step sizes, see Table 5.

We further investigate the sensitivity of the dynamic coefficient parameter β_2. For this, we keep the number of grid elements as before and the time step size to be the larger one in Table 5, that is, $\delta t = 90.25$ days. Then, we vary β_2, and observe its impact on the convergence of the scheme. Table 6 shows the convergence results for different values of β_2. As shown in Table 6, the scheme converges with the same number of iterations for all values of β_2. This implies that the proposed scheme is not affected by the speed of the capillary pressure alteration dynamics for this particular example.

Above, we studied the convergence of the iterative pseudo-monolithic scheme for the nonlocal two-phase flow model. Below, we investigate the impact of the dynamic capillary pressure model on the injected fluid distribution. Figure 4 compares the injected fluid distribution for the initial wetting condition capillary pressure (ie, $\beta_2 = 0$ in Equation (46)), and dynamic capillary pressure model (46) with $\beta_2 = 1\times10^5$.

In Figure 4, we observe that the displacing fluid leaves the resident fluid behind when we consider $\beta_2 = 0$ in Equation (46). This is due to the fact that the rock surfaces are water-wet in this case, that is, no WA, and thus, the resident fluid prefers to remain in the pores. On the other hand, the nonwetting fluid has displaced the resident fluid and concentrated near the injection area when we employed the dynamic capillary pressure model (46) with $\beta_2 = 1\times10^5$. In

this case, the wettability of the rock surfaces near to the injection area has been changed (in time) to the intermediate-wet system before the displacing fluid leaves the volume, and thus, the displacing fluid preferred to occupy these pores. That means the injected fluid pressure is able to displace the resident fluid with relatively small pressure. This shows that the dynamic capillary pressure results in a large change of fluid saturation as compared with the standard capillary pressure model, P_c^{ww}, in Equation (10). This might be one of the reasons that restrict the time step size choice of the iterative IMPES.

5 | CONCLUSION

In this article, we introduced fluid history and time-dependent dynamic capillary pressure model in a two-phase immiscible incompressible porous media flow model. We developed a linearization scheme for the resulting nonstandard two-phase flow model by treating the capillary pressure implicitly and adding stabilization terms. This implicit treatment of the dynamic capillary pressure model couples the pressure and saturation equations strongly, and makes the scheme stable. We gave a theoretical convergence analysis of the scheme under some meaningful assumptions. The scheme has been successfully implemented and tested for different illustrative examples. We found that the proposed scheme is efficient to approximate the solution of the resulting nonstandard two-phase flow model. Most importantly, the scheme demonstrates flexibility regarding the choice of time step size for dynamic capillary pressure alteration (possibly with capillary jumps). Thus, combining the scheme with a Newton method is a straightforward application. This implies that one can alternate between the iterative pseudo-monolithic scheme and the Newton method as mentioned in Reference 25. This may further improve the convergence speed and accuracy of the approximation to simulate such complex models. Furthermore, the convergence of the scheme shall be investigated for degenerate cases in the future.

ORCID

Abay Molla Kassa https://orcid.org/0000-0002-5396-5768

REFERENCES

1. Bear J, Verruijt A. *Modeling Groundwater Flow and Pollution: Theory and Application of Transport in Porous Medium*. 1st ed. Boston,MA: D. Reidel; 1987.
2. Chen Z, Huan G, Ma Y. *Computational Methods for Multiphase Flows in Porous Media*. London, UK: SIAM; 2006.
3. Landa-Marbán D, Radu FA, Nordbotten JM. Modeling and simulation of microbial enhanced oil recovery including interfacial area. *Transp Porous Med*. 2016;120:395-413. https://doi.org/10.1007/s11242-017-0929-6.
4. Nielsen SM, Shapiro AA, Michelsen ML, Stenby EH. 1D simulations for microbial enhanced oil recovery with metabolite partitioning. *Transp Porous Med*. 2010;85:785-802. https://doi.org/10.1007/s11242-010-9592-x.
5. Nordbotten JM, Celia MA. *Geological Storage of CO_2: Modeling Approaches for Large-scale Simulation*. Hoboken, NJ: John Wiley & Sons, Inc; 2012.
6. Van Genuchten MT. A closed-form equation for predicting the hydraulic conductivity of unsaturated soils. *Soil Sci Soc Am*. 1980;44:892-898. https://doi.org/10.2136/sssaj1980.03615995004400050002x.
7. Brooks RH, Corey AT. Hydraulic properties of porous media and their relation to drainage design. *Transactions of the ASAE*. 1964; 7(1):26-28.
8. Morrow NR. The effects of surface roughness on contact angle with special reference to petroleum recovery. *J Can Pet Technol*. 1975;14:42-53. https://doi.org/10.2118/75-04-04.
9. Morrow NR, Lim HT, Ward JS. Effect of crude-oil-induced wettability changes on oil recovery. *SPE Form Evaluat*. 1986;1(1):89-103. https://doi.org/10.2118/13215-PA.
10. Buckley JS, Liu Y, Monsterleet S. Mechanisms of wetting alteration by crude oils. *SPE J*. 1988;3:54-61. https://doi.org/10.2118/37230-PA.
11. Jadhunandan PP, Morrow NR. Effect of wettability on waterflood recovery for crude-oil/brine/rock systems. *SPE Reserv Eng*. 1995;10:40-46. https://doi.org/10.2118/22597-PA.
12. Haagh MEJ, Siretanu I, Duits MHG, Mugele F. Salinity-dependent contact angle alteration in oil/brine/silicate systems: the critical role of divalent cations. *Langmuir*. 2017;33:3349-3357. https://doi.org/10.1021/acs.langmuir.6b04470.
13. Singh R, Mohanty KK. Foams with wettability-altering capabilities for oil-wet carbonates: a synergistic approach. *SPE J*. 2016;21:1126-1139. https://doi.org/10.2118/175027-PA.
14. Kassa AM, Gasda SE, Kumar K, Radu FA. Impact of time-dependent wettability alteration on the dynamics of capillary pressure. *Adv Water Resour*. 2020;142. https://doi.org/10.1016/j.advwatres.2020.103631.
15. Larisa VB, Ghai SS, Stephen LL, Wu X. Challenges and technologies in reservoir modeling. *Commun Comput Phys*. 2009;6:1-23.
16. Monteagudo JP, Firoozabadi A. Comparison of fully implicit and IMPES formulations for simulation of water injection in fractured and unfractured media. *Int J Numer Meth Eng*. 2007;69:698-7282. https://doi.org/10.1002/nme.1783.

17. Chen Z, Huan G, Li B. An improved IMPES method for two-phase flow in porous media. *Transp Porous Med*. 2004;54:361-376. https://doi.org/10.1023/B:TIPM.0000003667.86625.15.
18. Kvashchuk A, Radu FA. A fully-implicit, iterative scheme for the simulation of two-phase flow in porous media. In: Florin A, Kundan K, Pop S, eds. *Numerical Mathematics and Advanced Applications ENUMATH 2017. Lecture Notes in Computational Science and Engineering*. Vol 126. Springer: Cham; 2017.
19. Radu FA, Nordbotten JM, Pop IS, Kumar K. A robust linearization scheme for finite volume based discretizations for simulation of two-phase flow in porous media. *J Comput Appl Math*. 2015;289:134-141. https://doi.org/10.1016/j.cam.2015.02.051.
20. Kou J, Sun S. A new treatment of capillarity to improve the stability of IMPES two-phase flow formulation. *Comput Fluids*. 2010;39:1923-2031. https://doi.org/10.1016/j.compfluid.2010.06.022.
21. Kou J, Sun S. On iterative IMPES formulation for two-phase flow with capillarity in heterogeneous porous media. *Int J Numer Anal Mod B*. 2010;1:30-40.
22. Coats KH. IMPES stability: selection of stable timesteps. *SPE J*. 2003;8:181-187. https://doi.org/10.2118/84924-PA.
23. Tseng P, Zyvoloski GA. A reduced degree of freedom method for simulating nonisothermal multi-phase flow in a porous medium. *Adv Water Resour*. 2000;23:731-745. https://doi.org/10.1016/s0309-1708(00)00006-3.
24. Lacroix S, Vassilevski Y, Wheeler JA, Wheeler MF. Iterative soltuion methods for modeling multiphase flow in porous media fully implicitly. *SIAM J Sci Comput*. 2003;25:905-926. https://doi.org/10.1137/S106482750240443X.
25. List F, Radu FA. A study on iterative methods for solving Richards' equation. *Comput Geosci*. 2016;20:341-353. https://doi.org/10.1007/s10596-016-9566-3.
26. Karpinski S, Pop IS, Radu FA. Analysis of a linearization scheme for an interior penalty discontinuous Galerkin method for two phase flow in porous media with dynamic capillarity effects. *Int J Numer Methods Eng*. 2017;112:553-577. https://doi.org/10.1002/nme.5526.
27. Illiano D, Pop IS, Radu FA. Iterative schemes for surfactant transport in porous media. *Comput Geosci*. 2020. https://doi.org/10.1007/s10596-020-09949-2.
28. Hassanizadeh SM, Celia M, Dahle HK. Dynamic effects in the capillary pressure saturation relationship and its impacts on unsaturated flow. *Vadose Zone J*. 2002;1:38-57.
29. Dahle HK, Celia MA, Hassanizadeh SM. Bundle-of-tubes model for calculating dynamic effects in the capillary-pressure saturation relationship. *Transp Porous Med*. 2005;58:5-22. https://doi.org/10.1007/s11242-004-5466-4.
30. Pop IS, Radu FA, Knabner P. Mixed finite elements for the Richards' equation: linearization procedure. *J Comput Appl Math*. 2004;168:365-373. https://doi.org/10.1016/j.cam.2003.04.008.
31. Lie KA. *An Introduction to Reservoir Simulation Using MATLAB/GNU Octave: User Guide for the Matlab Reservoir Simulation Toolbox (MRST)*. Cambridge, MA: Cambridge University Press; 2019.
32. Dedner A, Kane B, Klöfkorn R, Nolte M. Python framework for hp-adaptive discontinous Galerkin methods for two-phase flow in porous media. *Appl Math Model*. 2019;67:179-200. https://doi.org/10.1016/j.apm.2018.10.013.

SUPPORTING INFORMATION

Additional supporting information may be found online in the Supporting Information section at the end of this article.

How to cite this article: Kassa AMolla, Kumar K, Gasda SE, Radu FA. Implicit linearization scheme for nonstandard two-phase flow in porous media. *Int J Numer Meth Fluids*. 2021;93:445–461. https://doi.org/10.1002/fld.4891

Paper 5.1.4

Field-scale Impacts of Long-Term Wettability Alteration in Geological CO_2 Storage

A. M. Kassa, S. E. Gasda, D. Landa-Marbán, T. H. Sandve, and K. Kumar

D

Submitted to International Journal of Greenhouse Gas Control
arxiv.org/abs/2108.06601 [physics.geo-phy]

Field-scale Impacts of Long-Term Wettability Alteration in Geological CO_2 Storage

A.M. Kassa[a,b], S.E. Gasda[a], D. Landa-Marbán[a], T.H. Sandve[a], K. Kumar[b]

[a] *NORCE Norwegian Research Centre AS*
[b] *Department of Mathematics, University of Bergen*

Abstract

Constitutive functions that govern macroscale capillary pressure and relative permeability are central in constraining both storage efficiency and sealing properties of CO_2 storage systems. Constitutive functions for porous systems are in part determined by wettability, which is a pore-scale phenomenon that influences macroscale displacement. While wettability of saline aquifers and caprocks are assumed to remain water-wet when CO_2 is injected, there is recent evidence of contact angle change due to long-term CO_2 exposure. Weakening of capillary forces alters the saturation functions dynamically over time. Recently, new dynamic models were developed for saturation functions that capture the impact of wettability alteration (WA) due to long-term CO_2 exposure. In this paper, these functions are implemented into a two-phase two-component simulator to study long-term WA dynamics for field-scale CO_2 storage. We simulate WA effects on horizontal migration patterns under injection and buoyancy-driven migration in the caprock. We characterize the behavior of each scenario for different flow regimes. Our results show the impact on storage efficiency can be described by the capillary number, while vertical leakage can be scaled by caprock sealing parameters. Scaling models for CO_2 migration into the caprock show that long-term WA poses little risk to CO_2 containment over relevant timescales.

Keywords: dynamic capillary pressure; dynamic relative permeability; seal integrity; storage efficiency; wettability alteration; CO_2 storage simulation

1. Introduction

Geological CO_2 storage can be successfully implemented in deep saline aquifers that possess favorable characteristics [1], e.g., the storage formation has sufficient capacity, injectivity, and containment properties to store the desired quantity of CO_2 at the required injection rate. A competent caprock should be verified that provides a capillary and permeability seal to prevent buoyant CO_2 from migrating upwards and is free of defects that could leak or seep CO_2 out of the storage formation [2]. In addition, lateral migration of CO_2 should stay within the defined boundaries of the storage reservoir. In some cases, the boundaries are defined by a structural trap. In open stores with no defined trap, sufficient CO_2 trapping efficiency in residual and dissolved phase is needed to prevent unwanted lateral CO_2 migration [3].

There is a wide array of geological and operational factors affecting CO_2 storage migration and containment in deep, saline aquifer [4]. The physical and chemical rock-fluid interactions play an important role through their impact on the constitutive functions that govern macroscale capillary pressure and relative permeability. These functions, often called flow functions or saturation functions, govern the displacement processes in a multiphase flow setting and are central in constraining both storage capacity of the formation and sealing properties of the caprock [5, 6, 7, 8]. Capillary pressure and relative permeability functions for the storage reservoir and caprock are strongly influenced by wettability. The term wettability refers to the preference of one fluid over the other for the rock surface [9, 10] and is a pore-scale phenomenon that has direct influence on macroscale displacement processes [11, 12, 13].

Wettability has been shown to play a key role in geological CO_2 storage with regard to CO_2 migration, trapping and sealing capacity. Saline aquifers are brine-bearing formations, and thus often assumed to be strongly water-wet. However, differences in initial wetting state can be caused by a number of factors that affect the surface chemistry of rock minerals, including temperature and pressure conditions, brine salinity, mineralogy, and organic content (see [14] and references therein). Wettability significantly affects the capillarity between CO_2 and brine, which in turn impacts the efficiency of brine displacement. Studies have shown that wettability affects plume migration [15] and residual trapping [16]. In terms of containment, the capillary seal of the caprock barrier is reliant on a strongly water-wet condition to maintain a high capillary force in combination with smaller pore radii of a tight medium. An effective seal increases storage capacity in structural traps by supporting a thick column of CO_2 [14], which can be compromised if the seal weakens over time due to changes in wettability [17].

Although wettability is often considered a static property, there is a possibility for wettability to change dynamically over time. This process of *wettability alteration* (WA) is a dynamic process, that involves a complex interaction of surface mineralogy, fluid composition, and reservoir conditions that is percipitated by the introduction of a wettability-altering agent [9, 18]. WA has been long studied in the petroleum sector, and a variety of methods and agents, that include solvents such as supercritical CO_2, have been applied to enhance WA in oil reservoirs to the benefits of increased recovery [19, 20]. Modeling of WA often assumes an instantaneous change of wettability as a function of solvent concentration [21]. However, there are some cases where a WA process depends on exposure time that can extend for weeks or months to the wettability-altering agent [22, 23, 24, 25, 26, 27].

For CO_2 storage, there has been some intriguing evidence of long-term WA caused by CO_2 exposure that significantly weakens the strength of capillary forces of a water-wet medium, which can apply to both reservoir rocks and caprock material. For example, core-flooding experiments and capillary pressure measurements on storage reservoir samples have reported a instability or slow reduction in capillary pressure–saturation relationships over time [23, 28, 29, 30, 31, 32]. In particular, we note in [31] that wettability was measured through contact angle (CA) change in silicate and carbonate sands from strongly water wet to intermediate wet over the course of weeks and months. Studies on shales exposed to CO_2 over long periods show a steady increase in shale/water CA over days and

months [33, 24, 25], with trends that indicate additional exposure would lead to further CA increase. Similar studies using reservoir rocks also show an evolution from water- to CO_2-wet conditions due CO_2 exposure in core-flooding experiments [34, 35]. All these bench-scale experiments indicate that WA introduces long-term dynamics into the capillary pressure and relative permeability functions. Such dynamics could have a significant impact on CO_2 storage at the field scale in ways that may be positive or negative. On the one hand, a caprock that becomes intermediate-wet or hydrophobic is less effective than a water-wet caprock in providing an effective capillary barrier. On the other hand, capillary diffusion may be reduced in the storage reservoir through long-term WA, which can be beneficial to injectivity and capacity by causing the CO_2 to displace the resident fluid efficiently [36]. A wettability change, in general, affects the space-time evolution of CO_2 plume in the formation in ways that has not been fully understood yet.

There have been several attempts to understand the impact of static wettability on long-term CO_2 storage at field scales. In [15, 37, 38] the main conclusions are that CO_2 vertical migration is enhanced with more CO_2-wet systems, which is due to the lower residual trapping capacity of CO_2-wet rocks. The impact is stronger when considering heterogeneous wettability and increased temperature. These studies did not investigate the impact of CO_2 exposure that changes rock wettability over time. Another study investigated wettability alteration caused by increased reservoir temperature under CO_2 injection. The relative permeability curves were set in predetermined zones different temperature, but the curves were not adjusted dynamically in time [39].

Understanding how CO_2 storage is impacted by dynamic wettability caused by CO_2 exposure requires a different approach than previously used to study static wettability. Two simulation components are needed: (a) flow functions that capture the dynamics due to CO_2 exposure, and (b) analysis and characterization of long-term WA impacts through implementation of dynamic flow functions into field-scale simulation. We have recently addressed the first aspect in [40] and [41] where we successfully developed dynamic capillary pressure and relative permeability functions through mechanistic modeling combined with upscaling of wettability dynamics from pore to core scale. The developed models are extended forms of standard constitutive models either by interpolation between two end-state capillary pressure functions [40] or by incorporating WA dynamics directly into the parameters of the existing relative permeability model [41]. The dynamics in both models are driven by exposure time to CO_2 which is easily calculated from the local saturation history. We found that both models compare well against pore-scale simulation data where WA is modeled in individual pores. More interestingly, we determined that the upscaled model parameters have a clear relationship with the underlying pore-scale WA model parameter. Moreover, the developed constitutive models are robust and lend themselves to implementation within standard flow simulators.

To our knowledge, numerical simulation of the field-scale impacts of WA caused by long-term CO_2 exposure has not been performed previously. In this paper, we implement the aforementioned dynamic relative permeability and capillary pressure functions [40, 41] into flow models for CO_2 storage applications in the open porous media (OPM) framework [42]. We investigate the impact of long-term WA process for CO_2 storage with a focus on the migration patterns and containment in a saline

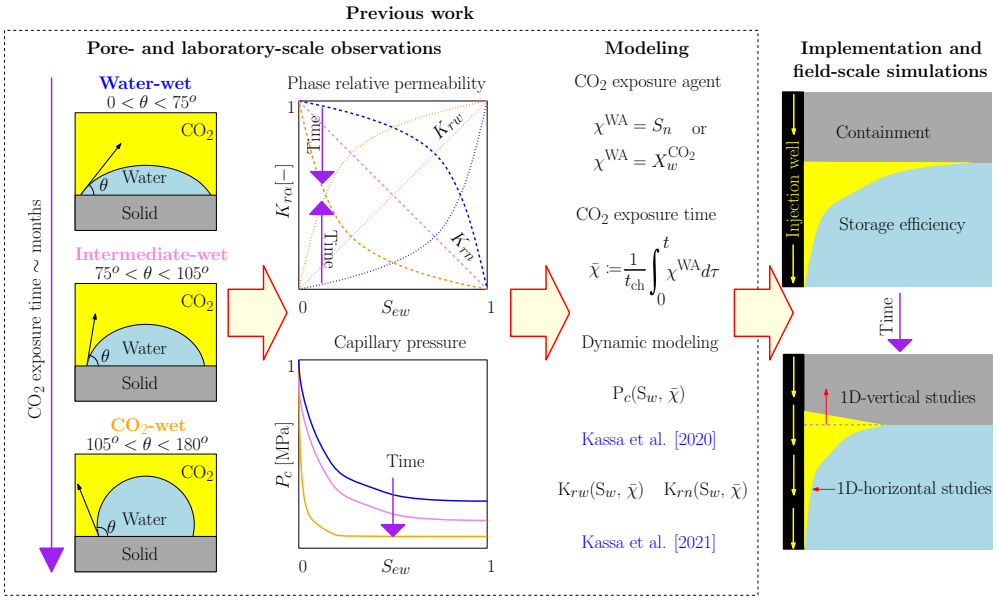

Figure 1: Model development involved in preparation for long-term wettability alteration field-scale studies. The boxed content illustrates key features of previous work [40, 41] implemented in this study. Further discussion of the "Modeling" formulations can found in Section 2.1.1.

aquifer that involves both viscous-driven flow in the storage aquifer and the potential for buoyancy flow through the caprock. Therefore, we concentrate our analysis on one-dimensional horizontal and vertical flow systems in order to understand the impact of dynamic changes in wettability on both flow regimes separately. For the horizontal case, we study the impact of WA on storage efficiency given by the front location, while for the vertical case, we focus on the impact of CO_2 containment under a capillary seal (i.e., caprock). In both cases, we study the sensitivity of wettability dynamics and subsequent field-scale impacts under different conditions (i.e., permeability, entry pressure, injection rate, and porosity) and ultimately seek an appropriate scaling relationship for the quantity of interest in order to generalize our findings. The quantified behavior contributes to increased understanding of the efficiency and integrity of long-term CO_2 storage subject to WA caused by CO_2 exposure.

2. Methodology

The goal of this study is to investigate the impacts of dynamic changes in wettability caused by long-term CO_2 exposure on field-scale CO_2 plume evolution and containment. In this section, we outline the methods that have been implemented to carry out the desired field-scale simulations. Figure 1 shows the relevant components of the dynamic saturation functions developed in previous work that are linked to the implementation and field-scale simulation study carried out in this work.

As discussed in Section 1, laboratory observations indicate that CO_2 exposure can induce chemical

alteration of the native rock. Assuming saline aquifers are initially water-wet, we consider that long-term CO_2 exposure on the order of months can shift wettability to intermediate wet or even CO_2 wet, where each wetting state is defined by the contact angle (CA) between water and solid as shown in the left-most illustrations in Figure 1. As a result, the saturation functions are altered continuously in time, which is shown schematically for both the phase relative permeability and capillary pressure functions (center Figure 1). Alteration continues until the wetting condition has reached a final state under maximum exposure.

When studying this phenomena at the field scale, we expect that dynamics in saturation functions will be inherently linked to local CO_2 exposure, which itself is controlled by migration of CO_2 at the field scale. As a result, different points of the aquifer will have a different local history of CO_2 exposure, which leads to local alteration of saturation functions that varies in space and time throughout the storage site. This spatial/temporal complexity in capillary pressure and relative permeability can in turn impact field-scale CO_2 migration in ways that are not easily predicted *a priori*. Field-scale studies are needed to quantify the impact of this interplay between dynamics in saturation functions and large-scale flow processes, illustrated in the right-most panels in Figure 1.

The link between CO_2 exposure and time-dependent saturation functions requires a model to evolve capillary pressure and relative permeability functions as the wetting condition continuously changes. As depicted under "Modeling" in Figure 1, we have previously developed new formulations for capillary pressure and relative permeability that incorporate exposure to CO_2 as an additional dynamic variable [40, 41]. These dynamic models are implemented in a standard field-scale simulation approach (described in Section 2.1) that includes a brief overview of the dynamic model development from previous work in Section 2.1.1.

2.1. Field-scale governing laws

CO_2 storage in saline aquifers is modeled as a three-dimensional flow system consisting of two immiscible fluids, CO_2 and brine, that are mutually soluble fluids. In this section, we introduce the model equations to describe the TPTC flow in a porous medium. The general form of the TPTC model is presented below, however we introduce some simplifications later during the model implementation (cf. Section 2.2). For the sake of brevity, we consider constant temperature and salinity in this study, but these effects can be included into the model in a straightforward manner.

Let $\Omega \in \mathbb{R}^d$, $d = 1, 2,$ or 3 be a permeable domain having a Lipschitz continuous boundary $\partial\Omega$ and saturated with two-phase fluids that have two components each. The phases, wetting and non-wetting, are indicated by subscripts $\alpha \in \{w, n\}$ and the two components are represented by index $k \in \{\mathrm{CO_2}, \mathrm{water}\}$. The mass conservation law of component k is described by:

$$\phi \sum_{\alpha} \partial_t (\rho_\alpha S_\alpha X_\alpha^k) + \sum_{\alpha} \nabla \cdot (\rho_\alpha X_\alpha^k \vec{u}_\alpha + \vec{j}_\alpha^k) = F^k \text{ in } \Omega, \tag{1}$$

where X_α^k is component k mass fraction in phase α, ϕ denotes the porosity of the porous domain, S_α is the phase α saturation, ρ_α is the density of phase α, $\vec{u}_\alpha$ is the volumetric phase flux, and F^k is the source term of component k.

For each phase $\alpha \in \{w, n\}$, the volumetric flux $\vec{u}_\alpha : \Omega \times [0, \mathrm{T}] \to \mathbb{R}^d$ is given by the multiphase extension of Darcy's law:

$$\vec{u}_\alpha = -\frac{\mathbb{K}k_{r\alpha}}{\mu_\alpha}\left(\nabla P_\alpha - \rho_\alpha \vec{g}\right), \tag{2}$$

where $\mathbb{K} : \Omega \to \mathbb{R}^{d\times d}$ is the intrinsic permeability tensor of the rock, $k_{r\alpha}$ is the relative permeability for phase α, μ_α is phase viscosity, P_α is phase pressure, and $\vec{g}$ is the gravitational vector. Hereafter, we will use $\mathbb{K}$ and K for a tensor and scalar permeability, respectively. The diffusive flux of component k in phase α, $\vec{j}_\alpha^k$, is represented by the Fick's law and has the form of:

$$\vec{j}_\alpha^k = -\rho_\alpha \mathrm{D}_\alpha^\mathrm{k} \tau_\alpha \mathrm{S}_\alpha \phi \nabla \mathrm{X}_\alpha^\mathrm{k}, \tag{3}$$

where $\mathrm{D}_\alpha^\mathrm{k}$ is the molecular diffusion coefficient and τ_α is tortuosity for phase α which is calculated as [43]:

$$\tau_\alpha = \frac{(\phi S_\alpha)^{\frac{7}{3}}}{\phi^2}. \tag{4}$$

The component mass fractions, X_α^k, satisfies:

$$\sum_k X_\alpha^k = 1. \tag{5}$$

The phase α saturation takes values between zero and one, and the sum of phase saturation equals one. That is:

$$0 \le S_\alpha \le 1, \text{ and } \sum_\alpha S_\alpha = 1. \tag{6}$$

The pressures, wetting and non-wetting, are connected by the capillary pressure relation as

$$P_c(\cdot, S_w) = P_n - P_w. \tag{7}$$

A model for mass transfer between the phases is needed to close the system of equations. In the general form, we consider the fugacity constraints

$$f_w^k(P_w, T, X_w^k) - f_n^k(P_n, T, X_n^k) = 0, \tag{8}$$

where they express the requirement that non-wetting (gas) and wetting (liquid) fugacities have to be equal for each component [44, 45]. The fugacity coefficients are calculated according to the work of Spycher and Pruess [46]. We note that other forms of mass transfer may be considered, including equilibrium partitioning. If mass transfer is not modeled, then this closure relation may be omitted from the model formulation.

Equations (1) through (8) with appropriate initial and boundary conditions can be used to describe TPTC flow dynamics in a porous medium. These equations provide a complete description of the physics of isothermal TPTC flow in a porous medium bearing in mind that the relative permeabilities

and capillary pressure parameterizations are given.

2.1.1. Previous work: Dynamic saturation functions

Capillary pressure in Equation (7) and phase relative permeability in Equation (2) can be modeled by functions such as Brooks-Corey [47] or van Genuchten [48] constitutive functions. However, these standard flow functions are limited to static wetting conditions and lack the time component needed to capture dynamics in constitutive relations due to long-term WA. In recent work, we have developed new dynamic models for both capillary pressure [40] and relative permeability [41] that capture the underlying pore-scale WA mechanisms caused by exposure to CO_2.

Below we briefly review the development of the upscaled dynamic flow functions from the pore scale to the Darcy scale performed in previous work. Although the development starts from pore-scale parameters, the final result are flow functions that solely rely on macroscale variables, where the additional dynamic parameters have been calibrated to the pore-scale simulations performed previously. The reader is referred to the referenced papers for more details.

The dynamic constitutive models in [40] and [41] were developed by applying an upscaling workflow that involves correlating Darcy-scale models to dynamic capillary pressure and relative permeability data generated from pore-scale numerical experiments. The key features to this workflow are:

1. A mechanistic model for CA change from an initial to final wetting state that is incorporated directly in pore-scale simulations.
2. A dynamic model formulation identified at the Darcy scale that incorporates exposure time and can be correlated to the dynamic data with as few parameters as possible.
3. A link between the correlated dynamic Darcy-scale parameter(s) and the pore-scale model for CA change.

We note that the above approach does not capture changes in residual saturation for CO_2 and brine as a result of different wetting conditions. Although the connection between residual saturation and wetting condition is well studied, incorporation into a dynamic framework is still a subject of ongoing work. As such, the dynamic models presented are limited, but still provide important insight into CO_2 migration patterns due to changing wetting conditions.

The first step in the previously published upscaling workflow is the pore-scale mechanistic model for CA change. The chosen model was motivated by experimental evidence that indicates a gradual and permanent change in the fluid-fluid CA when exposed to a WA agent, in this case CO_2, over a long period of time. CA change is caused by adsorption of the WA agent to the pore surface that subsequently alters surface chemistry and changes the affinity of fluids to the solid. In addition, a longer exposure time induces a greater change in CA. We thus designed a dynamic CA model that is sorption-based and time-dependent and has the form (see [40] for development details):

$$\theta = \theta^{\mathrm{i}} + \frac{(\theta^{\mathrm{f}} - \theta^{\mathrm{i}})\chi}{C + \chi}, \tag{9}$$

where θ^{i} and θ^{f} are the initial and final CA respectively, C is a model parameter that determines the

rate of WA over time, with increasing C indicating slower CA change, and χ is a cumulative measure of exposure time to the WA agent at the pore level. The quantity χ was evaluated by integrating the chosen measure of local exposure, i.e., agent concentration or saturation, over time. As χ is a quantity that always increases under exposure or remains constant under the absence of the WA agent, the above model leads to irreversible CA change.

With the above mechanistic WA model incorporated at the pore scale, a set of numerical experiments were performed to simulate laboratory measurements of capillary pressure and relative permeability, i.e., subsequent drainage and imbibition cycles with stepwise changes in saturation over time. The simulated data were obtained by modeling the pore scale as a bundle of cylindrical or triangular tubes. A schematic illustration of capillary pressure and relative permeability data obtained in our previous studies are shown in Figure 1.

Analysis of the simulated data showed that both saturation functions evolve smoothly from an initial to final state as the CA changes dynamically and heterogeneously with increasing exposure time to the non-wetting fluid. In the reported experiments, CA changed from a strongly water-wet system ($\theta^i = 0°$) to an intermediate-wet system ($\theta^f = 85°$), although the opposite WA process could equally have been simulated. Figure 1a shows that capillary gradually decreases over a period of months to years over several subsequent drainage and imbibition processes. Similarly, relative permeability alteration causes an overall decrease in non-wetting phase permeability with increasing exposure time compared with an increase in wetting phase permeability for the same exposure.

This temporal component motivated a new definition for upscaled exposure time at the Darcy-scale, given as:

$$\overline{\chi} := \frac{1}{t_{ch}} \int_0^t X^{\mathrm{WA}} d\tau, \tag{10}$$

where t_{ch} is a pre-specified characteristic time which is used to scale the history of exposure, and X^{WA} is the chosen measure of exposure of WA agent. Exposure may be either modeled as dissolved mass fraction $X^{\mathrm{WA}} = X_w^{\mathrm{CO_2}}$ or as fluid saturation $X^{\mathrm{WA}} = S_n$, depending on whether the WA agent is a dissolved solvent or invading fluid, respectively. We note that $\overline{\chi}$ is a dimensionless non-linear parameter that depends solely on CO_2 concentration or saturation and time, which are all readily available model variables in Darcy-scale simulators.

The above definition of exposure time was then used to formulate the dynamic models for capillarity and relative permeability. In [40], we found that alteration of capillary pressure could be modeled as an interpolation between two static states, where the interpolation coefficient is coupled to macroscale exposure time, $\overline{\chi}$. The resulting formulation is an interpolation-based dynamic capillary pressure model as follows:

$$P_c = \frac{\overline{\chi} S_{ew}}{\beta + \overline{\chi} S_{ew}} \left(P_c^{\mathrm{f}} - P_c^{\mathrm{i}} \right) + P_c^{\mathrm{i}}, \tag{11}$$

where P_c^{i} and P_c^{f} are the capillary pressure functions at the initial and final wetting states, respectively, $\overline{\chi}$ is the exposure time at the Darcy scale, β is a fitting parameter, and S_{ew} is effective saturation which

can be defined as:

$$S_{ew} = \frac{S_w - S_{rw}}{1 - S_{rw} - S_{rn}}, \tag{12}$$

where S_{rw} and S_{rn} are wetting and non-wetting residual saturations, respectively. The end wetting-state capillary pressure functions P_c^{i} and P_c^{f} are modeled as static functions that can be represented by a Brooks-Corey model:

$$P_c^{\mathrm{i}} = c^{\mathrm{i}} S_{ew}^{-1/\lambda} \text{ and } P_c^{\mathrm{f}} = c^{\mathrm{f}} S_{ew}^{-1/\lambda}, \tag{13}$$

where $1/\lambda$ is a parameter that represents pore-size distribution, c^{i} and c^{f} are entry pressures for initial and final wetting-state conditions, respectively.

Similar analysis in [41] showed that relative permeability dynamics could be more efficiently modeled by including the exposure time directly into the function parameters rather than following the interpolation approach used above. Furthermore, we found a reduced LET relative permeability model is preferable due to its flexibility. More specifically, from the original relative permeability models in [49] (six fitting parameters) we have obtained reduced models (two fitting parameters) based on assumptions in the pore geometry, and we have added a dynamic function to capture the wettability dynamics in the relative permeability-saturation curves. This approach results in a dynamic model for relative permeability as follows:

$$k_{rw} = \frac{\mathbb{F}(\overline{\chi}) S_{ew}^{\Lambda}}{1 - S_{ew} + \mathbb{F}(\overline{\chi}) S_{ew}^{\Lambda}}, \quad k_{rn} = \frac{1 - S_{ew}}{1 - S_{ew} + \mathbb{F}(\overline{\chi}) S_{ew}^{\Lambda}}, \tag{14}$$

where the dynamic function $\mathbb{F}(\overline{\chi})$ is given by

$$\mathbb{F}(\overline{\chi}) = \begin{cases} \eta\overline{\chi} + \mathrm{E}^{\mathrm{i}} & \text{if} \quad \overline{\chi} < \frac{E^{\mathrm{f}} - E^{\mathrm{i}}}{\eta}, \\ E^{\mathrm{f}} & \text{if} \quad \frac{E^{\mathrm{f}} - E^{\mathrm{i}}}{\eta} \leq \overline{\chi}. \end{cases} \tag{15}$$

E^{i} and E^{f} are empirical data fitting parameters for the initial and final wetting-state condition and η is a dynamic fitting parameter that controls the WA induced dynamics in the relative permeabilities.

The reader is referred to the cited papers for more details on the comparison between the simulated data and the correlated functions. In summary, the correlated models perform well for any general saturation history resulting in an excellent match with the simulated data, thus demonstrating the robustness of the dynamic models.

We emphasize that the above presentation is intended to provide background on the approach used to understand and model the manifestation of pore-scale WA at the field scale. In this study, only the resulting macroscale dynamic flow functions, Equations (11) and (15), and associated parameters are applied further in field-scale simulations. CA change is not explicitly modeled in these simulations, i.e., θ is not a variable at the field scale, but the mechanisms of CA change described in Equation 9 are implicitly captured in the dynamic flow functions. This implicit connection between pore scale and macroscale is described further in the next section.

2.1.2. Dynamic model implementation and parameterization

The above dynamic models in Equations (11) and (15) with associated parameters are substituted directly into the TPTC model in place of the usual static functions, i.e., capillary pressure relation in Equation (7) and the phase relative permeability functions as part of the Darcy flow equation in (2). The functions are easily implemented in a standard flow simulator, involving only an additional functional dependency on exposure time, itself a straightforward calculation from Equation (10) from model variables.

There are additional parameters in both Equations (11) and (15) which need to be obtained by characterization of the rock-fluid system of interest. For instance, capillary pressures at end wetting states needed in (11) can be obtained from laboratory analysis, possibly by rescaling curves obtained by nitrogen or mercury drainage experiments. For relative permeability, the initial wetting state needs to be fully characterized using a non-reactive fluid.

The dynamic β and η parameters are obtained by characterization of WA, either by fitting to laboratory or numerical pore-scale experiments performed for this purpose. In our analyses in [40] and [41], we found a direct connection between the dynamic parameters and the underlying pore-scale WA model for CA change. In both cases, β and η have a correlated relationship with the pore-scale parameter C in Equation (9). According to [40], the parameter β is represented as a power function of the pore-scale parameter C:

$$\beta = b_1 C^{b_2}, \tag{16}$$

where $b_1 > 0$ and $b_2 > 0$ are fitting parameters and are determined from WA experiments. As C decreases, indicating faster WA, β decreases. If $C = 0$, wettability changes from the initial to final wetting state instantaneously.

On the other hand in [41], the parameter η is related linearly, but inversely, with parameter C as:

$$\eta = -\nu_1 C + \nu_2, \tag{17}$$

where $\nu_1 > 0$ and $\nu_2 > 0$ are empirical fitting parameters. Faster WA (decreasing C) results in increasing η, reaching a maximum value, ν_2, when $C = 0$.

Equations (16) and (17) imply that the dynamic capillary pressure and relative permeability behaviors can be estimated by knowing the CA change at the pore level over exposure time to the WA agent. This could be characterized by relatively straightforward batch exposure experiments under different exposure times, and thus avoiding extensive drainage-imbibition experiments.

2.2. Implementation for macroscale simulation

There are numbers of powerful numerical porous media simulators for TPTC flow scenarios. For instance, DuMux [50], MRST [51], and OPM [42] are among the software that are used to solve multiphase flow models in a porous medium. These simulators solve the flow problem by reducing the continuous system of PDEs to an algebraic system of equations. In this paper, we employed the OPM framework to solve and analyze the TPTC model above.

OPM Flow is a reservoir simulator available in OPM capable of performing TPTC field-scale simulations. This simulator implements a reduced version of the presented TPTC model, where the components in the phases are computed by equilibrium partitioning and molecular diffusion is not included. This simplifications result in faster simulations for advection-dominated problems (e.g., continuous well injection of CO_2). In studies where it is necessary to include molecular diffusion (e.g., CO_2 migration into caprock), then the complete TPTC model implemented in opm-models can be used, which model the mass transfer between phases by fugacity constraints. We refer to the latter simulator as TPTC simulator.

Originally, both OPM Flow and TPTC simulators were developed for flow systems with standard saturation functions under the assumption of static and uniform wetting condition in space and time. We have implemented the dynamic saturation functions in both simulators. This is done by adding the dynamic saturation functions (Equations (11) and (15)) and a new variable $\bar{\chi}$ (Equation 10) to the simulator, whose value is approximated by the weighted (time step Δt over characteristic time t_{ch}) cumulative sum of the measure of exposure of WA agent (S_n or $X_w^{CO_2}$).

The OPM version which is used in this study is based on the 2021-04 Release. The two point flux approximation (TPFA) and backward Euler (BE) method are used to discretize the model in space and time, respectively. The resulting system of equations is linearized using the Newton-Raphson method. The simulator uses automatic-differentiation (AD) to calculate the Jacobian of the system. We refer to [42] for details on the implementation and model setup of Flow. The links to download the corresponding code to reproduce the numerical studies can be found at the end of the manuscript.

3. Numerical experiments and results

In this section, we apply the model and implementation in Section 2 to examine the effect of long-term WA on CO_2 plume migration in the reservoir and containment by the caprock. We consider a change in wettability between two wetting states that is caused by exposure to WA agent, which results in alteration of the saturation functions as described earlier. To understand the important factors affecting long-term WA, we consider different parameters that characterize the fluid-rock system, including intrinsic properties, K, ϕ, c^{i}, flow rate q, in combination with different values of the WA dynamic coefficients, $\beta(C)$, and $\eta(C)$.

The impact is investigated by simulating CO_2 migration under WA for two simple systems: (1) one-dimensional horizontal flow system (1D-H) of constant CO_2 injection and (2) one-dimensional vertical flow system (1D-V) of CO_2 placed under a caprock that is initially sealing. These examples give insight into the impact of WA on storage efficiency and storage containment. Finally, scaling relationships are proposed to understand the parameters for which the impact of WA is significant.

3.1. End-wetting state saturation functions

To start, we present the saturation functions applied in the reservoir for the initial- and final-wetting states. These functions form the basis of the dynamic models for both capillary pressure (Equation 11) and phase relative permeability (Equation 14) presented earlier. The model parameters used in this

study are given in Table 1, and the associated curves are depicted in Figures 2a and 2b. We note that the chosen parameter values for the saturation functions are not measured values but are consistent with values obtained under static wettability conditions in our previous work [40, 41]. However, any end-state saturation functions can be used if appropriate field or lab data are available.

Table 1: Table of model parameters for the numerical studies.

Symbol	Value	Unit
c^{i}	10^4	[Pa]
c^{f}	10^2	[Pa]
λ	3.6	[-]
Λ	1.3	[-]
E^{i}	0.48	[-]
E^{f}	3.37	[-]
ρ_n	716.7	kg/m^3
μ_n	5.916×10^{-5}	Pa·s
ρ_w	1050	kg/m^3
μ_w	6.922×10^{-4}	Pa·s
K	10^{-10}	m^2
S_{rw}	0.2	[-]

We observe that WA reduces the entry pressure to the non-wetting phase by two orders of magnitude, causing the capillary pressure function to shift downward while maintaining the same curvature. For relative permeability, WA dramatically decreases CO_2 mobility while having an opposite impact on the water mobility. The reduction of CO_2 relative permeability is explained by CO_2 preferring smaller pores with reduced entry pressure, which reduces the ease at which CO_2 can flow. On the other hand, larger pores become the preferred flow path for water, leading to higher water relative permeability with intermediate-wet/hydrophobic conditions.

We further analyze the static functions in order to understand the flow system before adding dynamics. To this end, it is useful to describe the predominant mechanisms affecting horizontal and vertical flow by way of the fractional flow function (neglecting capillary pressure):

$$f_n = \frac{1 + \frac{\mathrm{K}}{\mathrm{q}} \lambda_w \Delta\rho g \sin\vartheta}{1 + \frac{\lambda_w}{\lambda_n}}, \tag{18}$$

where λ_α are the phase mobilities defined as $k_{r\alpha}/\mu_\alpha$, $\Delta\rho = \rho_w - \rho_n$, q the total flow rate, and ϑ is the flow inclination angle. Note that the fractional flow in Equation (18) describes horizontal and vertical flow when $\vartheta = 0^\circ$ and $\vartheta = 90^\circ$, respectively.

The fractional flow functions are calculated with the values in Table 1 and depicted in Figures 2c and 2d. We make several observations based on Buckley-Leverett analysis, which is conducted under the assumption of zero capillary pressure for simplicity. When assuming a constant total flow in one dimension, neither end-wetting state will develop a shock as there is no inflection point in the flow functions. However, we note that the CO_2-water front will always advance further for the initial-wet

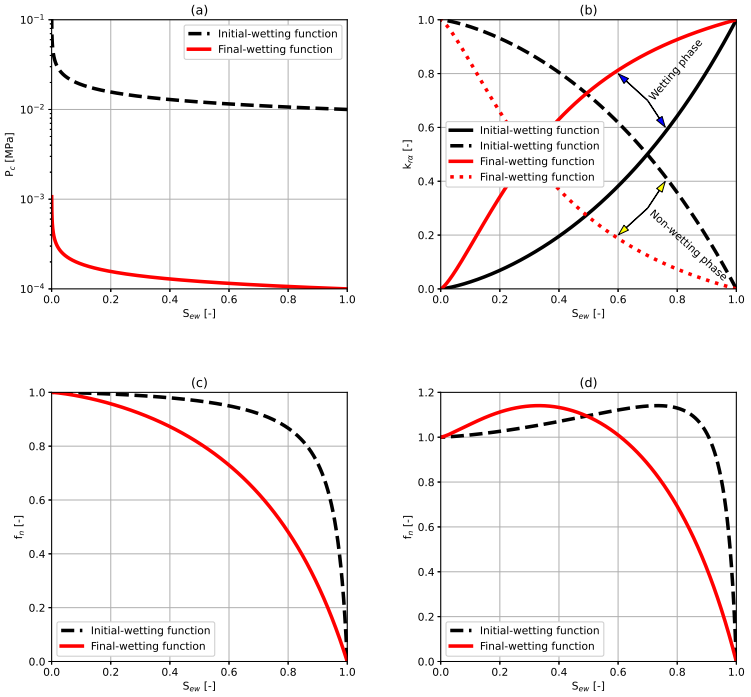

Figure 2: End-wetting saturation functions: (a) capillary pressure, (b) phase relative permeability, (c) fractional flow function for horizontal flow, and (d) fractional flow functions with gravity effect (using the parameters in Table 1 and q=10^{-3} m^3/s).

conditions compared to the final-wet conditions, which applies for both horizontal and vertical flow.

As these curves neglect capillarity, their saturation profile under horizontal and vertical flow will be affected by capillary pressure. Capillarity will smooth saturation shocks and retard the displacing fluid front, and this impact will be greater under initial wet conditions given a stronger capillarity. We also note that constant total velocity is also quite restrictive, but nevertheless gives important insight into flow behavior due to changes in relative permeability and provides a good complement to numerical simulations.

3.2. 1D-horizontal (1D-H) flow system

In this example, we consider a 1600-m homogeneous 1D flow system discretized into 640 equal-sized cells. The system is initially saturated with brine, and CO_2 is injected from the left boundary at a constant rate for one year. The saturation functions are dynamically varied according to the end-wetting states with parameters given previously in Table 1. In this section, we perform all simulations using the dynamic wettability implementation in the OPM Flow simulator. Here, we neglect the effect

of molecular diffusion term and consider the WA agent X^{WA} to be the non-wetting saturation S_n.

In [40, 41], we have found mathematical relationships between the pore-scale parameter C and the dynamic parameters β and η given in Equations (16) and (17). Based on [40, 41], for the simulations we consider the pore-scale parameter C in the interval $[10^{-5}, 10^{-4}]$. The parameters b_1, b_2, ν_1, and ν_2 are estimated by comparing to WA experiments. In this work, we set the values of these parameters to study their dynamical impact in a time scale of order of months ($\mathrm{t}_{ch} = 10^7$ s). For the simulations in the 1D-H study, these values are shown in Table 2. Then, the combination of values β and η are uniquely determined by the value of C. We remark that we use the value of the exponent parameter b_2 as calibrated in [41].

Table 2: Parameters describing the relationship between the pore-scale parameter C associated with CA change and dynamic coefficients β and η for the 1D-H studies ($\mathrm{t}_{ch} = 10^7$ s, $X^{WA} = S_n$).

b_1 [−]	b_2 [−]	ν_1 [−]	ν_2 [−]	C [−]	$\beta = b_1 C^{b_2}$ [−]	$\eta = -\nu_1 C + \nu_2$ [−]
				10^{-5}	1	45
				2.5×10^{-5}	5.2	37.5
10^9	1.8	4.999×10^5	50	5×10^{-5}	18.1	25
				7.5×10^{-5}	37.6	12.5
				10^{-4}	63.1	10^{-2}

3.2.1. 1D-H base-case scenario study

We begin with a base-case scenario where CO_2 is injected for one year for a fixed injection rate, permeability, and porosity, namely $q = 10^{-7}$ m^3/s, K=10^{-10} m^2, and $\phi = 0.1$. First, we examine the base-case scenario under static wetting conditions at the two end states. Figure 3a shows CO_2 migrates far into the domain at low saturation when both functions are in their initial state. Conversely, CO_2 migrates more slowly and fills more of the pore space behind the front when both functions are in their final-wetting states. These results reflect the fractional flow characteristics observed earlier in Figure 2, but now with the added effect of capillarity. We also observe an independent influence of the wetting state of each saturation function. For instance, we observe the impact of different wetting-state relative permeability functions is more significant when the P_c function is weaker (final-wetting) than for the initial-wetting P_c function.

Next, we investigate the isolated impact of wetting dynamics in capillary pressure by varying only the dynamic WA parameter $\beta(C)$ according to the values in Table 2 for the base case scenario. Here, the relative permeability model is kept static at the initial-wetting state. Figure 3b shows that a small C is required in order for the dynamics in P_c to have an observable impact during the one-year simulated time period, where we recall that smaller C implies faster WA dynamics in P_c. In addition, the power-law relationship $\beta(C)$ results in a non-linear dependence on C. An important observation can be made regarding the comparison between fastest WA case $C = 10^{-5}$ and the reference static case using the initial-wetting k_r and final-wetting P_c. One would expect that the dynamic case should be very similar to the static case since the WA dynamics are fast, but here we see that the CO_2 front

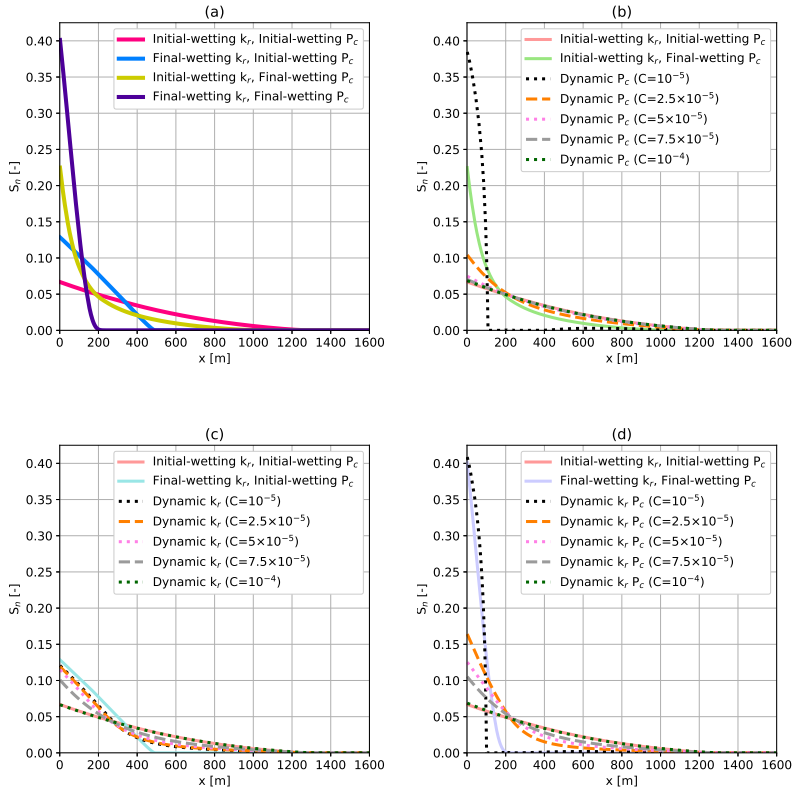

Figure 3: 1D-H CO_2 saturation profiles at one year comparing (a) all combinations of initial- and final-wetting functions, (b) different values of the dynamic capillary pressure, (c) different values of the dynamic relative permeability functions, and (d) both dynamic capillary pressure and relative permeability as given in Table 2.

migrates more slowly and builds to a higher saturation when dynamics are included. This difference indicates that the development of heterogeneous wettability along the horizontal column created by WA dynamics affects CO_2 flow in a complex way that can not be predicted by static wetting simulations alone.

For the isolated impact of dynamics in relative permeability (Figure 3c), we test the same values of C that result in the values of η listed in Table 2. In these simulations, the capillary pressure model is kept static at the initial-wetting state. Since the model for $\eta(C)$ is linear with C, the resulting change in CO_2 migration is more gradual with C than observed for dynamics in capillarity alone. We also observe that the fast-dynamics case ($C = 10^{-5}$) does not match the reference static end-state case (final-wetting k_r, initial-wetting P_c). The CO_2 front in the dynamic case approaches the reference static case towards the inlet (where the wettability has mostly reached the end state), but the front is

significantly more advanced where the wettability is still in a transition between initial and final states.

Combining the impact in both β and η simultaneously (Figure 3d), the results show that the most C cases with slower wettability dynamics remain close to the reference case with static wettability (initial k_r, initial P_c), which shows the impact of WA dynamics is relatively low given the base-case parameters. The saturation at the inlet begins to build evenly for increasing reflecting the altered wetting state there, but it is only for the fastest WA dynamics $C = 10^{-5}$ where we observe a significant alteration of the location of the CO_2 front. Here again, there is a discrepancy between the fast dynamic case and the final reference static case (final k_r, final P_c), showing the complex flow behavior when wettability is varying in space and time along the flow path.

Figure 4 shows the spatial evolution of the upscaled exposure time $\overline{\chi}$ and the non-wetting saturation S_n for the dynamic case $C = 10^{-5}$ in Figure 3d at three different injection times. We observe that after 30 days, the evolution of the dynamic S_n profile is practically the same as the static one. This is expected as the wettability alteration effects start to significantly impact the system after a few months, as observed on the saturation profiles at 180 days and one year respectively. These figures confirm the complex flow behavior when fast dynamics are presented.

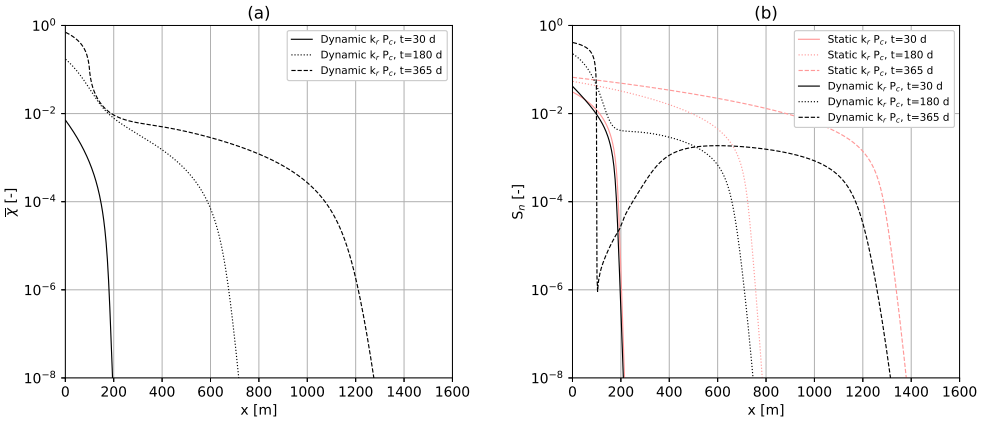

Figure 4: 1D-H (a) upscaled exposure time and (b) non-wetting saturation along the aquifer at three different times for the dynamic case $C = 10^{-5}$ in Figure 3d .

3.2.2. 1D-H capillary scaling

We now compare simulations where rock properties (K, ϕ), injection rate (q), and the pore-scale parameter (C) are considered to vary independently, as given in Table 3. For the purpose of quantifying the impact of WA dynamics in P_c and $k_{r\alpha}$ compared to a static-wet system, we define the scaled front location difference, SFLD, as:

$$\text{SFLD} = \frac{x^{\text{i}} - x^{\text{dy}}}{x^{\text{i}}}, \tag{19}$$

where x^{i} and x^{dy} denote the CO_2 front location using the static initial-wetting functions and dynamic-wetting functions, respectively. The values of x^{i} and x^{dy} are considered as the further spatial location from the injection well of the non-wetting saturation value greater than a threshold value (here 10^{-4}). We avoid x^{i} reaching the boundary by considering smaller values of q, K, and larger values of ϕ as observed in Table 3.

Table 3: Tested parameter values used in the 1D-H system. A set of simulations were performed for each individual value of q, K, and ϕ in which C is varied, where the combined impact on dynamic wettability functions is studied. For each value of C, the corresponding value of β and η is given in Table 2.

q [m^3/s]	K [m^2]	ϕ [-]	C [-]
10^{-7}	10^{-10}	0.1	10^{-5}
5×10^{-8}	5×10^{-11}	0.2	2.5×10^{-5}
2.5×10^{-8}	2.5×10^{-11}	0.4	5×10^{-5}
			7.5×10^{-5}
			10^{-4}

In addition, we employ a macroscale definition of capillary number, $\mathcal{C}a$, in order to characterize the impact of WA with respect to the flow regime for each parameter combination (Table 3). Following [52], we compute $\mathcal{C}a$ on the injection side using the initial entry pressure c^i as:

$$\mathcal{C}a = \frac{\mu_n q A \Delta x}{\phi \mathrm{K} c^i}, \tag{20}$$

where Δx is the length of the grid cell at the entry, A the transversal area, and other parameters are defined previously. The transversal area for these simulations is A=1 m^2. We perform a similar sequence of numerical experiments, first isolating the impact of dynamics in capillarity and relative permeability by allowing dynamics in one function while keeping the opposite function static in the initial-wetting state. Then, we perform experiments of the combined dynamics. The capillary number for these simulations over more than an order of magnitude from 10^{-5} to over 10^{-4}. For reference, the base-case scenario described above has a capillary number of approximately 5×10^{-5}.

We observe the relationship between SFLD and $\mathcal{C}a$ converges onto a single curve for a given C when considering the isolated dynamics in capillary pressure (Figure 5a) and relative permeability (Figure 5b). This implies that the flow regime influences the impact of WA dynamics. Noting the scale difference on the y-axis for both plots, it is evident that dynamics in P_c have a greater effect at low capillary number, slowing the CO_2 front migration by as much as 35%, than dynamics in k_r when C is large (fast WA dynamics) where there is only a 7% reduction in front location. However, the influence of capillarity diminishes more quickly with higher $\mathcal{C}a$ and higher C, and the relative permeability dynamics have a larger impact that is sustained for higher capillary number.

For impact of $\mathcal{C}a$ on the combined dynamics shown in Figure 6, we observe an increased impact at low capillary number when dynamics are modeled in both saturation functions. For example, the impact of WA dynamics in SFLD doubles for $C = 2.5 \times 10^{-5}$ when relative permeability dynamics

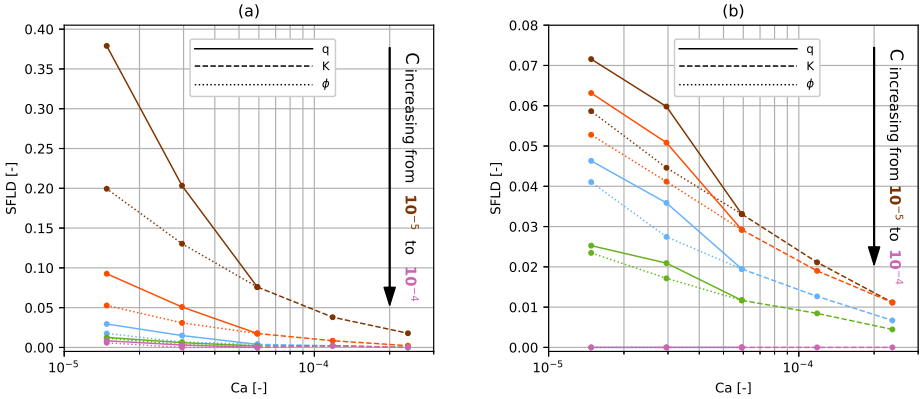

Figure 5: 1D-H scaled CO_2 front location difference (SFLD) as a function of capillary number ($\mathcal{C}a$) for all simulated parameter combinations (see Table 3) under isolated dynamics in saturation functions: (a) capillary pressure and (b) relative permeability.

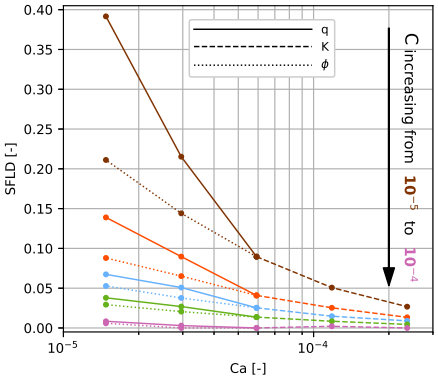

Figure 6: 1D-H scaled CO_2 front location difference (SFLD) as a function of capillary number ($\mathcal{C}a$) for the combined effect on the dynamics in the saturation functions using the values in Table 3.

are added to capillary dynamics, with the increase being greater at higher capillary number. Thus, relative permeability dynamics help to compensate for the disappearing impact of dynamic P_c at higher capillary number.

Intuitively, the results in Figures 5 and 6 reflect the fact that very viscous flows will not be greatly impacted by wettability dynamics in either saturation function. The minimal effect of capillarity at high capillary number is expected given that capillary effects disappear with higher $\mathcal{C}a$, and therefore any additional dynamics in P_c have a negligible effect. But we also see that the impact of relative permeability dynamics also decreases with higher capillary number albeit more slowly. For CO_2 storage

settings, these observations point to the increased importance of wettability dynamics farther from the injection well where capillary forces are likely to be dominant.

3.3. 1D-vertical (1D-V) flow system

In this section, we consider a 1D vertical cross-section of an aquifer-caprock system. This system is employed to demonstrate the impact of WA on containment of CO_2 beneath an initially sealing caprock. This system is modeled as a one-dimensional flow domain of A= 10 m^2 cross-sectional area by H =100 m height. The system is discretized into 100 elements along the height. The top and bottom zones have contrasting permeability and capillary entry pressure. The permeability and porosity in the aquifer are homogeneous and fixed at 10^{-10} m^2 and 0.2, respectively. The caprock permeability is homogeneous and varied in different simulations (see Table 4), while porosity is fixed at 0.2. The caprock is initially water-wet and altered by exposure to dissolved CO_2, such that the wettability altering agent is $X^{\mathrm{WA}} = X_w^{\mathrm{CO_2}}$ for all 1D-V simulations.

The saturation functions in the aquifer are set equal to the final state (intermediate-wet condition) and are kept static. We employ the same end-wetting state parameters used in the horizontal study (refer to Table 1) for the aquifer. On the other hand, different initial-wet entry pressure and permeability values are tested for the caprock section (see Table 4).

The initial condition, depicted in Figure 7a, is set such that a 50% CO_2 saturation is uniformly distributed in a column of height h=70 m. The reservoir pressure is considered to be hydrostatic with regard to brine density and depth of the formation. For this case, the temperature and salinity of the reservoir are considered to be 20°C and 0 ppm, respectively. The diffusion coefficient of CO_2 in the brine wetting phase is set to 2×10^{-9} m^2/s. All boundaries are closed to flow, and the residual saturation of each phase is $S_{r\alpha} = 0.2$. CO_2 mole fraction in the brine phase is set initially to 5×10^{-3}.

The above described condition is initially not at equilibrium due to capillarity and gravity gradients. In the absence of any other driving forces, the CO_2 and brine will redistribute in the aquifer according to buoyancy and capillarity to reach an equilibrium. Simultaneously, CO_2 dissolves into the brine and diffuses into the caprock, altering the capillary entry pressure over time. Since the capillary pressure in the aquifer is small, the equilibration in the aquifer with regard to gravity is in order of days, while the significant WA effects in the caprock starts in the order of years.

We begin with analysis of the static wettability system for different combinations of initial- and final-wetting states for each saturation function. Figures 7b-e show the CO_2 distribution along the column after 100 years for each combination. The first two cases Figures 7b and 7c maintain water-wet conditions in the capillary pressure curve. It is clear that the capillary seal is sufficient to contain CO_2 under the caprock, and containment is not sensitive to the parameters of the relative permeability functions. We also observe the resulting redistribution of CO_2 in the aquifer from the initial condition in Figure 7a results in a near complete gravity segregation of CO_2 and brine, leaving residual CO_2 (with saturation of 0.2) below the accumulated CO_2 column.

In comparison, when the end-wetting capillary pressure curve is directly applied in the caprock (Figures 7d-e), the capillary seal is no longer sufficient to contain CO_2. The difference between Figures 7d and 7e shows the extent to which the wetting properties of the relative permeability affects CO_2

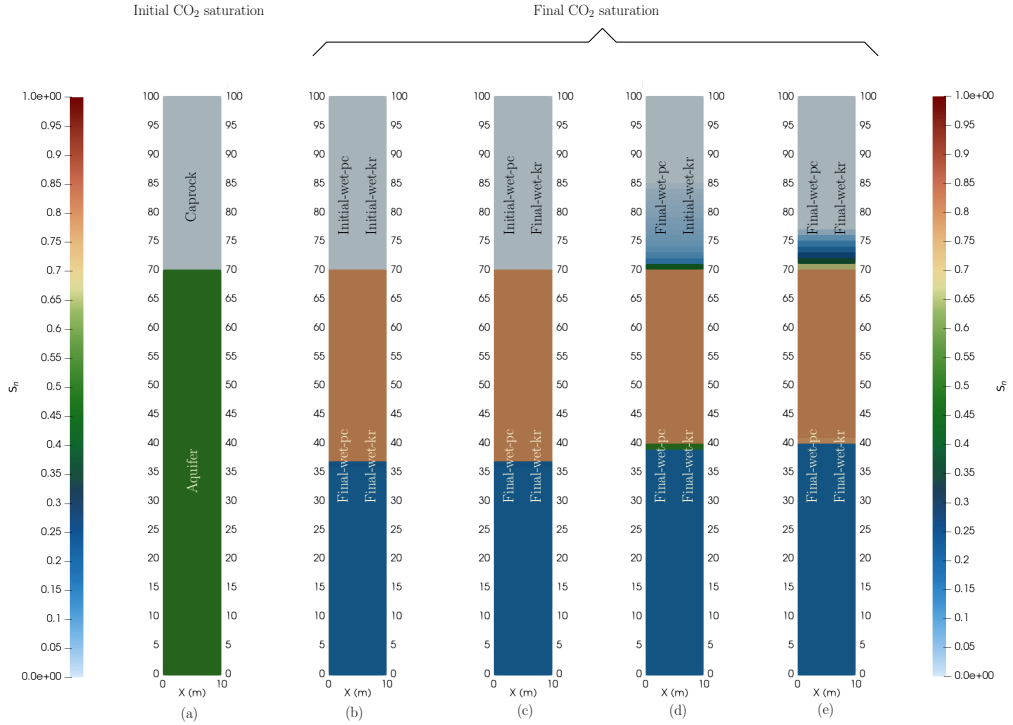

Figure 7: 1Dvfs (a) initial CO_2 saturation and final CO_2 saturation distributions for the (b) initial-pc-initial-kr functions, (c) initial-pc-final-kr functions, (d) final-pc-initial-kr functions, and (e) final-pc-final-kr functions after 100 years.

migration in the caprock over time. This result shows if the wettability state of an initially water-wet caprock is changed by exposure to dissolved CO_2, then CO_2 can eventually migrate into the caprock. The dynamics of the wettability change coupled with diffusion of dissolved CO_2 upward into the caprock will ultimately determine the behavior of CO_2 in this system over time.

Given the dimensions and initial conditions of this closed system, then the maximum amount of CO_2 migrating into the caprock can be estimated. Neglecting the dissolved CO_2 in the brine and assuming the non-wetting phase is mostly CO_2, then the initial mass of CO_2 in the system is $M^{\mathrm{i}}_{CO_2}/A \approx h\rho_n S^{\mathrm{i}}_n \phi = 5 \times 10^3$ Kg/m^2. Considering the residual CO_2 in the aquifer, this results in a maximum migration of CO_2 into the caprock of ca. $M^{\max}_{CO_2}/A \approx 3 \times 10^3$ Kg/m^2. Figure 8 shows the accumulated CO_2 in the caprock over time for the combinations of final capillary pressure function with the initial- and final-relative permeability functions for three different caprock permeability values. As expected, we observe that the CO_2 migrates faster into the caprock for the final-wetting functions, the lower the rock permeability the slower the CO_2 migrates into the caprock, and the amount of CO_2 is limited by the initial and residual saturation ($M^{\max}_{CO_2}/A = 2733$ Kg/m^2).

We now introduce dynamics into the wetting state of the caprock. In this vertical system, the WA

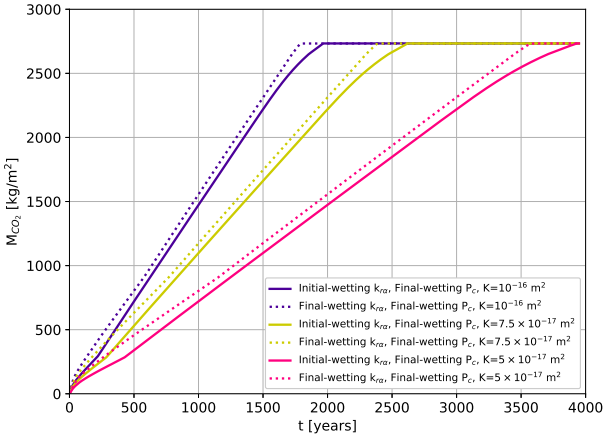

Figure 8: The evolution of CO_2 mass over time in the caprock.

agent is modeled as dissolved mass fraction, i.e., $X^{\mathrm{WA}} = X_w^{\mathrm{CO_2}}$. We recall that the alteration process, or the measure of exposure time, depends on the magnitude of the WA agent. The dissolved CO_2 mass fraction in water is of order 10^{-2} while the non-wetting saturation is of order 10^{-1}. To observe the WA effects within years in the 1D-V studies, we choose relatively higher values for model parameters b_1, b_2, ν_1, and ν_2 (Table 4) in comparison to the ones we considered in the 1D-H simulations (Table 2).

Table 4: Parameters describing the relationship between the pore-scale parameter C associated with contact angle change and dynamic coefficients β and η for the 1Dvfs ($t_{ch} = 10^7$ s, $X^{WA} = X_w^{CO_2}$).

b_1 [−]	b_2 [−]	ν_1 [−]	ν_2 [−]	C [−]	$\beta = b_1 C^{b_2}$ [−]	$\eta = -\nu_1 C + \nu_2$ [−]
				10^{-5}	10^{-2}	4.5×10^{-1}
10^7	1.8	4.999×10^3	5×10^{-1}	2.5×10^{-5}	5.2×10^{-2}	3.75×10^{-1}
				5×10^{-5}	1.81×10^{-1}	2.5×10^{-1}

Similar to the studies in Section 3.2, we perform a sensitivity analysis to quantify the impact of dynamic saturation functions on CO_2 migration into the caprock by varying rock properties (permeability and initial entry pressure) and dynamic parameters ($\beta(C)$ and $\eta(C)$. Here, we examine the impact of WA on the integrity of caprock by

- Case 1: considering WA dynamics only in the capillary pressure function and
- Case 2: considering WA dynamics in both the capillary pressure and relative permeability functions.

Table 5 presents the parameters combinations for the quantification of the two cases mentioned

above.

Table 5: Tested parameter values used in the 1D vertical simulation study. A set of simulations were performed for each individual value of c^{i} and K in which C is varied, where the isolated (only capillary pressure) and combined impact on dynamic wettability functions is studied. For each value of C, the corresponding value of β and η is given in Table 4.

c^{i} [Pa]	K [m^2]	C [-]
10^4	1×10^{-16}	10^{-5}
5×10^4	7.5×10^{-17}	2.5×10^{-5}
10^5	5×10^{-17}	5×10^{-5}

An example of the impact of dynamics in wettability on the vertical CO_2 distribution is shown in Figure 9 for the parameter combination of c^i=10^4 Pa, K=10^{-16} m^2, and C=5×10^{-5} under two different dynamic cases. For Case 1 (Figure 9a), the caprock capillary entry pressure is reduced by exposure to dissolved CO_2, allowing mobile CO_2 to migrate upwards into the low permeability domain. For Case 2 (Figure 9b), an added effect occurs in the caprock. CO_2 migrates upwards into the caprock at a higher saturation when relative permeability is altered, which is in agreement with the shift in fractional flow function for vertical flow from initial to final wetting condition (Figure 2d). Figure 9c shows the evolution of WA induced CO_2 saturation over time in the first grid cell within the caprock domain. For this set of parameters, we observe breakthrough into the caprock after approximately 10 years. Once CO_2 begins to migrate vertically, both cases are characterized by a steep increase followed by a more gradual accumulation of CO_2 in the selected grid cell.

A set of simulations were performed for each individual value of c^{i} and K in which C is varied (Table 5). These numerical results are shown in Figure 10a for Case 1 (isolated P_c dynamics) and Figure 10b for Case 2 (combined dynamics). Comparing the two cases, we observe the build-up of CO_2 follows qualitatively the same response to changes in parameter values, but where the amount of CO_2 in the caprock is less when dynamics are limited to capillary pressure function (Case 1, Figure 10a) than when dynamics are presented in both saturation functions (Case 2, Figure 10b).

As expected, the larger the value of caprock entry pressure, the longer it takes for the CO_2 to start entering the caprock. This starting migration time increases with smaller values of C (slower dynamics on the saturation functions). On the other hand, smaller values of rock permeability result in slower CO_2 migration into the caprock (see also Figure 8), which is also affected by the value of the pore-scale parameter C and entry pressure c^i as observed in Figure 10.

Given the above observations, it may be possible to obtain a general relationship for the impact of WA on CO_2 containment. We first divide the variables by reference values to make them dimensionless. The reference curves for the scaling are the ones giving by the static saturation functions (purple curves in Figures 8 and 10). We have tested different functions for the scaling and selected the ones we describe next. For the time variable, we suggest a translation as a function of the entry pressure and pore-scale

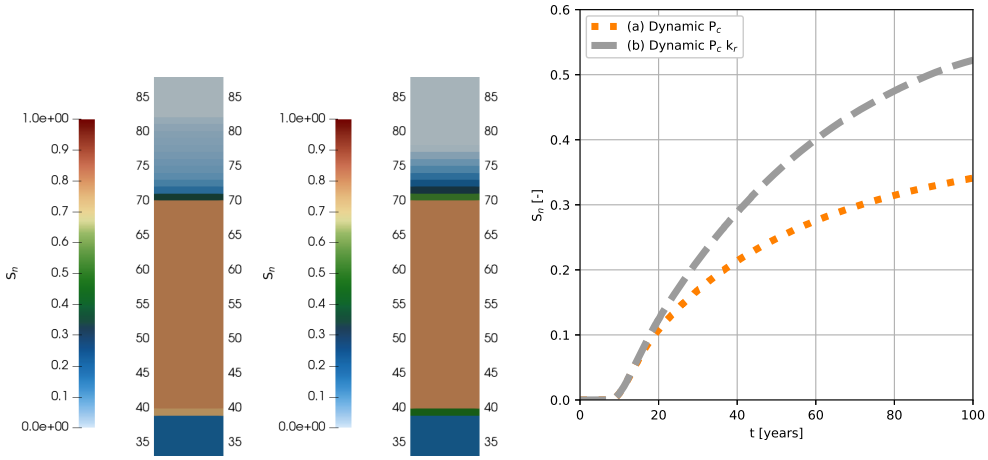

Figure 9: (a) CO_2-water distribution in a column after 100 years given dynamic capillary pressure only and (b) dynamic capillary pressure and relative permeability functions. (c) The evolution of CO_2 over time for the first grid cell on the caprock for cases (a) and (b).

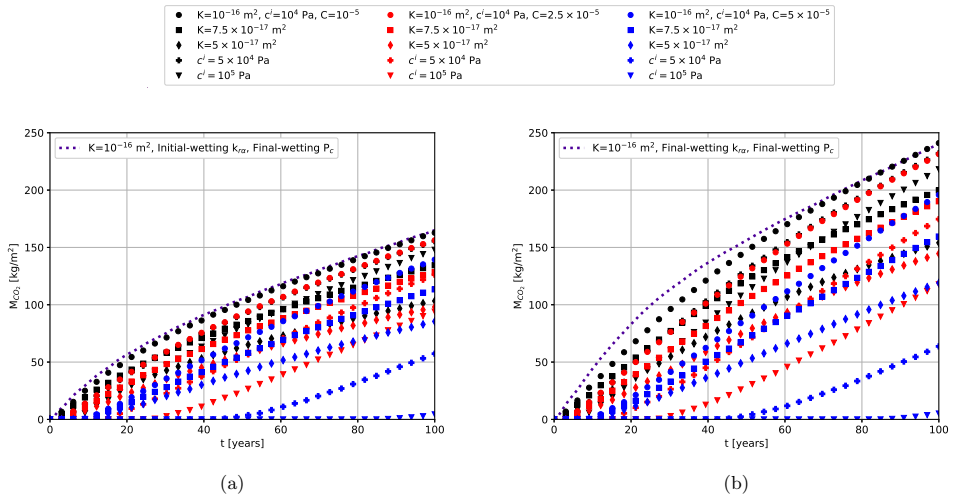

Figure 10: Total CO_2 mass in the caprock over time for each simulated parameter combination: (a) Case 1: dynamic P_c and (b) dynamic P_c and $k_{r\alpha}$.

parameter:

$$\hat{t} = \frac{t}{t_{ref}} - a_0 \frac{c^i}{c_{ref}} \left(\frac{C}{C_{ref}} \right)^{a_1}, \tag{21}$$

where a_0 and a_1 are fitting parameters. For the CO_2 mass in the caprock, we suggest the following scaling function:

$$\hat{M}_{CO_2} = \frac{M_{CO_2}}{M_{CO_2}^{max}} \left[\left(\frac{K}{K_{ref}} \right)^{a_2} \left(\frac{C}{C_{ref}} \right)^{a_3} + a_4 \left(\frac{c^i}{c_{ref}} \right)^{a_5} \left(\frac{C}{C_{ref}} \right)^{a_6} \right], \tag{22}$$

where $a_2, \ldots, a_6$ are fitting parameters.

From Figure 8 we observe a linear behavior between CO_2 mass and time, until reaching a maximum value of mass. This motivates the following relationship between scaled mass and time:

$$\hat{M}_{CO_2} = \min\left(\psi_0 \hat{t}, 1\right) \tag{23}$$

where ψ_0 is a fitting parameter.

Table 6 shows the values of the reference and fitting parameters for both cases. Figure 11 shows the different scaled simulation results. Thus, we have obtained simple models to describe the impact of WA change on CO_2 containment given caprock parameters K and c^i, and dynamic WA parameter C.

Table 6: Reference and fitting parameters.

Case	t_{ref} [y]	c_{ref} [Pa]	C_{ref} [–]	K_{ref} [m^2]	$M_{CO_2}^{\max}$ [kg/m^2]	a_0 10^{-5}	a_1 10^{0}	a_2 10^{-1}	a_3 10^{-1}	a_4 10^{-3}	a_5 10^{0}	a_6 10^{0}	ψ_0 10^{0}
1	10^4	10^4	10^{-5}	10^{-16}	2733	5.3	1.7	4.9	1.2	2.0	1.6	2.4	6.9
2						5.3	1.7	5.0	1.5	2.5	1.6	2.5	10

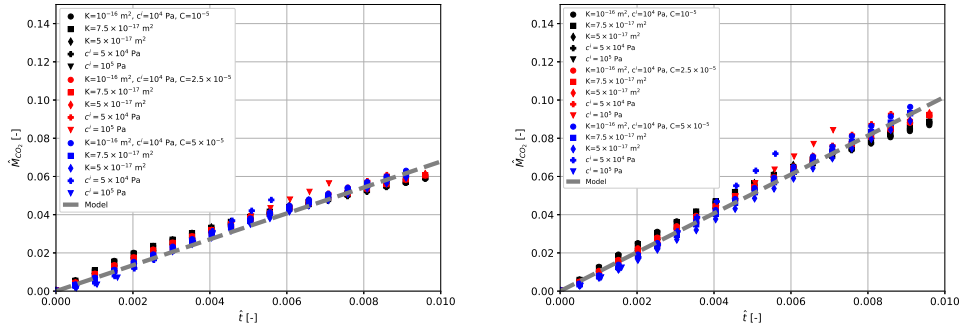

(a) (b)

Figure 11: The scaled amount of CO_2 $\hat{M}_{CO_2}$ in the caprock along the scaled time $\hat{t}$ for the (a) dynamic P_c and (b) dynamic P_c and $k_{r\alpha}$.

4. Discussion

We have implemented dynamic capillary pressure and relative permeability functions to simulate and quantify the impact of WA on CO_2 storage and containment. Horizontal and vertical field-scale test cases were used to demonstrate the effect of WA in CO_2 front migration. These simplified scenarios allowed for testing of a wide range of different rock-fluid and wettability parameters in order to understand the impact of WA in relation to other multiphase flow processes. Our findings show that long-term WA can be characterized according to capillary number for horizontal flow and to caprock integrity parameters for vertical migration. These results can be used to understand the response of CO_2 storage mechanisms to wettability alteration by long-term exposure to supercritical and dissolved CO_2.

4.1. CO_2 storage efficiency

The horizontal case study that focused on the impact of WA on storage efficiency shows the importance of dynamics in both saturation functions, P_c and $k_{r\alpha}$, during CO_2 injection. Wettability change sharpens and delays the front movement, and thus a greater CO_2 storage efficiency results with increasing exposure to injected CO_2. A defining feature of long-term WA is time-dependent heterogeneous wettability, resulting in a wettability gradient outwards from the injection well. Longer exposure time towards the inlet significantly alters wettability over time, while the leading edge of the CO_2 front remains near water-wet. The interplay between dynamically changing saturation functions and heterogeneous wettability leads to an increasingly complex evolution of CO_2 migration with increased injected volumes, even for a simple 1D system. Altered wetting conditions can spontaneously draw CO_2 back towards the inlet by capillary action. These interesting dynamics that may occur over months and years and can have important implications for storage efficiency in systems where WA is expected. More investigation is needed to fully understand the complex behavior caused by long-term WA in non-idealized storage systems.

The horizontal case study results also provide additional insight to the role of WA on storage efficiency as a function of capillary number. The advancing CO_2 front, which can be considered a proxy for storage efficiency, can be significantly impacted at lower capillary numbers, but where the rate of dynamics in the saturation functions plays a important role. At higher capillary numbers, storage efficiency is much less impacted by long-term WA, regardless of the underlying parameters controlling the wettability dynamics. This result gives important insight into the flow regimes where long-term WA is a relevant process (and similarly, where WA dynamics could be neglected). CO_2 storage systems often have a range of flow regimes across the domain at any given time, with highly viscous flows near the injection well and capillary-dominated flow further afield.

4.2. CO_2 containment

The second vertical case with CO_2 migration into the overburden due to long-term WA shows how the same dynamics in P_c and k_r impact storage containment. In contrast to the horizontal case, the vertical WA process is dependent on a certain sequence of effects: (1) diffusion of dissolved CO_2 into

the caprock; (2) reduction of caprock entry pressure by CO_2 exposure that allows supercritical CO_2 to break the capillary seal; (3) vertical migration of CO_2 in caprock. We note that the impact of altered relative permeability only acts once CO_2 is mobile in the caprock. This sequence of processes implies that even if WA induces a loss of containment, it is first and foremost a slow process. CO_2 continually encounters unexposed caprock along its vertical migration path that must be altered by the same slow process in order for vertical flow to continue.

Although we observe that long-term WA by CO_2 exposure leads to loss of containment, our simulations show that CO_2 advances very slowly, but steadily, over time. Our scaling analysis shows that CO_2 migration follows a characteristic evolution that is amenable to scaling by the underlying parameters, which gives insight into a unified model for long-term CO_2 migration into a caprock due to long-term WA. The scaling model is a function of the rate of WA dynamics, caprock permeability, and initial capillary entry pressure. The model is an important generalization and valuable for making use of experimental/surveyed data to predict the integrity of caprocks exposed to CO_2 over long timescales, i.e., one can quantify *a priori* the potential for unwanted CO_2 migration without having to perform field-scale simulations. More importantly, this scaling relationship shows that long-term WA poses very little risk to CO_2 containment. Only with a dramatic reduction in the initial strength of the capillary seal and relatively high caprock permeability will CO_2 migrate vertically in non-negligible quantities over several decades. For the Sleipner CO_2 storage project where caprock permeability is on the order of 100 nanoDarcy and a plume that covers an area of 10 km^2, this would translate to ca. 5 tons over 200 years (assuming WA on both saturation functions, c^i=3 MPa, and C=10^{-5}).

4.3. Numerical implementation of dynamic flow functions

All numerical studies presented in this paper are conducted using the open-source framework OPM. One of the advantages of using OPM is that utilizes modern hardware architecture (i.e., multiple cores and vectorization). We extended the TCTP and flow simulators in OPM to include dynamics in the saturation functions (P_c and $k_{r\alpha}$). Studies on the 1D-H system for large $\mathcal{C}a$ by increasing the injection flow rate would require a large domain to avoid the saturation front to reach the boundary, while keeping the grid size small to reduce numerical errors in the computation of the scaled front location difference (SFLD). Smaller values of K also result in larger $\mathcal{C}a$ while keeping the saturation front closer to the injection well. However, using small grids close to the injection well result in convergence issues. This is expected since the general purpose of OPM Flow is for large field-scale simulations. Then, one could modify further the code (specially the well models) to conduct studies with smaller grids. The time scale for the numerical studies on the 1D-V system is of order of decades, which is computationally expensive for simulations using full TPTC models since dynamics in the saturation functions in addition to computations of phase compositions restrict the size of the time step. Further investigation on solution strategies for this system is required to reduce the computational cost (e.g., by not updating $\bar{\chi}$ after each time step but at certain times).

4.4. Extension to realistic systems

This study has applied the dynamic WA model to relatively simple 1D systems under controlled conditions and homogeneous media. Additional effects become relevant if we are to extend this understanding to realistic 2D and 3D storage reservoirs. For example, CO_2 migration in the reservoir is more complex when affected by gravity and reservoir heterogeneity. In the horizontal 1D systems, we observed a longer CO_2 exposure at the inlet versus further out in the reservoir. With the introduction of gravity, this dynamic could lead to slower upward migration for CO_2 injected down-dip or at the bottom of a thick reservoir. Heterogeneity either in permeability, porosity, or initial wettability will add complexity to dynamics in wettability that needs to be further studied. We note that differences expected in realistic systems apply mainly for migration within the reservoir itself. Vertical migration in a low-permeability caprock is primarily a 1D process even in 3D systems. The main difference in moving to 2D/3D is the possibility for varying CO_2 column height under the caprock interface, which plays a role in the buoyancy forces acting on the rising CO_2.

Another important aspect is the impact of wetting dynamics on CO_2 trapping efficiency as a residual phase. We have not accounted for dynamics in residual saturations in our simulations as the examples used in this study are mainly focused on drainage processes. However, real systems will experience imbibition, especially for CO_2 storage dependent on migration-assisted trapping. Intermediate-wetting conditions will reduce the capillary trapping capacity of reservoir rocks, which leads to a greater portion of CO_2 remaining in a free phase. The change in residual trapping from water- to CO_2-wetting conditions by CO_2 exposure will be strongly coupled to the impacts observed due to dynamic alteration of the flow functions studied here. Although residual trapping has been characterized under static wettability, more work is needed to develop models for dynamic changes in residual trapping due to CO_2 exposure and couple them to the dynamic flow functions implemented in this study. Future studies may address this by adapting the approach proposed by Kassa et al. [40, 41]; however, with additional complexity to the porous medium (i.e., pore-network model instead of parallel capillary tubes).

4.5. Additional pore-scale impacts

In this study, we have seen a marked difference in horizontal and vertical CO_2 migration depending on the rate of wettability alteration as controlled by the pore-scale parameter C. We recall that the implemented dynamic flow functions have been upscaled from pore to core scale. Our results show how pore-scale dynamics are manifested at the field scale and the importance of quantifying C through laboratory experiments. To date, only a few experiments have measured contact angle change through exposure to CO_2 over long timescales, but none have described the temporal evolution of contact angle needed to calibrate pore-scale CA change models such as Equation (9). More experimental evidence is needed to determine if continual CO_2 exposure could fully transform a water-wet rock to strongly CO_2-wet over the long timescales relevant for CO_2 storage.

There are other pore-scale effects that can be of interest for further study, particularly with regard to geochemical impacts. First, CO_2-induced reactions can dissolve and precipitate minerals, thus altering the pore topology of reservoir rocks and caprocks [53]. Changes in pore topology could alter the

flow functions in a similar manner as changes in contact angle, but characterization of the connection between topological alteration and capillary pressure/relative permeability curves requires further investigation. Geochemical alteration can also lead to an increase in permeability, which could enhance vertical CO_2 migration in addition to WA. On the other hand, an increased porosity can counteract the permeability increase. Further study is needed to quantify and characterize the combined impact of geochemical and wettability alteration on CO_2 migration.

5. Conclusion

In this work, we present a macroscale TPTC mathematical model to study long-term WA effects in CO_2 storage applications. Particularly, this model includes macroscale dynamic capillary pressure and relative permeability functions derived from pore-scale WA models. We use OPM to implement the model and perform the numerical studies. Two simple 1-D systems are considered to investigate the WA effects on different flow regimes.

Based on this work our conclusions are as follows:

- Horizontal and vertical field-scale test cases can be used to demonstrate the effect of long-term WA in CO_2 front migration.
- Long-term WA can be characterized according to capillary number for horizontal flow and to caprock integrity parameters for vertical migration.
- Scaling models to quantify CO_2 migration into the caprock show that long-term WA poses little risk to CO_2 containment.

Nomenclature

List of symbols

$\beta,\ \eta$	Dynamic parameters (capillary pressure and relative permeability functions)
$\chi,\ \overline{\chi}$	Cumulative measure of exposure time (pore and Darcy scale)
Δx	Length of a grid cell
$\lambda,\ \Lambda$	Fitting parameters (capillary pressure and relative permeability functions)
$\lambda_w,\ \lambda_n$	Mobilities (wetting and non-wetting phase)
$\mathbb{F}$	Dynamic function for the relative permeability functions
$\mathbb{K},\ \mathrm{K}$	Intrinsic permeability (tensor and scalar)
$\mathbb{R}$	Set of real numbers

$\mathcal{C}a$	Capillary number
$\mu_w,\ \mu_n$	Viscosities (wetting and non-wetting phase)
$\nu_1,\ \nu_2$	Fitting parameters for the dynamic parameter η
Ω	Spatial domain (reservoir)
ϕ	Porosity
$\rho_w,\ \rho_n$	Densities (wetting and non-wetting phase)
τ	Tortuosity
$\theta^{\mathrm{i}},\ \theta^{\mathrm{f}}$	Contact angle (initial and final)
ϑ	Flow inclination angle
$\vec{g}$	Gravitational constant
$\vec{j}_w^k,\ \vec{j}_n^k$	Component k diffusive flux (wetting and non-wetting phase)
$\vec{u}_w,\ \vec{u}_n$	Darcy flux (wetting and non-wetting phase)
A	Cross-sectional area (reservoir)
$b_1,\ b_2$	Fitting parameters for the dynamic parameter β
C	Pore-scale parameter
$c^{\mathrm{i}},\ c^{\mathrm{f}}$	Entry pressures (initial and final)
$D_w^k,\ D_n^k$	Component k molecular diffusion parameter (wetting and non-wetting phase)
$E^{\mathrm{i}},\ E^{\mathrm{f}}$	Wetting-state parameters for the relative permeability functions (initial and final)
F^k	Component k source term
f_n	Non-wetting fractional flow function
$f_w^k,\ f_n^k$	Component k fugacities (wetting and non-wetting phase
$h,\ H$	Height (aquifer and aquifer+caprock)
$k_{rw},\ k_{rn}$	Relative permeability functions (wetting and non-wetting phase)
L	Length (aquifer)
$M_{CO_2}^{\mathrm{i}},\ M_{CO_2}^{\max}$	CO_2 mass (initial and maximum)
$P_c^{\mathrm{i}},\ P_c^{\mathrm{f}}$	Capillary pressure functions (initial and final)

P_w, P_n	Pressures (wetting and non-wetting phase)
q	Injection rate
$S_w,\ S_n$	Saturations (wetting and non-wetting phase)
S_{we}	Wetting phase effective saturation
$S_{wr},\ S_{nr}$	Residual saturations (wetting and non-wetting phase)
t_{ch}	Characteristic time
$x^{\mathrm{i}},\ x^{\mathrm{dy}}$	Non-wetting phase front location (initial and dynamical saturation functions)
$X_w^k,\ X_n^k$	Component k mass fraction (wetting and non-wetting phase)
T	Reservoir temperature

Data availability: The numerical simulator OPM used in this study can be obtained at https://github.com/OPM. Link to complete codes for the numerical studies can be found in https://github.com/daavid00/kassa-et-al-2021.

Acknowledgements: This work was supported by the Research Council of Norway [grant number 255510] and CLIMIT-Demo/Gassnova [grant number 620073] .

References

[1] IPCC. IPCC special report on carbon dioxide capture and storage. Technical report, 2005.

[2] A. Busch, S. Alles, Y. Gensterblum, D. Prinz, D. N. Dewhurst, M. D. Raven, H. Stanjek, and B. M. Krooss. Carbon dioxide storage potential of shales. *Int. J. Greenhouse Gas Control*, 2(3): 297–308, 2008. doi:10.1016/j.ijggc.2008.03.003.

[3] O. Tucker. *Carbon capture and storage*. 2399-2891. IOP Publishing, 2018. ISBN 978-0-7503-1581-4. doi:10.1088/978-0-7503-1581-4.

[4] J. T. Birkholzer, C. M. Oldenburg, and Q. Zhou. CO_2 migration and pressure evolution in deep saline aquifers. *Int. J. Greenhouse Gas Control*, 40:203–220, 2015. doi:10.1016/j.ijggc.2015.03.022.

[5] H. Mori, L. Trevisan, and T. H. Illangasekare. Evaluation of relative permeability functions as inputs to multiphase flow models simulating supercritical CO_2 behavior in deep geologic formations. *Int. J. Greenhouse Gas Control*, 41:328–335, 2015. doi:10.1016/j.ijggc.2015.05.023.

[6] A. Negara, M. F. El-Amin, and S. Sun. Simulation of CO_2 plume in porous media: Consideration of capillarity and buoyancy effects. *Int. J. Numer. Anal. Mod. B*, 2(4):315–337, 2011.

[7] M. Oostrom, M. D. White, S. L. Porse, S. C. M. Krevor, and S. A. Mathias. Comparison of relative permeability–saturation–capillary pressure models for simulation of reservoir CO_2 injection. *Int. J. Greenhouse Gas Control*, 45:70–85, 2016. doi:10.1016/j.ijggc.2015.12.013.

[8] M. Sarkarfarshi, F. A. Malekzadeh, R. Gracie, and M. B. Dusseault. Parametric sensitivity analysis for CO_2 geosequestration. *Int. J. Greenhouse Gas Control*, 23:61–71, 2014. doi:10.1016/j.ijggc.2014.02.003.

[9] D. Bonn, J. Eggers, J. Indekeu, J. Meunier, and E. Rolley. Wetting and spreading. *Rev. Mod. Phys.*, 81:739–805, 2009. doi:10.1103/RevModPhys.81.739.

[10] H. B. Eral, D. J. C. M. 't Mannetje, and J. M. Oh. Contact angle hysteresis: a review of fundamentals and applications. *Colloid Polym Sci*, 291:247–260, 2013. doi:10.1007/s00396-012-2796-6.

[11] W. Anderson. Wettability literature survey-part 5: The effects of wettability on relative permeability. *J. Pet. Technol.*, 39(11):1453–1468, 1987. doi:10.2118/16323-PA.

[12] J.E. Bobek, C.C. Mattax, and M.O. Denekas. Reservoir rock wettability–its significance and evaluation. *Trans.*, 213(01):155–160, 1958. doi:10.2118/895-G.

[13] O. Falode and E. Manuel. Wettability effects on capillary pressure, relative permeability, and irredcucible saturation using porous plate. *J. Pet. Eng.*, 2014:1–12, 2014. doi:10.1155/2014/465418.

[14] S. Iglauer, C. H. Pentland, and A. Busch. CO_2 wettability of seal and reservoir rocks and the implications for carbon geo-sequestration. *Water Resour. Res.*, 51:729–774, 2014. doi:10.1002/2014WR015553.

[15] E. A. Al-Khdheeawi, S. Vialle, A. Barifcani, M. Sarmadivaleh, and S. Iglauer. Impact of reservoir wettability and heterogeneity on CO_2-plume migration and trapping capacity. *Int. J. Greenhouse Gas Control*, 58:142–158, 2017. doi:10.1016/j.ijggc.2017.01.012.

[16] S. Krevor, M. J. Blunt, S. M. Benson, H. Pentland, C, C. Reynolds, A. Al-Menhali, and B. Niu. Capillary trapping for geologic carbon dioxide storage – from pore scale physics to field scale implications. *Int. J. Greenhouse Gas Control*, 40:221–237, 2015. doi:10.1016/j.ijggc.2015.04.006.

[17] R. Rezaee, A. Saeedi, S. Iglauer, and B. Evans. Shale alteration after exposure to supercritical CO_2. *Int. J. Greenhouse Gas Control*, 62:91–99, 2017. doi:10.1016/j.ijggc.2017.04.004.

[18] J. S. Buckley, Y. Liu, and S. Monsterleet. Mechanisms of wetting alteration by crude oils. *SPE J.*, 3:54–61, 1988. doi:10.2118/37230-PA.

[19] S. Drexler, F. Hoerlle, W. Godoy, A. Boyd, and P. Couto. Wettability alteration by carbonated brine injection and its impact on pore-scale multiphase flow for carbon capture and storage and enhanced oil recovery in a carbonate reservoir. *Appl. Sci.*, 10:6496, 2020. doi:10.3390/app10186496.

[20] X. Sun, C. Dai, Y. Sun, M. Du, T. Wang, C. Zou, and J. He. Wettability alteration study of supercritical CO_2 fracturing fluid on low permeability oil reservoir. *Energy Fuels*, 31(12): 13364–13373, 2017. doi:10.1021/acs.energyfuels.7b02534.

[21] H. R. Lashgari, Y. Xu, and K. Sepehrnoori. Modelling dynamic wettability alteration effect based on contact angle. SPE, 2016. doi:10.2118/179665-MS.

[22] M. J. Blunt. *Multiphase flow in permeable media: A pore-scale perspective*. Cambridge university press, 2017.

[23] R. B. Farokhpoor, J. A. Bjørkvik, E. Lindeberg, and O. Torsæter. Wettability behaviour of CO_2 at storage conditions. *Int. J. Greenhouse Gas Control*, 12:18–25, 2013. doi:10.1016/j.ijggc.2012.11.003.

[24] A. Fatah, Z. Bennour, H. B. Mahmud, R. Gholami, and M. Hossain. Surface wettability alteration of shales exposed to CO_2: Implication for long-term integrity of geological storage sites. *Int. J. Greenhouse Gas Control*, 110:103426, 2021. doi:10.1016/j.ijggc.2021.103426.

[25] R. Gholami, A. Raza, P. Andersen, A. Escalona, N. Cardozo, D. Marín, and M. Sarmadivaleh. Long-term integrity of shaly seals in CO_2 geo-sequestration sites: An experimental study. *Int. J. Greenhouse Gas Control*, 109:103370, 2021. doi:10.1016/j.ijggc.2021.103370.

[26] M. Jafari and J. Jung. The change in contact angle at unsaturated CO_2-water conditions: Implication on geological carbon dioxide sequestration. *Geochem. Geophys. Geosyst.*, 17:3969–3982, 2016. doi:10.1002/2016GC006510.

[27] S. Saraji, L. Goual, M. Piri, and H. Plancher. Wettability of sc-CO_2/water/quartz systems: Simultaneous measurement of contact angle and interfacial tension at reservoir conditions. *Langmuir*, pages 1–39, 2013. doi:10.1021/la3050863.

[28] W. J. Plug and J. Bruining. Capillary pressure for the sand-CO_2-water system under various pressure conditions. application to CO_2 sequestration. *Adv. Water Resour.*, 30:2339–2353, 2007. doi:10.1016/j.advwatres.2007.05.010.

[29] T. K. Tokunaga, J. Wan, J. Jung, T. W. Kim, Y. Kim, and W. Dong. Capillary pressure and saturation relations for supercritical CO_2 and brine in sand: High-pressure $p_c(s_w)$ controller/meter measurements and capillary scaling predictions. *Water Resour. Res.*, 49:4566–4579, 2013. doi:10.1002/wrcr.20316.

[30] S. Wang and T. K. Tokunaga. Capillary pressure-saturation relations for supercritical CO_2 and brine in limestone/dolomite sands: Implications for geologic carbon sequestration in carbonate reservoirs. *Environ. Sci. Technol.*, 49:7208–7217, 2015. doi:10.1021/acs.est.5b00826.

[31] S. Wang, I. M. Edwards, and A. F. Clarens. Wettability phenomena at the CO_2-brine-mineral interface: Implications for geologic carbon sequestration. *Environ. Sci. Technol.*, 47:234–241, 2013. doi:10.1021/es301297z.

[32] S. Wang, T. K. Tokunaga, J. Wan, W. Dong, and Y. Kim. Capillary pressure-saturation relations in quartz and carbonate sands: Limitations for correlating capillary and wettability influences on air, oil, and supercritical CO_2 trapping. *Water Resour. Res.*, pages 6671–6690, 2016. doi:10.1002/2016WR018816.

[33] P. Chiquet, D. Broseta, and S. Thibeau. Wettability alteration of caprock minerals by carbon dioxide. *Geofluids*, pages 112–122, 2007a. doi:10.1111/j.1468-8123.2007.00168.x.

[34] C. A. Fauziah, A. Al-Yaseri, E. A. Al-Khdheeawi, N. K. Jha, H. R. Abid, S. Iglauer, C. Lagat, and A. Barifcani. Effect of CO_2 flooding on the wettability evolution of sand-stone. *Energies*, 14 (17), 2021. doi:10.3390/en14175542.

[35] L. M. Valle, R. Rodríguez, C. Grima, and C. Martínez. Effects of supercritical CO_2 injection on sandstone wettability and capillary trapping. *Int. J. Greenhouse Gas Control*, 78:341–348, 2018. doi:10.1016/j.ijggc.2018.09.005.

[36] A. M. Kassa, K. Kumar, S. E. Gasda, and F. A. Radu. Implicit linearization scheme for non-standard two-phase flow in porous media. *Int. J. Numer. Meth. Fluids*, 93(2):445–461, 2021. doi:10.1002/fld.4891.

[37] E. A. Al-Khdheeawi, S. Vialle, A. Barifcani, M. Sarmadivaleh, and S. Iglauer. Effect of wettability heterogeneity and reservoir temperature on CO_2 storage efficiency in deep saline aquifers. *Int. J. Greenhouse Gas Control*, 68:216–229, 2018. doi:10.1016/j.ijggc.2017.11.016.

[38] E. A. Al-Khdheeawi, S. Vialle, A. Barifcani, M. Sarmadivaleh, and S. Iglauer. Influence of CO_2-wettability on CO_2 migration and trapping capacity in deep saline aquifers. *Greenhouse Gases Sci. Technol.*, 7(2):328–338, 2017. doi:10.1002/ghg.1648.

[39] M. Abbaszadeh, S. Shariatipour, and A. Ifelebuegu. The influence of temperature on wettability alteration during CO_2 storage in saline aquifers. *Int. J. Greenhouse Gas Control*, 99:103101, 2020. doi:10.1016/j.ijggc.2020.103101.

[40] A. M. Kassa, E. G. Sarah, K. Kumar, and A. F. Radu. Impact of time-dependent wettability alteration on dynamic capillary pressure. *Adv. Water Resour.*, 142:103631, 2020. doi:10.1016/j.advwatres.2020.103631.

[41] A. M. Kassa, E. G. Sarah, K. Kumar, and A. F. Radu. Modeling of relative permeabilities including dynamic wettability transition zones. *J. Pet. Sci. Eng.*, 203:108556, 2021. doi:10.1016/j.petrol.2021.108556.

[42] A. F. Rasmussen, T. H. Sandve, K. Bao, A. Lauser, J. Hove, B. Skaflestad, R. Klöfkorn, M. Blatt, A. B. Rustad, O. Sævareid, K. Lie, and A. Thune. The open porous media flow reservoir simulator. *Comput. Math. with Appl.*, 81:159–185, 2019. doi:10.1016/j.camwa.2020.05.014.

[43] A. C. Millington and J. P. Quirk. Permeability of porous solids. *Trans. Faraday Soc.*, 57(8): 1200–1207, 1961. doi:10.1039/TF9615701200.

[44] K. H. Coats. An equation of state compositional model. *SPE J.*, 20, 1980. doi:10.2118/8284-PA.

[45] D. V. Voskov and H. A. Tchelepi. Comparison of nonlinear formulations for two-phase multi-component eos based simulation. *J. Pet. Sci. Eng.*, 82:101–111, 2012. doi:10.1016/j.petrol.2011.10.012.

[46] N. Spycher and K. Pruess. CO_2-h_2o mixtures in the geological sequestration of CO_2. ii. partitioning in chloride brines at 12–100°c and up to 600 bar. *Geochim. Cosmochim. Acta*, 69(13):3309–3320, 2005. doi:10.1016/j.gca.2005.01.015.

[47] R. H. Brooks and A. T. Corey. Hydraulic properties of porous media. Technical report, Colorado State University, 1964.

[48] M. T. van Genuchten. A closed-form equation for predicting the hydraulic conductivity of unsaturated soils. *Soil Sci. Soc. Am. J.*, 44:892–898, 1980. doi:10.2136/sssaj1980.03615995004400050002x.

[49] F. Lomeland, E. Ebeltoft, and T. W. Hammervold. A new versatile relative permeability correlation. In *International Symposium of the Society of Core Analysts*. Society of Core Analysts, 2005.

[50] B. Flemisch, M. Darcis, K. Erbertseder, B. Faigle, A. Lauser, K. Mosthaf, S. Müthing, P. Nuske, A. Tatomir, M. Wolff, and R. Helmig. Dumu^x: Dune for multi-{phase, component, scale, physics, ...} flow and transport in porous media. *Adv. Water Resour.*, 34:1102–1112, 2011. doi:10.1016/j.advwatres.2011.03.007.

[51] K. A. Lie. *An Introduction to Reservoir Simulation Using MATLAB/GNU Octave: User Guide for the Matlab Reservoir Simulation Toolbox (MRST)*. Cambridge University Press, Cambridge CB2 8BS, 2019. doi:10.1017/9781108591416.

[52] R. T. Armstrong, A. Georgiadis, H. Ott, D. Klemin, and S. Berg. Critical capillary number: Desaturation studied with fast x-ray computed microtomography. *Geophys. Res. Lett.*, 41:55–60, 2014. doi:10.1002/2013GL058075.

[53] D. Landa-Marbán, S. Tveit, K. Kumar, and S.E. Gasda. Practical approaches to study microbially induced calcite precipitation at the field scale. *Int. J. Greenhouse Gas Control*, 106:103256, 2021. doi:10.1016/j.ijggc.2021.103256.

Graphic design: Communication Division, UiB / Print: Skipnes Kommunikasjon AS

uib.no

ISBN: 9788230842645 (print)
9788230863404 (PDF)